PhD Thesis

A study of the Milky Way disk at different scales: *Insights from red clump stars and open cluster polarimetry*

Submitted in partial fulfillment of the requirements
of the degree of

Doctor of Philosophy

by

Namita Uppal
(Roll No. 18330015)

Under the guidance of

Prof. Shashikiran Ganesh
Astronomy and Astrophysics Division
Physical Research Laboratory, Ahmedabad, India

Department of Physics
INDIAN INSTITUTE OF TECHNOLOGY GANDHINAGAR
2023

Dedicated to my beloved Family

Declaration

I, Namita Uppal, declare that this written submission represents my ideas in my own words and where others' ideas or words have been included, I have adequately cited the original sources. I also declare that I have adhered to all principles of academic honesty and integrity and have not misrepresented or fabricated or falsified any idea/data/fact/source in my submission. I understand that any violation of the above will be cause for disciplinary action by the Institute and can also evoke penal action from the sources which have thus not been properly cited or from whom proper permission has not been taken when needed.

Namita Uppal

(Roll. No. 18330015)

Date: 13-12-2023

Certificate

It is certified that the work contained in the thesis entitled **"A study of the Milky Way disk at different scales: Insights from red clump stars and open cluster polarimetry"** by Ms. Namita Uppal (Roll no 18330015), has been carried out under my supervision and that this work has not been submitted elsewhere for any degree or diploma.

Shashikiran

(Shashikiran Ganesh)
Thesis Supervisor
Professor
Astronomy & Astrophysics Division
Physical Research Laboratory
Unit of Department of Space, Govt. of India
Ahmedabad-380009, Gujarat, India.

Date: 13-12-2023

Acknowledgement

"The journey matters as much as the goals."

- Kalpana Chawla, *1962-2003*

A Ph.D. is a remarkable journey filled with moments of excitement, enthusiasm, and at times frustration and overwhelming that help to transfer a person to a researcher. The successful completion of this journey would not have been possible without the support and contributions of numerous individuals. I would like to acknowledge all of them who have helped or supported me along the way.

First of all, I would like to express my deepest appreciation to my Ph.D. supervisor *Prof. Shashikiran Ganesh*, whose unwavering belief in my potential, invaluable guidance, and the freedom to explore my area of interest have been the basis of my academic growth. I hold deep admiration for his insightful thinking, vision, way of expressing ideas, and, above all, his patience. I have learned a lot from him, and I am certain that my journey of learning will continue indefinitely. I extend my sincere thanks to my Doctoral studies committee members, *Dr. Manash Samal, Dr. Vishal Joshi, and Dr. Durga Prasad*, for their insightful feedback, fruitful discussions, and encouragement throughout the course of the Ph.D. Their suggestions, both in the DSC meetings and outside it, have greatly helped me to improve the quality of my work. I am deeply grateful to my collaborator *Prof. Mathias Schultheis* for the invaluable discussions held over Google Meets, the fruitful exchange of ideas, and the constructive comments and feedback provided. I am truly fortunate to have had the opportunity to collaborate with such a passionate and supportive individual. I would also like to extend my appreciation to my other collaborators *Prof. Santosh Joshi, Dr. Devendra Bisht, and Dr. Vincent Pelgrims* for their contribution to my research projects. I express my profound gratitude to the Director, Physical Research Laboratory (PRL), *Prof. Anil Bhardwaj*, the Dean, PRL, *Prof. Pallam Raju*, and all the academic committee members. I would like to especially mention the names of *Prof. U.C. Joshi* and *Prof. K.S. Baliyan* for the constructive discussions and reviewing of my manuscripts. I am indebted to my Master's dissertation supervisor, *Prof. Sandeep Sahijpal*, who was my inspiration to pursue research in Astronomy. His enthusiasm, tireless dedication, and profound passion for his research have been tremendously encouraging. I wish to express my appreciation to *Prof. Leo Girardi* and *Dr. Ligang*

Hou for generously granting me permission to use figures from their publications in my thesis. I am thankful to all the faculties in the Astronomy and Astrophysics division of PRL for the discussions in the area seminars, which helped to shape my vision towards the different approaches to tackling scientific problems. I am extremely thankful to the time allocation committee (TAC) of both the Mount Abu Observatory, PRL, and Sampurnanand Telescope, ARIES, for giving me enough observation time on the telescopes to accomplish my goals. I thank the telescope operating staff of both observatories for helping in getting smooth observations.

I am grateful to my office colleagues for creating a healthy and friendly work environment. I express my love to my super-senior, *Dr. Archita Rai* for her warm and attentive presence, whether in person or over phone calls. I am truly grateful for the consistent encouragement and support she has offered me at different stages of my PhD journey. I would also like to thank my senior *Dr. Aravind K.* for introducing me to observations and data reductions. The engaging discussions on various astronomical topics, and the efforts to implement our ideas in Python coding, have been both enjoyable and enlightening. A heartfelt thanks to his wife, *Silpa*, for inviting me home, sharing delicious food, especially dosas, and engaging in long conversations filled with stories and experiences. My gratitude extends to *Dr. Prithish Halder*, a PDF in our group, for insightful discussions on ISM dust modeling and your heartfelt wishes for my successes. I thank my junior, *Goldy Ahuja* for infusing humor into the office environment and our discussions on mathematical problems. He has been a great company and motivation for me to work till late-night in the office. I will always cherish the moments spent together discussing and working until the early hours. I am also grateful to my office-colleague-cum-brother *Prashanth* for the care, support, and encouragement provided throughout my PhD. I extend my appreciation to my other office-colleagues-cum-friends, *Deekshya*, and *Alka*, for their love, care, and support. I also thank *Prachi* and *Dr. Anwesh* for helping me with observations whenever needed. Working in such an amazing office group has been a true blessing. A special mention to *Dr. Sandeep Rout*, a senior and an excellent listener. It has always been a pleasure to share both joyful and frustrating moments with him. Thanks to all the seniors in the Astronomy and Astrophysics Division—*Shawnlee, Neeraj, Sushant, Abhay, Biswa, Vipin, Abhijit*—for being a continued source of inspiration and valuable discussions that influenced decisions at various stages of my PhD journey.

I extend my thanks to my junior colleague, *Vineet Rawat*, for engaging in academic discussions that have contributed in many ways to my PhD work. It has been a pleasure to know such talented and dedicated researchers. I also appreciate the continuous support and learning from other juniors in the department—*Birendra, Arup, Sanjay, Arijit, Ashish, Narendra, and Akash*—throughout my PhD.

Hostel life has been an integral aspect of my academic journey, providing a home away from home. I extend my heartfelt appreciation to my batch-mates and friends, including *Dayanand Mishra, Pranav Bhardwaj, Naval Kishore Bhadari, Naba Prakash Nayak, and Monika Devi*, who have become an extended family. The shared laughter, late-night study sessions, discussions on various topics, and joyous moments, all have contributed to making each experience deeply cherished. I am profoundly thankful for the companionship and support from friends -*Akanksha Khandelwal, Vikas Soni, Anju Rani, Sunil, Deva, Sandeep Singh, Tanya Sharma, Meghna Soni, Deepak Gaur, Deepak Rai, Sanjit, Yogesh, Ashu, Siddhartha, Supriya, Anupam, Arijit Roy*. The IIT bus trips to attend lectures were the most enjoyable journeys in my PhD. The support and companionship of Batch 2018 have made this journey unforgettable. Together, we faced challenges, celebrated victories, and created a tapestry of memories that will forever hold a special place in my heart. I would like to extend a special note of thanks to *Yash Srivastava*, my constant food partner and one of the greatest friends I have ever had in my life. His unwavering encouragement, presence during challenging and joyous times, and enduring belief in me, have been invaluable. In his company, I have found the strength to overcome obstacles and grow not only as a person but also as a researcher. His friendship has enriched my life in countless ways, and for that, I am eternally grateful. His passion for research and contributions to the scientific community has always been a great inspiration to me.

The festive celebrations, like Holi, Diwali, Christmas, New Year, and others, were truly elevated by the active participation of both seniors and juniors in the hostel. My heartfelt gratitude is extended to all hostel members who played a role in making these festive seasons incredibly memorable. Special thanks go to hostel-mates *Subir, Alka Rani, Harish, Shivani, Sana, Anshika, Ankit, Madhu, Varsha, Kiran, Shreya, Soumya, Malika, Neha, Kimi, Trinesh, Dibyendu, Soumik*, and many others who contributed in various ways in my PhD journey.

I express heartfelt gratitude to my dearest friend, *Rishabh Bansal* whom I befriended during my Master's at Panjab University, Chandigarh. His consistent support during challenging times, despite the busy schedules, has been priceless. The phone conversations, even after long intervals, have always provided comfort and uplifted my spirits. His friendship has been a constant source of strength in my life.

I am deeply in debt to my family, who have been my pillar of strength throughout my whole journey. Their boundless love, support, and constant encouragement have been instrumental in helping me overcome the countless challenges I encountered along the way. I am forever obliged to my parents, my guiding lights, for their sacrifices and unconditional love and for providing me with an environment where I could thrive and pursue my dreams. I am grateful to my younger brother, *Ankush*, and elder sister, *Shilpa*, for their constant support, encouragement, and inspiration, which always motivated me to move forward in my life. I am thankful to the cute little member of my family, my dear *Jainish*. Simply hearing her sweet voice fills my day with joy and adds a cheerful touch to every moment. I dedicate this thesis to my beloved family, whose unwavering belief in me has been the driving force behind my achievements.

In additions to mentors, family and friends, I would also like to acknowledge the *Coldplay band* for providing a melodic backdrop to my academic journey. Their songs, such as 'Everyday life', 'Everything's Not Lost', 'Fly-on', 'The Scientist,' and 'The sky full of stars,' have been a source of inspiration, accompanying me through the highs and lows of my research. Lastly, to all those who have contributed in big or small ways, I am sincerely grateful. Your collective impact has left an unforgettable imprint on my academic and personal growth.

Abstract

Understanding the formation and evolution of the galaxies has been a topic of interest for centuries. While our location within the Galaxy allows us to investigate individual stars in greater detail, this position also limits our ability to gain a clearer picture of its structure. Converting the 2D positions of celestial objects, in the plane of the sky, into their 3D distributions is particularly challenging due to uncertainty in the distance information. Despite these challenges, we know that the Milky Way is a barred spiral galaxy, though the finer details like the number of arms, their position, and extent are still highly debated. In addition to the inner structures, the outer parts of our galactic disk have many interesting features, including the warp and the flare, whose origin is not very well known. Most of the present understanding of the Milky Way disk structure has come from younger tracers like HI, HII, HMSFR, OB stars, young open clusters, and Cepheids. However, there are some evidences of age dependency on these features. Therefore it becomes essential to study the Galactic disk structures in terms of different age populations, especially using older traces.

In this work, the red clump (RC) stars, an indicator of the older populations, have been utilized to unravel the inner and outer structures of the Galactic disk. A sample of ~ 8.8 million red clump stars is selected from 2MASS with foreground contamination eliminated using Gaia data. It represents the largest sample of RC stars now available in the literature, systematically covering the entire Galactic plane in the range $40^\circ \leq \ell \leq 320^\circ$ and $-10^\circ \leq b \leq +10^\circ$, avoiding the directions towards the Bulge. The obtained over-density of RC stars mapped the spiral structure beyond the extent of the structures traced by Gaia. This over-density map also shows a 6 kpc long feature of the Outer arm extended beyond the previously known limits. The 3D distribution of red clump stars offers insights into the face-on view of the Galactic disk and unveils strong flare and warp signatures in the Galactic disk. Comparisons between structural

features identified in red clump stars and those detected in younger populations provide valuable constraints for models of Galactic evolution.

In contrast to stars, dust is more confined to the Galactic disk, which makes it an ideal candidate for tracing the structures at large and small scales. Although the distribution of dust become profound at longer wavelength, but the distance estimation at these wavelengths suffers large uncertainties. Thus, constructing a three-dimensional map directly based on the dust distribution is challenging. Nevertheless, the properties of interstellar dust, such as extinction and polarization at optical wavelengths, can be explored as an indirect probe of the dust distribution. Several attempts have been made to construct 3D extinction maps, but extinction being a derived quantity, may lead to potential ambiguities. On the other hand, the polarization of starlight from the intervening dust grains is a directly observed quantity. Therefore, the study of polarized light presents a promising approach to trace the dust distribution when combined with the distance information of the respective stars. Despite the potential usefulness of polarization observations for mapping dust, not many dedicated studies have targeted this approach. A systematic study of polarization, covering the Galactic plane, could be helpful to map the dust in the disk and trace the underlying structures. This thesis demonstrates the utility of polarization as a powerful tool for deciphering both small-scale and large-scale structures associated with dust distribution. In pursuit of this objective, open clusters are selected as observation targets, leveraging the presence of multiple stars at similar distances to obtain statistically robust constraints on distance and polarization measurements. The polarization observations of a total of fifteen Galactic open clusters were performed using Indian observational facilities. The clusters were targeted in three different lines of sight in the northern sky, firstly to cover the regions of low, high, and intermediate extinction and secondly to explore the distribution of dust in the sight-lines crossing the spiral arms and parallel to the spiral arms. The resulting variation in polarization measurements towards each line of sight traces the dust distribution at different scales. It also provides strong evidence, at optical wavelengths, for the alignment of large scale magnetic field along the spiral arms of the Galaxy.

The work described in this thesis exemplifies the significance of the distribution of the older population in comparison to the younger population in tracing the large-scale

structure of the Galactic disk. This thesis also presents a strong justification for the requirement of the ISM polarization observations of background stars along with their distance information covering wider regions of the Galactic plane for mapping dust distribution at different scales.

List of Publications

Peer - Reviewed Journals

1. **Uppal, N.**, Ganesh, S. and Bisht, D., 2022. *Optical linear polarization study towards Czernik 3 open cluster at different spatial scales.* The Astronomical Journal, 164(2), p.31. DOI: 10.3847/1538-3881/ac7445.

2. **Uppal, N.**, Ganesh, S. and Schultheis, M., 2023. *The Outer spiral arm of the Milky Way using Red Clump stars*. Astronomy & Astrophysics, 673, A99. DOI: 10.1051/0004-6361/202244548.

3. **Uppal, N**, Ganesh, S. and Schultheis, M., *Warp and flare of the old Galactic disc as traced by the red clump stars*. Monthly Notices of Royal Astronomical Society, Volume 527, Issue 3, January 2024, Pages 4863–4873. DOI: 10.1093/mnras/stad3525

Under preparation

4. **Uppal, N.**, Ganesh, S., Pelgrims, V., Joshi, S., *Linear polarization study of open clusters towards anti-centre direction: Signature of spiral arms*.

5. **Uppal, N.**, Ganesh, S., et al., *Polarization study of open clusters towards extincted regions of the first Galactic quadrant.*

Conference Proceedings (Refereed)

1. **Uppal, N.**, Ganesh, S., Joshi, S., Sarkar, M., Prajapati, P. and Dileep, A., *Optical polarization study of Galactic Open Clusters*, Bulletin of Liège Royal Society of Sciences,

3rd Belgo-Indian Network for Astronomy and Astrophysics (BINA), Accepted for publication. DOI: 10.48550/arXiv.2311.09617

2. Ganesh, S., Rai, A., Aravind, K., Singh, A., Prajapati, P.V., Mishra, A., Kasarla, P., Sarkar, D.R., Patwal, P.S., **Uppal, N**. and Chandra, S., 2020, December. *EMPOL: an EMCCD-based optical imaging polarimeter*. In Ground-based and Airborne Instrumentation for Astronomy VIII (Vol. 11447, p. 114479E). International Society for Optics and Photonics. DOI: 10.1117/12.2560949.

Conference/ Workshop

Oral presentations

1. Oral Presentation on 'Tracing the Large Scale Structure of the Galactic Disk: Insights from 2MASS red clump stars' in a hybrid International conference **Surveying the Milky Way: The Universe in Our Own Backyard** held in Caltech, Pasadena during 23-27 Octobber 2023 (attended online).

2. Oral Presentation on 'The Outer Arm of the Milky Way from red clump stars' in an in-person International conference **The Milky Way Revealed by Gaia: The Next Frontier** held in Institute of Cosmos Sciences (ICCUB-IEEC), Barcelona during 5-7 September 2023.

3. Oral presentation titled 'Detection of Galactic warp using intermediate age population' in an in-person, national conference: **41st meeting of Astronomical Society of India** at Indian Institute of Technology, Indore (1-5 March 2023)

4. Oral presentation titled 'Optical polarization study of Galactic Open Clusters' in an in-person International conference, **3rd BINA workshop** hosted by ARIES at Graphic Era Hill University, Bhimtal (22-24 March 2023)

5. Oral presentation titled 'Polarization observations of Open clusters using AIMPOL' in national conference/workshop **Role of meter-class telescopes in modern-day Astronomy** held on 17-19 October 2022 (in-person) at ARIES Nainital in celebration of Golden Jubilee of 104-cm Sampurnanand telescope.

Poster presentations

1. Poster Presentation on ‘Galactic Morphology and magnetic field tomography using interstellar polarization’ in a hybrid International conference **Surveying the Milky Way: The Universe in Our Own Backyard** held in Caltech, Pasadena during 23-27 Octobber 2023 (attended online).

2. Poster presentation titled ‘Milky Way disk revealed by Red clump stars’, Ph.D. Research Showcase at IIT Gandhinagar on January 27, 2023.

3. e-Poster presentation titled ‘Milky Way disk revealed by red clump stars’ in national conference **Young Astronomers’ Meet** held on 9-13 November 2022 (Hybrid mode) at Aryabhatta Research Institute of Observational Sciences (ARIES), Nainital, India.

4. e-Poster presentation titled ‘Dust distribution towards Czernik3 at different spatial scales in 2nd Galactic quadrant’ in inter-national conference **Gaia Symposium-DR3 and beyond** held on 11-15 July 2022 (hybrid) at Indian Institute of Astrophysics, Bangaluru, India.

5. Poster presentation titled ‘Optical linear polarization towards Czernik 3: A distant open cluster in Galactic plane.’ in a national conference 40^{th} **meeting of the Astronomical Society of India** held on 25-29 March 2022 (in-person) at Indian Institute of Technology, Roorkee, India.

Attended

1. Attended an international conference - **Galactic Science and CMB foregrounds** held at Tenerife, Spain (Hybrid) on 12-15 December 2022.

2. Attended an international online conference - **2021 GALAH science meeting** held on 22-24 July 2021

3. Attended an international online conference, **Looking at the polarized Universe: past, present, and future**, held from 24-28 May 2021 at University of Crete in Heraklion, Greece

4. Attended a national conference (online) - **39th Annual meeting of Astronomical Society of India**, held on 18 to 23 February, 2021.

5. Attended an international conference (online) **Gaia Symposium DR2 and beyond**, organized by IIA on 2-6 November 2020.

Seminar Details

Seminars outside institute

1. 'The structure of Milky Way galaxy at different scales' at Lagrange Observatoire de la Côte d'Azur, Nice, France on 03 October 2023 (in-person).

2. 'Probing the Galactic disk structures using red clump stars and interstellar dust.' at Institute of Astrophysics, FORTH; University of Crete, Greece on 08 November 2023 (online).

Division seminars

1. **Topic**:*Distance estimation from Gaia Parallax*
   Date : *July 23, 2020*
   Mode : *Online*

2. **Topic**: *Interstellar polarization towards Czernik 3 Open cluster*
   Date : *July 15, 2021*
   Mode : *Online*

3. **Topic**: *Tracing the Milky Way disk structure using red clump stars*
   Date : *April 7, 2022*
   Mode : *Offline*

4. **Topic**: *Inner and outer structures of Galactic disk traced by red clump stars*
   Date : *May 25, 2023*
   Mode : *Offline*

Weekend student seminars

1. **Topic** : *An Introduction to Galactic Astronomy*
   Date : *October 2, 2021*
   Mode : *Online*

2. **Topic** : *Probing Milky Way structure*
   Date : *April 17, 2022*
   Mode : *Online*

Other contributions (Not related to thesis)

Astronomical Telegram

Uppal, N., Chandra, S., Ganesh, S., Prince, R. and Rakshit, S., 2022. *High optical linear polarization of the blazar S4 0954+ 65 observed from MIRO.* The Astronomer's Telegram, 15419, p.1

Unpublished posters

Aravind K., Prithish Halder, **Namita Uppal**, Prachi Prajapati, Shashikiran Ganesh, Optical polarimetric study of cometary dust, e-poster, 40^{th} meeting of Astronomical Society of India, 2022.

Contents

List of Figures

List of Tables

List of Abbreviations

2MASS	Two Micron All Sky Survey
ADQL	Astronomical Data Query Language
AIMPOL	ARIES Imaging POLarimeter
APOGEE	Apache Point Observatory Galactic Evolution Experiment
ARIES	Aryabhatta Research Institute of Observational Sciences
CC	Color-color (diagram)
CCD	Charged Coupled Device
CDS	Centre de Données astronomiques de Strasbourg
CHeB	Core Helium Burning
CMD	Color Magnitude Diagram
DR	Data Release
DSS	Deep Sky Survey
EDR	Early Data Release
EMCCD	Electron Multiplying Charge Coupled Device
EMGAIN	Electron Multiplicative GAIN
EMPOL	EMCCD based POLarimeter
FOV	Field Of View
HI	Neutral Hydrogen
HII	Ionized Hydrogen
HB	Horizontal Branch

HMSFR	High Mass Star-Forming Region
HR	Hertzsprung-Russell (diagram)
HWP	Half Wave-Plate
IR	Infrared
ISM	Interstellar medium
LAMOST	Large Sky Area Multi-Object Fibre Spectroscopic Telescope
MS	Main Sequence
NIR	Near Infrared
OB	O and B type stars
Pan-STARRS	Panoramic Survey Telescope and Rapid Response System
RC	Red clump
RGB	Red Giant Branch
SDSS	Sloan Digital Sky Survey
SNR	Signal to noise ratio
WISE	Wide Field Infrared Survey Explorer

Chapter 1

Introduction

"Astronomy, by the eminence of its subject and the flawlessness of its theories, is the most beautiful monument of the human spirit, the most distinguished decoration of its intellectual achievement."

- Pierre-Simon Laplace, *Exposition du Systéme du Monde (1835)*

On a moonless night, away from the light pollution of the city, one can see a spectacular view of the heavens in the sky. The mesmerizing sight of a faint white nebulous glow with some dark patches in between, stretching from one horizon to the other (as seen in Fig. 1.1), is nothing but our Galactic home, named the Milky Way galaxy. The term "Milky Way" is a translation of Latin *Via Lactea* and came from Greek mythology, which relates the band of faint hazy light with the stream of spilled milk. However, the name of our galaxy and folktales differ from one culture to other. In the Indian context, the Milky Way is referred to as *Akashganga* and is considered as a path or heavenly 'avatar' of the sacred river Ganges. Today, we know that the cloudy structure is composed of billions of stars, dust, and gases, which seem so close together that an unaided eye

Figure 1.1: Milky Way in the northern hemisphere from Hanle, Ladakh, India. Mosaic photographed and assembled by Dorje Angchuk, Indian Institute of Astrophysics (IIA). *Image credit: Dorje Angchuk.*

cannot distinguish them as individual objects. There are around a hundred billion such galaxies in the universe, and the Milky Way is just one of them. Understanding the formation and evolution of the galaxies has been a topic of interest for centuries. The unique advantage of studying the Milky Way is our ability to investigate individual stars in great detail due to our position within the galaxy. This makes the Milky Way a Rosetta Stone for understanding galaxies in general. Before learning about the formation and evolution history of our galaxy, one should know the current structure of the Galaxy. Despite being located inside the galaxy, we still do not have a detailed picture of its structure. Our location in the Galaxy makes it challenging to map the whole structure. It is analogous to mapping the whole city just by looking outside the window of your room. In other words, we cannot observe our own Galaxy in the same way as we could observe from a vantage point outside the Galaxy to understand its structure. Scientists all around the world have long been fascinated with the study of our home galaxy. The contributions of a few researchers are highlighted in the next section to describe the beginning and evolution of the Galactic studies.

1.1 Evolution of our understanding of the Milky Way

The late medieval picture of the world was dominated by the geocentric theory of Aristotle. The glowing, hazy path, i.e., the Milky Way galaxy, was first observed from a telescope by Galileo Galilei (Galilei, 2016, translated version of 1610 edition). He discovered that the path is not made up of a celestial fluid but consists of innumerable individual stars close together, which cannot be resolved by the naked eye. Hence, the Milky Way band is just an optical effect of a large number of stars. In the middle decades of the Eighteen century, three observers, Thomas Wright (An Original Theory or New Hypothesis of the Universe, Wright, 1750), Immanuel Kant (General natural history and theory of heavens, 1755), and Heinrich Lambert (Cosmologische Briefe, Lambert, 1761), tried to explain the milky band of stars in the night sky and proposed a disk-like shape of the Galaxy. Around the same time, the Herschel family (William, Caroline, and John) mapped the sky to find the shape of the Galaxy (Herschel, 1785) by observing stars in 683 different sightlines using a reflecting telescope. In interpreting the 2D observations into the 3D structure, they assumed that: i) all the stars have the same intrinsic brightness, and ii) they could see the stars up to the edge of the Galaxy. Mapping the distribution of stars with these assumptions, they concluded that the Milky Way galaxy has a disk shape, i.e., the distribution of stars centered at the Sun extends approximately five times in the plane region of the Galaxy as compared to the direction perpendicular to it (map shown in Fig. 1.2). William Herschel also observed hundreds of nebulae in different

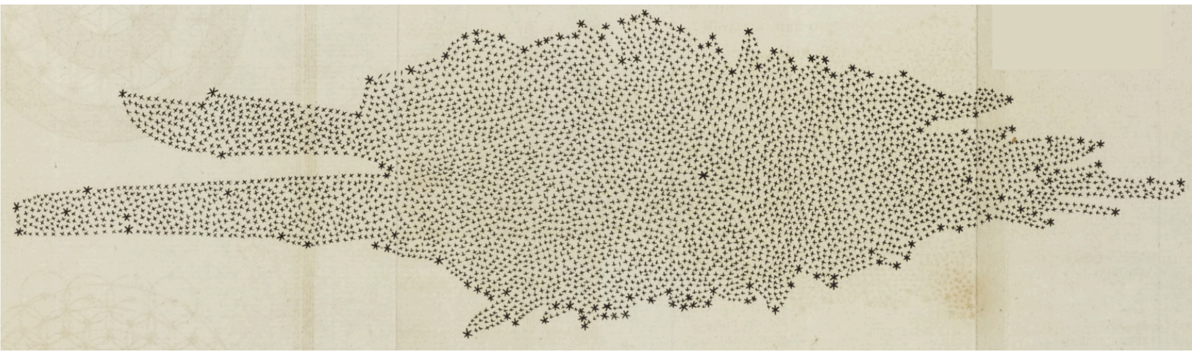

Figure 1.2: Herschels' map of the Milky Way galaxy derived by counting stars in different directions of the sky. *Image source: On the construction of Heavens, William Herschel, 1785*

sky parts; some were truly nebulous, while others could be resolved into stars. In 1845, the third Earl of Rosse observed the spiral structure of the nebula, Messier 51, with his 6ft reflector at Birr Castle in Ireland. He was the first to discover the spiral structures in many nebulae (Hoskin, 1985). Since then, many observers at Birr have found spiral structures in several more nebulae. Some astronomers suggested that our galaxy also has a spiral structure. However, whether the spiral nebulae were part of our galaxy or an *island universe* was a matter of debate, which depended on the size of the Galaxy.

In the early 1900s, with the advent of photographic plates, Jacobus Kapteyn studied the proper motion of stars of different magnitudes in 200 directions to understand the 3-dimensional picture of the Milky Way galaxy referred to as the Kapteyn universe (Kapteyn & van Rhijn, 1920; Kapteyn, 1922). Kapteyn's universe was in agreement with the Herschel map of the Galaxy, with the sun as the center of the spheroidal distribution of stars and the density of stars falling uniformly from the center of the Galaxy. On the other hand, Harlow Shapley presented an entirely new view of the Milky Way galaxy (Shapley, 1918a,b; Shapley & Shapley, 1919; Shapley, 1919a,b). While studying the Globular clusters, he found that the different Globular clusters were distributed in a spherical arrangement, with the Center not at the Sun but towards the brightest portion of the Milky Way. Based on this observation, he proposed that the dynamical center of the Milky Way is in the direction of the Sagittarius constellation, which is 15 kpc away from the Sun. On the basis of the distance of Globular clusters (assuming the same size and luminosities), he concluded that the extent of the Milky Way was ten times larger than the Kapteyn universe. Although the idea of Shapley's model of the Galaxy discarded the Heliocentric system, his enlarged Milky Way model was not universally accepted. In view of the large size of the Milky Way model, Shapley believed the spiral nebulae present in the night sky to be a part of the Milky Way galaxy. On the other hand, researchers favoring Kepteyn's smaller universe consider the spiral nebulae as independent systems like the Milky Way. The controversy concerned with the scale and makeup of the universe was discussed as a part of a lecture series at the National Academy of Science in 1920, now known as the 'Great Debate' (more details in Hoskin, 1976). In the meeting, Harlow Shapley presented his ideas favoring his enlarged model of the Galaxy, while Heber Curtis from the Lick Observatory favored the extra-galactic nature of spiral nebulae. The debate ended when Hubble observed Andromeda nebula with the 100 cm Mount Wilson telescope (Hubble, 1922). Through his observations of a Cepheid variable star and utilizing Shapley's theories on distance determination for nebulae, Hubble calculated the distance to Andromeda to be one million light-years, placing it well beyond the boundaries of Shapley's model. He hesitated to publish his results of spirals as an independent universe at that time. But at the end of 1924 with more data, he finally broke his silence and presented his findings in a paper (Hubble, 1925) at a meeting of the American Astronomical Society in 1925. The galactic dynamical models proposed by Lindblad and Oort further substantiated Shapley's earlier suggestions regarding the location of the Galactic center. Nevertheless, the distance of the Sun to the Galactic center calculated by Oort was one-third the size of Shapley's estimate. The overestimation of distance by Shapley was due to his unawareness of the absorbing material along the line of sight. Till 1930, the dark regions in the sky were thought of as holes in the cosmos or regions devoid of stars. The obscuration by dust between the stars was first recognized by Trumpler while studying a sample of open clusters (Trumpler, 1930a,b). He observed that the distant clusters were systematically fainter than expected from their distances (calculated from the angular diameter and by assuming the same intrinsic size for all the clusters). The excess dimming was demonstrated to be due to the presence of a strongly absorbing interstellar medium.

Our understanding of the Galactic structure has evolved significantly since 1920. Several astronomers proposed that our Galaxy has features similar to the spiral nebulae. A major breakthrough towards understanding the Galactic spiral structure happened in the 1950s when Morgan and his colleagues found imprints of three spiral arm segments in the solar neighborhood using photometry of OB stars (Nassau & Morgan, 1951; Gingerich, 1985, and references therein) This study was inspired by the work of Baade, where he found type-I stars (luminous OB, open cluster) were present in the spiral arms of M31 and its satellite galaxies (Baade, 1944). Later, Morgan, together with Stewart Sharpless, and Donald Osterbrock, studied Galactic HII regions (emission nebulae) and confirmed the presence of two spiral arms in the Galaxy (Morgan et al., 1952, 1953).

The advent of radio astronomy in the 1940s, free from the effect of interstellar extinction, offered a new opportunity to investigate the spiral structure of the Galaxy. In 1951, American physicists Harold Ewen and Edward Purcell at Harvard University discovered 21 cm radiation. It was realized that, in contrast to optical bands, longer wavelength regions are free from being affected by dust extinction, offering new opportunities to investigate the Galactic spiral structure. Soon after the discovery of 21 cm radiation, Ook, and Bok, with their students, began the investigation of the Milky Way structure using radio data and obtained the signatures of spiral arms in our home galaxy (Oort & Muller, 1952), which were later confirmed in Van de Hulst et al. (1954).

1.2 Large scale features of the Milky Way galaxy

Despite the difficulty in mapping the structure of the Galaxy sitting at a vantage point inside the Galaxy, astronomers have done a remarkable job of deciphering the different structural components of the Galaxy thanks to the availability of multi-wavelength observations (optical, infrared, sub-millimeter, radio). Dedicated large-scale surveys (photometry, spectroscopy, astrometry) in different wavelength regimes and galaxy models inspired by external galaxies reveal that the large-scale structure of the Milky Way broadly consists of three components, namely the Halo, the Bulge, and the Disk (shown in the right side of Figure 1.3). Each of these components is further comprised of several substructures. This thesis aims to investigate the structure of the Disk component of the Milky Way galaxy. The Bulge and Halo components will be only discussed in the following subsections, briefly.

1.2.1 The Halo

The Halo of the Milky Way galaxy is the region surrounding the central disk of the Galaxy, extending thousands of light-years outwards. It comprises of multiple components, including stellar, gaseous, and dark matter Halo. The different components of the Halo are interconnected and interact with each other through various physical processes.

The stellar halo is an almost spherical component of the Milky Way Galaxy (hazy sphere in edge-on view of our galaxy, right side of Figure 1.3) and extends to $\sim$ 100

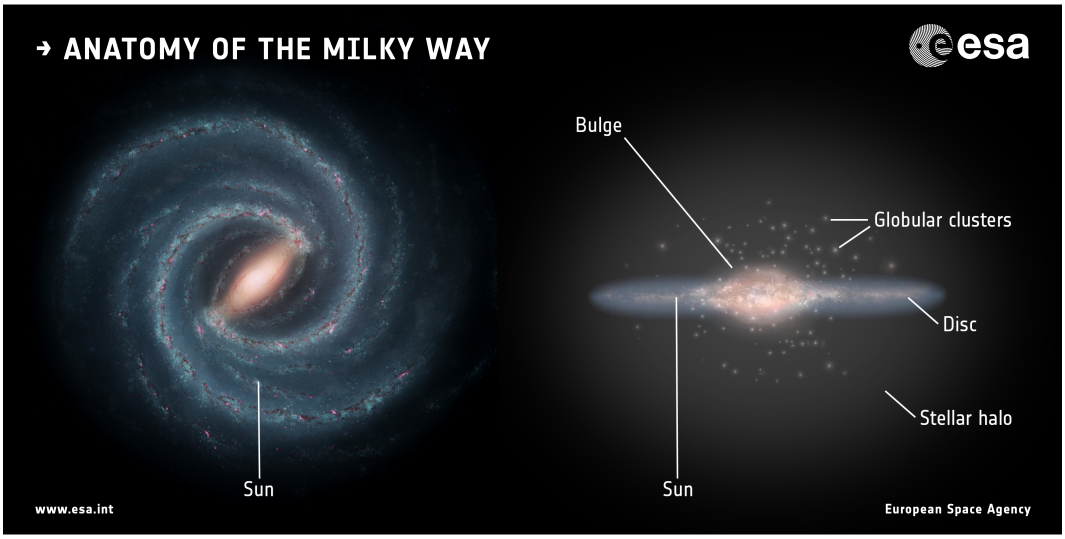

Figure 1.3: Artistic impression of the Milky Way galaxy; edge-on (right panel, *credits: ESA*) and face-on (left panel, *credits: NASA/JPL-Caltech*) view. *Layout credits: ESA/ATG medialab.*

kpc (Sirko et al., 2004). Despite its enormous size, it accounts for only 1% of the total stellar mass of the Galaxy (Bland-Hawthorn & Gerhard, 2016). It is home to many metal-poor, high-velocity stars at high latitudes and globular clusters. Halo stars exhibit large random motions, little-to-no rotation, and a spheroidal to spherical spatial distribution. In the classical picture, the stellar Halo was assumed to be a smooth envelope of ancient stars dating back to the time of the Galaxy's initial collapse (Eggen et al., 1962). However, Searle & Zinn (1978), based on their observations of a wide range of metal abundances in the halo globular clusters independent of galactocentric distance, suggested that the halo could be formed from independent in-falling debris. The vast data from large-scale sky surveys show that the stellar halo possesses complex substructures or enhanced-density regions like the Sgr Dwarf stream, Monoceros ring, Triangulum-Andromeda overdensity, and many more (more details in Helmi, 2004; Belokurov et al., 2006; De Lucia & Helmi, 2008). Cosmological simulations suggest that the Galaxy may have accreted approximately 100 satellite galaxies that were mostly disrupted by the tidal field, leading to the buildup of the stellar halo. Consequently, the stellar halo is a crucial region for studying the formation and merger history of the Milky Way galaxy. The gaseous halo of the Galaxy contains hot plasma surrounding the Galactic disk. Strong evidence for extended coronae/ halos has come from the first reliable detections of hot halos around nearby massive disk galaxies (e.g., Anderson & Bregman, 2010). The dark matter halo is a hypothetical region containing dark matter and extends way beyond the stellar and gaseous disk.

1.2.2 The Bulge

The Bulge is a spheroidal component of the Galaxy present at the center of the disk (see the central part of edge-on and face-on views in Figure 1.3). It contains approximately 1/5 of the Galaxy's total stellar mass, making it around ten times more massive than the halo (Zoccali & Valenti, 2016). The Bulge is primarily composed of old stars, ~ 10 Gyr (Wegg & Gerhard, 2013; Martinez-Valpuesta & Gerhard, 2011; Ness et al., 2013, etc). Even though the stars in this region have similar ages, the metallicity distribution shows a wide range in abundance, ranging from [Fe/H]= -2.5 to 1.0 dex (Zoccali et al., 2008; Ness et al., 2013). The formation of the bulge has been debated for many years, with the classical bulge hypothesis suggesting that it was built through mergers during the early formation of the Milky Way. Evidence supporting the classical bulge hypothesis includes the presence of an older age population in the bulge (Clarkson et al., 2008). However, determining the shape of the bulge through direct observations of its stellar population in the visible wavelength is challenging due to high dust extinction towards the center of the Galaxy. Therefore, the star count method at longer wavelengths (mainly in near-infrared) has been employed to probe the structure of the bulge. Despite copious studies of the bulge in the near-infrared(NIR), its shape and inner structure remain uncertain. Recent studies using the star count method have presented conflicting evidence regarding whether the bulge is boxy/peanut-shaped, spheroidal, or X-shaped (López-Corredoira et al., 2005; Babusiaux & Gilmore, 2005; McWilliam & Zoccali, 2010; Pietrukowicz et al., 2015; Ness & Lang, 2016; Zoccali & Valenti, 2016; López-Corredoira, 2016). Numerous investigations have established that the Milky Way is a barred spiral galaxy. The presence of a bar was first suggested by de Vaucouleurs (1964) to explain the non-circular motion seen in the HI line profile at 21cm. Subsequent research based on kinematics, surface brightness, and distribution of stellar population has been conducted to detect and examine the structure of the bar in the central region of the Milky Way (e.g., Alard, 2001; Wegg & Gerhard, 2013; Pietrukowicz et al., 2015). Besides the main bar, there are indications of the presence of a smaller nuclear bar (Nishiyama et al., 2005; Gonzalez et al., 2011) and long bar (Benjamin et al., 2005; Churchwell et al., 2009; López-Corredoira et al., 2007; Amôres et al., 2013) in the Galaxy. However, Martinez-Valpuesta & Gerhard (2011), in their simulations, showed that the long bar and main bar are two parts of the same structure. Nevertheless, while the general properties in terms of morphology, kinematics, and chemical content of the boxy/peanut structure have been extensively studied, the characterization of the metal-poor spheroids is far from complete.

1.2.3 The Disk

As the name implies, the Disk is a flat and roughly circular component of the Galaxy. The total luminosity of the Disk is around $1.5-2.0\times10^{10}$ $L_{\odot}$ (Sparke & Gallagher, 2000). It is the most prominent and massive structure (mass $\sim 6\times10^{10}$ $M_{\odot}$) that comprises most of the star-forming regions, stars, dust, and gas. Our solar system also resides inside the disk of the Galaxy. Being situated inside the disk of the Galaxy, it is advantageous for getting a vast amount of information about the stars in great detail. However, our vantage point within the disk limits our ability to gain a clearer view of its overall structure. The dust present in the Galaxy obscures the starlight and makes the situation even worse. Many pioneering works have been done to understand the structure of the disk of our Galaxy. It is now well known that, in the disk, the stellar density decreases exponentially with galactocentric radius and height above and below the Galactic plane. On top of these smooth structures, the disk of our galaxy also exhibits numerous substructures. For example, Gilmore & Reid (1983) studied the vertical stellar density profile of the Milky Way disk using the star count method towards the south galactic pole and found that the vertical density profile is more accurately fitted by the sum of two exponential components having different scale heights rather than a single exponential. This suggests that the disk of our galaxy is further divided into two components, i.e., the thin disk (scale height $\sim$ 300 pc) and the thick disk (scale height $\sim$ 1350 pc). It is observed that most of the star-forming regions, gas, dust, and stars with age < 10 Gyr having metallicity $[Fe/H] > -0.4$ are present in the thin disk while the older stars (> 10 Gyr) and metal-poor stars ($[Fe/H] < -0.4$) are part of the thick disk (Binney & Merrifield, 1998).

The disk of our galaxy is known to have spiral arms (as seen in the face-on view of Figure 1.3). However, observing these spiral structures in optical and infrared wavelengths is extremely difficult due to the high extinction caused by dust & gas in the disk. The maximum understanding of the disk structure in the literature is based on the molecular data obtained from radio and sub-millimeter observations because the data is less affected by dust extinction in these wavelength regions (Hou, 2021). As most of the materials like gases and dust are part of the disk, so, the molecular cloud, young and massive stars, and open clusters are the best tracer to find the structure of the spiral arms. In addition to the different components of the disk, the outer part of the disk is also of great interest. Various observations have shown that the disk of our galaxy is not flat, but it is warped. Another feature that can be seen in the outer part of the disk is that the scale height of the Galactic disk increases with the Galactocentric radius and height, indicating a flaring structure. The detailed discussion of the warp and the flare is presented in Sections 1.3.2 and 1.3.3, respectively.

1.3 Current picture of the Milky Way Disk

The disk of our galaxy is quite a busy place as it is home to billions of stars, star-forming regions, dust, and gases. Various dedicated; photometric, astrometric, and spectroscopic surveys have been carried out to cover large areas of the disk across the electromagnetic spectrum. These surveys have generated publicly available catalogs that contain information on millions of stars with their observed properties, which can be utilized to study stellar distributions. Tracing the distribution of material (stars, dust and gases) present in the disk will help to reveal the underlying disk structure. The 3D distribution requires information on both the location in the sky plane and the distance to the Sun. In the past few decades, technology has rapidly advanced, leading to numerous endeavors aimed to increase our knowledge of the structure of Galactic disk. While significant progress has been made in this area, there are still several unanswered questions that continue to challenge our understanding. This section will provide a brief overview of recent research on the disk structure or substructures of the Galaxy, which will lead us to open questions and build the motivation of the thesis.

1.3.1 Spiral arms

In the local group, about 30% of disk galaxies are spiral in nature (Willett et al., 2013; Ann et al., 2015; Kuminski & Shamir, 2016). Milky Way galaxy was also believed to have a spiral structure since the 1850s (Alexander, 1852). Several models are created to explain the spiral arms formation in the Galaxy. The spiral density wave (Lin & Shu, 1964) is the most successful theory in explaining the spiral arm formation in the galaxies. In this model, spiral arms are considered as the regions of the thin disk that are denser than average and move around the galaxy more slowly than the individual stars and interstellar material. As these density waves pass through the galaxy, they compress the gas and dust within them. These regions of higher density can trigger the formation of new stars and star clusters. The most luminous of these new stars have very short lifetimes compared to the amount of time it takes for them to orbit the galaxy. For this reason, they are only found in, or very close to, the spiral arm in which they were formed. Less luminous stars are also formed in the spiral arms, however, and these objects have longer lifetimes than their brighter counterparts. Images of spiral galaxies taken in the infrared bands clearly show that these less massive stars are found throughout the galactic disk, including between the spiral arms, as would be expected from this model. Hence, according to this theory, the position of spiral arms can be best mapped with the tracers associated with the star-forming regions. Hence, massive young stars, neutral hydrogen (HI), Giant molecular clouds (GMC) or HII regions associated with high-mass star formation regions (HMSFR), OB stars, open clusters, and cepheids have been extensively studied in the past few decades to uncover the structure of the Milky Way disk (Xu et al., 2018; Hou, 2021, and references therein). One advantage of using these tracers is that they are observed in the radio regime, making them largely insensitive to extinction. However, the kinematic distances derived from rotation curves for these tracers have significant errors (Sanna et al., 2017), imposing large uncertainties on the identification of spiral arms. Therefore, the debate continues over such basic facts as the existence of some spiral arms, the number of arms, and the size of the Milky Way. Measuring distances as accurately as possible using spiral tracers is key to settling these disputes and correctly uncovering the Galaxy's spiral structure. Recently, substantial progress in tracing the Galactic structure using young objects has been achieved. The spiral patterns traced by the young populations are summarized in Figure 1.4, where different color symbols represent various tracers. The curved lines and their thickness

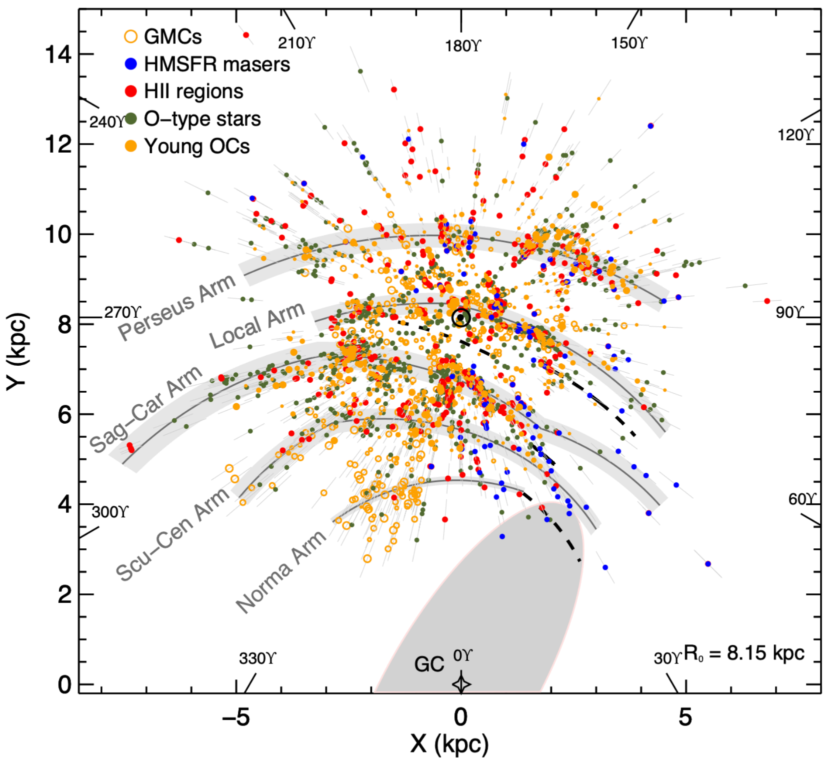

Figure 1.4: Distribution of GMCs (yellow open circles), HMSFR (blue points), HII (red points), O-stars (green points), and young open clusters (yellow points) on a face-on view of the Galaxy (used with permission from Hou, 2021). The positional uncertainty for each data point is shown by an underlying gray line segment. The curved solid lines indicate the best-fitted spiral arm model. The shaded areas around spiral arms denote the fitted arm widths.

represent the best-fitted log-normal spiral arm model given in Hou (2021). The figure shows that the younger population represents a four-arm model, including the Norma arm, Scutum-Centarus arm, Sagittariuss-Carina arm, and Perseus Arm, along with a spur commonly known as the Local arm. Combining the observational signature of masers and other star-forming region tracers, Xiang-Wu Zheng and Mark Reid created a conceptual image of the face-on view of the Milky Way galaxy which is presented in Figure 1.5. It is currently the most significant and accurate visualization of the face-on view of the Milky Way galaxy. It is worth noting that only a small segment of the spiral

Figure 1.5: Conceptual map of face-on view of the Milky Way galaxy based on the available data from VLBI and BeSSeL surveys and spiral model of Reid et al. (2019). *Image credit: Xing-Wu Zheng & Mark Reid BeSSeL/NJU/CFA.*

arms has been constrained from the observations, which are characterized by a small number of tracers. For example, the outer segment of the Norma-outer arm towards the anticenter direction, which is not displayed in Figure 1.4, is constrained by the presence of only five masers, which is too low to statistically constrain the features in the Galaxy composed of billions of stars.

In addition to the younger tracers, the Galaxy has a plethora of older populations as well. The distribution of the older population in the Galaxy in comparison to the younger population helps to study Galactic evolution. Galactic structure studies related to the older populations (Drimmel et al., 2000; Benjamin et al., 2005; Churchwell et al., 2009), suggested that the spiral arms traced by the older population are dominated by only two major stellar arms, the Perseus arm and the Scutum-Centaurus arm by analyzing the arm tangencies from integrated number counts of near-infrared and mid-infrared stars from the Spitzer/GLIMPSE (Galactic Legacy Mid-Plane Survey Extraordinaire) and COBE/DIRBE/ZSMA surveys of the Galactic plane. These results were in contrast to the spiral arms traced by the younger populations. Such disagreements regarding the spiral structure of the Milky Way might be explained by the different tracers and approaches used to determine their distances by different researchers. Total star counts may not allow good mapping of the spiral arms in the Milky Way, where evolved stars and gas might have different contents.

Furthermore, recent studies highlighted the age dependency on spiral arms. For example, Skowron et al. (2019a) from the age tomography of all the cepheids in their sample observed that the younger stars (20-140 Myr) are more concentrated in the inner arms (Norma-cygnus, Scutum- Crux- Centaurus, and Sagittarius-Carina arms), whereas the older stars (140-260 Myr) are spread towards outer arms (Perseus and Norma-Cygnus arm). The age dependency on the spiral structure is further discussed in Hou & Han (2015); He et al. (2021); Vallée (2022). This may question the formation of spiral arms in the Galaxy. The best way to resolve the matter is to systematically study the distribution of different age populations in the Galaxy.

1.3.2 Warp structure

Unlike the inner spiral structure, the outer regions of the stellar disk are more difficult to constrain due to low-density stellar populations at large distances. The outer Galactic disk has many interesting features, such as warp and flare. Understanding the dominant processes in this part of our galaxy is crucial for constructing models of galactic evolution and predicting its future.

The warp is a global characteristic among the disk galaxies. From surveys of edge-on galaxies, it is found that $\sim$ 50 to 70% of spiral disk galaxies present stellar warped discs (e.g, Sánchez-Saavedra et al., 1990; Reshetnikov & Combes, 1998; Sánchez-Saavedra et al., 2003; Guijarro et al., 2010). The ubiquity of warps in spiral galaxies suggests that they are either repeatedly regenerated or long-lived phenomena in the lives of galactic disks (Sellwood, 2013). The disk of our galaxy is also not flat, but it represents an S-shaped warp, as shown in Figure 1.6. The warp in the Milky Way was first detected with 21-cm observations of the HI gas (Westerhout, 1957; Kerr, 1957; Oort et al., 1958) and was confirmed later by Weaver & Williams (1974); Henderson (1979); Nakanishi & Sofue (2003); Levine et al. (2006b), among others. Since then, warp structure has been studied extensively, not just in neutral hydrogen but also in dust, (Freudenreich et al., 1994; Drimmel & Spergel, 2001; Marshall et al., 2006), molecular clouds (Grabelsky et al., 1987; Wouterloot et al., 1990; May et al., 1997), and different stellar tracers or their kinematics (López-Corredoira et al., 2002; Momany et al., 2006; Reylé et al., 2009; López-Corredoira et al., 2014; Amôres et al., 2017; Poggio et al., 2017, 2018; Romero-Gómez et al., 2019; Skowron et al., 2019a,b; Chen et al., 2019b; Li et al., 2019; Poggio et al., 2020; Li et al., 2020; Wang et al., 2018; Chrobáková et al., 2020; López-Corredoira et al., 2020; Cheng et al., 2020; Yu et al., 2021a; Lemasle et al., 2022; Chrobáková et al., 2022; Li et al., 2023). Despite

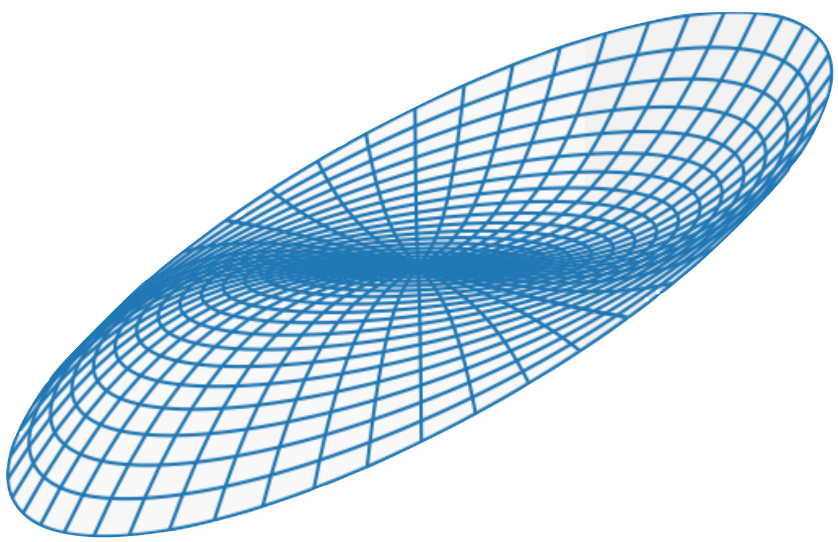

Figure 1.6: Schematic representing the S-shape warped disk of the galaxy

the extensive study of the warp structure from stellar counts and their kinematics, the amplitude and morphology of warp are only roughly constrained and are still being debated within the community. The presence of warp features in the gas, dust, and stellar components implies that the warp is a long-lived structure. Several theories have been proposed to explain the formation of the warp structure in disk galaxies.

The theoretical models can be broadly divided into two classes. One possibility is that the warp formed due to gravitational interactions, such as interaction with the satellite galaxies (Burke, 1957; Kim et al., 2014; Bailin & Steinmetz, 2003; Weinberg & Blitz, 2006; Bailin, 2003)) or a misaligned dark matter halo (Debattista & Sellwood, 1999; Shen & Sellwood, 2006). Other models propose non-gravitational mechanisms such as the accretion of intergalactic gas (Ostriker & Binney, 1989; Quinn & Binney, 1992; López-Corredoira et al., 2002) or interactions with intergalactic magnetic fields (Battaner et al., 1990; Battaner & Jiménez-Vicente, 1998) as a possible explanation of warping.

A recent study by Poggio et al. (2018) using upper main sequence stars selected from 2MASS and Gaia data suggests that the warp parameters remain constant across different stellar age groups. A similar interpretation was also given by Cheng et al. (2020) using the stellar abundances from the APOGEE survey and StarHorse distance computed by Queiroz et al. (2020). This result supports the idea that the warp is the result of an external, gravitationally induced phenomenon. However, there are several lines of evidence suggesting that the parameters of warp change with the average age of the tracers being used (Drimmel et al., 2000; Amôres et al., 2017; Romero-Gómez et al., 2019; Poggio et al., 2020; Chrobáková et al., 2020; Wang et al., 2020). The difference in the warp amplitude with the age of the tracers implies that the warp is a nonsteady feature that is evolving with time, contrary to the steady warp formed due to gravitational forces alone. Therefore, it must have originated from some non-gravitational effects, such as magnetic fields or hydrodynamical pressure from infalling gas.

The studies reporting a decrease of amplitude with increasing age (e.g Chen et al., 2019b; Wang et al., 2020; Chrobáková et al., 2020; Li et al., 2023), support the models that propose the involvement of gas in the formation of the warp. The underlying reason is that younger populations, which trace the distribution of gas, tend to exhibit a larger warp amplitude. Whereas, the old population may had more time to reduce the amplitude of the warp due to the self-gravity in the models in which the torque affects mainly the gas and not the stars. On the other hand, a group of studies (Amôres et al., 2017; Romero-Gómez et al., 2019) noticed more pronounced warp traced by older population as compared to younger giving different interpretations of warp formation scenario. The different interpretations of the formation of the warp are still being hotly debated. Most of the studies referred to above are based on kinematic information and /or limited sky coverage using different data sets. Hence, a detailed study of different age tracers homogeneously covering the whole Galactic disk is required to study the outer warped structure of our galaxy.

1.3.3 Flare

In addition to the warp, another discernible feature observed in the outer Galaxy is the flaring in the Disk. The flare is an increase in the scale height of the Galactic disk with a galactocentric radius. A visual representation of the mathematical model (given in eq. 1.1 - 1.3) of the disk along with flare and warp is shown in Figure 1.7, where the stellar density distribution (represented in color-bar) is modeled in XZ-plane at Y = 8.314 kpc.

$$\rho(R,Z) = \rho_\odot \; exp\left(-\frac{R-R_\odot}{H}\right) \; exp\left(-\frac{|Z-Z_w|}{h_Z(R)}\right) \tag{1.1}$$

Where,

$$h_z(R) = h_z(R_\odot) \; exp\left(\frac{R-R_\odot}{H_{R,flare}}\right) \tag{1.2}$$

and

$$Z_w = [C_w \; R(pc)^{\epsilon_w} \sin(\phi - \phi_w)] \; pc \tag{1.3}$$

The flare has been detected in various tracers including atomic hydrogen gas (HI; Nakanishi & Sofue, 2003; Levine et al., 2006a), molecular clouds (CO; Grabelsky et al., 1987; May et al., 1997), dust (Drimmel & Spergel, 2001), and the stellar components such as Cepheids (Feast et al., 2014; Chakrabarti et al., 2015), OB stars (Li et al., 2019; Wang et al., 2018; Yu et al., 2021a), older population stars (López-Corredoira et al., 2002; Momany et al., 2006; Reylé et al., 2009; Yu et al., 2021b), F and G type stars selected from Sloan Extension for Galactic Understanding and Exploration (SEGUE) survey

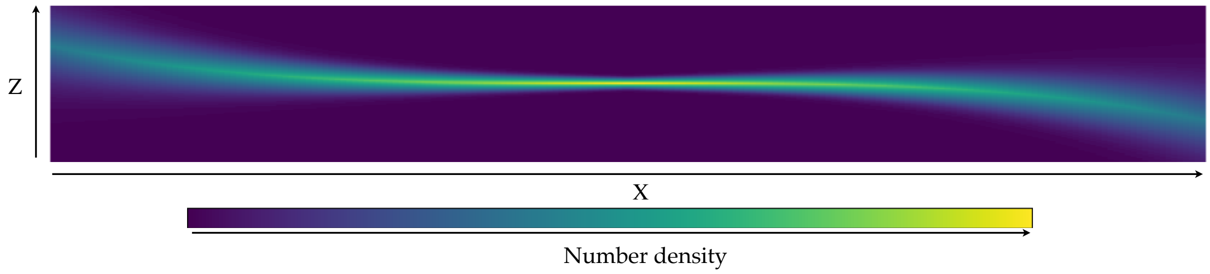

Figure 1.7: Modelled density distribution of stars in XZ-plane at the position of the Sun (Y = 8.314 kpc). A clear warp and flare can be seen in the form of the density distribution as a gradient in color. X and Z values in the figure are not of the same scale.

López-Corredoira & Molgó (2014), pulsars (Yusifov, 2004), and recently in supergiant and whole Gaia EDR3 data (Chrobáková et al., 2022). The presence of flare in all the tracers: gas, dust, and stellar components suggests that it is a global property and persistent feature of the Milky Way disk and can be observed by various tracers. In addition to the Milky Way, de Grijs & Peletier (1997) showed that the scale height of edge-on galaxies in their sample increases along the major axis of the galaxy and is more prominently seen in the early-type disk galaxies. A three-dimensional view of the density distribution in a disk galaxy having warp and flare is shown in Figure 1.8, based on different viewing angles.

The flare was first modeled by Narayan & Jog (2002), taking three components, HI, HII, and stars as gravitationally coupled to calculate the scale height of each component and their flares. It was then modeled by Sánchez-Salcedo et al. (2008) using modified Newtonian dynamics (MOND), Kalberla et al. (2007) using a dark matter ring, by Saha et al. (2009) in terms of lopsided halo, by López-Corredoira & Betancort-Rijo (2009) from an accretion of intergalactic material onto the Galactic disk. The phenomenon of flaring in disks is believed to be associated with the process of disk heating, and numerous theories have been proposed to elucidate this phenomenon (e.g, Cheng et al., 2019; Yu et al., 2021a). Some internal disturbances such as spiral arms (Sellwood, 2013), Giant molecular clouds (Lacey, 1984) or stellar migration (Bovy et al., 2016) have been suggested as potential contributors to the disk flaring events. In addition, external perturbations like the mergers with dwarf or satellite galaxies (Kazantzidis et al., 2008; House et al., 2011) can also play a significant role in heating the disk and cause flaring

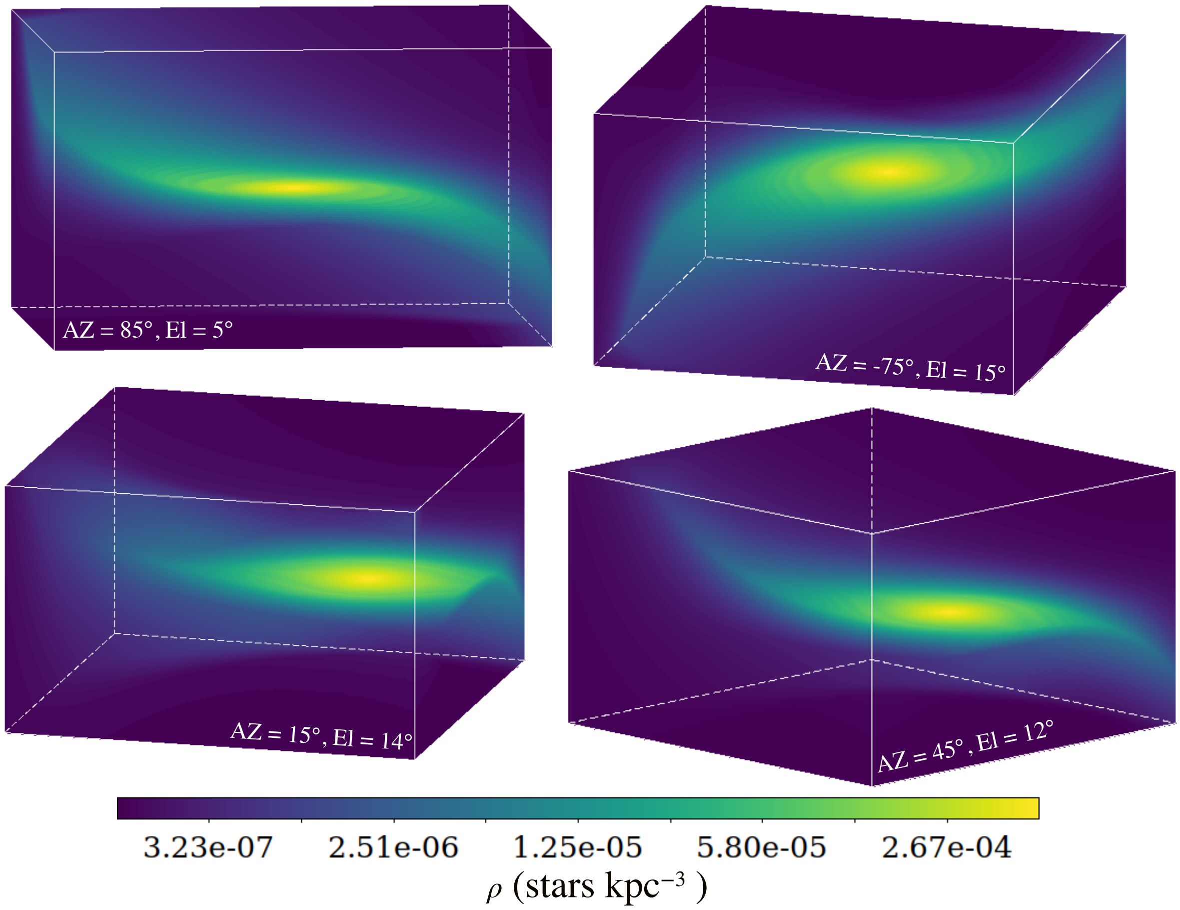

Figure 1.8: Modelled density distribution of stars in three-dimensional galactocentric XYZ-space from four different viewing directions to emphasize the effect of warp and flare seen from various locations.

in the outer regions of the galaxies. The formation mechanisms of a flare can be broadly classified into two types: secular evolution (Narayan & Jog, 2002; Minchev et al., 2012, 2015) and the cumulative effect of interaction with passing dwarf galaxies (Kazantzidis et al., 2008; Villalobos & Helmi, 2008; Laporte et al., 2018). Observationally, both scenarios expect that the scale height of the disk should increase smoothly with the radius. In the case of secular evolution, the older population is expected to exhibit a stronger flare compared to the younger population. However, no age dependency in flare strength is expected for flares formed by perturbations, as all the stellar populations would be equally disturbed.

Recently, Yu et al. (2021a) studied the flare and warp of the Galactic disk using OB-type stars from the LAMOST survey. Comparing their flare results with the older RGB population from Wang et al. (2018) suggested that secular evolution may not play a major role in flare formation. Instead, the perturbations caused by the internal components or the external mergers could be the main contributors to the formation scenario. Similar results were also reported in the earlier studies; for example, Wang et al. (2018), by comparing the red giant branch stars (RGB) population with the RC stars selected by Wan et al. (2017), and Xu et al. (2020), favored perturbation scenarios of flare formation on secular evolution. Nevertheless, many competing studies still favor the secular evolution of the flare in the Disk. These studies include the works of Bovy et al. (2012); Li et al. (2019); Chrobáková et al. (2022), etc.

Based on the preceding discussion, it is evident that despite the significant progress made in the investigation of disk flare over the past decades, there still remain ongoing debates concerning its parameters, structure, and formation mechanisms. The discrepancies between different studies may be attributed to the lack of good distance indicators that are present numerously in the Galaxy, homogeneous sky coverage, and statistically significant samples. Therefore, there is a need for a systematic study of the flare using stellar populations that serve as good distance indicators and are abundantly present in the Galaxy.

1.4 Motivation

As discussed in Section 1.3, most of the understanding of the Galaxy has come from the younger tracers. In contrast, there are some pieces of evidence of the age dependency on these features. The age dependency on these structures has been studied many times but still is a subject of debate. The main reason is that there are no dedicated studies to trace the older age population covering a large area of the sky. Most of the studies have either considered all the NIR stars (having mixed populations Reylé et al., 2009), or the studies dedicated to a definite population (like red clump stars) are confined to the smaller regions (López-Corredoira et al., 2002; Ganesh et al., 2009; Wang et al., 2018; Yu et al., 2021a). The properties of old stellar arms are essential to better constrain the formation and evolution of spiral arms, warp, and flare of the disk. Dedicated work is required to trace the older population along with accurate distance information to construct a three-dimensional disk map. Red clump stars are numerously present over the entire Galaxy and being distance indicators can serve as the ideal candidates to trace the structure of the old disk.

According to density wave theory (Lin & Shu, 1964), the stars can move from their birthplace and be present between spiral arms during their evolution. However, the dust is highly confined to the spiral structure of the Galaxy. Hence, dust is an excellent tracer to map the disk and, specifically, the spiral arms of the Galaxy. The mid-infrared images of the external galaxies from James Webb Space Telescope (JWST), like Messier 74[1], reveal that dust not only traces the large-scale spiral structure but also traces the small-scale structures present in between the spiral arms. Drimmel & Spergel (2001) presented a three-dimensional Galactic dust distribution model using COBE/DIRBE data and found the disk scale length of 2.26 kpc and scale height of 134.4 pc. Studying the dust distribution in the Galaxy at longer wavelengths for 3D dust distribution may cause discrepancies due to distance ambiguity caused by unknown Galactic potential. For instance, the molecular cloud G9.62+0.20 has near and far kinematic distances of approximately 0.5 and 15 kpc, respectively, but its actual distance is ~ 5.2 kpc (Sanna et al., 2009). Thus the kinematic distance may result in significant uncertainties in locating molecular clouds and hence constructing the morphology of Galactic spiral arms.

Nevertheless, instead of direct tracing the dust in longer wavelengths, the properties of the dust, i.e., extinction and polarization, can be utilized as an indirect way to trace the small-scale and large-scale dust distributions. Several 3D (Marshall et al., 2006; Schultheis et al., 2014; Sale et al., 2014; Green et al., 2019; Gontcharov, 2017; Lallement et al., 2018; Chen et al., 2019a; Rezaei Kh. et al., 2018) extinction maps have been constructed to decipher the dust distribution in the Galaxy. Yet most of the extinction maps do not exhibit large-scale spiral structures, partially due to the fact that interstellar extinction is a derived quantity and hence model dependent, which may produce inherent bias. Alternatively, the polarization of starlight from the intervening dust grains is a direct observational quantity. Polarization measurements combined with the distance information can be used to study the number of dust layers and their distances

[1]https://esawebb.org/images/potm2208a/

along the line of sight (e.g., Eswaraiah et al., 2012; Uppal et al., 2022; Pelgrims et al., 2023). Despite the potential usefulness of polarization observations for mapping dust distribution, not many dedicated studies have targeted this approach. A systematic study of polarization observations is required to investigate polarization as a tool to infer the large-scale and small-scale 3D dust distribution.

1.5 Thesis Objective

This thesis aims to deepen the understanding of the structure and evolution of the Milky Way, our home galaxy. The structure and evolution of galaxies have been a topic of interest for centuries. As we live inside the Milky Way Galaxy, it can be used as a test bed to understand the structure and formation history of the galaxies, in general. The disk of the Milky Way is one of its most important components, as it contains dust, stars, gases, and star formation regions. In recent years, a wealth of observational data has become available that allows us to study the disk of the Galaxy in unprecedented detail. At the same time, theoretical models of disk formation and evolution have made significant progress, providing new insights into the physical processes that shape galactic disks. With the advancement in the field, a plethora of work has been done in the past few years to increase the understanding of the disk structure, but many questions still remain open as addressed in the previous sections.

This thesis aims to build on these advances by conducting a comprehensive analysis of the disk, using a combination of observational and archival data. In the thesis, we investigated the global and small-scale substructures of the Disk following the spatial distribution of stars and dust. Most of the earlier stellar distribution studies targeted younger populations which are expected to follow the disk structure. However, it is essential to study the different age populations and compare them to investigate the evolutionary history of the disk. The objective of the thesis is to investigate the disk in the following respects.

1. Develop a method to identify and select the red clump stars using 2MASS and Gaia all-sky survey data.

2. Trace the spiral arms, flare, and warp sub-structures of the Disk by tracing intermediate-old populations, i.e., the red clump stars.

3. Comparison of flare and warp traced by different age populations to constrain their formation mechanism.

4. Investigate dust distribution towards the different lines of sight to study the structures at various scales.

Overall, the thesis will significantly contribute to our understanding of the Milky Way's disk by providing a comprehensive analysis of its structure.

1.6 Outline of the thesis

The thesis comprises eight chapters; the brief details of the following chapters are given in the subsections below.

Chapter 2: Red clump stars and their selection

This chapter starts with an overview of the red clump stars and outlines the reasons for selecting them to trace the structure of the disk. A complete methodology developed to select the red clump stars from the 2MASS color-magnitude diagram, its implementation, and its automation process using R-programming language is presented in detail. A part of this chapter is published as Uppal et al. (2023).

Chapter 3: Milky Way disk revealed by red clump stars

This chapter describes the detailed analysis and results obtained from the three-dimensional distribution of selected red clump stars in the Galactic disk and their overdensity maps. The different density models used to describe the radial and vertical stellar density are also explored. In addition, this chapter presents the flare and warp structure obtained from the distribution of red clump stars and their comparison with the younger population (from the literature) to constrain their formation and evolution mechanism. The results presented in this chapter are part of the published paper Uppal et al. (2023), and Uppal et al. (2024).

Chapter 4: Polarization observations and data reduction

This chapter introduces some basic concepts of interstellar polarization and describes the target selection for polarization observations. It summarizes the strategy for the polarization observation of selected Galactic open clusters using two Indian observational facilities: 1.2 m Mount Abu telescope of PRL and 1.04 m Sampurnanand telescope of ARIES. A detailed description of instruments used for the observation at the two observatories, their similarities and differences are highlighted in it. The intricate reduction procedures and pipelines developed for each instrument are also discussed in respective subsections.

Chapter 5: Linear polarization towards a distant cluster in the 2nd Galactic quadrant

This chapter emphasizes the possible reasons for selecting the target in the second Galactic quadrant. It presents the results obtained from the observations of the distant open cluster, Czernik 3, targeted in this direction. The small-scale and large-scale properties of dust distribution are derived by combining the polarization data of Czernik 3 with other nearby clusters present within 15° region around it. The results presented in this chapter are part of the paper Uppal et al. (2022).

Chapter 6: Optical linear polarization towards anti-center direction

This chapter discusses the results and the implication on dust distribution towards anticenter direction using the polarization observations of five clusters, Kronberger 1, Berkeley 69, Berkeley 71, Berkeley 19, and King 8. These clusters are located at different distances, enabling us to probe distant dust layers.

Chapter 7: Polarization study in a direction tangential to the spiral arms

This chapter aims to show the analysis related to the polarization observations of nine clusters selected in the first Galactic quadrant. The results obtained from the polarization information of all the clusters in this direction observed from EMPOL as well as AIMPOL are summarized.

Chapter 8: Summary and future work

This chapter provides a comprehensive summary of the entire thesis, including a discussion of the main results and their significance. It lists the key highlights of each chapter of the thesis and places them in the context of our current understanding. This chapter also discusses the limitations of the study and suggests directions for future research.

This page was intentionally left blank.

Chapter 2

Red clump stars and their selection

"Do not look at stars as bright spots only. Try to take in the vastness of the Universe."

- Maria Mitchell, *1818-1889*

Understanding the structure and formation of our Milky Way galaxy is a fundamental pursuit in galactic astronomy. The study of disk morphology in our galaxy provides valuable insights into the processes that have shaped our galaxy over time. As highlighted in Chapter 1, most of the earlier studies have been devoted to mapping the disk structure of the Galaxy with younger tracers like HI, HII, HMSFR, OB stars, young open clusters, and cepheids. Since the Milky Way is composed of young and old stars, dust, and gas, it is necessary to study the distribution of all the components to obtain a complete view of the Galactic structure. Moreover, some recent studies highlighted the difference in the various substructures of the disk derived from the older population in contrast to the younger population (e.g., Miyachi et al., 2019; Lin et al., 2022, and other references in Chapter 1). The older populations can serve as a valuable chronometer for understanding the evolution of different regions of the Galaxy. Analyzing their spatial distribution, kinematics, and abundance patterns helps to understand the geometry, formation, and evolution of the different structural features in the disk, such as spiral arms, stellar streams, warp, and flare. Hence, it is important to carry out a systematic study to trace the different substructures of the Galaxy from older populations as well.

Previous studies (e.g., Drimmel et al., 2000; Benjamin et al., 2005; Churchwell et al., 2009) investigating the Galactic structure from the older populations relied on the integrated NIR, MIR, or FIR data as a proxy to the older populations. However, such an approach can result in mixed data containing a combination of different populations of stars and dust, which may exhibit distinct patterns. To resolve this issue, high-precision distance measurements for a large number of old stars of similar populations are required. Nevertheless, any method used to obtain the distance to large-scale structures suffers from four primary challenges (Paczyński & Stanek, 1998);

- the accuracy of determining the absolute magnitude of the stars involved,
- the effect of interstellar extinction
- effect of the internal properties of the stars such as mass, age, and chemical composition
- sample size of the population under study

The spectroscopic methods offer an effective means to estimate the distances of specific spectral types and investigate their spatial distribution to trace underlying structures. However, ground-based spectroscopy has limitations regarding sky coverage completeness and the inability to observe fainter stars. As a result, it is primarily suitable for studying structures within the solar neighborhood. In recent years, the space-based telescope Gaia has played a crucial role in providing parallax information, enabling the estimation of accurate distances for billions of stars. Taking advantage of Gaia Data Release 2 (DR2), Miyachi et al. (2019) selected a population of stars approximately 1 billion years (1 Gyr) in age and studied the overdensities in the Local arm of the Milky Way. Standard candles like RR Lyrae are also indicators of older populations and can be studied in the disk (Mateu & Vivas, 2018). Furthermore, red clump stars (detail in Section 2.1), which are evolved phases of low-mass stars with masses less than 2.2 solar masses and ages spanning from 0.5 to 6 Gyr (Girardi, 2016), can also be used as distance indicators. The red clump stars are numerously present in the Galaxy as compared to other standard candles such as RR Lyrae and Cepheids. The larger sample size of RC stars and well-calibrated absolute magnitudes Ruiz-Dern et al. (2018); Plevne et al. (2020) result in lower statistical errors in distance estimations. Therefore, we chose the red clump stars to study the disk structure traced by older populations.

In this chapter, we introduce the red clump stars, their observational signatures, and the reasons for them to be treated as standard candles. We developed an automatic method to extract the red clump stars from the homogeneous 2MASS data and estimate their distances from the distance modulus. A detailed description of the methodology, its implementation, and the automation process using R-programming language are described in this chapter. Complete discussion on the sample validation, i.e., the completeness, contamination, and distance accuracy of the selected sample of ~ 10 million RC candidates is presented by comparing our results with the existing catalogs in the literature.

2.1 Red clump stars

Red clump (RC) stars are low-mass, core helium-burning (CHeB) stars having almost constant luminosity and a small range in temperature during their phase of evolution. Hence, they represent a striking clump feature towards the redder side of the main sequence in the color-magnitude diagrams (CMDs) of intermediate-age star clusters and nearby galaxies. The clumpy feature of RC stars is shown in Figure 2.1. The figure represents the Gaia (BP-RP, G) CMD for globular cluster NGC 104, on the left and NGC 6362 on the right, and the RC stars are highlighted in red color.

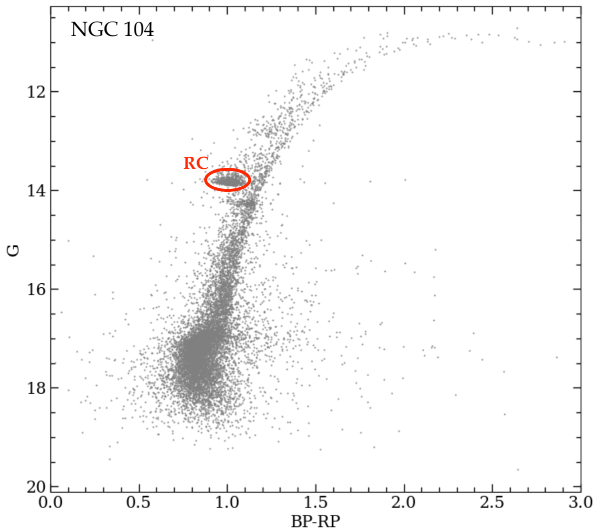

Figure 2.1: Gaia CMD (BP-RP, G) of globular clusters NGC 104 (left panel) and NGC 6263 (right panel). The RC stars are highlighted with red color, and the HB sequence is pointed in blue.

2.1.1 Evolution to Red clump phase

A star is born from the gravitational collapse of molecular clouds. As these clouds collapse, their density and temperature increase, eventually leading to the formation of a dense central region capable of initiating nuclear fusion. At this stage, the hydrogen in the core is converted into helium (shown artistically in stage (a) in Figure 2.2), and the envelope is stabilized against gravity by the radiation pressure. The subsequent evolution of the star is determined by the initial mass of the star, which is reflected in changes over time in surface temperature and luminosity that can be described using the Hertzsprung-Russell (HR) diagram.

Stars with an initial mass greater than 0.08 $M_{\odot}$ burn hydrogen in their central core and reach the Main Sequence (MS) phase. On the other hand, stars with lower initial masses lack sufficient mass for hydrogen fusion to take place and remain in a hydrostatic equilibrium without burning hydrogen in their cores, known as brown dwarfs. During the MS phase, stars spend most of their lifetime burning hydrogen until all the hydrogen in the core is converted into helium. Once this happens, the star transitions out of the MS phase, as there is no nuclear fusion to power the star. With the absence of radiation pressure from nuclear burning, gravity becomes the dominant force, causing the star to contract and enter the sub-giant phase (stage (b) of Figure 2.2). The gravitational potential energy released during this contraction is converted into thermal energy, which heats the surrounding gas. For stars with an initial mass greater than 0.5 $M_{\odot}$, a shell surrounding the inert helium core becomes hot enough to start hydrogen fusion into helium. The energy generated through nuclear fusion is transported throughout the envelope by convection, causing the envelope to expand and the surface temperature to decrease. As a result, the color of the star becomes redder than the MS stage, hence called a red giant star. This stage is called the red giant phase (Figure 2.2c), and the star evolves along the red giant branch (RGB). During this process, the ashes of the hydrogen-burning shell are continuously accumulated by the contracting core, making it denser and more massive, thereby increasing the core temperature. Even at this stage, the low-mass stars do not attain sufficient temperature to ignite helium in their cores. As the core continues to contract and accumulate matter from the hydrogen-burning shell, the electrons within the core become degenerate. The degeneracy pressure, which depends only on density, dominates over the thermal pressure (function of both density and temperature). Hence, it prevents any further changes in pressure with increasing temperature to stabilize the core against gravitational compression. The isothermal core, thus formed, continues to contract and accrete matter from the hydrogen-burning shell until it reaches a mass of about 0.47 $M_{\odot}$ (Girardi, 2016). At this stage, the temperature in the core reaches to 100-200 million kelvins, which is sufficient to burn helium. The ignition of helium initially occurs off-center within the core but rapidly spreads throughout, generating a substantial amount of energy. This energy release further increases the temperature and, hence, the reaction rate until the temperature increases to a point where thermal pressure becomes dominant again. Thus, this runaway process results in an explosion, generating enormous energy known as helium flash, which lifts up the degeneracy. After the flash, the core expands and burns helium at normal rates to form carbon and oxygen, switching the star's path from RGB to the horizontal branch (HB, Figure 2.2d). The hydrogen and helium regions are the primary source of the luminosity of the star and are determined by the core and envelope masses set by their previous evolution stage, i.e., before the start of the core helium burning. This stage is known as zero-age core helium burning, which is analogous to the zero-age main sequence. The helium

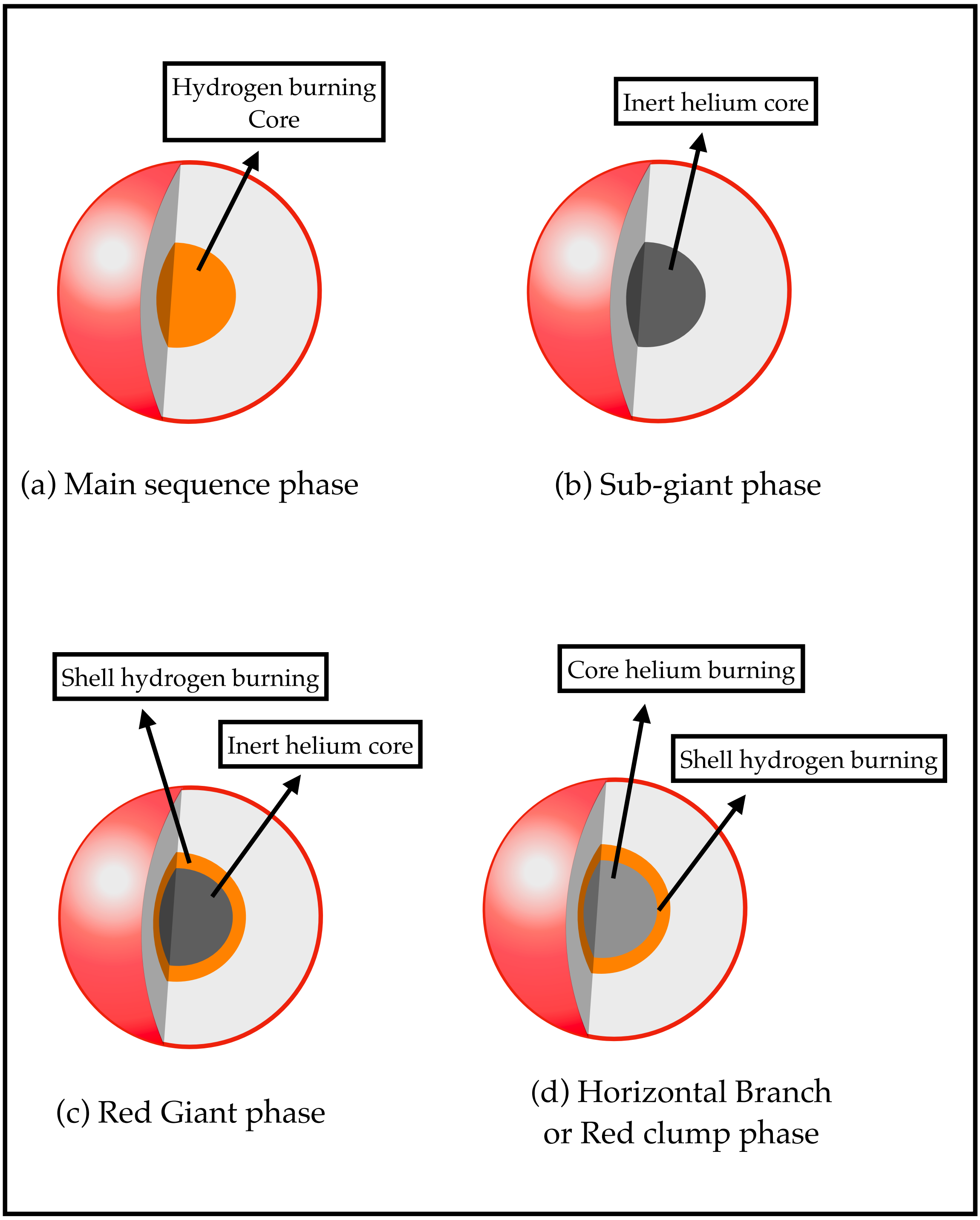

Figure 2.2: Schematic layout representing the different phases of evolution of a star, i.e., MS, SG, RGB, and HB or RC phase in (a), (b), (c), and (d), respectively.

burning in low-mass stars can only begin if the core mass attains a critical limit of 0.47 $M_{\odot}$. Therefore, all the low-mass stars with an initial mass less than the helium flash limit (M_{HeF}, maximum initial mass for a star to have electron degeneracy in the core) will undergo helium flash and possess a similar degenerate core masses near the plateau of 0.47 $M_{\odot}$. This explains why all the low-mass stars ($\sim 0.5 - 2.0 M_{\odot}$), spanning a wide range of turn-off ages, exhibit nearly constant luminosity and hence give rise to a distinct grouping known as red clump stars in the CMD. In general, M_{HeF} values range from 1.7 to 2.0 $M_{\odot}$ (e.g., Castellani et al., 2000). The RC stars show only a weak dependency on the color, age, and metallicity of the star (Girardi, 2016).

In contrast, massive stars do not experience electron degeneracy in their cores due to the quiescent central helium burning resulting from high core temperature sufficient enough to burn helium at normal rates before electron degeneracy can set in. Consequently, these stars directly settle onto the quiescent He-burning stage, where they burn helium at higher effective temperatures, leading to the formation of more extended features known as the horizontal branch (HB). The HB stars exhibit a wide range of effective temperatures, unlike red clump (RC) stars, which show a narrow range in temperatures that is only weakly dependent on the age and metallicity of the star. RC stars are sometimes referred to as the red extremities of HB stars. In general, RC stars are associated with low-mass and higher-metallicity stars compared to HB stars and are far more abundant than the HB stars.

2.1.2 RC: A distance indicator

The first detection of RC stars as a clumpy feature in CMD was made by Cannon (1970) and Faulkner & Cannon (1973) in the intermediate-age open clusters. Using stellar evolution models, they correctly interpreted the RC stars as the result of the evolution of low-mass stars after the RGB phase. The RC stars represent the old (1 -4 Gyr) and metal-rich counterparts of the HB stars covering a spectral range of G8III-K2III, and effective temperatures between $4500K \leq T_{eff} \leq 5300K$ (Zhao et al., 2001; Soubiran et al., 2003; Girardi, 2016). Owing to the nearly constant luminosity of low-mass stars ($M < 2.2 M_{\odot}$, Girardi, 2016), Cannon (1970) suggested that the RC stars can be used to determine the distance and extinction of the hosting cluster. The distance (d) can be estimated in single-step from the distance modulus (μ), following equation 2.1.

$$\mu = < m_{x,RC} > - M_{x,RC} = 5log(d) - 5 + A_x \tag{2.1}$$

Where $< m_{x,RC} >$ and $M_{x,RC}$ are the mean apparent and absolute magnitude of the RC in the x-band. A_x represents the extinction along the line of sight. This is one of the precise and most used techniques to find the distance of celestial objects using RC stars. The uncertainties in the distance increases with distance of the objects. This can be seen from equation 2.2-2.5, which is derived by ignoring the effect of extinction for simplification.

$$d = 10^{0.2\ (m-M+5)} \tag{2.2}$$

$$\sigma_d = \sqrt{\left(\frac{\partial d}{\partial m}\right)^2 \sigma_m^2} \tag{2.3}$$

$$= 10^{0.2\ (m-M+5)}\ log(10)\ \sigma_m \tag{2.4}$$

$$= d\ \sigma_m \tag{2.5}$$

In these equations, we have simply replaced the $< m_{x,RC} >$ by m and $M_{x,RC}$ by M.

The use of RC stars as a distance indicator gained importance after the precise parallax measurements by the Hipparcos mission, which provided a large sample of RC stars with very small parallax errors. These data highlighted the concentrated nature of the RC region in the HR diagram. It served as a valuable reference point for utilizing RC stars as a standard candle for sources within our galaxy and to nearby galaxies and clusters. Paczyński & Stanek (1998) used the RC stars in I-band from Hipparcos data to determine the distance of the Sun to the Galactic centre. Since then, the RC stars have been extensively used to infer the structure of the bulge region of our Galaxy, particularly by using the I-band of Optical Gravitation Lensing Experiment (OGLE) and then spread over the NIR photometric bands with the availability of wide-area surveys like 2MASSS, DENIS (e.g., Stanek et al., 1994; Babusiaux & Gilmore, 2005; Nishiyama et al., 2005; McWilliam & Zoccali, 2010; Pietrukowicz et al., 2015; Zoccali & Valenti, 2016, etc.). The thick disk of the Milky Way has also been characterized by using the properties of RC stars (Soubiran et al., 2003; Siebert et al., 2003). Regardless of the inner galactic structure, the photometric and spectroscopic selection of red clump stars has been utilized to infer the warp and flare in the outer disk of our galaxy (López-Corredoira et al., 2002; Wang et al., 2018; Cheng et al., 2020; Yu et al., 2021a,b). In addition to the structures of our galaxy, RC stars have been used to estimate the distances of other celestial objects, such as the Small Magellanic Cloud (SMC, Udalski, 1998), the Large Magellanic Cloud (LMC Udalski, 1998; Stanek & Garnavich, 1998; Salaris et al., 2003), IC 1613 (Dolphin et al., 2001), Carina (M33, Kim et al., 2002), and Fornax (Rizzi et al., 2007).

It is worth mentioning that the recent data releases on the Gaia satellite have provided the accurate parallax (uncertainties of the order of a few μas) of billions of stars. The distances of the RC stars can also be obtained from Gaia parallaxes, but the parallax measurements will be plagued by large uncertainties in the distant Galaxy. The distance uncertainties derived from error propagation of parallax ($\bar{\varpi}$) vary as distance squared (follow equation 2.6-2.9).

$$d = \frac{1}{\bar{\varpi}} \tag{2.6}$$

$$\sigma_d = (\sqrt{\left(\frac{\partial d}{\partial \bar{\varpi}}\right)^2 \sigma_{\bar{\varpi}}^2}) \tag{2.7}$$

$$= \left(\frac{\sigma_{\bar{\varpi}}}{\bar{\varpi}^2}\right) \tag{2.8}$$

$$= d^2 \, \sigma_{\bar{\varpi}} \tag{2.9}$$

Whereas the uncertainties in the distance estimation of RC stars (equation 2.5) by considering them as standard candles, vary linearly with distance. It has been observed that with high precision photometry, RC stars can provide distances up to ~ 10 kpc with uncertainties less than 6% (Bovy et al., 2014; Hawkins et al., 2017; Ting et al., 2018). Therefore, the standard candles can provide more precise distances for objects at distant positions in the Galaxy than the parallax information.

Although it is relatively easy to visually pinpoint the clump on the CMD, identifying individual RC candidates is not trivial because they highly overlap with the RGB stars. Moreover, observationally, the clump of stars can only be seen if all the stars are present

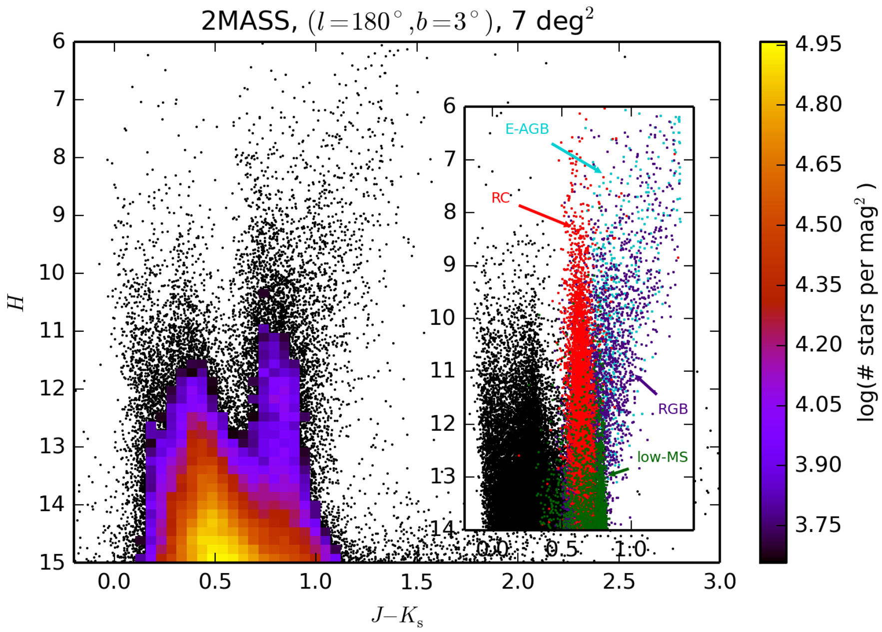

Figure 2.3: Apparent 2MASS CMD of a low latitude field towards the anti-center direction with color gradient represents the number density of stars per unit color-mag bin. A simulated CMD of the same field is also shown in the inset of the figure to highlight the typical position of different populations (in different colors) in the CMD (Girardi, 2016). (Source file provided by Prof. Leo Girardi)

at the same distance and suffer similar extinction. In the general field of the Milky Way, the RC stars can be present at varying distances along the line of sight, suffering different extinction. The star's position in the CMD is determined by absolute magnitude, intrinsic color, distance, and extinction. Any change in the distance will shift the star in the vertical direction on the apparent CMD (see equation 2.10). At the same time, the extinction causes the star to move both in the horizontal and vertical directions (as extinction, A is present in both equations 2.10 and 2.11).

$$m_x(y - axis) = M_x + 5\,log(d) - 5 + A_x \tag{2.10}$$

$$m_x - m_y(x - axis) = (M_x - M_y) + (A_x - A_y) \tag{2.11}$$

where x and y are the wave bands in which measurements are taken.

The combination of the two effects causes the stars of similar spectral types at different distances to appear as a strip in the CMD. Instead of a clumpy feature, the RC stars manifest as a distinct band in the CMD, an example of which can be seen as a dense region around $J - K_s = 0.75$ mag color in the 2MASS CMD of $7 deg^2$ wide field centered at $\ell = 180°$ and $b = 3°$, shown in Figure 2.3. The inset figure represents the CMD from *TRILEGAL: TRIdimensional modeL of thE GALaxy* population synthesis model (Girardi et al., 2005, 2012) of the same 2MASS field. Various colors in the modeled CMD denote different populations, i.e., MS, RC, RGB, and AGB. The second dense region of the CMD is populated by RC stars. However, it is important to note that the RGB and low-mass MS dwarf stars can contaminate the RC population. Therefore, it is crucial to carefully select the sample of RC stars to ensure their purity. Moreover, in the low extinction fields, this RC locus will be almost vertical. However, it will be displaced towards the redder side of the region towards directions with higher extinction. López-Corredoira et al. (2002) conducted a study where they selected red clump stars from the 2MASS CMD in twelve different fields. However, visually selecting the red clump locus throughout the entire Galaxy can be challenging and time-consuming due to the varying extinction experienced by stars along different sightlines. Therefore, an automated procedure is required to account for these effects and systematically identify red clump stars across the entire Galactic disk.

2.2 RC selection

The accurate and reliable preparation of a sample of RC stars necessitates a meticulous selection process. This involves the development of an automated procedure implemented through R-programming scripts, which are specifically designed to handle large data sets. The procedure effectively selects the RC stars and estimates their distances. This section provides a comprehensive overview of the methodology and criteria utilized for the automatic identification and selection of RC stars from a large population of stars of different spectral types present along the line of sight. The choice of the data used to select the RC stars is also justified and presented in this section.

2.2.1 Data used

Our objective is to map the large-scale structures of the disk using RC stars. In order to accomplish this, we require data obtained from a homogeneous sky survey. Although the recent Gaia data release offers uniform sky coverage and observes billions of stars in our galaxy, it is an optical survey resulting prominent extinction effects. As a consequence of large extinction, the identification of red clump locus in their CMDs becomes challenging. On the other hand, the 2MASS data maps the entire sky in near-infrared wavebands J (1.25 μm), H (1.65 μm) and K_s (2.17 μm), where the interstellar extinction is greatly reduced. The data has been acquired using similar telescopes and detectors in the northern (Mt. Hopkins, Arizona, USA) and southern (CTIO, Chile) hemispheres. The resulting data contains 472 million sources down to 15 mag in the H band. The 3σ limiting magnitudes in J, H, and K_s bands are 17.1, 16.4, and 15.3 mag, respectively, with S/N = 10. We have used the best quality 2MASS point source data (with qflag = AAA) to select red clump stars in different lines of sight. The stars with J-magnitude brighter than 14.5 mag and photometric uncertainty less than 0.1 mag (in J, H, and K_s) are considered in our selection procedure. To cover the disk portion of the sky, we limited our selection of RC stars to a latitude range of $-10° \leq b \leq +10°$.

In addition, we also utilized the data from the Gaia space-based telescope in our analysis. Since the parallax measurements from Gaia accurately determine the nearby distances, so, we used Gaia early data release (EDR3) (Gaia Collaboration et al., 2021b), which has the data for the first thirty-four months of its operational phase, to remove the foreground contaminations in our sample. It contains information on 1.8 billion sources ranging from 3 to 21 G-band magnitude. This data release gives full astrometric data (Lindegren et al., 2021) of 1.4 billion sources. We make use of the distance information of Gaia EDR3 stars provided in (Bailer-Jones et al., 2021) and astrophysical parameters from Gaia data release 3 (DR3) (Andrae et al., 2022) to remove foreground and evolved stars contamination.

2.2.2 Sample selection and RC extraction

The 2MASS data is downloaded in $1° \times 1°$ bins of $\ell \times b$ using 'stilts tapquery' (Taylor, 2006) in an iterative way. We then built 2MASS CMDs $(J - K_s, J)$ in 1 deg^2 region around central ℓ and b with boundaries of $\ell - 0°.5 \leq \ell < \ell + 0°.5$ and $b - 0°.5 \leq b < b + 0°.5$. The majority of the stars lie in the main sequence and giant phase in the CMDs. The most common type of giants are K-giants; therefore, the redder dense region of the CMD corresponds to RC stars (also described in Figure 2.3 and in the text of Section 2.1.2). The stars lying on the bluer side of the RC stars are predominantly foreground dwarf stars, while the redder regions contain M-giant or AGB-type evolved stars at higher extinction and larger distance.

To trace the red clump locus, we implemented the horizontal cuts in the CMD using adaptive binning in J-magnitude starting from the fainter end. This is illustrated by the 1-10 numbered J-bins in the middle panel of Figure 2.4, representing a 1 deg^2 field centered at $l = 45°$ and $b = 5°$. Initially, a default bin size of 0.5 mag was employed in the J-band. However, in cases where the number of stars fell below 50, an additional 0.5 mag was added to the previous bin size, ensuring statistically significant results. A $(J - K_s)$ color histogram of each J-bin is analyzed to select the most probable value of color associated with the second dense region, which indicates the presence of RC stars. Panels 1-10 of Figure 2.4 show the density histograms of the corresponding J-bin, where the maxima and minima are denoted by blue and red points, respectively. vertical lines in these panels represent the selected RC peak color. The obtained RC locus points are shown by black points in the central panel of Figure 2.4. The RC stars have some intrinsic color range, which may increase due to extinction effects. The spread in color (orange points in the central panel of Figure 2.4) around the central peak is determined from the standard deviation in the color of all the stars present between 'lo' and 'hi' $J - K_s$ color cuts in each histogram. Where 'lo' and 'hi' colors are calculated as

shift = color corresponding to second maxima - color at first minima

lo = locus point - shift

hi = locus point + shift

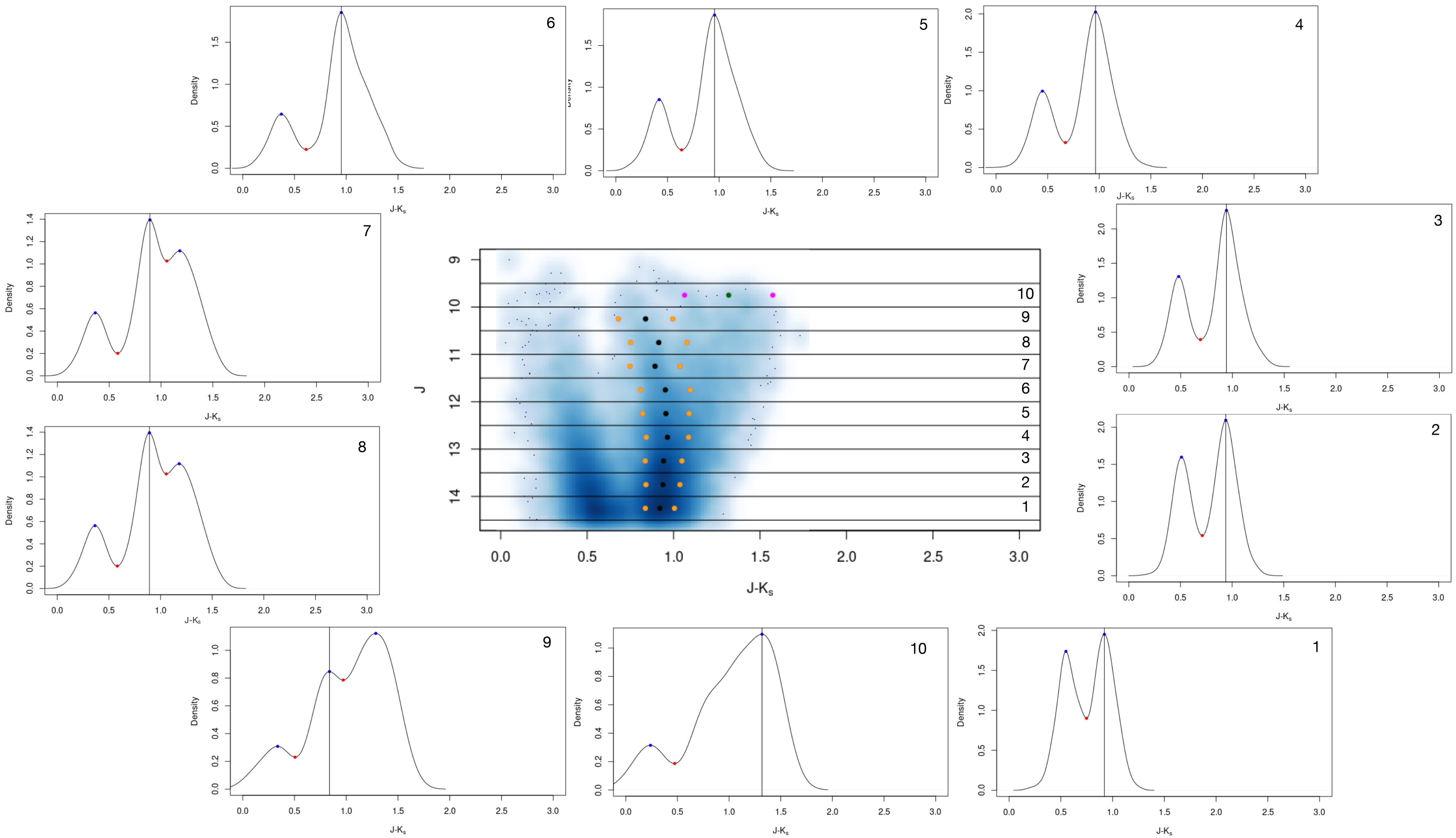

Figure 2.4: Selection of RC locus (black points) and its color spread (represented in orange points) from 2MASS color-magnitude diagram ($J-K_s, J$; central panel) for $1^\circ \times 1^\circ$ field around centered at $\ell = 45^\circ$ and $b = 5^\circ$. The panels labeled 1-10 represent $J-K_s$ density histograms of corresponding J magnitude bins. A detailed discussion is presented in the text. The black dots in the central plot shows the last hundred points in the lowest-density region.

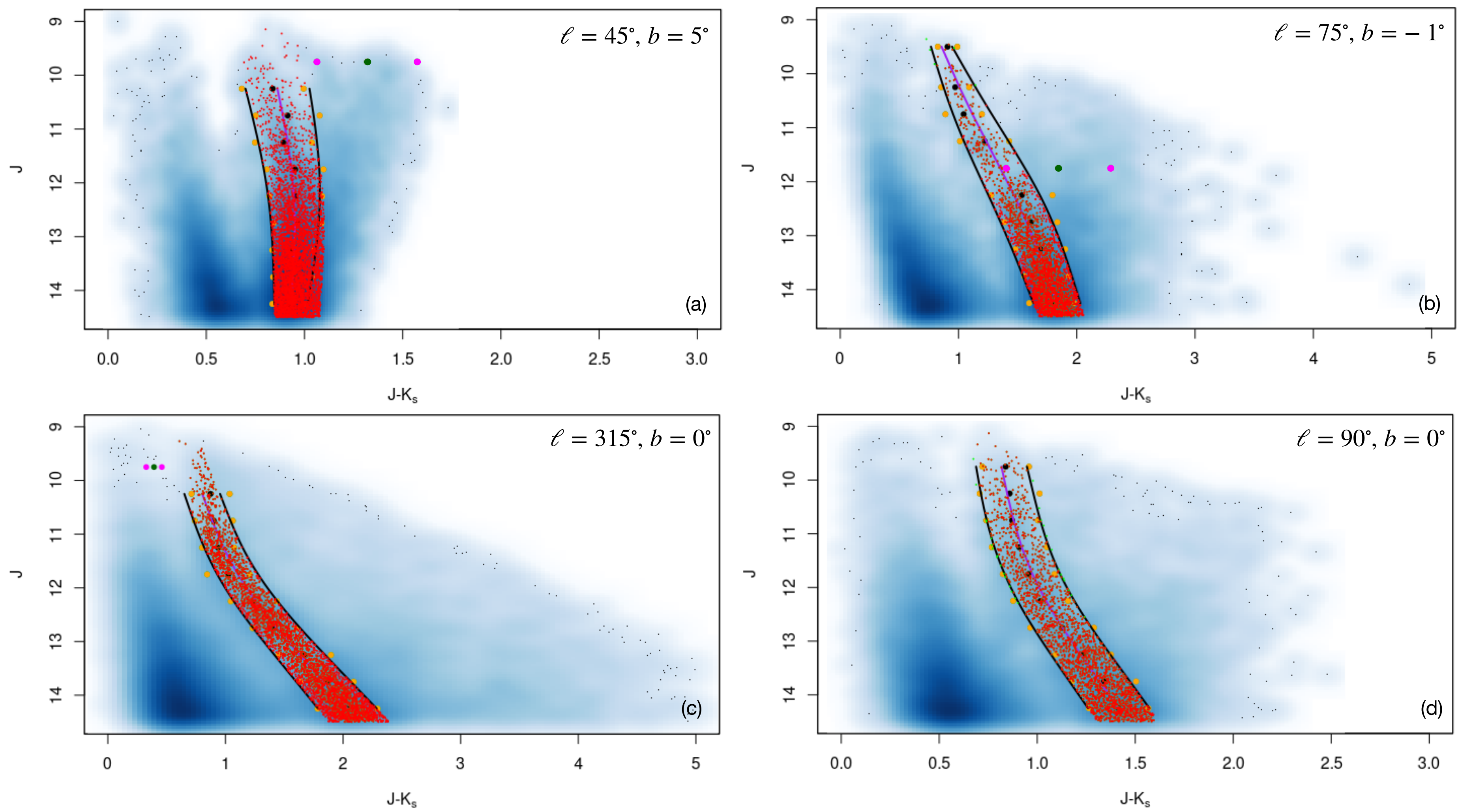

Figure 2.5: 2MASS color-magnitude diagram $(J-K_s, J)$ of $1^\circ \times 1^\circ$ region centered at $\ell = 45^\circ$, $b = 5^\circ$; $\ell = 75^\circ$ $b = -1^\circ$; $\ell = 315^\circ$, $b = 0^\circ$; and $\ell = 90^\circ, b = 0^\circ$ respectively in panel (a), (b), (c), and (d). Red points represent the selected RC star candidates. The black dots in the density plots are used to show the last 100 points in the lowest-density region.

Subsequently, smooth spline functions are fitted (black lines in Figure 2.5) on points 1σ region away from central RC locus (orange points in the example field) on both sides. In some cases, certain points selected as RC locus points may deviate from the actual locus. One such case is exemplified in the histogram of bin 10, as illustrated in the 10th panel of Figure 2.4. Here, the second peak in the histogram indicates a color that is shifted towards the redder side of the RC locus (also represented by the green point in the middle panel), potentially indicating the presence of another stellar population. These points are treated as outliers in our RC locus. Identifying and removing these outliers are crucial before fitting the splines because the presence of outliers within the RC locus could adversely impact the fitting results. However, blindly identifying and removing these outliers becomes challenging, particularly considering that the RC locus can vary depending on the extinction experienced by stars in different lines of sight. This highlights the difficulty in automatically selecting RC stars, despite the RC locus being readily observable through visual inspection. To mitigate this, we employed various color-cut criteria to identify and remove outliers in a systematic manner.

All the stars within the 1σ region are considered as candidate RC stars (red points in example fields shown in Figure 2.5). It is important to note that the likelihood of contamination by low-mass dwarfs increases at the faint end of the CMD, as illustrated by the green-colored points in the simulated 2MASS CMD of Figure 2.3. Thus, the choice of selecting the 1σ region around the central locus serves as a compromise between the necessity to avoid contamination while at the same time including most of the RC stars. It is noted that in certain low extinction fields (e.g., panel (a) of Figure 2.5), the selection color limits(marked by black lines) become narrower than the intrinsic color spread (~ 0.3 mag, Indebetouw et al., 2005) in RC stars towards the fainter end. In such cases, a color cut of 0.15 mag is considered on the redder side of the central locus instead of the method described above. A similar cut on the bluer part is not implemented to avoid contamination from the low-mass main sequence stars. A glimpse of the RC selection in different directions is provided in panel (a) $\ell = 45°$, $b = 5°$, (b) $\ell = 75°$ $b = -1°$, (c) $\ell = 315°$, $b = 0°$ and (d) $\ell = 90°, b = 0°$ of Figure 2.5.

Assuming $\frac{A_J}{A_K} = 2.5$ (Ganesh et al., 2009), the distance (d) and extinction (A_J) of each extracted RC star is calculated from equation 2.12 and 2.13.

$$A_J = \frac{(m_J - m_{K_s}) - (J - K_s)_0}{0.6} \tag{2.12}$$

$$d = 10^{\frac{m_J - M_J + 5 - A_J}{5}} \tag{2.13}$$

Where, m_J and m_{K_s} represent apparent magnitude in J and K_s bands, respectively. We have assumed a Dirac delta luminosity function for K-giant stars having absolute magnitude M_J and M_{K_s} of -0.945 ± 0.01 and -1.606 ± 0.009 (Ruiz-Dern et al., 2018). The effect of metallicity on the absolute magnitude and intrinsic colors of RC stars observed in the Sloan Digital Sky Survey's (SDSS) Apache Point Observatory Galactic Evolution Experiment (APOGEE) and the GALactic Archaeology with HERMES (GALAH) is calculated in Plevne et al. (2020) by using Bayesian-based distance from Bailer-Jones et al. (2018). The median colors of RC stars in the near IR bands $J - K_s = 0.62 \pm 0.05$ mag are the same for low alpha production element abundance and high alpha-abundance RC stars. While, the median value of absolute magnitude in the J-band shows a slight difference, i.e., $M_J = -1.05 \pm 0.21$ for low-α RC stars and $M_J = -0.89 \pm 0.27$ mag for high-α sources. The distance derived using these values of absolute magnitude and colors for the low and high metallicity in APOGEE RC sample (Bovy et al., 2014) shows an offset of ~ 200 pc only. Hence, it is safe to assume solar neighborhood values of absolute magnitude and intrinsic color in near-infrared bands to calculate the distance. Overall, the errors in the distance determination will include the errors in the absolute magnitude (0.5% contribution), extinction and intrinsic color (3% contribution), and the errors by assuming a Dirac delta luminosity function (5%). The photometric error will have a negligible contribution while using mean magnitude in a bin with more than 50 stars. Including all the uncertainties, the error in the distance determination is less than 10%. A comparison of the distance estimated by our method with those provided by Gaia and APOGEE is discussed in section 2.3.2. Using this method, we have selected ~ 10.5 million RC star candidates in $40° \leq \ell \leq 320°$ and $-10° \leq b \leq 10°$ region. It is important to note that we excluded the region bounded by $-40° < \ell < +40°$ from our selection process. This decision was made because the bulge RC/RGB sequence starts to appear in the color-magnitude diagram (CMD), overlapping with the disk RC sequence. Consequently, it becomes challenging to distinguish between the two sequences accurately.

2.2.3 Contamination

We have chosen the 1σ region around the central locus in CMD to extract RC stars. This selection reduces the contamination level. There may still be significant contamination from overlapping foreground dwarf or giant stars, particularly at the fainter end of the CMD. To address this issue, we utilized the high-accuracy astrometric data from the Gaia space-based telescope. The Gaia counterparts corresponding to our selected 2MASS RC stars are obtained by matching our sample with the best neighbors of Gaia DR3 and EDR3 using Marrese et al. (2022) through ADQL query in the Gaia archive. Out of 10.5 million candidate RC star sample, we found the counterparts for 10.3 million stars in Gaia DR3 and EDR3. The RC candidate stars having fractional Gaia distance (r_{pgeo}) error less than 10% and absolute difference in r_{pgeo} and distance obtained by our method more than 1.5 kpc, are assumed as foreground low mass star contamination. The resulting contamination in our sample is thus found to be $\sim$ 15%. Additionally, we crosschecked the contamination level using the latest release of Gaia data, i.e., GAIA DR3, independent of the previous contamination check by Gaia EDR3 distances. We found that a total of 14% of the sources are expected to be contaminating our sample, i.e., stars having positive parallax, parallax uncertainty less than 10% and the absolute distance difference $|d_{our\ method} - \frac{1}{parallax}| > 1.5$ kpc. The contaminating stars, thus obtained, are removed from the sample, and the remaining stars are considered as 'pure' RC stars. Consequently, our final sample contains $\sim$ 8.8 million RC stars.

A further crosscheck on the contamination and completeness in the sample is estimated by considering the latest Besançon model[1] (Robin et al., 2004) for catalog simulation without introducing the stellar kinematics mode. We performed the simulation around a $1^\circ \times 1^\circ$ field centered at $\ell = 45^\circ$, $b = 5^\circ$ and employed Marshall's extinction map

[1] Web service of the Besançon model at https://model.obs-besancon.fr/

(Marshall et al., 2006) in the 2MASS photometric system. The modeled CMD contains 11,539 stars down to J = 14.5 mag. Comparing the actual number of RC stars present in the field (5154) with our selected value (5133), we found that around 16% of the RC stars are missed by our selection criteria. In addition, the comparison revealed that around 14% of the stars in our sample are contaminated by dwarf and giant stars. This result is consistent with the contamination rate determined using Gaia foreground stars.

The above-discussed contamination estimation criteria, based on Gaia data, relied on utilizing high-accuracy Gaia distances for foreground stars. On the other hand, the astrophysical parameters are better suited to select a particular spectral type in the $logg - T_{eff}$ plane. The recent Gaia Data Release 3 provide the astrophysical parameters such as effective temperature, surface gravity, metallicity, absolute magnitude M_G, radius, distance, and extinction for a homogeneous sample of 471 million sources with $G < 19$ mag (Andrae et al., 2022). It is a part of the results from the astrophysical parameters inference system (Apsis) within the Gaia Data Processing and Analysis Consortium. These parameters were calculated by the simultaneous fitting of BP/RP spectra, parallax, and G-mag using Bayesian forward modeling based on isochrone models. While the astrophysical parameters obtained from GSP-phot offer accurate measurements for main-sequence (MS) stars, they can exhibit substantial uncertainty in estimated temperatures for the case of evolved or redder stars due to the temperature-extinction degeneracy. The redder stars could either be evolved cool stars or intrinsically hot stars that undergo significant dust extinction along the line of sight. Distinguishing between these two scenarios using only the low-resolution optical BP/RP spectra is challenging and is highlighted in Figure 6a of Andrae et al. (2022). The use of additional information on parallax and apparent magnitude may improve the selection but cannot fully break the degeneracy. Andrae et al. (2022) shows that the GSP-phot is expected to give reliable temperatures for RGB or RC stars if we use data with high-quality parallaxes ($\frac{\varpi}{\sigma_{\varpi}} > 20$). Using only high-quality parallax data corresponding to our RC sample stars and $log\ g > 4$ dex (for RC stars), we found contamination of only $\sim 2\%$ by other populations. For completeness, we also used a cut of $T_{eff} < 6000$ K, on the crossmatched stars and found that the resulting contamination remained within 5%.

2.3 Sample validation: Comparison with other available catalogs

In this section, the obtained RC sample is cross-matched with other RC star catalogs available in the literature to verify the completeness and accuracy of the distance determination.

2.3.1 Sample completeness

Our RC selection criteria are a balance between completeness and contamination. In order to minimize the contamination, we used the 1σ region around the central locus. Considering a perfect Gaussian around the central locus implies that the 1σ region would encompass $\sim 66.6\%$ of the RC stars. Increasing the completeness limit to 2σ or 3σ will lead to an increase in the contamination by dwarf stars as well as giants. This can be observed in panels 7, 8, and 9 of Figure 2.4, where an increasing color spread leads to the overlap of the second (representing RC stars) and the third Gaussian (associated with the other giant population). Even if we are missing 33% (upper bound) of RC stars, we are consistent in our selection criteria to use the 1σ region around the central locus. Ultimately, our goal is to identify overdensities compared to the surrounding regions of the Disk. The completeness of our sample in relation to other RC catalogs will be discussed in the following subsections.

2.3.1.1 APOGEE value added RC catalog

The Sloan Digital Sky Survey's (SDSS) Apache Point Observatory Galactic Evolution Experiment (APOGEE, Majewski et al., 2017) contains high-resolution near-infrared spectroscopic data of mainly giant stars. Using this data, a highly pure (95%) sample of RC stars is selected from the position of stars in color-metallicity-surface gravity-temperature space by Bovy et al. (2014). This sample contains minimal contamination from the RGB, secondary red clump, and asymptotic giant branch stars. The RC value-added catalog of APOGEE recent data release (DR17) lists 50,837 RC stars[2] in the entire survey region. The sample size reduces to 20,564 if we consider the stars in the region bounded by $40° \leq \ell \leq 320°$ and $-10° \leq b \leq 10°$ along with the magnitude cut on J-band,i.e., J < 14.5 mag. Out of 20,564 stars, 16,878 (~82%) are also selected as RC candidates in our sample. Only 18% of the APOGEE RC stars are missing in our sample. In order to investigate the position of missing stars in the color-magnitude space, a J-K_s versus J diagram of $1° \times 1°$ field around $l = 251°$ and $b = 0°$ (containing sufficient APOGEE RC stars) is plotted in the upper panel of Figure 2.6. A closer inspection of the figure reveals that the missing sources are present on the redder side of our selection window. However, increasing the selected color range to include the missing sources may result in the enhancement of the contamination.

2.3.1.2 Lucey et al., 2020 catalog

Recently Lucey et al. (2020) (L20 hereafter) have used available photometric data from Gaia DR2, PansTARRS, 2MASS, and ALLWISE to select the RC stars. They provide a sample of 2.6 million RC stars. Their method involves predicting astroseismic (ΔP, $\Delta \nu$) and spectroscopic parameters (T_{eff}, $logg$) obtained from SED using neural networks. They divided their RC sample into two categories: stars with a contamination rate of 20% and completeness of 25% as "tier1" and 33% contamination rate and 94% completeness rate as "tier2". Cross-matching their catalog with our candidate stars results in 73% of overlapping in our survey region. In sub-classification, we are able to recover 85% of more reliable stars from "tier1" and 71% of tier2 stars. To have a clear idea of completeness, a color-magnitude diagram of a low extinction field 2MASS $\ell = 45°$ and $b = 5°$ is shown in the lower panel of Figure 2.6. L20 RC stars of that region and RC candidates from our sample are over-plotted on the same figure with blue and red points, respectively. Similar to the APOGEE RC, the missing L20 RC stars are mostly present on the redder side of the RC locus. It is clear from the figure that increasing our color selection criteria to 2σ or 3σ will lead to an increase in contamination.

[2]URL link to APOGEE RC catalog

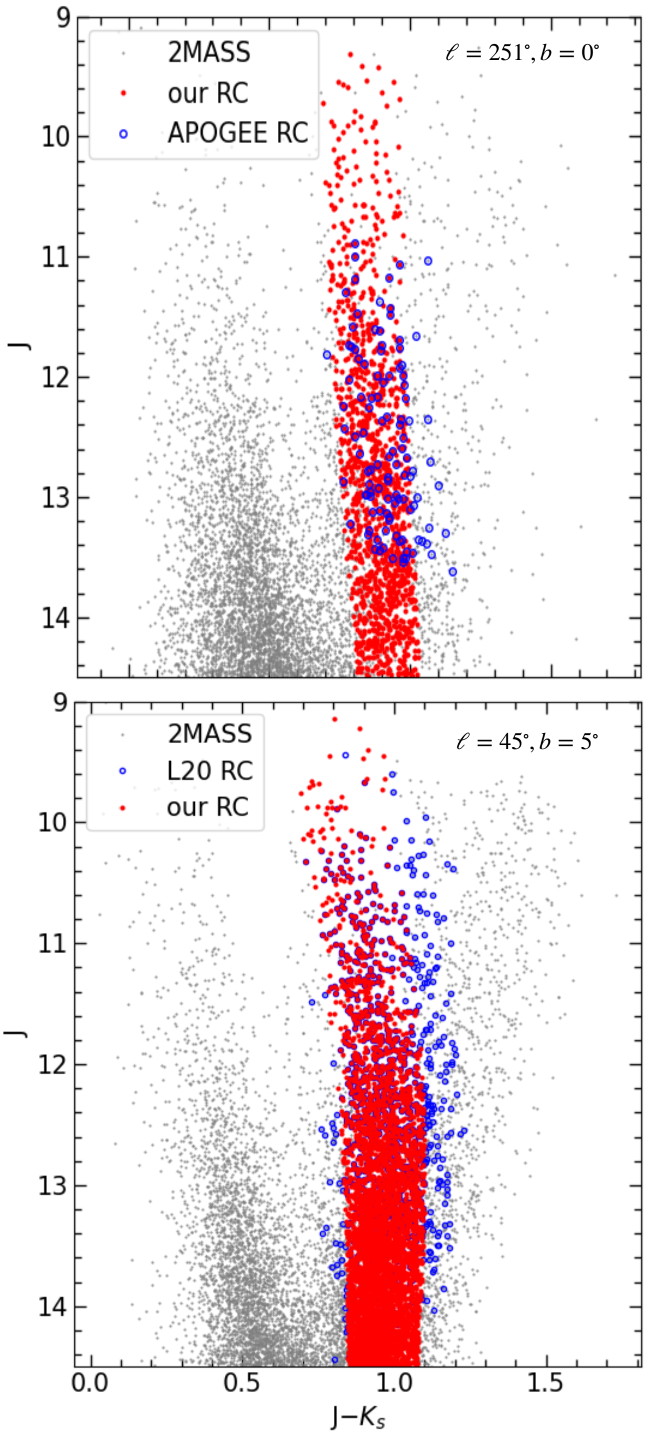

Figure 2.6: CMD (J, J-K_s) for $1^{\circ} \times 1^{\circ}$ field centered around $\ell = 251^{\circ}$ and $b = 0^{\circ}$ (upper panel) and $\ell = 45^{\circ}$ and $b = 5^{\circ}$ (lower panel) in grey-cross points. RC stars in APOGEE value-added catalog and L20 "tier1" and "tier2" RC stars are over-plotted in blue open circles in respective panels. RC stars selected by our method are represented by red points.

2.3.2 Estimated Distance Comparison

We calculate the distance of RC stars within 10% uncertainty level by assuming the constant luminosity function of K-type giants (as discussed in section 2.1.1). The distance information of giant stars can also be obtained from available astrometric, spectroscopic, and photometric data. This section compares the distances obtained by different methods with the estimated distance for RC stars listed in our sample.

2.3.2.1 APOGEE RC and StarHorse distances

The narrowness of the RC locus in color-metallicity-luminosity space accounts for the precise measurement of the distance of stars in the APOGEE value-added RC star catalog. The distance of common stars from the APOGEE value-added catalog is compared with our estimated distances in the upper-left panel of Figure 2.7. Most of the stars show the same distance, with a small number showing a slight deviation from the APOGEE RC distances.

APOGEE has another value-added catalog named 'StarHorse' dedicated to finding the distance, extinction, and astrophysical parameters of the stars by combining the high-resolution spectroscopic data from APOGEE with broadband photometric data (Pan-STARRS, 2MASS, and ALLWISE) and parallax (Gaia EDR3) using Bayesian statistics (Santiago et al., 2016; Queiroz et al., 2020). StarHorse DR17 catalogs list 562,424 (RC as well as non-RC) APOGEE sources having distance uncertainties of $\sim 5\%$. 111,438 StarHorse stars are found in $39.5° < \ell \leq 320°$ and $-10° \leq b \leq 10°$ region. Cross-matching these stars with our catalog in $1''$ sky region results in 45,580 common stars. The distance comparison of cross-matched stars obtained from our method (x-axis) with StarHorse median distance is shown in the bottom-left panel of Figure 2.7. The majority of the stars lie close to the 1:1 line, with some scattering of the outliers.

The distance of our selected stars matches well with both the APOGEE catalogs. However, the APOGEE spectroscopic sample has a brightness limit of $H < 13$ mag, which corresponds to stars in nearby regions only (d < 3-5 kpc). Hence, the APOGEE sample can be used to check the reliability of our catalog distance up to about 5 kpc.

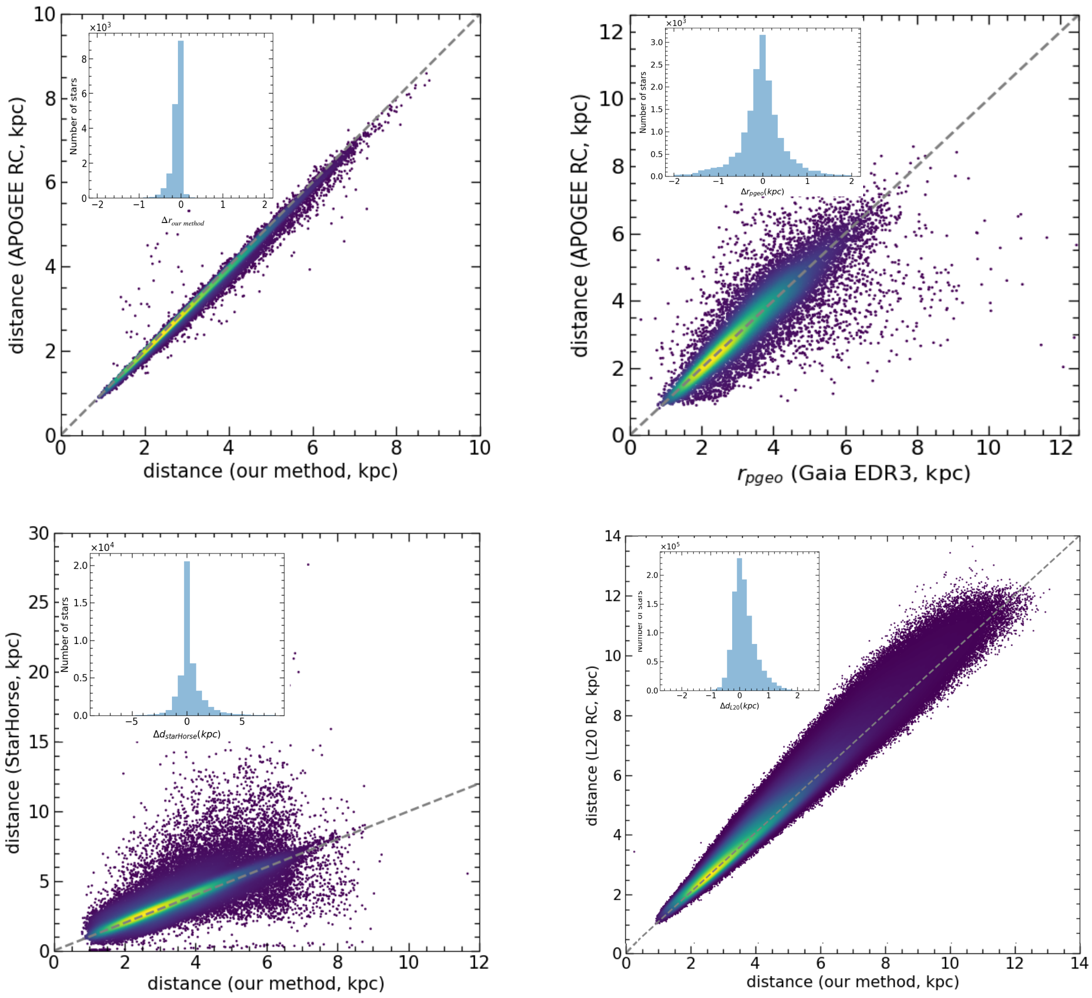

Figure 2.7: Comparison of distance obtained from different methods: our method with APOGEE (in the upper-left panel), Gaia EDR3 (r_{pgeo}) with APOGEE RC (in the upper-right panel), our catalog with StarHorse (bottom-left), and L20 catalog (bottom-right). The inset histograms in each panel represent the difference in respective distances.

2.3.2.2 Gaia Distances

The Gaia space-based telescope provides parallax measurements with uncertainties typically of the order of a few microarcseconds. It has been demonstrated by Bailer-Jones (2015) that using the inverse of parallax as a distance estimator is not suitable when the parallax error exceeds 20%. A probabilistic approach utilizing Bayesian statistics with appropriate prior assumptions is recommended in such cases. In this probabilistic approach, when the data is of high quality, the probability distribution of the distance of a star, given its parallax measurements and error ($P(r|\varpi, \sigma_{\varpi})$ referred to as the posterior), should primarily rely on the likelihood, i.e., the probability distribution of parallax measurement for a particular distance ($P(\bar{w}|r, \sigma_{\bar{w}})$. However, in the presence of large measurement errors, the resulting posterior distribution will be influenced by the prior assumptions ($P(r)$). Selecting a reliable and appropriate prior is important, especially when studying fainter or distant sources where uncertainties are expected to increase.

In the Gaia EDR3, two types of distance estimations were provided by Bailer-Jones et al. (2021): "geo (r_{gep})" and "photogeo (r_{pgeo})," which were derived using Bayesian statistics with different priors. While, in the recent Gaia DR3, distances were calculated through the simultaneous fitting of BP/RP spectra, parallax, and G-magnitude using Bayesian forward modeling (Andrae et al., 2022). To determine the most appropriate distance estimator among these methods, Gaia Collaboration et al. (2022) compared them with the RC distances obtained from APOGEE DR17 (Abdurro'uf et al., 2022). In their analysis, Gaia Collaboration et al. (2022) found that the "photogeo" distance estimator exhibited less dispersion and was therefore considered a better distance estimator compared to the other two methods. To validate the distance estimation accuracy of our study, we compared the APOGEE RC distances of a common sample of 16,878 stars (consisting of our sample stars, APOGEE, and Gaia EDR3) with the "photogeo/r_{pgeo}" distances in the upper-right panel of Figure 2.7, and distance obtained by our study in the upper-left panel along with the respective difference in the distance histograms (inset Figures). It can be seen that both the distance estimators (r_{pgeo} and our distances) show a one-to-one correlation with the APOGEE RC distances. However, it is evident that our method yields a narrower distribution which is closer to the APOGEE distance as compared to the larger dispersion in 'r_{pgeo}' distance (see the inset histograms of Figure 2.7). This highlights the robustness of our RC selection and distance estimation method.

2.3.2.3 Lucey et al., 2020 RC distances

APOGEE and Gaia distances can only be used to compare nearby distances ($< 3-5$ kpc). On the other hand, the L20 catalog provides the distances of 2.4 million stars with $\sim 75{,}000$ stars at distances > 10 kpc. A comparison of L20 distances with ours (bottom-right panel of Figure 2.7) depicts that the vast majority of the stars are showing a one-to-one correlation. The distance to the fainter stars seems to be overestimated in the L20 catalog, which may result from an uncertain extinction in the W1 band.

2.4 Summary

The chapter focuses on the importance of RC stars as distance indicators and presents a methodology to extract RC stars from 2MASS Color-Magnitude Diagrams (CMDs). The automated scripts were written in R-programming language to select the RC stars systematically from $1° \times 1°$ bins in $\ell \times b$ from 2MASS CMDs, covering a range of $40° \leq \ell \leq 340°$ and $-10° \leq b \leq +10°$. The detailed methodology followed to identify and select red clump stars is demonstrated, with importance to the outlier removal. Thanks to the high accuracy distances available in the Gaia data we were able to minimize the foreground contamination by dwarf and giant stars in our sample, which was estimated to be less than 15% . The resulting sample consists of ~ 8.8 million 'pure' RC stars. To further validate our methodology, we estimated the contamination and completeness of our sample with respect to RC value-added catalog in APOGEE and L20 catalogs. The comparison of distance estimated of the sample stars in our method is compared with the APOGEE, StarHorse, and Gaia distances, which confirms the reliability of our distance estimation. These findings validate the robustness and accuracy of our RC sample, laying a solid foundation for our subsequent analysis and investigation of over-densities in the Galactic Disc.

In conclusion, the validation of our RC sample, by comparing with different catalogs in the literature, demonstrates the effectiveness of our selection criteria and distance estimation method. We have successfully assembled the largest known homogenous sample of RC stars, comprising approximately 8.8 million stars covering a wide area of the Galactic plane. This dataset is particularly valuable as it extends to distant regions where the accuracy of Gaia distances is limited. With this extensive data-set, we hope to gain a better understanding of the structure and dynamics of our Milky Way galaxy.

Chapter 3

Milky Way disk revealed by red clump stars

"Have we discovered our Galaxy yet?" And I think the answer to this question is "No, not quite". There is plenty of work ahead for the next generation of astronomers.

- Heather Couper, *1949-2020*

The structure of the Milky Way disk is characterized by the presence of spiral arms in its inner regions, while the outer regions exhibit flare and warp features. These features have been studied thoroughly using various populations in the past few decades, primarily focusing on the younger, $\sim$ Myr tracers (refer to Section 1.3.1, 1.3.2, and 1.3.3 of Chapter 1). While extensive research has been conducted to understand the structure of the Milky Way disk using younger tracers, the dedicated investigation focusing on the identification of spiral features specifically from the distribution of RC stars (intermediate-to-old age population) is limited. Studies conducted by Lucey et al. (2020) and Gaia Collaboration et al. (2022) have shown that the older population of stars, including RGB or RC stars, exhibits a homogeneous distribution across the disk, lacking clear indications of spiral arms. However, a recent study by Lin et al. (2022) found evidence of the Local spiral arm from the overdensity maps of RC stars selected from Gaia and 2MASS data, which shows a difference from the gas arm. Furthermore, their study also gives the signature of the Perseus arm; but, due to limitations in their sample completeness at greater distances, the precise geometry of this arm was not constrained. Nevertheless, this research serves as a remarkable demonstration of the potential of RC stars as invaluable tracers for mapping spiral arms in the Milky Way. It is important to note that the use of Gaia data is limited up to five kpc only due to large uncertainties beyond that. Consequently, there is no evidence of the Outer arm in the RC distribution by (Lin et al., 2022) or any other tracer utilizing Gaia data (e.g., Xu et al., 2021; Hou, 2021). The Outer arm is the distant curved feature, supposed to have the same pitch angle as the Norma arm. In other words, it could be a continuation of the Norma arm in the Galactic third and Fourth quadrants. The RC sample compiled in Chapter 2, which employed distance estimation based on the distance modulus rather than relying solely on Gaia parallax or distances, constitutes the largest known sample of RC stars to date. This extensive data-set holds the potential to probe deeper and more distant structures of the Galactic disk.

In contrast to the inner spiral structures, the outer structure of the disk has been studied extensively using various age populations, including RC and RGB stars. As discussed in Section 1.3.2 and 1.3.3, comparing the structures traced by older and younger stars reveals the age dependency of warp and flare features in the outer disk. However, the exact nature of this age dependency is not well constrained (detail description in respective sections of Chapter 1), primarily due to differences in data sets used and the inhomogeneous coverage of the sky. The flare and warp structure traced by the RC stars is presented in (López-Corredoira et al., 2002; Romero-Gómez et al., 2019; Yu et al., 2021a; Li et al., 2020); however, their sample is confined to small areas of the sky. On the other hand, our RC sample, selected from a significantly wider area (see Chapter 2), offers a unique opportunity to reanalyze the structure of the outer Galaxy, to better constrain the origin mechanism of the outer disk features.

In this chapter, we analyze the density distribution of RC stars using the comprehensive catalog prepared in Chapter 2 with the aim of investigating the presence and characteristics of the spiral structure, flare, and warp in the Galactic disk. Furthermore, we model the Galactic disk using our RC sample to map the 3D morphology of the disk as traced by the RC stars.

3.1 Distribution of RC in the Galactic plane

In this section, we present RC distribution in the Galactocentric XY-plane to represent the face-on view of the MW galaxy. The density and overdensity maps are presented to trace the spiral pattern and to investigate the asymmetry in the spiral arms.

3.1.1 Density maps

To obtain the face-on maps of the Galaxy from the distribution of the RC stars, the distance information (r), along with the position of stars (ℓ, b) from our RC catalog, is converted to right-handed Galactocentric spherical coordinates using the following transformation:

$$X = r \sin\ell \cos b \tag{3.1}$$

$$Y = r \cos\ell \cos b - R_\odot \tag{3.2}$$

$$Z = r \sin b \tag{3.3}$$

Where r is the distance of the star to the Sun and ℓ, b are the Galactic longitude and latitude, respectively. The Sun is located at $R_\odot = 8.34$ kpc (Reid et al., 2014) from the Galactic center.

The complete density map of selected RC stars in the Galactocentric coordinates (X, Y) is obtained by using kernel density estimation with 0.1 kpc bandwidth. The resulting spatial distribution of RC stars is shown in Figure 3.1, where color-bar denotes the probability density. The point (0,0) represents the Galactic center (black cross) and (-8.3, 0) corresponds to the position of the Sun (orange circle). The lack of stars closer to the

Sun is due to our selection criteria discussed in Sections 2.2.2. The spatial distribution of stars does not show any arm-like feature, which is expected for older age population stars. The density distribution is rather dominated by the global density of stars in the Galactic disc, i.e., exponentially decreasing star counts as moving away from the Galactic center. The spiral pattern is thus difficult to disentangle from the old star population.

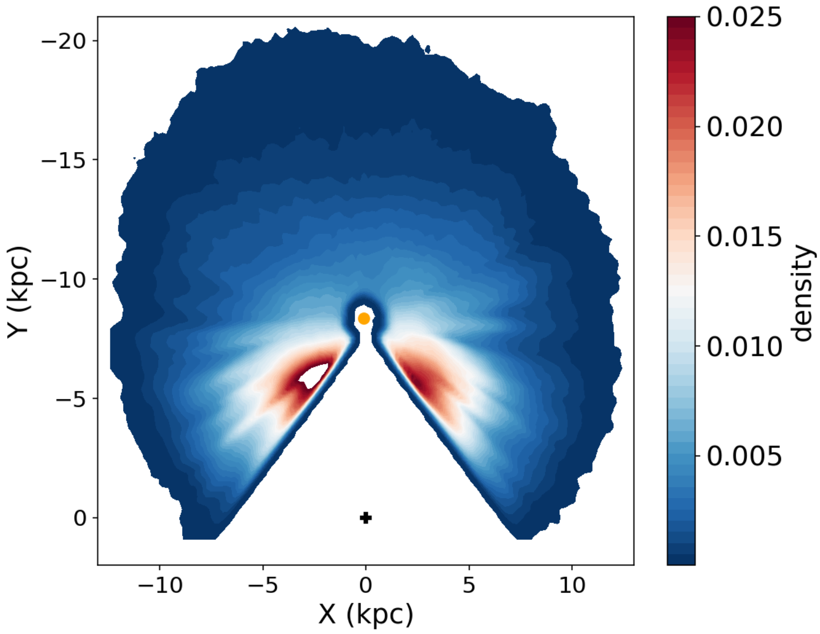

Figure 3.1: Spatial density distribution of RC stars projected onto the Galactic plane in Galactocentric coordinates with the location of the Galactic center marked by black cross and the Sun by orange point. The empty regions towards the inner Galaxy represent the density above the maximum limit shown in the corresponding color bars.

3.1.2 Overdensity maps: Detection of the Outer arm

In order to reveal the underlying spiral structure if present, we used the bi-variate kernel density estimator method. The stellar over-density is determined following (Poggio et al., 2021).

$$\Delta_\Sigma(X,Y) = \frac{\Sigma(X,Y)}{<\Sigma(X,Y)>} - 1 \tag{3.4}$$

The local density $\Sigma(X,Y)$ and mean density $<\Sigma(X,Y)>$ at (X, Y) are calculated using the bi-variate kernel density estimator in R-programming, with a bandwidth of 0.3 and 2 kpc, respectively. The over-density map shown in Figure 3.2 reveals some discernible curvy features. To look at the correspondence of the feature with the spiral arms, we used the log-periodic spiral arm model from Reid et al. (2019) (eq. 3.5) to map the spiral arms in the RC over-density plot.

$$\ln \frac{R_G}{R_{G,ref}} = -(\theta_G - \theta_{G,ref}) \tan \psi \tag{3.5}$$

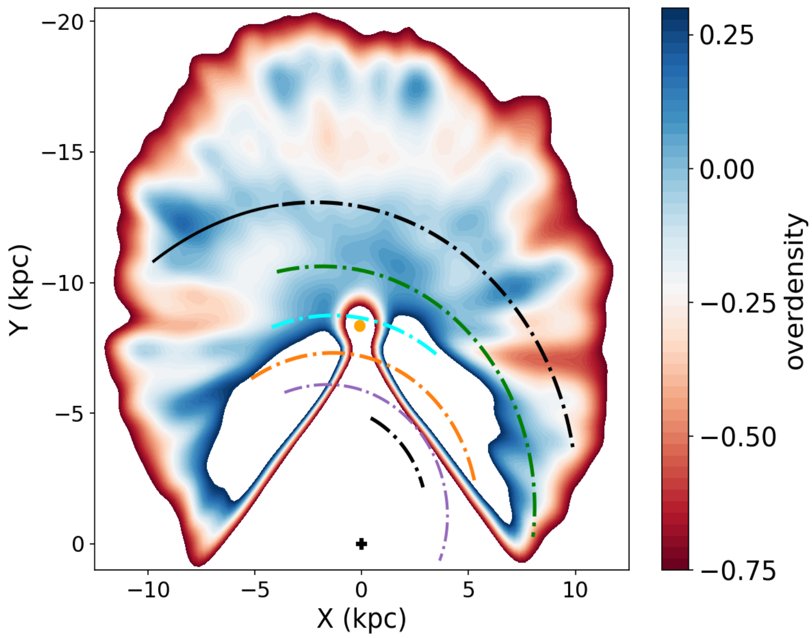

Figure 3.2: Overdensity map of RC stars in Galactocentric XY-coordinates. Spiral arms from Castro-Ginard et al. (2021) (Scutum: purple, Sagittarius: orange, Local: cyan, Perseus: green) and Reid et al. (2019) (Norma-Outer: black) are over-plotted in dashed-dotted lines. The solid black line corresponds to the extension of Outer arm (Reid et al., 2019) in the 3rd Galactic quadrant. The empty regions towards the inner Galaxy in both panels represent the density or over-density above the maximum limit shown in the corresponding color bars.

R_G and θ_G in eq. 3.5 are Galactocentric radius and azimuth (defined as 0 towards the sun and increasing in the direction of Galactic rotation) along the arm, respectively. $R_{G,ref}$, $\theta_{G,ref}$, and ψ are the reference Galactocentric radius, azimuth, and pitch angle for a given arm. Castro-Ginard et al. (2021) have determined the parameters for four arms (Perseus, Local, Sagittarius, and Scutum) by fitting the above model on the distribution of Galactic open cluster in Gaia EDR3 data and a high mass star-forming region in the Galaxy from Reid et al. (2014). These parameters are used to construct the corresponding arm segments. The parameters of arms (Norma and Outer arms) not considered in Castro-Ginard et al. (2021) are taken from Reid et al. (2019). The Galactocentric coordinates for corresponding arms are then calculated using the following equations.

$$X = R_G \sin \theta_G \tag{3.6}$$

$$Y = -R_G \cos \theta_G \tag{3.7}$$

Over-plotting the spiral arm as dashed-dotted lines (Perseus: green, Local: cyan, Sagittarius: orange, and Scutum: purple, Norma-Outer: black) in Figure 3.2 presents a remarkable agreement between the location of the Outer arm (black dashed-dotted line) defined in Cantat-Gaudin et al. (2020) and the over-density of RC stars. To the best of our knowledge, this is the first study to identify and trace the Outer arm using the distribution of RC stars. Interestingly, our investigation goes beyond simply confirming the previously modeled Outer arm. We observe a significantly higher density of RC stars in the third Galactic quadrant, which is represented by the solid black line in Figure 3.2. This line is plotted by extending the model parameters of the Outer arm proposed by Reid et al. (2019) within the range of (X, Y)~ (-4,-13) to (-10, -10.5) kpc. Most of the earlier studies of Galactic structure by star count method using different tracers either do not show such a distant Outer arm structure (Poggio et al., 2021; Lin et al., 2022, etc.) or show the presence of Outer arm mainly in the second quadrant with a small extension into the third quadrant (from (X, Y)~ (10, -3) to (-4, -13) kpc) (Reid et al., 2019). In contrast, our selected RC stars are able to trace the Outer arm $\sim 6kpc$ farther into the 3rd Galactic quadrant, thus providing new insight into the morphology of the Outer spiral arm beyond the earlier understanding. In addition, the regions closer to the Perseus arm also show enhanced number density.

Overall, we are able to trace the distant arms in the outer Galaxy, unlike in Lin et al. (2022) where only the Local arm of the Galaxy was traced using RC stars extracted from the 2MASS CMD. The use of Gaia parallax to estimate the distance in Lin et al. (2022) and their selection criterion on relative parallax uncertainties $\frac{\varpi}{\sigma_{\varpi}} > 5$ resulted in the confinement of structure towards the nearer regions of the Galaxy, thereby limiting their ability to trace structures beyond the Local arm. It should be noted that we have excluded the large portion of the inner Galaxy ($|\ell| < 40$), which explains why the Local arm feature is not visible in our over-density maps.

Furthermore, as discussed in Section 2.2.3, we have implemented effective measures to mitigate contamination in our RC sample. By utilizing the Gaia EDR3 r_{pgeo} distances of foreground dwarf stars, we have successfully reduced contamination to approximately 15%. Additionally, a small additional contamination of around 5% is identified when employing astrophysical parameters such as t_{eff} and $logg$ for selecting pure RC stars. This slight variation in sample contamination does not significantly impact the overall structure revealed by the RC stars. To assess the impact of contamination removal, we compare the distribution of RC stars in the XY plane after applying the Gaia EDR3 distance-based contamination removal (approximately 15%), the Gaia DR3 astrophysical parameters-based contamination removal (approximately 11%), and the combined removal from both sources (approximately 20%) in respective panel (a), (b), and (c) of Figure 3.3. The figure clearly shows that despite the varying levels of contamination removal, the structural features observed in the distribution of RC stars remain consistent across the three panels. This highlights the robustness and reliability of our RC sample for investigating the density distribution and structural characteristics of the Galactic disk.

3.1.3 Asymmetry in the Galactic Disc

In a symmetric Galaxy, the number of RC stars above and below the Galactic plane would be expected to be nearly equal at all longitudes. However, our analysis of the ratio of RC stars above ($Z > 0$) to below ($Z < 0$) the Galactic plane in the longitude range of $40^\circ \leq \ell \leq 320^\circ$ with 1° bins does not show a symmetric structure (see Figure 3.4). There is clear evidence of the wave-like asymmetry in the Disk characterized by an excess of RC stars above the Galactic plane ($Z > 0$) compared to $Z < 0$ for $\ell < 180^\circ$ and

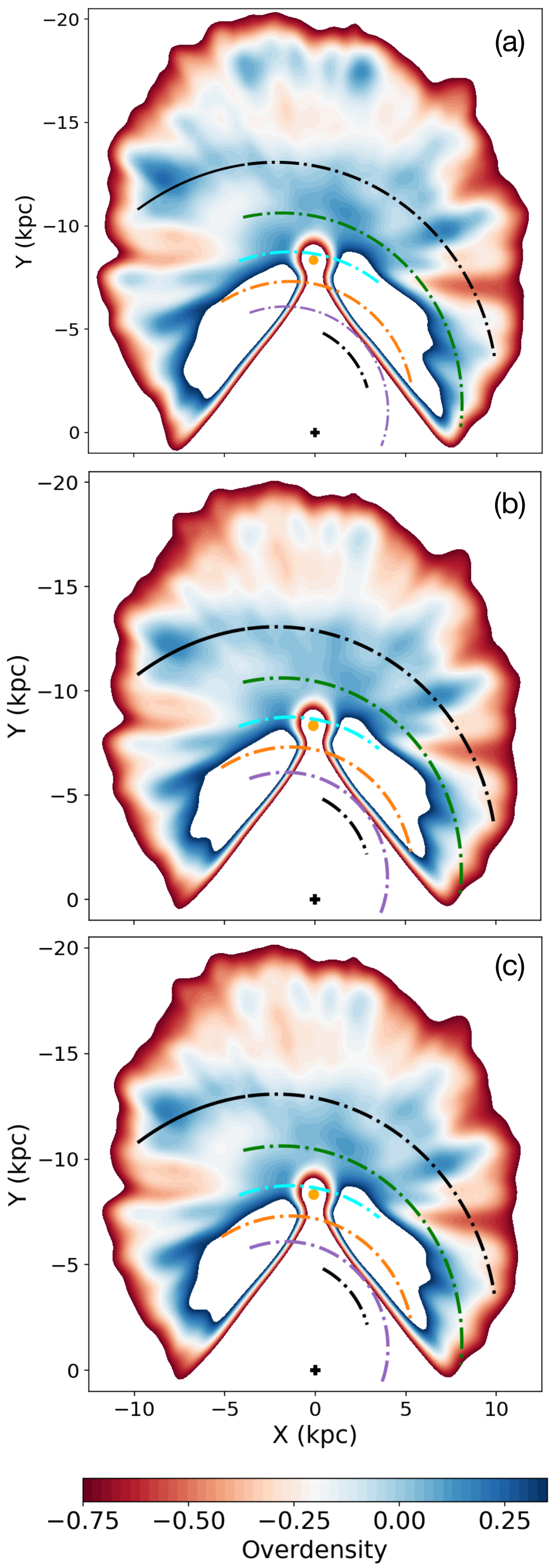

Figure 3.3: Comparison of RC over-density obtained by removing contamination using (a) Gaia EDR3 r_{pgeo} distance and (b) astrophysical parameters from DR3. The bottom panel shows over-density by taking contributions from both (a) and (b).

the opposite trend for $\ell > 180°$. The asymmetry above and below the Galactic plane

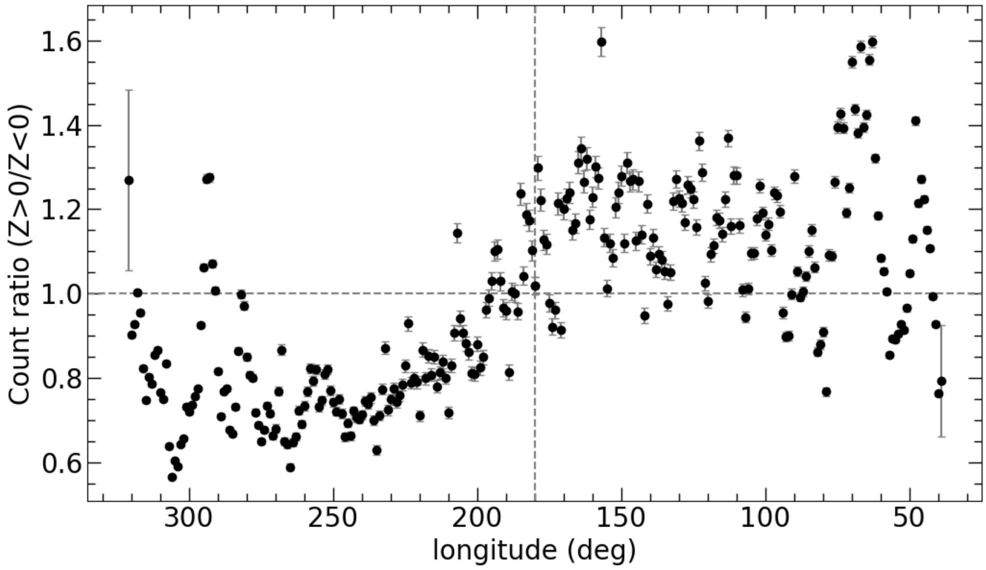

Figure 3.4: Distribution of the ratio of RC stars above and below the Galactic plane as a function of longitude in 1° bins of ℓ.

with respect to longitude has also been observed earlier in a few regions of the Galactic plane using various stellar tracers, (e.g., López-Corredoira et al., 2002; Ferguson et al., 2017). In contrast, we analyzed the asymmetry in the disk continuously spanning a wide range of longitudes from $40° \leq \ell \leq 320°$. This asymmetry could possibly be the manifestation of a warped disk.

3.1.4 Asymmetry in the Outer spiral arm

It is well known that there exists an asymmetry in the stellar densities along the azimuthal direction in the Milky Way as well as other disk galaxies (e.g., Henry et al., 2003) due to different spiral arms present in the galaxies. However, the asymmetry in the spiral arms above and below the Galactic plane has never been studied so far. We analyze the distribution of RC stars above ($Z > 0$, Figure 3.5a) and below the Galactic plane ($Z < 0$, Figure 3.5b) separately to investigate the asymmetry of spiral arms along the vertical direction. Interestingly, we found that the overdensity in the RC distribution does not continuously trace the Outer arm from one quadrant to another. An over-density towards the Outer arm is observed exclusively in the 2nd quadrant for stars above the

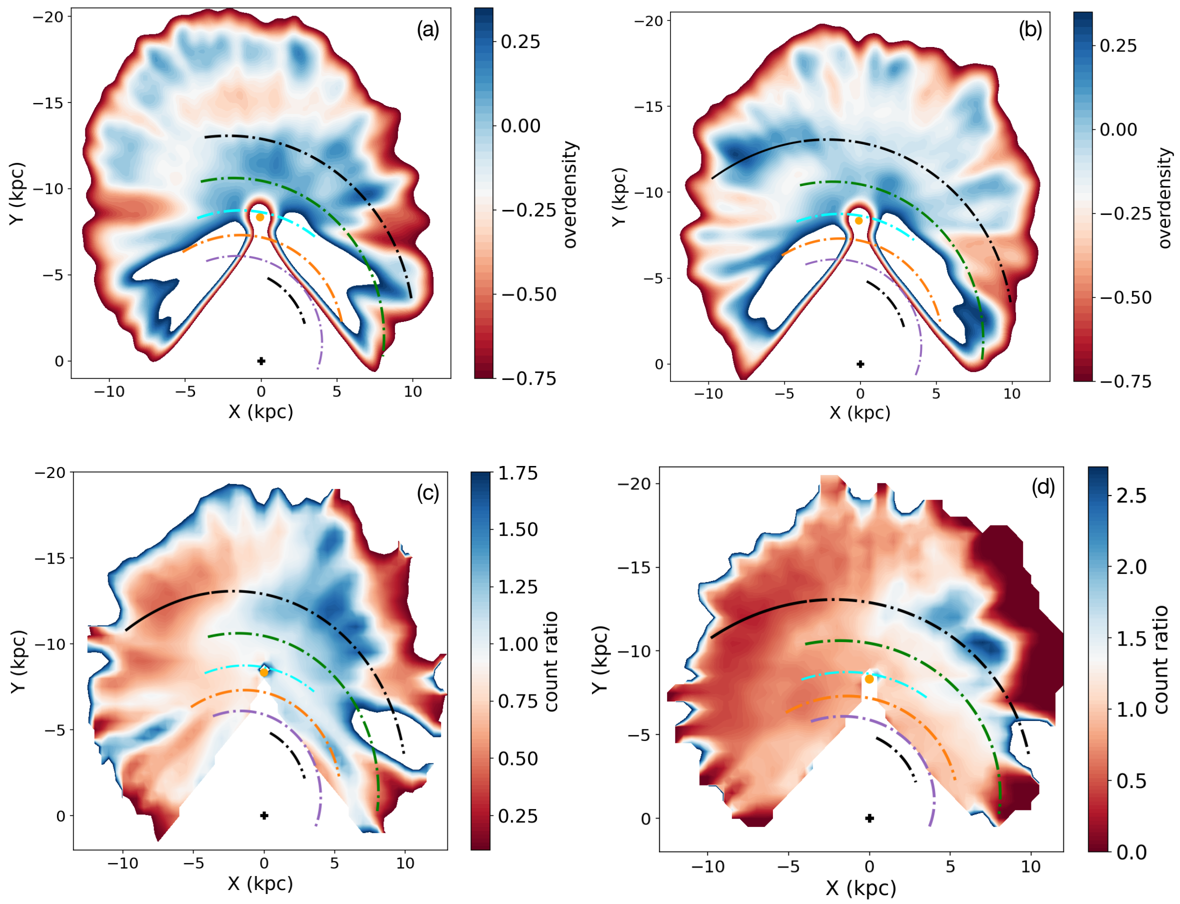

Figure 3.5: Over-density map of RC stars above (Z>0) and below (Z<0) the Galactic plane, in top panels (a) and (b) respectively. The bottom panels represent the distribution of the ratio of RC stars above and below the Galactic plane in the Galactocentric coordinate system with ℓ range of $40° \leq \ell \leq 320°$ and $-10° \leq b \leq 10°$ (in panel (c)) and $|b| = 5°$ in panel (d). The spiral arm pattern (dot-dashed) follows the same color codes as in Figure 3.2

Galactic plane. In contrast, the distribution of RC stars below the Galactic plane shows over-density at the Outer arm in the third Galactic quadrant. The different parts of the Outer arm are thus traced by the RC above and below the Galactic plane, giving the signature of significant asymmetry, which could be related to the warping of the spiral arm, especially the outer arm.

We further analyzed the ratio of RC stars above and below the Galactic plane to better understand the structure. The ratio of RC stars is plotted in Galactocentric XY-plane with 200 pc bins of both X and Y for the range of Galactic latitude; $-10° \leq b \leq 10°$ (see Figure 3.5c) and for $b = \pm 5°$ in 3.5d. Upon careful examination of the figures, a notable large-scale asymmetry becomes apparent, characterized by distinct color variations for $\ell < 180°$ and $\ell > 180°$. Furthermore, a closer inspection reveals curvy features within the count ratios. To explore the correlation between these curvy features and the spiral arms, we overlaid the log-periodic spiral arm model, described by equations 3.5, 3.6, and 3.7, onto the count ratio map. The analysis uncovered an interesting association between the count ratios and the Outer arm. Specifically, in the second quadrant, the count ratio exceeded 1, indicating an over-density above the Galactic plane in this direction, while the count ratio became less than 1 in the third quadrant. This suggests an asymmetry in the spiral pattern above and below the Galactic plane. The observed asymmetry in the spiral arms gives direct observational evidence that the spiral arms are warped upward for $\ell < 180°$ and downwards in the southern direction, $\ell > 180°$, similar to the Galactic disc.

3.2 Disk Modeling

We model the Galactic disk with RC stars by assuming a smooth density distribution model to infer the RC star counts in the Galactic disc. The stellar density in the disk is known to be decreasing exponentially with Galactocentric radius, R, and height, Z above or below the Galactic plane (Bland-Hawthorn & Gerhard, 2016). The density distribution is given by the equation 3.8.

$$\rho(R,Z) = \rho_\odot \, exp\left(-\frac{R - R_\odot}{H}\right) exp\left(-\frac{|Z|}{h_Z}\right) \tag{3.8}$$

Where H and h_Z are the scale length and scale height of space density in the Galactic disk, $\rho_\odot$ denotes the RC density in the Solar neighborhood. In our analysis, we are only dealing with low latitude fields ($-10° \leq b \leq 10°$) where the contribution of the thick disk will be very small, so following López-Corredoira et al. (2002), we are using a single exponential function to model the disk. We call the disk an 'Old disk' depicting the average structure traced by the intermediate-older population.

We have a sample of RC stars at each distance spanning a large volume of the sky.

But to model the Galactic disk with RC stars in the Galactic disk with respect to the smoothed model (equation 3.8), we have to convert the RC stars into the stellar density. The stellar density (D, stars pc^{-3}) in a particular solid angle $w = d\ell \times db$ is calculated from star counts (N) using the fundamental equation of stellar statistics (Bahcall, 1986) described in equation 3.9.

$$N(m) = w \int_0^\infty r^2 D(r) \Phi(m)\, dr \tag{3.9}$$

Here, $N(m)$ is the number of stars per unit solid angle in the interval m to $m + dm$, and $\Phi(m)$ is the luminosity function which can be replaced with the delta function in our case since we are considering only the K2-type giants, with an absolute magnitude of $M_J = -0.945$ mag (Ruiz-Dern et al., 2018) in our analysis. The density $D(r)$ at a distance r from the Sun is calculated by dividing the sample of RC stars into Galactic longitude ℓ, Galactic latitude b, and apparent magnitude m with a bin size of 5°, 2° and 0.2 mag, respectively using the equation 3.10 obtained by inverting the equation 3.9.

$$D(r) = \frac{N(m)\delta m}{w r^2 dr} \tag{3.10}$$

Since the defined model for a smooth density distribution in a typical disk galaxy is in Galactocentric cylindrical coordinates. So, the obtained mean density is converted into the Galactocentric cylindrical system using the following equations.

$$R = \sqrt{R_\odot^2 + (r\cos b)^2 - 2rR_\odot \cos b \cos l} \tag{3.11}$$

$$\phi = tan^{-1}\left(\frac{-Y}{-X}\right) \tag{3.12}$$

$$Z = r \sin b \tag{3.13}$$

Where R is the radial distance from the Galactic center, and Z is the disk height above or below the Galactic plane. The angle ϕ is the azimuth angle, and $\phi = 0°$ points from the Galactic center to the Sun, increasing counterclockwise.

3.2.1 Radial distribution and scale length

The RC star density falls exponentially as we move away from the Galactic center. To simplify equation 3.8, we are considering the distribution of stars only in the Galactic plane, i.e., for Z ≈ 0 pc. The equation 3.8 is then reduced to the following:

$$\rho(R, Z=0) = \rho_{\odot}\ exp\left(-\frac{R - R_{\odot}}{H}\right) \tag{3.14}$$

Here, we utilized 1° bins in b, centered at $b = 0°$ and 5° bins in longitude, ℓ for a range $40° \leq \ell \leq 340°$ to calculate the stellar density following the procedure outlined in Section 3.2. The RC stellar density obtained in cylindrical coordinates is analyzed as a function of Galactocentric radius in bins of ϕ with a bin size of 5°. For illustrative purposes, Figure 3.6 displays the variation of RC density with Galactocentric distance in four distinct ϕ-directions: $0° \leq \phi \leq 5°$ (top-left panel), $15° \leq \phi \leq 20°$ (top-right panel), $345° \leq \phi \leq 350°$ (bottom-left panel), and $355° \leq \phi \leq 360°$ (bottom-right panel). This depiction provides a visualization of the RC density distribution across different regions of the Galactocentric space. The figure shows the decrease in stellar density (black points) as a function of the Galactocentric radius by taking 500 pc bins of R. To determine the density of RC stars in solar neighborhood and scale length of the disk, we fitted equation 3.14 on the RC density (red line in Figure 3.6) in each $\phi-$bin.

For the fit, we employed '*curve_fit*'; function of *SciPy* package from Python, which uses non-linear least squares to fit the function to the data. The model, shown by red lines in Figure 3.6, gives the best-fitted parameters: the scale length (H) and RC density in the solar neighborhood of $\rho_{\odot}$. The scale length obtained in different $\phi-$bins is plotted in Figure 3.7. We consider the range in azimuth, $|\phi| < 50°$ since the coverage is incomplete beyond this range. We see that the scale length depends weakly on the Galactic azimuth, as shown in Figure 3.7. The average scale length determined at various azimuths was found to be 1.95 kpc (marked by a grey dashed line) with a dispersion of 0.26 kpc, shown as 1σ shaded region (1.95 ± 0.26 kpc) around the dashed line. The values agree with the previous works as indicated in Table 3.1.

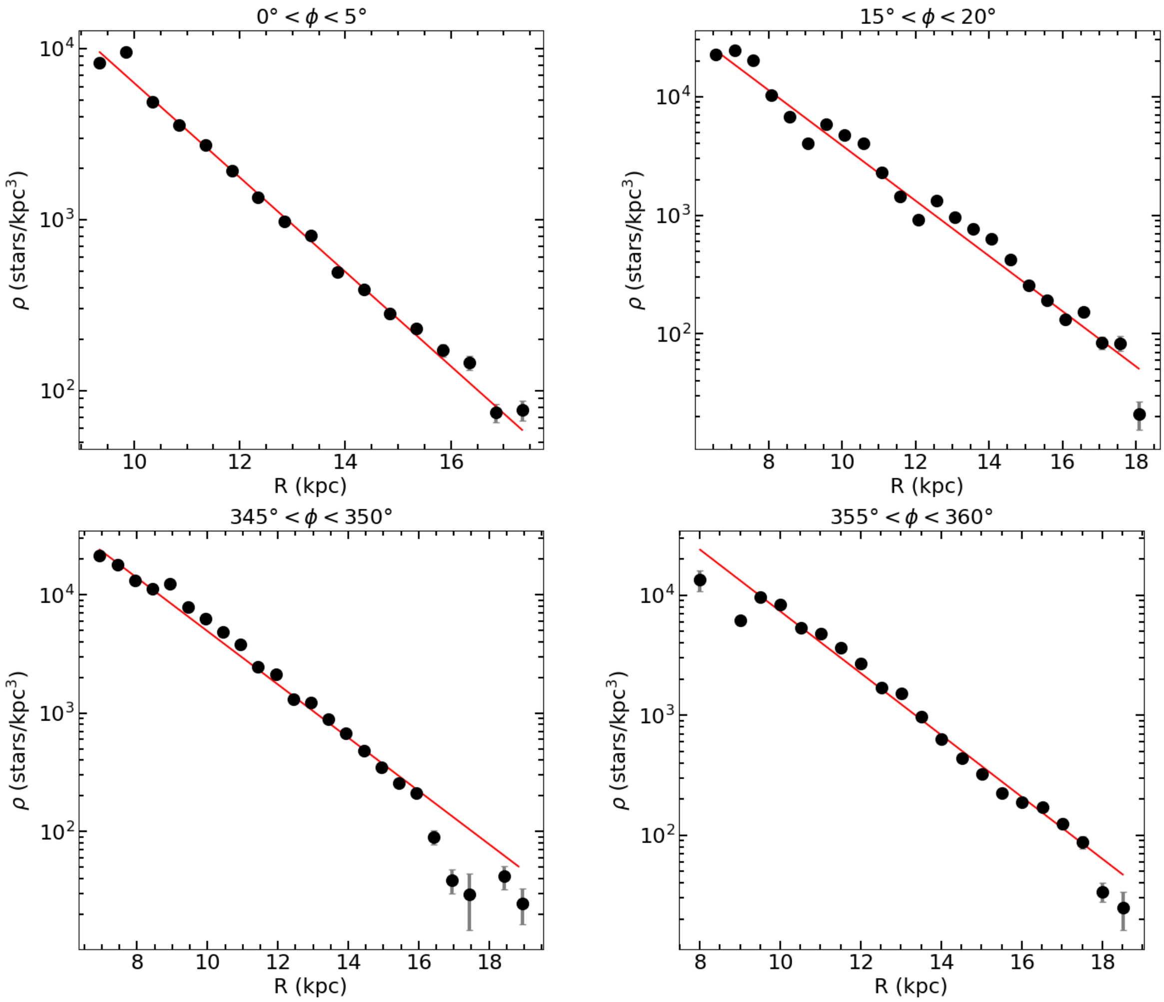

Figure 3.6: Variation of Space density of RC stars in four different $\phi-$bins, $\phi = [0°, 5°]$ (top-left); $[15°, 20°]$ (top-right); $[345°, 350°]$ (bottom-left); $[355°, 360°]$ (bottom-right), as a function of mean Galactocentric distance in logarithmic scale. The best-fitted solar neighborhood density towards this line of sight and scale length is added in the legend of the figure.

3.2.2 Vertical distribution and Flare analysis

The RC stellar density in the Galactic plane is assumed to decrease in the vertical directions (see the second part of equation 3.8). In order to determine the scale height of the old disk, we examined the RC stellar density in off-plane regions. We binned the data into several bins of the Galactocentric radius with a 500 pc bin size. We used the R-range of $7 \leq R \leq 16$ kpc and $-50° \leq \phi \leq +50°$ in our analysis to avoid the low number statistics towards the galactic center ($R < 7$ kpc) and contamination in the outer

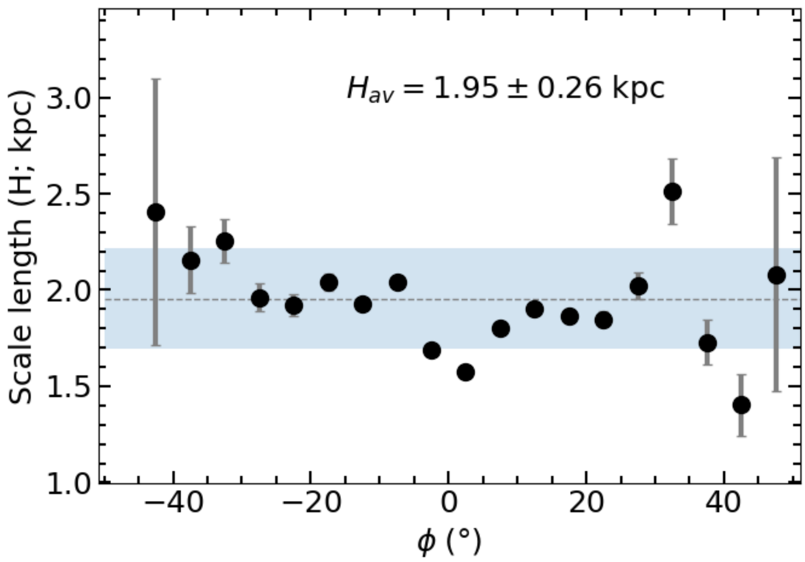

Figure 3.7: Variation of scale length (H) as a function of azimuth (ϕ). The dashed gray line represents the average scale length with 1σ dispersion highlighted as a shaded region.

galaxy (R > 16 kpc). Additionally, the data points closest to the Galactic plane were not included in the analysis to avoid high extinction areas affecting the statistics. In each R-bin, we examined the change in mean vertical density as a function of height above or below the Galactic plane in 0.05 kpc bins of Z. The variation of stellar density in the solar neighborhood ($8.0 \leq R < 8.5$ kpc) is presented by black points in the left panel of Figure 3.8. It is evident from the figure that the density decreases with height above or below the plane. Equation 3.8 models the density by assuming the first term, depending on R as constant in R to $R + dR$ bin of Galactocentric radius. We obtained a best-fit scale height of 0.38 ± 0.1 kpc in the solar neighborhood, as represented by the red line in the figure.

The same analysis is repeated for various R-bins, and the RC density above and below the Galactic plane in specific R-bins are highlighted in the right panel of Figure 3.8 for illustrative purposes. The RC density is presented for the bins centered at R = 7.75, 9.25, 11.75, and 13.75 kpc in blue, orange, green, and red colors, respectively. The best-fitted modeled curves are also added to the figure as dashed lines of the same color. The figure shows that the stellar density at a particular $|Z|$ decreases with a Galactocentric radius. Furthermore, the scale height obtained by fitting the data with

Table 3.1: Scale length of the Galactic disk obtained from different studies based on various tracers

tracers	Scale length (kpc)	reference
RC	1.95 ± 0.26	this study
supergiants	1.99 ± 0.13	Chrobáková et al. (2022)
whole Gaia EDR3 population	2.19 ± 0.18	Chrobáková et al. (2022)
Whole Gaia DR2 population	2.09 ± 0.08	Chrobáková et al. (2020)
OB	2.10 ± 0.1	Li et al. (2019)
RG	2.13 ± 0.23 (thin)	Wang et al. (2018)
RG	2.72 ± 0.57 (thick)	Wang et al. (2018)
F and G dwarf	$2.0^{+0.3}_{-0.4}$ (thin)	López-Corredoira et al. (2014)
F and G dwarf	$2.5^{+1.2}_{-0.3}$ (thick)	López-Corredoira et al. (2014)
RC	$2.10^{+0.22}_{-0.17}$	López-Corredoira et al. (2002)
dust	2.26 ± 0.16	Drimmel & Spergel (2001)

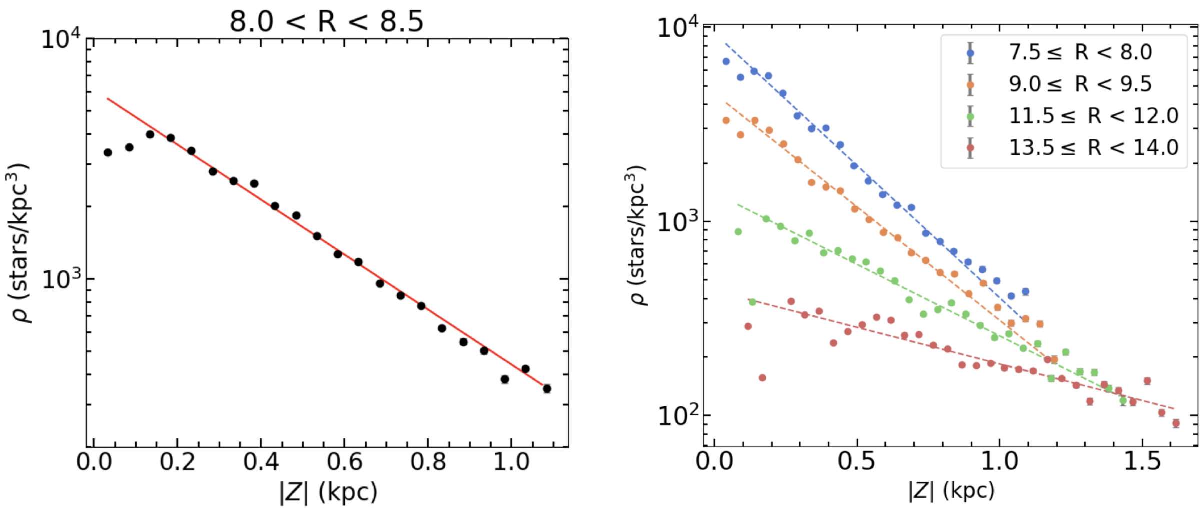

Figure 3.8: Variation of the density of RC stars as a function of absolute height above and below the Galactic plane ($|Z|$, in kpc). The left panel exhibits the density variation in the solar neighborhood, $R = [8.0, 8.5]$ kpc, while the right panel represents the variation in four R-bins; $R = [7.5, 8.0]$ kpc in blue, [9.0, 9.5] in orange, [11.5, 12.0] kpc in green, and [13.5, 14.0] in red. The smooth curves in respective panels show the best-fitted models.

the exponentially decreasing model in each R-bin is listed in Table 3.2.

Table 3.2: Scale height of disk in each 0.5 kpc bins of Galactocentric radius obtained by fitting the RC vertical distribution with the z-dependent part of equation 3.8.

Radius	Scale height (kpc)	errors (kpc)
$7.0 < R < 7.5$	0.317	0.005
$7.5 < R < 8.0$	0.318	0.008
$8.0 < R < 8.5$	0.380	0.009
$8.5 < R < 9.0$	0.387	0.012
$9.0 < R < 9.5$	0.372	0.011
$9.5 < R < 10.0$	0.371	0.011
$10.0 < R < 10.5$	0.398	0.009
$10.5 < R < 11.0$	0.444	0.011
$11.0 < R < 11.5$	0.495	0.013
$11.5 < R < 12.0$	0.589	0.020
$12.0 < R < 12.5$	0.689	0.026
$12.5 < R < 13.0$	0.825	0.049
$13.0 < R < 13.5$	0.921	0.044
$13.5 < R < 14.0$	1.151	0.085
$14.0 < R < 14.5$	1.530	0.174
$14.5 < R < 15.0$	1.720	0.181
$15.0 < R < 15.5$	1.911	0.249
$15.5 < R < 16.0$	2.197	0.434

Table 3.2 and left panel of Figure 3.9 show that the scale height increases from 0.380 ± 0.009 in the Solar neighbourhood (R = [8.0, 8.5]) to 2.2 kpc at $\sim$ 15.75 kpc. This increasing trend clearly indicates the flaring of the disk, which has also been observed in other tracers. The flaring of the disk has earlier been observed in RC by López-Corredoira et al. (2002), considering only a few lines of sight. In order to compare the flare parameters, we fitted an exponentially increasing scale height model (equation 1.2) on our RC sample as described in López-Corredoira et al. (2002). The parameter $h_z(R_\odot)$ in the equation is a scale length in the Solar neighborhood, and $H_{R,flare}$ is the

scale length of the flare. Fitting the equation 1.2 on the scale height with Galactocentric distance resulted in the solar neighborhood scale height of 0.35 ± 0.01 kpc and the flare scale length of 7.18 ± 0.93 kpc, shown by dashed grey line in Figure 3.9. The obtained

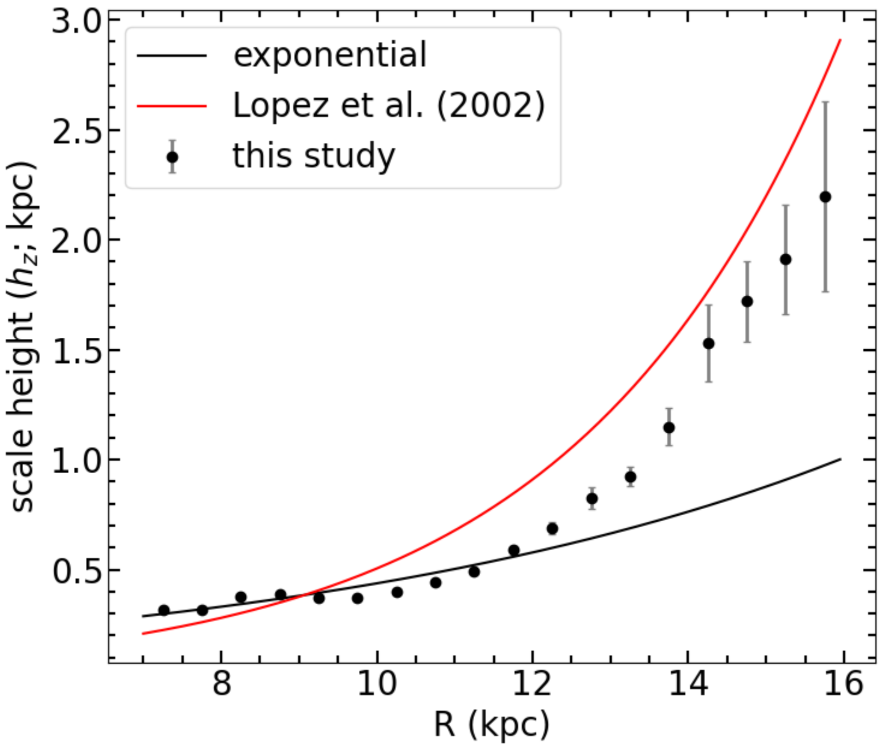

Figure 3.9: Variation of scale height (h_z) as a function of Galactocentric distance (R) exhibiting flaring disc traced by RC stars in black points. The black line represents the best-fitted exponential model while the red line denotes the exponential flare from López-Corredoira et al. (2002).

parameters from our study differs from that of López-Corredoira et al. (2002), where $h_z(R_\odot) = 0.31^{+0.06}_{-0.04}$ kpc and flare scale length $H_{R,Flare} = 3.4 \pm 0.4$ and is shown in the right panel of Figure 3.9. However, it should be noted that the results show similarity within the error bars when considering the same volume for analysis.

3.2.2.1 Geometry of flare

The scale height estimated from various tracers shows that the Milky Way disk shows a flare in the outer regions of the Galaxy (e.g., Drimmel et al., 2000; Yusifov, 2004; López-Corredoira & Molgó, 2014; Li et al., 2019; Yu et al., 2021a; Chrobáková et al., 2022). However, the geometric functional form of the flare is not well known. Some studies use exponential model (López-Corredoira et al., 2002; Li et al., 2019), whereas single order or second order polynomial has also been used in recent times to explain the flare (Yusifov, 2004; Chrobáková et al., 2022, etc.). We compared exponential (equation 1.2) and polynomial models of second (equation 3.15) and third order (equation 3.16) to constrain the geometry of the flare. The fits corresponding to the aforementioned functional forms are plotted in Figure 3.10 as blue, orange, and green curves, respectively. The weighted residual corresponding to each model is also presented in the bottom panel of the figure. The residues indicate that the third-order polynomial models provide better results compared to the exponential and second-order polynomial models.

$$\begin{aligned} h_z(R) &= (0.326 \pm 0.010)\,[1 + (0.043 \pm 0.027)\,(R - R_\odot) \\ &\quad + (0.058 \pm 0.012)\,(R - R_\odot)^2] \end{aligned} \tag{3.15}$$

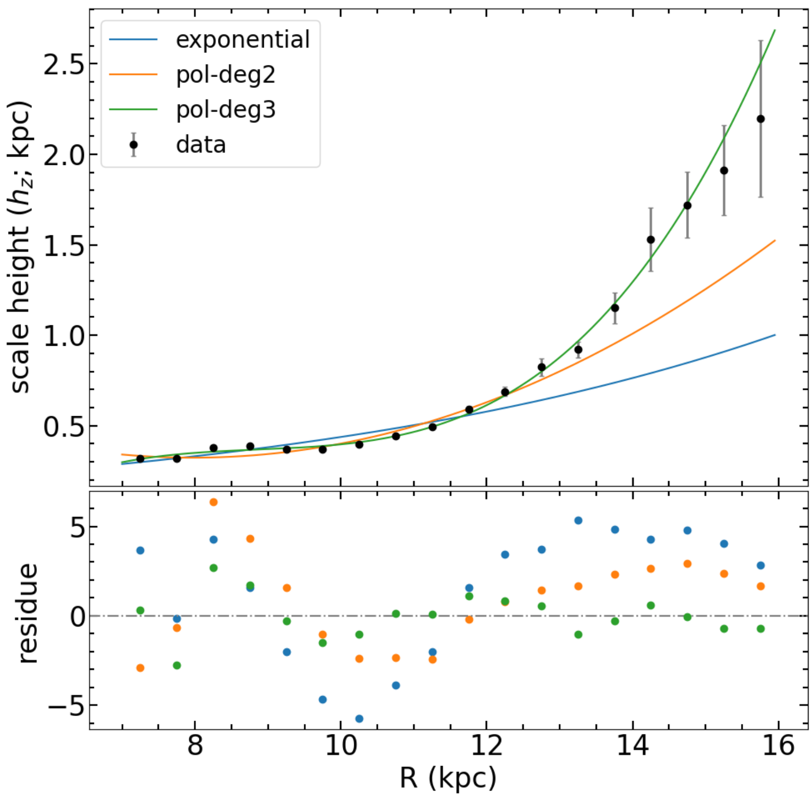

Figure 3.10: Comparison of exponential (in blue), second order polynomial (in orange), and third order polynomial (in green) models of flare fitted on RC scale height data. The weighted residuals corresponding to each model are also plotted in the bottom panel.

$$
\begin{aligned}
h_z(R) &= (0.358 \pm 0.007)\,[1 + (0.060 \pm 0.012)\,(R - R_\odot) \\
&\quad + (-0.021 \pm 0.011)\,(R - R_\odot)^2 + \\
&\quad (0.017 \pm 0.002)\,(R - R_\odot)^3]
\end{aligned} \tag{3.16}
$$

We concluded that, at least for the RC stars, the scale height of the old stellar disk is increasing as the cubic polynomial of Galactocentric distance (equation 3.16).

3.2.2.2 Northern and southern flare

We explored the asymmetry in the flare with respect to above and below the Galactic plane. In Figure 3.11, we plot the scale height as a function of Galactocentric distance for stars above the Galactic plane (in blue), below the Galactic plane (in green), and combined scale height (orange). We notice that there is no significant difference in the scale height of three different sets close to the solar neighborhood. However, the flaring disk may seem to be asymmetric towards larger distances (R > 11 kpc).

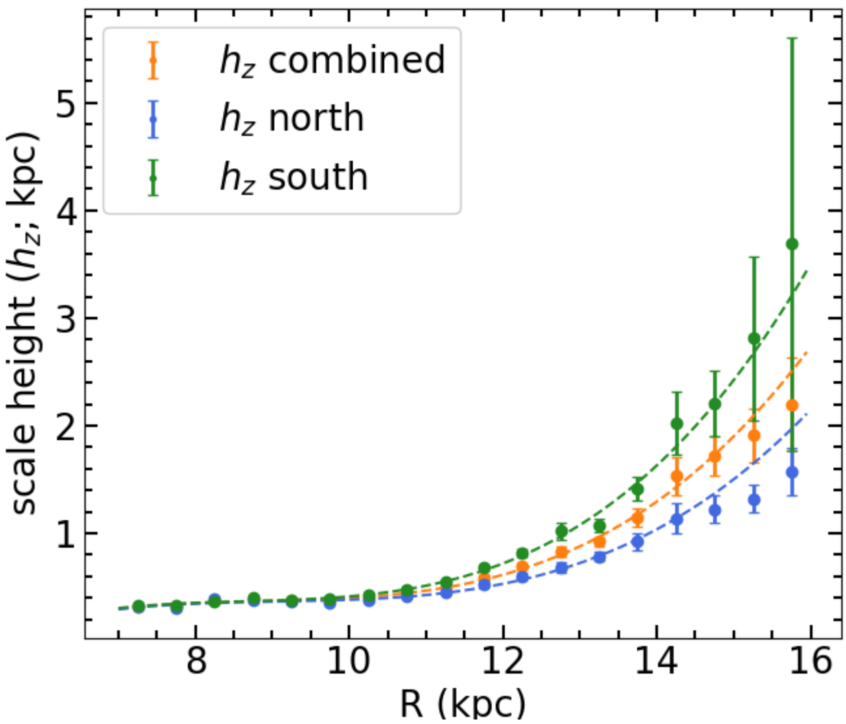

Figure 3.11: Variation of scale height with distance from Galactic center to compare northern (blue), southern (green), and combined (orange) flare.

The best-fitted parameters obtained on fitting third-order polynomial geometry of the flare to either side of the disk are tabulated in Table 3.3. Analyzing the fitted parameters for the Northern and Southern flares reveals that the scale height of the Galactic disc below the Galactic plane is ~ 0.92 kpc higher than that of the Northern flare at Galactocentric distance, $R = 15$ kpc. A recent study by Chrobáková et al. (2022) identified a similar asymmetry in the flare for supergiant stars, where the value of h_z for the Southern flare is approximately one kpc higher than that of the Northern flare in the outer regions of the Galaxy ($R \geq 15$ kpc). However, no North-South asymmetry was observed in the flare for a sample of LAMOST OB stars as reported by Yu et al. (2021a).

Table 3.3: Model ($h_z(R) = h_z(R_\odot)\,[1 + k_1(R - R_\odot) + k_2\,(R - R_\odot)^2 + k_3\,(R - R_\odot)^3]$) parameters for the northern, southern and combined flare.

Region	$h_z(R_\odot)$ (kpc)	k_1	k_2	k_3
Combined	0.358 ± 0.007	0.060 ± 0.012	-0.021 ± 0.011	0.017 ± 0.002
North	0.353 ± 0.009	0.060 ± 0.016	-0.028 ± 0.014	0.014 ± 0.003
South	0.360 ± 0.007	0.057 ± 0.012	-0.012 ± 0.011	0.021 ± 0.002

3.2.3 Warp modeling

The variation of the distribution of RC stars as a function of the longitude indicates that the disk of our galaxy is not flat, but it warps upward in one direction and downwards in the other (Figure 3.8). In this section, we analyze this structure in greater detail and model the warp observed from RC stars. To ensure the data reliability, we removed the data in the azimuth range of $90° \leq \phi \leq 270°$ from our analysis because of the incompleteness in the RC sample towards the inner regions of the Galaxy. The RC stars with Galactocentric distance $R < 7$ kpc were also excluded due to low number statistics. We calculated elevation above the Galactic plane (Z_w) as the highest frequency or mode value of Z in 200 pc bins of X and Y. Following the approach of Chrobáková et al. (2022), we fitted the estimated Z_w values with the warp model defined in equation 3.17.

$$Z_w = [C_w \ (R - R_w)^{\epsilon_w} \sin(\phi - \phi_w)] \ pc \tag{3.17}$$

Where C_w, R_w ϵ_w, and ϕ_w are the free parameters characterizing the warp. The warp parameters obtained by fitting equation 3.17 on the elevation of the Galactic plane are given by

$$C_w = (1.40 \pm 0.62) \times 10^{-10} \tag{3.18}$$

$$\epsilon_w = 3.13 \pm 0.05 \tag{3.19}$$

$$\phi_w = -1^\circ.93 \pm 0^\circ.18 \tag{3.20}$$

$$R_w = 7.4 \pm 0.4 (kpc) \tag{3.21}$$

The maximum and minimum warp amplitude obtained from best-fit model are shown as black curves in Figure 3.12 and compared with the warp obtained in López-Corredoira et al. (2002) ($C_w = 2.1 \times 10^{-19}$, $\epsilon_w = 5.25 \pm 0.5$, and $\phi_w = -5^\circ \pm 5^\circ$, in red line).

Furthermore, we conducted an analysis to investigate the north-south asymmetry in the structure of the warp. This was accomplished by separately fitting the warp model (equation 3.17) to the northern ($\phi > -2.03$) and southern side ($\phi < -2.03$) of the warp, which was defined based on the nodal line. The maximum amplitude of the northern warp at R = 14 kpc is found to be 1.30 kpc while the minimum amplitude on the southern side is -1.52 kpc, indicating a small asymmetry, as shown in Figure 3.13. The asymmetry in the warp is also noted in various studies, a comparison of which is presented in table 3.4. Notably, most studies suggest that the amplitude of the northern warp is greater than the southern. However, our study indicates an opposite trend, which was also observed in the warp traced by RGB stars in Romero-Gómez et al. (2019) and Cepheids in Lemasle et al. (2022). Chrobáková et al. (2022) investigated the whole Gaia EDR3 population, corresponding to an average age of $\sim 6-7$ Gyr and supergiant stars representing the younger population. The warp amplitude of both the population

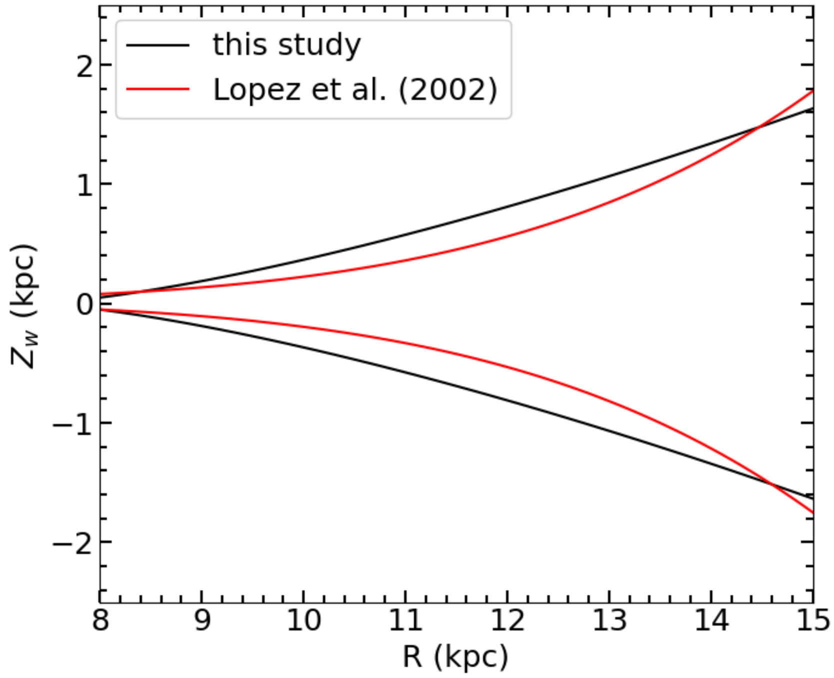

Figure 3.12: Comparison of minimum and maximum modeled warp amplitude for RC stars from our study, presented in black lines, with that of López-Corredoira et al. (2002), shown in red lines.

shows asymmetry, with higher amplitude on the southern side (Gaia EDR3: -0.375; Supergiants: -0.717) as compared to the northern (Gaia EDR3: 0.360; supergiants: 0.658) at R = [19.5, 20.0] kpc.

3.3 Comparison with earlier studies

In this work, we have modeled the Milky Way disk using the large sample of RC stars covering a wide area of the Galactic plane. Our investigation of the distribution of RC stars within the disk has revealed that the thickness of the disk is not constant, but it is increasing with the Galactocentric distances, exhibiting a discernible flaring pattern. In addition, we found that the Disk traced by RC stars is not flat but curved in outer directions, indicating a distinct warp feature. We modeled the outer Galactic disk from RC stars and constrained the geometry of flare and warp. Warp and flare in the Milky Way disk from RC stars have also been discussed in López-Corredoira et al.

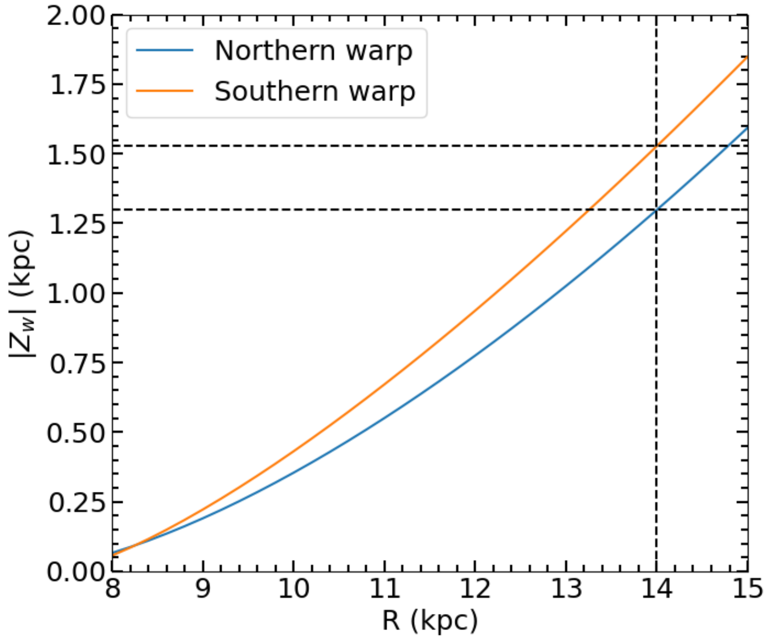

Figure 3.13: A comparison of minimum and maximum warp amplitude for RC stars as a function of radial distance, illustrating the northern and southern warp in blue and orange colors, respectively.

.

Table 3.4: Values of the warp up (Z_{up}) and down (Z_{down}) amplitude with respect to the Galactic plane at Galactocentric radius R = 14 kpc expressed in kpc for different tracers.

Tracer	Z_{up} (kpc)	Z_{down} (kpc)	references
RC	1.30	-1.52	this study
Cepheid	0.53	-0.79	Lemasle et al. (2022)
Cepheids	0.65	-0.54	Skowron et al. (2019b)
RGB	0.97	-1.22	Romero-Gómez et al. (2019)
OB	0.23	-0.19	Romero-Gómez et al. (2019)
2MASS NIR	0.50	-	Reylé et al. (2009)
HI	0.74	-0.75	Levine et al. (2006a)
dust	0.74	-0.68	Marshall et al. (2006)
Pulsar	0.62	-0.58	Yusifov (2004)
RC/ 2MASS NIR	1.23	-	López-Corredoira et al. (2002)
COBE/DIRBE, NIR & FIR	1.34	-	Drimmel & Spergel (2001)

(2002) (LC02). However, the analyses presented in the previous sections yielded more constrained results than that of LC02. The difference in the obtained parameters can be attributed to two main factors. Firstly, the estimated structure in LC02 is a result of the distribution of RC stars in a few selected lines of sight (12 fields, see Table 1 from LC02) , whereas we have used RC stars covering nearly the entire galactic disk in the range $40^\circ \leq \ell \leq 340^\circ$ and $-10^\circ \leq b \leq 10^\circ$. Secondly, the density model fitting in LC02 suffered from low number statistics, the effect of which is reflected in the large uncertainties in their fitted parameters. These factors may hinder the interpretation of the flare and warp of the disk.

In addition to LC02, we compare our results with the earlier studies based on different age tracers with the aim of investigating the age dependency on the flare and warp of the disk. In the following subsections, we present the comparison of the flare and warp model from RC stars based on our study with that of various tracers from literature and their implication on the formation theories.

3.3.1 Comparison of Flare

Figure 3.14 displays a comparison of the disk flare revealed from the RC stars in our study (shown in black) with that of previous research, represented by different colored curves. The flare model considered in the figure represents the most recent literature on different tracers, including dust (red, Drimmel et al., 2000, D01), pulsar (purple, Yusifov, 2004, Y04), F and G- type dwarf (grey, López-Corredoira & Molgó, 2014, LM14), OB stars (blue, Li et al., 2019, Li19), RC stars (light green, Yu et al., 2021a, Yu21), and whole Gaia EDR3 population (golden, Chrobáková et al., 2022, ZC22). The solid and dashed line of the same color represents the variation of scale height of the thick disk (solid) and thin disk (dashed-dotted) of the corresponding tracer with Galactocentric distance. The figure demonstrates that the scale height of the disk increases with Galactocentric radius for all tracers, implying that flaring is a global property of the disk.

The phenomenon of flaring in disks is believed to be associated with the process of disk heating, and numerous theories have been proposed to elucidate this phenomenon (e.g., Cheng et al., 2019; Yu et al., 2021a). Some internal disturbances such as spiral arms (Sellwood, 2013), Giant molecular clouds (Lacey, 1984) or stellar migration (Bovy et al., 2016) have been suggested as potential contributors to the disk flaring events. In addition, external perturbations like the mergers with dwarf or satellite galaxies (Kazantzidis et al., 2008; House et al., 2011) can also play a significant role in heating the disk and causing flaring in the outer regions of the galaxies. The formation mechanisms of a flare can be broadly classified into two types: secular evolution (Narayan & Jog, 2002; Minchev et al., 2012, 2015) and the cumulative effect of interaction with passing dwarf galaxies (Kazantzidis et al., 2008; Villalobos & Helmi, 2008; Laporte et al., 2018). Observationaly, both scenarios expect that the scale height of the disk should increase smoothly with the radius. In the case of secular evolution, the older population is expected to exhibit a stronger flare compared to the younger population. However, no age dependency in flare strength is expected for flares formed by perturbations, as all the stellar populations would be equally disturbed.

Figure 3.14 presents compelling evidence for the influence of age on scale height as a function of radial distance. Specifically, our findings demonstrate that the older age populations, such as the RC (indicated by the black lines in this study and sea-green line from Yu et al. (2021a)) and all Gaia EDR3 stars (6-7 Gyr average age, in golden color), exhibits the most pronounced flare. While the flare represented by F and G type dwarf (dashed and dotted grey lines) from LM14 exhibits a less steep curve. Moreover, the scale height of the younger OB stars (in light blue) and the dust (in light red color) is further lower than that of the remaining population. Comparing all the curves, we observe a positive correlation between age and flare strength. An age dependency has also been observed in the flare properties of many external galaxies (Streich et al., 2016). This aspect favors the secular evolution of the disc. However, a case against the secular evolution was presented in Yu et al. (2021a) by comparing the flare of OB stars from the LAMOST survey with the RGB population from Wang et al. (2018). Their results indicate a larger flare in younger populations (OB stars) compared to older (RGB), favoring the perturbations caused by the internal components or the external mergers as the major contributor to the disk heating or formation of the flare. Similar results were also suggested in earlier studies; for example, Wang et al. (2018); Xu et al. (2020). Nevertheless, many competing studies (Bovy et al., 2012; Li et al., 2019) still favor the

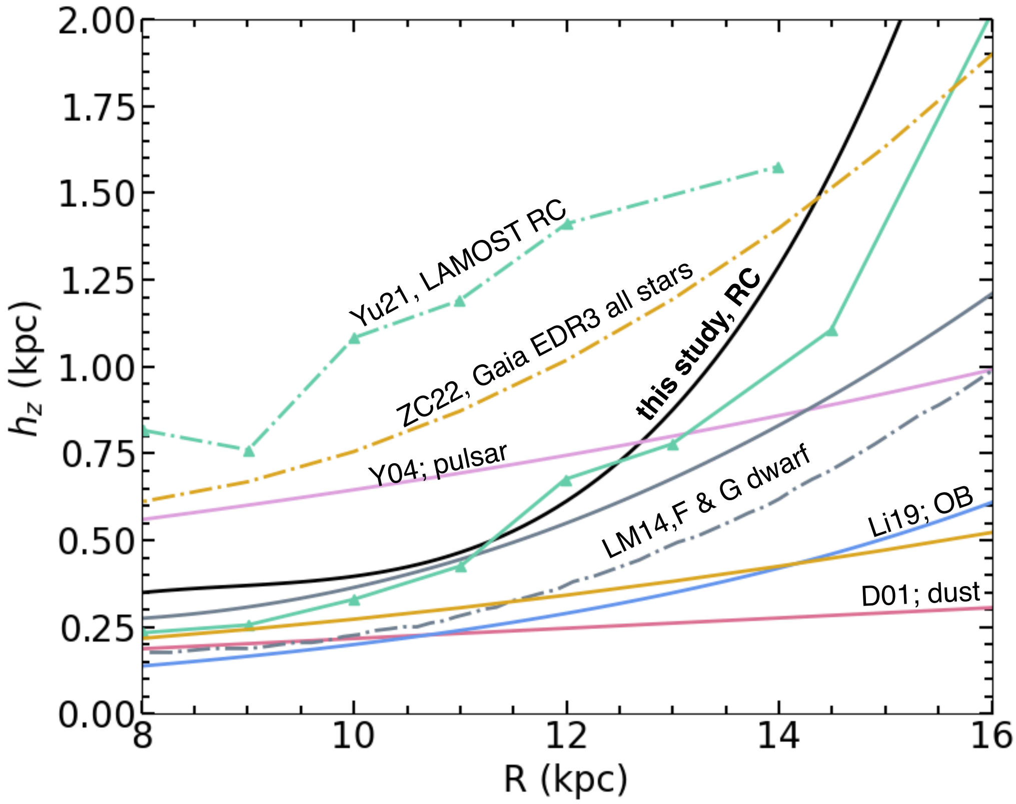

Figure 3.14: Variation of scale height with Galactocentric distance depicting the comparison of disk flare of our study (black line) with the other tracers shown by different colors. The dashed and solid lines of the same color represent the thick and thin disk of the corresponding tracer.

secular evolution of the flare in the Disk. It has been shown in cosmological simulations that a strong flare can be produced with galaxy merger events and may have an age dependency on scale height (Martig et al., 2014). In our study, we are not ruling out the possibility of disk perturbation events, but the age dependency in the scale height and no conclusive evidence of north-south asymmetry (see section 3.2.2.2) gives strong evidence for the secular evolution of the disk.

3.3.2 Comparison of Warp structure

In recent years, many models have been proposed to understand the formation of the disk warp (more details in section 1.3.2). The gravitational origin suggests that all the age population should exhibit similar warp amplitude. Hence, no age dependency is expected in the case of gravitational origin. However, for the non-gravitational origin, like in-falling gas on the outer parts of the Galaxy, the younger population will get more affected than older ones. The reason is that the young population following the gas distribution will always have a larger warp amplitude, whereas the old population had more time to reduce the amplitude of the warp due to the self-gravity in the models in which the torque affects mainly the gas and not the stars.

In Figure 3.15, the warp model obtained from RC star distribution in our study (black curve) is presented together with some former works. The figure includes the warp model based on dust (light-red, Drimmel & Spergel, 2001, D01), pulsar (purple, Yusifov, 2004, Y04), HI (light-green, Levine et al., 2006a, L06), OB stars (light-blue, Li et al., 2019, Li19), Cepheid (violet, Lemasle et al., 2022, BL22), and supergiants (cyan, Chrobáková et al., 2022, ZC22). The warp obtained from younger stars with $M_G < -2$ mag from Gaia DR2 data, as observed by Chrobáková et al. (2020) (ZC20), and all Gaia EDR3 sources in Chrobáková et al. (2022) (ZC22) are also added in the figure in pink and golden curves, respectively. It is important to note that the sample of bright stars from Gaia DR2 and all EDR3 stars comprises a heterogeneous mixture of various age populations rather than representing a specific age group. Consequently, comparing the warp traced by these populations with other age tracers is not straightforward. Therefore, we refrain from directly comparing the warp traced by these populations with the remaining age tracers in the subsequent discussion.

The different shapes of curves in Figure 3.15 represent differences in the model used in the respective studies. Nevertheless, the existence of warp in the disk traced by different populations suggests that the Milky Way disk warp is a long-lived feature. Moreover, it is evident from the figure that the amplitude of the warp varies with the age of the tracer. The difference in the warp amplitude across different age groups implies that the warp is not a static feature solely influenced by gravitational forces but rather a dynamic phenomenon that evolves over time. Therefore, it must have originated from some non-gravitational effects. The asymmetry in the amplitude of the northern and southern warp, as discussed in section 3.2.3, also favors the non-gravitational origin of the warp formation.

A closer inspection of Figure 3.15 reveals that the amplitude of warp is significantly

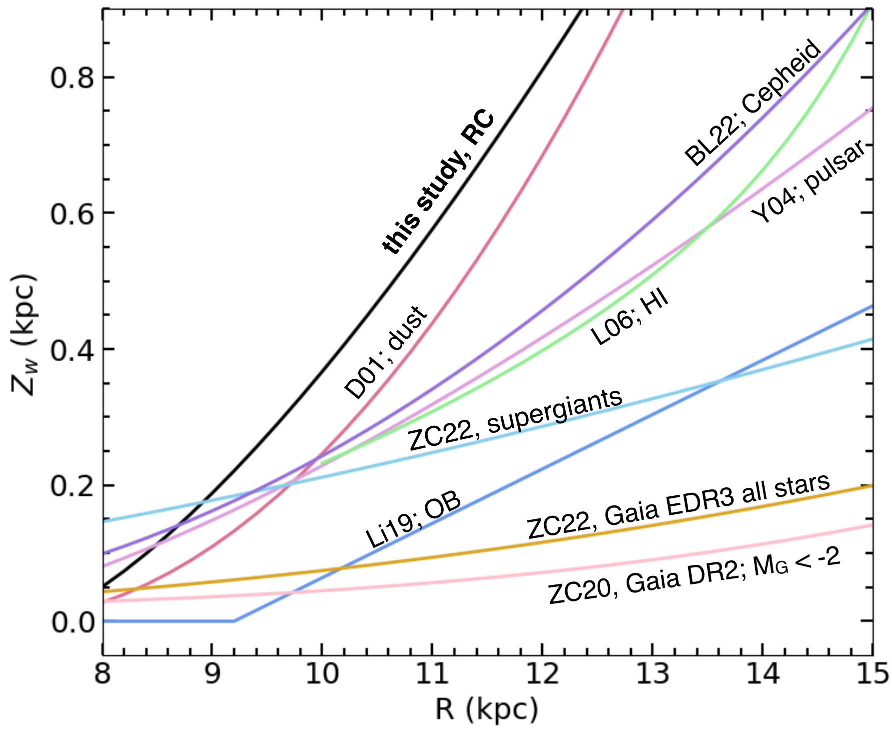

Figure 3.15: Variation of maximum warp height above the Galactic plane with Galactocentric radius for various age tracers outlined by different colors. The result from our study is shown in the black line.

higher for dust (in green line) and older population (RC in black line) as compared to the younger populations such as Cepheids, pulsar, Supergiant, and OB stars. The younger sample of Gaia DR2 (pink curve) also shows lesser warp amplitude than the whole Gaia EDR3 sample (golden curve), which is dominated by older populations. This suggests that the warp is more prominent in older tracers relative to the younger ones. This trend aligns with previous studies such as Amôres et al. (2017) and Romero-Gómez et al. (2019). In contrast, some studies (e.g., Chen et al., 2019b; Wang et al., 2020; Chrobáková et al., 2020; Li et al., 2023) have reported a decrease in the amplitude of warp with age and support the models in which gas is necessary for warp formation. The varying interpretations of the warp amplitude with age may be attributed to differences in geometric models and the region of the Galaxy covered in different studies. Identifying the possible mechanism for the formation of the warp is challenging. However, the observed increase in warp amplitude with age could be related to warp dynamics, such as the precession of the disk (Poggio et al., 2020).

3.4 Summary

This chapter explores the use of RC stars as structure tracers, both in the inner as well as outer Galactic disk. While RC stars have been extensively used to study the Bulge, their application for mapping the Galactic disk has been limited. This chapter highlights the novel findings obtained from the distribution of RC stars that contribute to our understanding of the morphology of the Milky Way disk.

The face-on distribution of RC stars exhibits a decreasing density as one moves outwards in the disk, without any apparent signature of the spiral arms in the density analysis. However, an overdensity map reveals curvy features that match the spiral arms of the Galaxy. The Outer arm, being a distant feature, was not very well observed in earlier studies using different structural tracers. However, our study, for the first time, shows an over-density of RC stars, which matches with the position of the Outer arm. We also identify a 6 kpc long extension of the Outer arm in the distant regions of the third Galactic quadrant beyond the previously known extents. The chapter highlights the fact that new and exciting results can be obtained even from 20-year-old data when used in a comprehensive and systematic manner. Our analysis not only detects the Outer arm but also reveals asymmetry in the Galactic disk above and below the Galactic plane, providing the first observational evidence of the warping of the Outer spiral arm.

Leveraging a large data set, we model the Galactic disk to generate a 3D view of the Galaxy. Various parameters of the disk are determined using a simple exponentially decreasing model in the Galactic disk. Our results indicate the existence of a symmetric flare and an asymmetric warp in the disk of the Galaxy traced by RC stars. Comparisons between the modeled flare and warp derived from RC stars and features observed in various age populations in the literature help constrain their formation mechanisms. We observe that the strength of the flare and the amplitude of the warp increase with the age of the tracer, suggesting that these features are more prominent in older tracers. This age dependency suggests that the secular evolution of the disk may play a crucial role in the formation of the flare. Furthermore, the age-dependent behavior of the warp could be attributed to the intricate dynamics governing the warped disk.

Overall, this chapter provides valuable insights into the various structures of the Galactic disk, emphasizing the role of RC stars as important tracers in understanding their formation and evolution.

This page was intentionally left blank.

Chapter 4

Polarization observations and data reduction

"The study of astronomy has taught me to look at the world in a different way and has given me a deeper appreciation for the beauty and wonder of the universe."

- Caroline Herschel, *1750-1848*

In Chapter 3, we investigated the outer structures of the Galactic disk using red clump stars. While significant insights were gained from this analysis, limitations in our selection area hindered our ability to trace the spiral features of the inner arms. Previous studies on stellar distribution have consistently revealed that the stars are distributed in the Galactic plane with higher densities observed in spiral arms. In contrast, the interstellar dust tends to be more confined to the Galactic disk, making it an ideal tracer for mapping the Disk structure. One advantage of studying interstellar dust is that it emits thermal radiation primarily in longer wavelengths, where the effect of extinction is minimized. As discussed in section 1.4, the 3D dust distribution studies in longer wavelength use the kinematic methods from the radial velocity measurements to find the distance. The typical radial velocity of an object varies with distance in any given direction due to its orbital path around the galactic center. Kinematic distances are derived by measuring the local standard of rest (LSR) velocity and assuming a Galactic rotation model (Anderson et al., 2012, and references therein). For the object orbiting in circular orbits outside the solar circle, a unique kinematic distance can be derived. However, within the solar circle, objects at near and far distances share the same radial velocity in a given line of sight, resulting in distance ambiguity inside the solar circle. Thus, errors in kinematic distances are caused by both inaccurate Galactic rotation models and kinematic distance ambiguity resolution methods. Although efforts are continuously being made to improve the kinematic distance estimation methods, they can still introduce significant uncertainties in the precise locations of the sources. Consequently, the ongoing debate regarding the basic facts, such as the existence of some spiral arms, the number of arms, and their extent, persists. Thus, constructing a three-dimensional map of the Galaxy solely based on dust distribution is a challenging task. Nevertheless, the properties of interstellar dust, such as extinction and polarization, can be utilized as indirect probes of dust distribution. The advent of large-scale, multi-wavelength, all-sky surveys has provided valuable data for constructing three-dimensional extinction maps of the Galaxy. Numerous efforts have been made to trace the distribution of interstellar dust using extinction maps (e.g., Lallement et al., 2018; Rezaei Kh. et al., 2018; Green et al., 2019). However, it is noteworthy that most of these extinction maps do not exhibit a clear spiral structure, despite the fact that the spiral arms are rich in dust. This lack of the spiral feature in their maps can be partially attributed to the inherent biases and model-dependent nature of the extinction measurement techniques employed.

Alternatively, the polarization of starlight from the intervening dust grains can also be utilized to study the distribution of dust. This is based on the observation that the degree of polarization and polarization angle exhibit abrupt changes when starlight encounters a dust layer. By analyzing the polarization information as a function of distance, valuable insights could be gained regarding the number of dust layers and their distances along the line of sight (e.g., Medhi et al., 2008; Eswaraiah et al., 2012; Singh et al., 2020; Pelgrims et al., 2023). This approach offers a unique perspective on studying the distribution of dust in the interstellar medium and provides complementary information to other methods, such as extinction mapping. Despite the usefulness of polarization observations for mapping dust distribution, not many dedicated studies have targeted this approach. Systematic polarization observations across the Galactic plane could be helpful to map the distribution of dust in the disk and trace the underlying structure like spiral arms.

One of the primary objectives of the thesis is to examine the potential of ISM polarization in revealing information regarding the Galactic disk structures. We aim to demonstrate this by conducting linear polarization observations and subsequent analysis in three different lines of sight. This chapter outlines the target selection procedure for the observations and data processing techniques to convert the raw data into a science-ready form. The detailed analysis of the polarization measurements and their interpretation in regard to the Galactic structure of each chosen line of sight is presented in the subsequent chapters.

4.1 Basics of polarization & its formalism

Polarization is a fundamental property of light describing the evolution of electric and magnetic field oscillations as the light propagates. It gives the directional nature of the wave. For example, the electric field vector oscillates in a random direction perpendicular to the direction of propagation for unpolarized light, whereas for polarized light, it vibrates in some specific direction. Light from astronomical sources is polarized to some extent. Astronomical polarimetry provides additional information on the physical state of the medium as compared to spectroscopy and photometry alone. Several formalisms exist to describe the state of polarization of the light, the application of which depends on the polarimetric principle. Jones formalism describes the state of polarization of the light in terms of the electric field vectors and contains phase information. This concept is applied to the submillimeter or radio regime, where the detectors are antennae and directly measure the electric field. However, in the optical and near-infrared range, where intensity measurements are taken instead of electric field measurements, the Jones formalism is not applicable. Instead, the Stokes-Mueller formalism is employed to study polarization in astronomical sources. In this method, the state of polarization is described by Stokes vector, S, which is defined in terms of 4 components: I, Q, U, and V, given by the following equation.

$$S = \begin{bmatrix} I \\ Q \\ U \\ V \end{bmatrix} = \begin{bmatrix} I_{0^\circ} + I_{90^\circ} \\ I_{0^\circ} - I_{90^\circ} \\ I_{45^\circ} - I_{-45^\circ} \\ I_{LHC} - I_{RHC} \end{bmatrix} \tag{4.1}$$

Here, I denote the total intensity regardless of the polarization. Q and U represent the state of linear polarization, while V describes the state related to left-handed circular (LHC) and right-handed circular polarization (RHC). Any state of polarization can be described by the linear combination of these four parameters.

Furthermore, the state of polarization of the incoming light can be altered after interaction with the scattering matter or the active optical elements present in the instrument. The transformation of the polarization state of light can be mathematically described using various ways such as the Poincare sphere, Jones Formalism, Müller matrices based on Stokes parameters. Among these methods, the Müller matrix (after Hans Müller, who devised this method in 1943) is the best method to determine the polarization state in the case of optical and IR to deal with partial polarization. According to the third formalism, the incoming beam is related to the outgoing beam Stokes parameters by a 4×4 transformation matrix.

$$\begin{bmatrix} I' \\ Q' \\ U' \\ V' \end{bmatrix} = \begin{bmatrix} m_{11} & m_{12} & m_{13} & m_{14} \\ m_{21} & m_{22} & m_{23} & m_{24} \\ m_{31} & m_{32} & m_{33} & m_{34} \\ m_{41} & m_{42} & m_{43} & m_{44} \end{bmatrix} \times \begin{bmatrix} I \\ Q \\ U \\ V \end{bmatrix} \tag{4.2}$$

Here, (I, Q, U, V) and (I', Q', U', V') are the incident and final stokes parameters respectively. The 4×4 matrix is a transformation matrix (Müller matrix) having (m_{ij}) elements. Some properties of Müller Matrix are

- Müller Matrices for n-optical elements are multiplicative but not commutative.

- If any optical element is placed at some angle (say α) with respect to incident light, then the Müller matrix can be expressed as

$$M' = R(-\alpha)\, M\, R(\alpha) \tag{4.3}$$

where R is rotational matrix and is given by

$$R(\alpha) = \begin{pmatrix} 1 & & 0 & 0 \\ 0 & \cos 2\alpha & \sin 2\alpha & 0 \\ 0 & -\sin 2\alpha & \cos 2\alpha & 0 \\ 0 & 0 & 0 & 1 \end{pmatrix} \tag{4.4}$$

When conducting astronomical polarimetry, it is important to consider the presence of different scattering agents and the optical components within the instruments, which can alter the state of polarization of the observed source. Therefore, a careful analysis of the transformation of the Stokes parameters is needed to ensure the accurate interpretation of the data.

4.2 Interstellar polarization

Historically, till the early 20^{th} century, the dark regions in the Milky Way (dark lanes in Figure 1.1) were thought of as holes in the cosmos or the region devoid of any stars. Later, it was realized that the space between stars is not empty but filled with the interstellar medium. Around 1% of the mass of ISM is locked in sub-micron-sized solid particles called interstellar dust (Whittet, 2003). The dust grains absorb, scatter, and re-radiate the starlight and hence have a significant impact on our view of the universe. It is the dust extinction (absorption and scattering) that is responsible for the dark lanes seen in the edge-on galaxies, including the Milky Way. In addition to the absorption and scattering, the star-light interacting with the aligned dust grains can also exhibit polarization. Interstellar polarization was first discovered in optical wavelength about 70 years ago (Hall, 1949; Hiltner, 1949). Hall and Hiltner, in their study, aimed to investigate the intrinsic polarization in distant OB stars and discovered a distinct pattern of position angle coherence across the sky in multiple directions. This pattern could not be attributed solely to the intrinsic polarization of individual stars, as their rotation axes were expected to be distributed randomly over the sky. Consequently, it was inferred that other global mechanisms must be responsible for the strong correlation in position angle between stars. Subsequently, through further observations, it became evident that stars affected by extinction (a property of the interstellar dust) exhibited higher levels of polarization, indicating a positive correlation between extinction and polarization. This led to the realization of the interstellar origin of polarization. Thereafter, many theories were put forward to explain the origin of interstellar polarization. Among these, the most commonly accepted model is the one given by Davis & Greenstein (1949), and it is based on the concept of linear dichroism resulting from asymmetric or anisotropic grains, which are partially aligned with the local or global magnetic field. In simpler terms, when the light coming from an unpolarized star interacts with the interstellar dust containing asymmetric (say elongated) grains, a part of the light is absorbed by these grains. Since the longer axis of the grain has a larger crossectional area, it absorbs more light along the longer axis. As a result, the transmitted light becomes partially polarized towards the shorter axis of the grain when observed in optical and NIR. The light that was absorbed by the dust grains heats the grain and re-radiates in the longer wavelengths. The emitted light also becomes partially plane polarized but in a direction perpendicular to what is observed in optical and NIR wavelengths. This mechanism of interstellar polarization is illustrated in Figure 4.1.

The angle of polarization (E) depends on the orientation of the magnetic field (B). The relationship between the polarization and the magnetic field is determined by comparing the polarization angle observed in optical or NIR with those of synchrotron radiation. Synchrotron polarization is a well-understood phenomenon, with the polarization angle perpendicular to the magnetic field. By comparing the position angles of the two types of polarization, it was observed that optical or NIR polarization has position angles perpendicular to those of synchrotron radiation. This implies the dust grains are aligned with their small axis parallel to the magnetic field. This makes

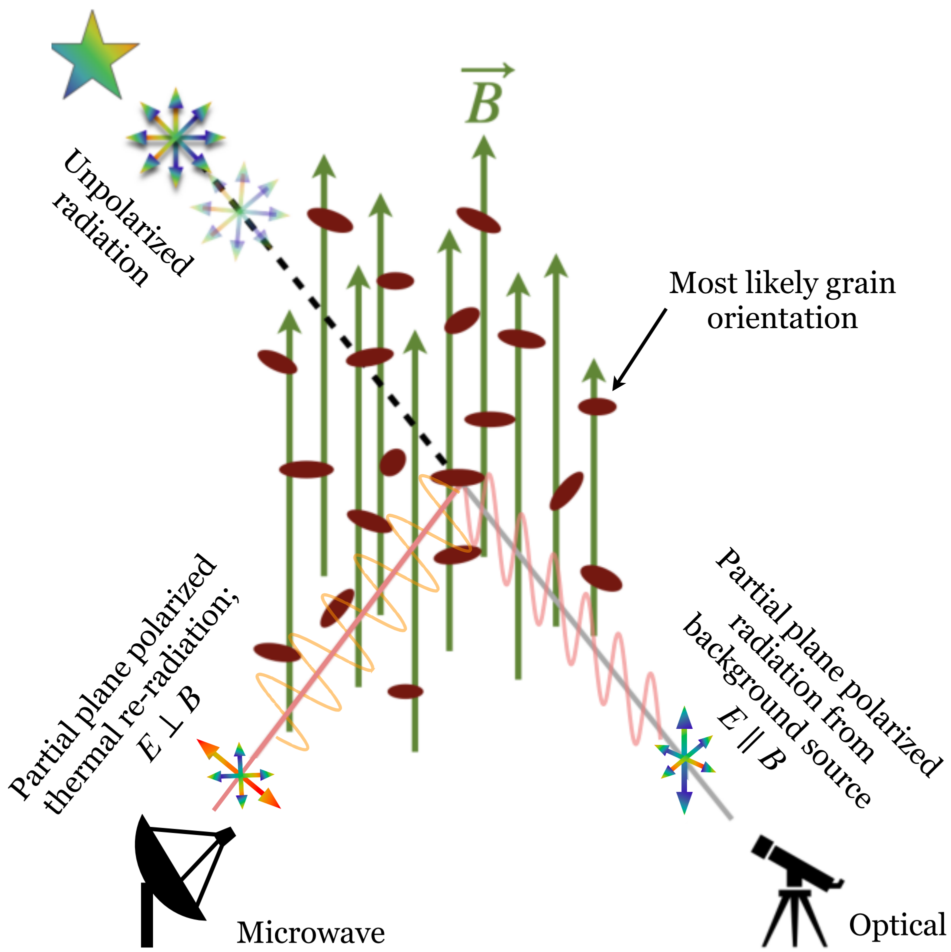

Figure 4.1: A schematic diagram illustrating the mechanism of ISM polarization, showing the polarization of background starlight in the optical range and dust emission in the microwave range. The resulting polarization direction (E) aligns parallel to the orientation of the magnetic field (B) in the optical regime, whereas the polarization angle in the microwave regime exhibits a perpendicular orientation relative to the magnetic field.

ISM polarization an efficient tool for studying the plane of the magnetic field and dust properties of the sky.

The ISM polarization has been extensively studied for more than half a century to trace the plane of sky magnetic field in global and local regions (Goodman et al., 1990) and to determine the dust properties (Mathewson & Ford, 1971; Axon & Ellis, 1976; Berdyugin et al., 2014; Clemens et al., 2020). However, combining the distance information of the stars with their polarization to infer the dust distribution and magnetic field tomography are newly evolving subjects. We aim to study the Galactic tomography from the three-dimensional distribution of the dust using polarization observations in the Galactic plane.

4.3 Observational facilities

The observations were conducted using meter-class telescopes from two Indian observational facilities, Mount Abu observatory and Aryabhatta Research Institute of Observational Sciences (ARIES) in-house observatory. To carry out the observations, we utilized two state-of-the-art instruments: the single-channel Electron-Multiplying Charged-Coupled Device (EMCCD) based optical polarimeter (EMPOL) and the dual-channel ARIES imaging polarimeter (AIMPOL). A detailed description of the telescopes and the instruments is provided in the following subsections.

4.3.1 Mount Abu Observatory

The Mount Abu Observatory is located (Longitude: $72^\circ\ 46'\ 45''.9$ East; Latitude: $24^\circ\ 39'\ 10''.9$ North, and Altitude: ~ 1680 m) within the Aravai ranges at Mount Abu. This facility has been run by Physical Research Laboratory, India, since 1990. The site offers good sky conditions for the observations with median seeing of $\sim 1''$ in the visual band. The Observatory comprises multiple facilities, i.e., 43 cm, 50 cm, 1.2 m, and a recently developed 2.5 m telescope. The polarization observations were carried out from the 1.2 m telescope. It is an f/13 Ritchey-Chretien equatorial mount telescope. Various backend instruments are being used on this telescope to perform imaging, photometry, spectroscopy, and polarimetry. For our observations, we employed the EMPOL instrument, the details of which are discussed in the following subsection.

EMPOL

EMPOL is an EMCCD-based, single-channel imaging polarimeter working in the optical regime. It was built in-house using off-the-shelf optical element (Ganesh et al., 2020). It has been extensively used for optical linear polarization from various celestial objects, from Solar system bodies to extragalactic sources. The instrument comprises a rotating half wave-plate (HWP), used to modulate the intensity of the stars to measure polarization, and a wire grid polarizer, which acts as an analyzer. The rotating HWP is driven by a stepper motor, allowing it to complete its rotation in 48 steps. Each step of the HWP corresponds to a rotation of 7.5 degrees and is accompanied by 0.5 s exposure. The exposure time at each position of HWP is limited to 0.5 s due to the constraint by the rotation of the HWP. To achieve an effective exposure of, say, 10 s, a total of 1008 images are recorded. In general, the number of frames (N) captured by the CCD according to user-defined effective exposure per frame is calculated by equation 4.5.

$$N = \left(\frac{effective\ exposure\ per\ frame}{0.5} + 1 \right) \times 48 \tag{4.5}$$

The captured images are saved at intervals of 1 s. Therefore, to obtain an effective exposure of 10 s per frame, an observation time of 1008 s is required.

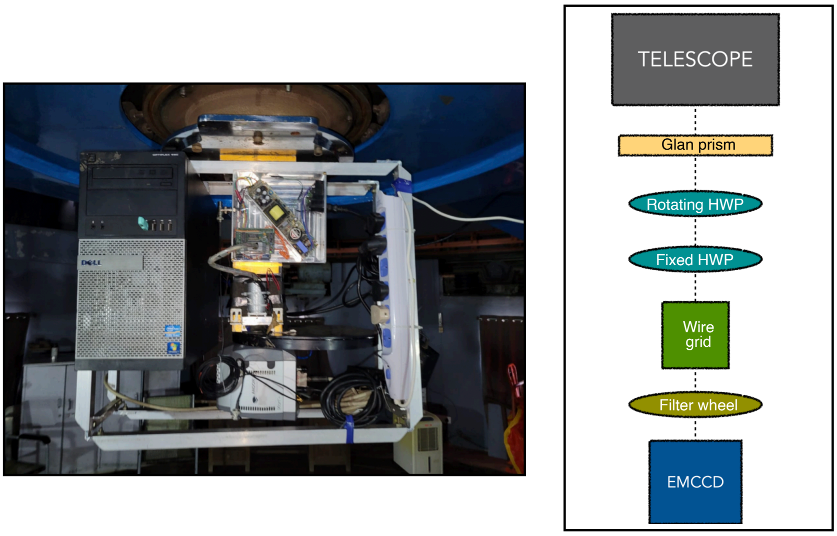

Figure 4.2: The left panel shows the EMPOL instrument mounted on the 1.2 m Mount Abu telescope, and the right panel represents the schematic optical layout of the instrument.

A fixed half-wave plate is also used just below the rotating half-wave plate to compensate for the wavelength dependence of the position angle of the half-wave plate. This pair of identical half-wave plates are as per the super achromatic wave plate design provided by Pancharatnam (1955). The use of the super achromatic half-wave plates ensures that there is no wavelength dependence on position angle. The light, after passing from the polarization optics, goes through the 12-positioned filter wheel, housing the Johnson-Cousins broadband filters (B, V, R, and I), as well as the Sloan filters (g, r, i, z) and three narrow-band filters. Finally, the light is detected at the Andor Xian EMCCD detector, having $1K \times 1K$ pixels of 13 μm size. The advantage of using EMCCD is its capability of fast readout with minimal read noise and an on-chip gain functionality. The instrument is mounted on the Cassegrain focus of the telescope, providing a plate scale of 0.18″ pixel^{-1} at the focal plane. Figure 4.2 illustrates the EMPOL instrument mounted on the 1.2 m Mount Abu telescope (on the left panel) and its schematic optical layout (on the right panel). We have used 4×4 on-chip binning to get a final plate scale of 0.72″ pixel^{-1} with a field of view of $\sim 3' \times 3'$. The option of user-defined EMGAIN helps to observe faint objects.

In addition to the complete setup for measuring the polarization of an astronomical object, a retractable Glan prism can also be used before the light enters the polarization optics. The Glan prism provides 100% polarized light, which can be used for calibration purposes. This prism has to be removed manually from the light path for regular observations of the science targets.

Polarization formalism for EMPOL

There are three active optical elements present in the EMPOL: Rotating HWP, Fixed HWP, and Wire grid polarizer. When light from stars with I, Q, U, and V Stokes parameters is incident on the rotating HWP at an angle α, the Stokes parameters undergo modification, as discussed in Section 4.1. The transformation matrix is given by the equation 4.6.

$$M(HWP, \alpha) = R(-\alpha)\, M(HWP)\, R(\alpha) \tag{4.6}$$

The Müller matrix for perfect retarder introducing a phase difference of ϕ is expressed by equation 4.7.

$$M(\phi) = \begin{pmatrix} 1 & 0 & 0 & 0 \\ 0 & 1 & 0 & 0 \\ 0 & 0 & \cos\phi & \sin\phi \\ 0 & 0 & -\sin\phi & \cos\phi \end{pmatrix} \tag{4.7}$$

For HWP, $\phi = \pi$.

The light will then pass through the fixed HWP, giving the conversion matrix,

$$M(fixed\ HWP) = \begin{pmatrix} 1 & 0 & 0 & 0 \\ 0 & 1 & 0 & 0 \\ 0 & 0 & -1 & 0 \\ 0 & 0 & 0 & -1 \end{pmatrix} \tag{4.8}$$

Finally, it will pass through the wire grid polarizer, and the Müller matrix for a polarizer is given by the following equation.

$$M(wire\ grid) = \begin{pmatrix} 1 & 1 & 0 & 0 \\ 1 & 1 & 0 & 0 \\ 0 & 0 & 0 & 0 \\ 0 & 0 & 0 & 0 \end{pmatrix} \tag{4.9}$$

The stokes parameter S(incident), after passing through the entire instrument, is transformed as

$$S'_j = M(wire\ grid) \times M(fixed\ HWP) \times \\ R(-\alpha_j)\, M(rotating\ HWP)\, R(\alpha_j) \times S(incident).$$

Where α_j is the rotation angle of the rotating HWP, and j runs from 0 to 47. Using equation 4.6, 4.8 and 4.9, the total intensity of the beam recorded at the detector is given by equation 4.10

$$I'_j = \frac{1}{2}[I \pm Qcos4\theta_j \pm Usin4\theta_j] \tag{4.10}$$

4.3.2 Sampurnanand telescope

The 1.04 m Sampurnanand telescope (ST) is located in the ARIES at Manora Peak, Nainital (Longitude: 79°.458 East; Latitude: 29°.359 North, and Altitude: 1951 m). It was installed by Carl Zeiss, Germany, in 1972. The telescope is an f/13 Ritchey-Chretien equatorial 2-pier English mount with a cassegrain focus. The telescope houses three backend instruments: Tek $1k \times 1k$ CCD, $1k \times 1k$ pylon CCD, and an ARIES IMaging POLarimeter (AIMPOL). We utilize the AIMPOL instrument for our observation purposes.

AIMPOL

AIMPOL is a back-end instrument at the cassegrain focus of 104 cm Sampurnanand telescope(as shown in the left panel of Figure 4.3). It has been operational since 2004 and is designed to measure the linear polarization of various celestial objects using the $BVRI$ broad-band filters. Unlike EMPOL, it is a double-channel polarimeter, having two orthogonally polarized, ordinary (o-ray) and extraordinary (e-ray) rays emerging from a Wollaston prism. The measurement of both e-ray and o-ray are sufficient to define the Q or U Stokes parameter of the incoming light. The instrument also encompasses an achromatic rotating HWP that rotates at 0°, 22.5°, 45°, and 67.5° to modulate the intensity of the star. The measurements of o-ray and e-ray after rotating the HWP give another measure of orthogonally polarized rays to determine both Stoke's parameters. The schematic diagram of the optical components is shown in the right panel of Figure 4.3. A liquid nitrogen-cooled $1k \times 1k$ pylon CCD is used to detect the modulated light coming from the celestial object, giving a larger field view of $\sim 8'$ in diameter. In addition, the CCD offers various readout speeds (50, 100, 200, 500 kHz, 1, 2, 4 MHz) and gain options (low, medium, and high). Detailed information about AIMPOL can be found in Rautela et al. (2004), with an upgraded version described in Pandey et al.

(2023). The e-ray and o-ray from Wollaston get focused onto the same CCD plane but with a fixed separation of ~ 34 pixels.

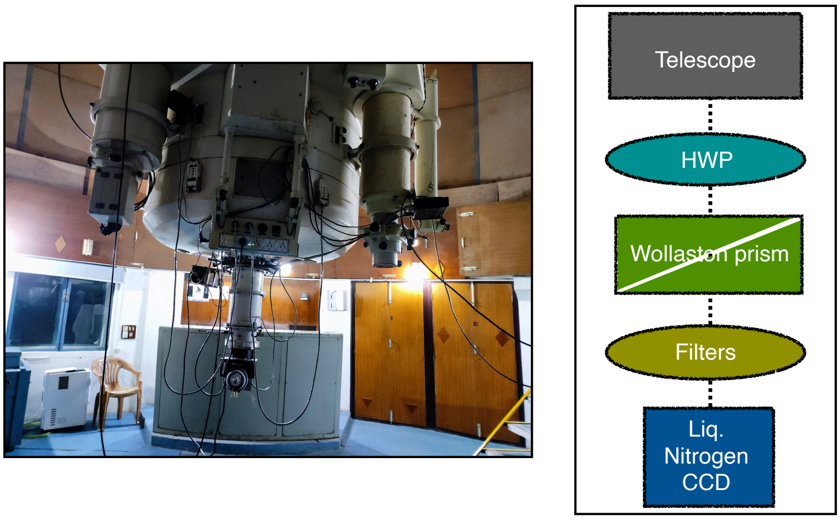

Figure 4.3: AIMPOL instrument mounted on 1.04 m Sampurnanand telescope in the left panel and the optical layout of the instrument in the right panel.

The intensity of the e-ray (I_e) and o-ray (I_o) components are related to the polarization of light through equation 4.11 and 4.12.

$$I_e(\alpha) = \frac{I_{up}}{2} + I_P \cos^2(\theta - 2\alpha) \tag{4.11}$$

$$I_o(\alpha) = \frac{I_{up}}{2} + I_P \sin^2(\theta - 2\alpha) \tag{4.12}$$

Here, I_{up} and I_P are the un-polarized and polarized intensity, respectively.
A ratio of ordinary and extra-ordinary rays gives a modulation factor, and it is defined in equation 4.13

$$R(\alpha) = \frac{I_e/I_o - 1}{I_e/I_o + 1} = P\cos(2\theta - 4\alpha) \tag{4.13}$$

where $p = \frac{I_P}{I_{up}+I_p}$, represents the fraction of polarized radiation. This modulation equation is used to estimate the degree of polarization and polarization angle.

4.4 Observation Strategy

To study the dust distribution in the Galactic plane, we planned to carry out the polarization observations of a few Galactic open clusters. Open clusters can be a good candidate for polarization observations because all the member stars have common properties such as distance, age, and proper motion. Moreover, a bunch of stars present at similar distances and locations in the sky will provide statistically stronger results than randomly selected stars. The open clusters, being the spiral arm tracers, will provide a unique opportunity to target the polarization observation for 3D dust tomography of the Galactic disk. Open clusters are not only useful to target dust distribution, but their polarization measurement also helps to study the plane of the sky magnetic field and plays a significant role in deciphering the cluster membership.

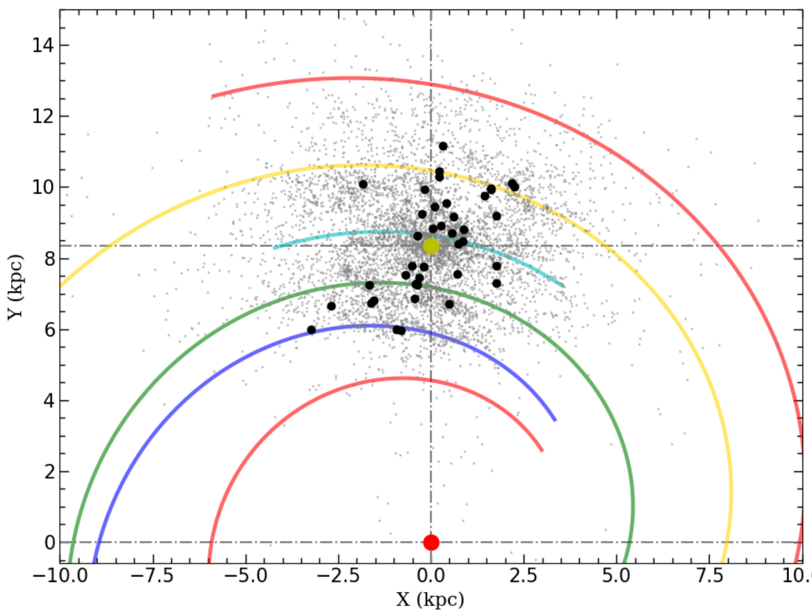

Figure 4.4: Distribution of the Galactic open clusters detected from Gaia DR3 in Galactocentric XY-plane, shown as gray points. Black solid circle corresponds to the clusters having polarization observations in the literature. Solid curved lines correspond to the spiral arms, Norma-Outer arm: red, Perseus arm: yellow, Local arm: cyan, Sagittarius-Carina: green, and Scutum arm: blue. The position of the Galactic center (0,0) and Sun (0, 8.314) kpc are highlighted by red and yellow points, respectively.

With the recent Gaia data release, Gaia DR3, more than 7200 Open clusters have been detected (Hunt & Reffert, 2023) and are plotted in Galactocentric XY-plane as gray color dots in Figure 4.4. The curved lines in the figure correspond to the spiral arms determined by extrapolating the arms constrained in Reid et al. (2019) and Castro-Ginard et al. (2021). Out of these 7200 clusters, only around 40 (from literature) clusters have been observed to date with polarimetry (highlighted as a black-filled circle in Figure 4.4). Most of the observed clusters in the literature are confined to nearer distances (distance < 3 kpc). Most studies related to cluster polarization focused on investigating the dust properties towards individual clusters and confirming the cluster membership of the stars observed. In contrast, Galactic tomography requires observation of a large number of open clusters covering wider areas of the sky. In order to investigate the role of open cluster polarization for the 3D dust tomography studies, we chose clusters in the same line of sight but located at different distances, thereby encompassing the distant clusters. In this regard, we carried out the polarization observations of open clusters in three directions of the Galactic plane confined by $-5° < b < +5°$.

4.4.1 Cluster selection criteria

We selected the clusters that are accessible in the observational season from the location of our observing facilities. In addition to this, various other criteria have been checked for selecting a particular target. These selection criteria include,

- **Distance**
  Our first selection criteria involved choosing clusters with similar longitudinal directions but present at different distances, covering solar neighborhood to distant locations of the Galactic plane.

- **Member stars brightness**
  In order to study dust tomography, it is necessary to observe both nearer and distant clusters. However, it is crucial that the member stars of the distant clusters possess adequate brightness to be detectable by the meter-class telescopes utilized for observations. Faint cluster members may not provide a satisfactory signal-to-

noise ratio, which can ultimately affect the accuracy of polarization measurements. Therefore, we targeted the clusters having a sufficient number of members with Gaia G-mag brighter than 17 mag for reliable observations.

- **Size of the cluster**
  The cluster radius is not a prime criterion for selecting the observed targets but can be used as a sorting parameter. Our objective is to observe clusters along the same line of sight but distributed across varying distances. Since clusters in a similar line of sight are typically observable during the same observing season, capturing multiple clusters within the allocated telescope time can become challenging. Therefore, in order to study a large number of clusters within the limited available observation time, we must carefully select clusters that can be observed within a single telescope pointing, with at least the core of the cluster being captured. Therefore, sorting clusters based on their size becomes important. Since the nearer clusters often have large angular spread, they are observed from AIMPOL (FOV $\sim 8'$), while the distant clusters, with smaller angular extents, are targeted from EMPOL (FOV $\sim 3'$. This approach allows us to efficiently observe clusters at different distances while optimizing the use of telescope time.

- **Number of members**
  After filtering the potential targets based on the aforementioned criteria, if multiple cluster options still exist, an additional criterion is applied: the maximum number of member stars. This criterion is implemented because a larger number of stars within a cluster can yield statistically more significant polarization results.

Based on the prioritized criteria mentioned previously, we initially identified over twenty clusters as potential targets. However, the data quality obtained from our regular observing instrument, EMPOL, which is a single-channel polarimeter, is greatly influenced by sky conditions. Hence, the observations from EMPOL require dark and stable skies. Unfortunately, the progress of our observations was significantly hindered by the temporary closure of the observatory during the waves of the COVID-19 pandemic. Nevertheless, with the dedicated efforts of the telescope operating staff, remote observations became possible. However, the majority of the allocated nights in 2021 were affected by unfavorable weather conditions, further reducing the efficiency

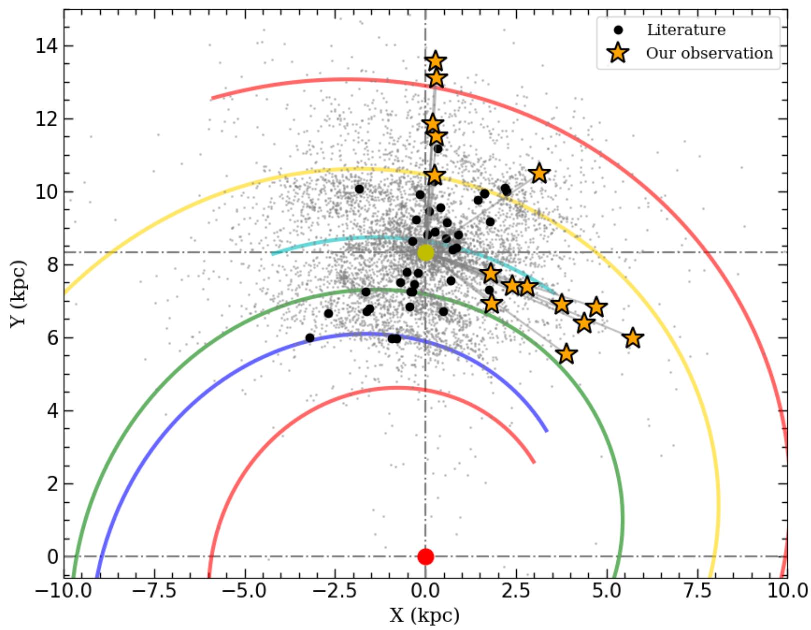

Figure 4.5: Same as Figure 4.4, with the added orange stars, highlighting the position of clusters observed in this thesis.

of our observing campaign. With the combined effect of these unforeseen conditions, we were only able to observe a total of 15 clusters. In some cases, we were limited to observing only the core regions of the clusters. The successfully observed clusters are listed in Table 4.1 along with their position in Galactic coordinates and their distances from Hunt & Reffert (2023). The position of the observed clusters on the face-on view of the Galaxy is shown as orange star symbols in Figure 4.5 with the background of known clusters from Gaia DR3 (as gray points). The clusters already having polarization observations (from literature) are also plotted in the figure as black points to compare and highlight the selection of our targets, which are located at greater distances compared to the previous observations.

4.4.2 Selection of broadband filter for observations

As our objective is to study the dust distribution along the line of sight, unlike the study related to constraining the dust properties, the observation of clusters in different broad-band filters is not required. Serkowski et al. (1975), observed a systematic variation

Table 4.1: Observation details of the targeted open clusters.

Cluster	ℓ	b	distance (pc)
Berkeley 47	52.544	-0.042	2317.27
Kronberger 79	54.176	-0.611	4789.72
Berkeley 83	66.094	-0.931	4800.37
Kronberger 52	67.623	0.848	6204.70
Kronberger 69	68.520	0.426	2568.44
Kronberger 54	69.104	0.519	4024.96
Berkeley 49	70.977	2.580	2962.87
Teutsch8	71.859	2.419	1903.98
Berkeley 51	72.147	0.295	4969.34
Czernik 3	124.266	-0.057	3807.47
Kronberger 1	173.107	0.046	2338
Berkeley 69	174.442	-1.851	3179.51
King 8	176.384	3.104	4787.78
Berkeley 71	176.635	0.901	3501.53
Berkeley 19	176.919	-3.612	5251.64

of polarization with the wavelength, displaying a broad symmetric peak in the visible region for most of the stars. He gave an empirical relation for the spectral (λ) dependency on linear polarization (P_λ) known as the Serkowski law and is described below.

$$P_\lambda = P_{max}\ exp\left\{-K\ ln^2\left(\frac{\lambda_{max}}{\lambda}\right)\right\} \tag{4.14}$$

where, P_{max} represents the maximum polarization observed at $\lambda = \lambda_{max}$. The wavelength of maximum polarization (λ_{max}) varies from star to star with a typical range of $0.3-0.8\mu m$ and a mean value of $0.55\mu m$. Hence, optical wavelength, especially the V-filter covering 0.55 μm, is an optimal choice to study polarization. However, the V-band would experience larger extinction, as a result, hampering the observation of distant clusters, especially in the extincted region of the Galaxy. In the longer wavelengths, where extinction effects get minimized, the polarization also decreases, requiring precise and accurate measurement to get sufficient polarization SNR. Therefore, selecting the R-band or I-band is a suitable compromise, balancing the effects of extinction while capturing a signal of sufficient strength to achieve a good polarization SNR. Consequently, we conducted the observations of selected Galactic open clusters in the R-band with both instruments (EMPOL and AIMPOL) except Czernik 3 cluster. For this particular cluster, we employed the Sloan-i band since the R-band filter was not available in the instrument during that time.

4.5 Observations and Data reduction

The polarization measurement requires well-planned observations and careful data reduction techniques. This section discusses the observations of the selected clusters from EMPOL as well as AIMPOL instruments and the procedure required for subsequent data reductions.

4.5.1 Observations

Observations of polarization, wherein the intensity of light diminishes by half, are challenging and time-consuming, especially when focusing on fainter stars. Moreover, achieving accurate measurements of interstellar medium (ISM) polarization requires clear and stable skies, as the average value of ISM polarization itself does not exceed 10% (in general). It is, therefore, crucial to carefully plan the observations, considering all the relevant aspects to have fruitful observations.

During the observation season of 2021-2022, we conducted regular observations with EMPOL, utilizing 3-4 nights per month. These observations focused on several open clusters within our target range. Among them, we successfully observed the core region of the distant cluster, Czernik 3, located in the second Galactic quadrant, using the Sloan i-band. In addition, six clusters residing in the first Galactic quadrant, including Kronberger 79, Berkeley 83, Kronberger 52, Kronberger 54, Teutsch8, and Berkeley 51, were observed in R-band. All the clusters observed from EMPOL are marked as light-blue stars in Figure 4.6. In most cases, an effective exposure of 30 s per frame was set, resulting in 2928 frames in 48.8 minutes of observation time to record one set of a particular cluster field. Given EMPOL's limited field of view, multiple pointings are required to cover the entire cluster region, depending on the size of the cluster. In most of the cases, we focused on observing at least the core part of the cluster. Furthermore, as mentioned in Section 4.3.1, we employed 4 × 4 on-chip binning and an electron multiplicative gain(EMGAIN) of 10-30, depending on the brightness of the stars towards the cluster regions.

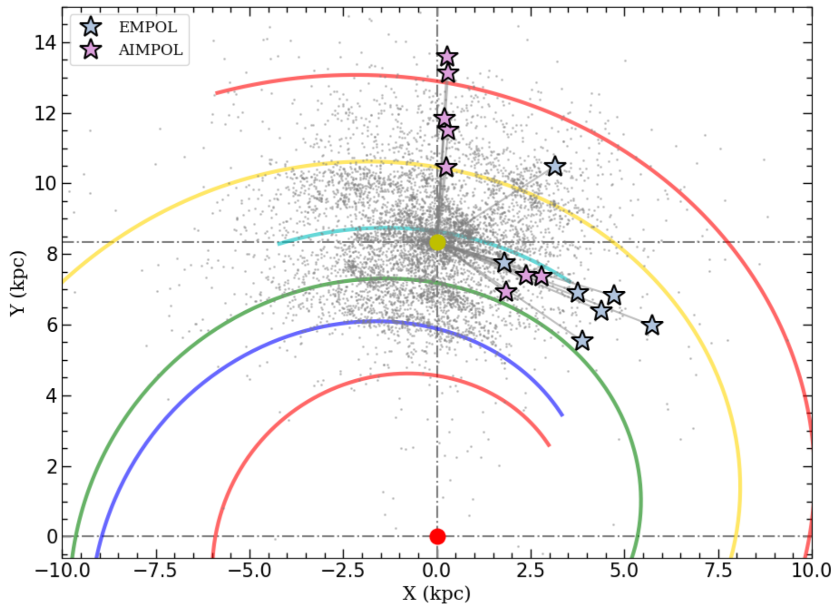

Figure 4.6: Same as figure 4.5, showing the clusters observed from EMPOL in light-blue color star-symbol and AIMPOL in light-pink.

For the AIMPOL observations, we submitted proposals to observe several open clusters, primarily focusing on nearby clusters with larger sizes that could be fully covered within a single pointing of AIMPOL (as a requirement in selecting the cluster discussed in Section 4.4.1). In total, we were allocated 13.5 nights spread over three observation cycles. We conducted observations of 8 Galactic open clusters using AIMPOL in the R-band, with a readout speed of 100 kHz and the medium gain option. Among the observed ones (shown as light-pink star symbols in Figure 4.6), five clusters are located towards the anticenter direction: Kronberger 1, Berkeley 69, King 8, Berkeley 71, and Berkeley 19. The remaining three clusters (Berkeley 47, Berkeley 49, and

Kronberger) are situated in the first Galactic quadrant. Open clusters present relatively crowded fields, and it becomes very challenging to identify the clusters in the case of AIMPOL due to over-crowding by the e-ray and o-ray image of the stars on the same CCD plane. Therefore, careful consideration was given in selecting the clusters that could be observed from AIMPOL.

In addition to the cluster fields, at least two highly polarized and unpolarized standard stars are observed each night for polarization angle correction and instrumental polarization estimation. We also checked the response of the instrument to 100% polarized light with EMPOL by introducing the glan prism into the light path.

4.5.2 Data Reduction

Acquiring high-quality polarization data requires a significant amount of both luck and effort. The subsequent data reduction and analysis are equally crucial in ensuring the credibility of the observed data.We developed fully automated pipelines to reduce the raw data to science-ready information using self-scripted Python routines. The basic data reduction process involves Bias subtraction, Flat fielding followed by Shifting and Stacking, astrometry, photometry, and polarization measurement. The details of these tasks for both instruments are presented in this section.

4.5.2.1 EMPOL

The data acquired from EMPOL consists of a large number of frames, which is calculated from equation 4.5, and these are multiple of 48 (equals to the number of HWP rotation steps). Consequently, all the processing tasks involved in reducing the EMPOL data are carried out in cycles of 48. Equation 4.10 shows that the observed intensity at the detector varies as 4θ (the angle of the HWP). Therefore, one complete rotation of HWP encompasses four cycles of intensity variation. As a result, the four cycles can be further folded into one, corresponding to a 12-step of HWP rotation. This enables the data reduction processing in cycles 12, 24, 36, or 48, all of which are expected to show the same polarization state.

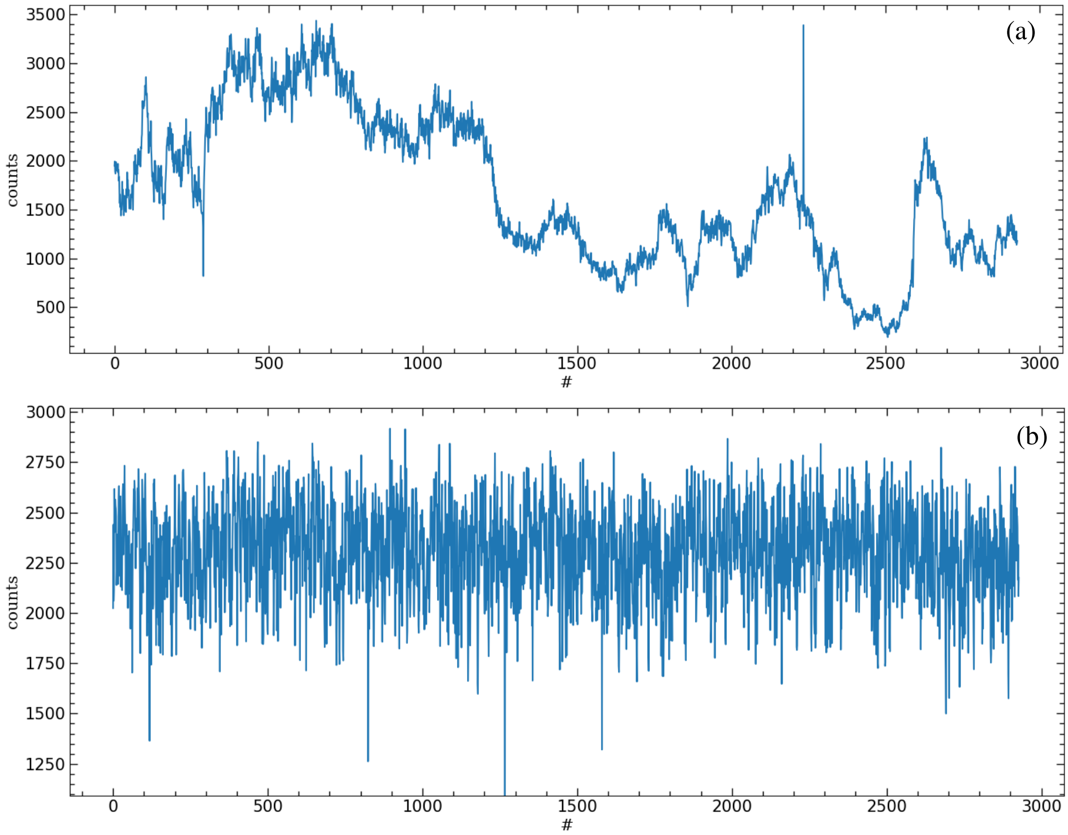

Figure 4.7: Variation of star counts with the number of frames obtained in 30s effective exposure in EMPOL observation. Panel (a) depicts the star counts for bad sky conditions, while panel (b) represents relatively stable sky conditions.

For the reduction, basic tasks like bias subtraction and flat fielding to correct the images from the CCD response are applied to all the science images. Before proceeding forward to the stacking, we made a small script to investigate the effect of atmospheric conditions on the acquired data. The script analyzes the counts of the brightest star in each frame, which corresponds to a 0.5 s exposure, for the complete observation set. An illustrative example is provided in Figure 4.7, which depicts the variation of ADU counts for a star in the Czernik 3 field over a set of frames acquired on November 7, 2021 (panel a) and January 6, 2022 (panel b). In the figure, Panel (a) represents the large-scale intensity variation, randomly distributed across all the frames observed, indicating the influence of atmospheric conditions (moving clouds) on the observed star counts. In contrast, the bottom panel (b) displays the variation of counts due to the position of the half-wave plate (HWP) while maintaining a consistent average value, suggesting a stable sky condition. The data with the modulation of counts showing large scattering, as shown in the top panel of Figure 4.7, are discarded at this stage and are not further reduced.

Shifting and stacking

The frames showing nearly constant mean counts (as discussed above) are stacked in the cycle of 12 or 48 (corresponding to the rotation of HWP) to increase the SNR. Prior to stacking the images, it is crucial to align them by ensuring they have the same center. This is accomplished by iteratively calculating the shift between each image, achieved by determining the center position of a common star in the subsequent image. We then use

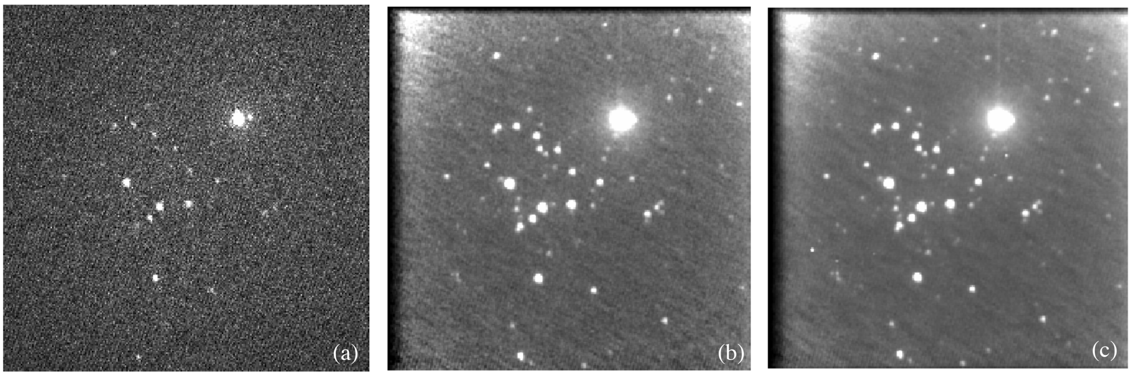

Figure 4.8: The images of the Czernik 3 cluster observed from EMPOL. Panel (a) represents the raw image with 0.5 s exposure, while panel (b) and (c) corresponds to the stacked images showing the effective exposure of 10 s and 40 s, respectively.

the shifting task in the 'ndimage' package (Virtanen et al., 2020) of the *Scipy* library in Python to shift the images to a common center. The counts in the non-overlapping area are set to be zero, as shown by dark borders (right and top) in the right panel of Figure 4.8. Subsequently, the shifted images are mean/median combined to build the signal. Figure 4.8 presents a comparison between a single frame with a 0.5 s exposure (panel a) and the stacked images corresponding to effective exposures of 10 s and 40 s (panels b and c). The panels clearly demonstrate the increase in SNR achieved through stacking.

Astrometric calibration

The scientific analysis of the image requires the sky position of the observed stars, especially in the case of crowded fields. However, the raw CCD images do not contain any information on sky coordinates. We can only obtain the pixel coordinates of the stars in the image, which can be a tedious task if done manually, particularly when dealing with crowded fields. We utilized SExtractor (Bertin & Arnouts, 1996), an efficient general-purpose software for extracting the pixel coordinates of the stars. This software identifies pixels with signals above a certain threshold value. It is important to note that false detections may occur in the vignetted regions, primarily located in the corners due to the circular aperture of EMPOL. To avoid this issue, we excluded the sources detected in the boarder and corners from our analysis.

The transformation of pixel coordinates to the sky co-ordinates, i.e., the astrometric correction, is done by utilizing *Image World Coordinate Setting* (imwcs) program of *World coordinate System tools (WCStools)* software. This process involved matching the pattern of detected sources with astrometric catalogs such as Ub1 (Monet et al., 2003), ua2 (Monet, 1998), and 2MASS (Skrutskie et al., 2006), among others. The imwcs program updates the transformation matrix element into the header of the image, which can be used to convert image coordinates to sky and vice-versa. In our analysis, the astrometric uncertainty is typically below 0.5″ for most cases.

In crowded fields, the source extractor occasionally identifies only one star for two close-by overlapping stars. To mitigate this issue, we selected stars from the Gaia DR2 or DR3 catalog after the astrometric calibration and implemented a cut based on G-magnitude. Additionally, our pipeline offers the option of re-centering the coordinates of stars using the *centroid* from the *Photutils* package in Python, helping to improve accuracy.

Photometry

Once the accurate pixel coordinates of all the stars in the field are obtained, aperture photometry is performed utilizing the *photutils* module of Python with global background selection. A constant optimal aperture of 3 × FWHM was used to carry out the photometry of the stacked 48 images. In a crowded field, there is a finite probability for the aperture to overlap the close-by stars (as shown in Figure 4.9). In order to minimize the effects of the overlap, we have applied aperture corrections, i.e., chosen the photometric results from smaller apertures of 2 × FWHM or 1× FWHM scaled to 3 × FWHM using a scaling relation derived from the isolated stars.

Polarization Calculation

To determine the polarization information, only the relative intensity of the star is

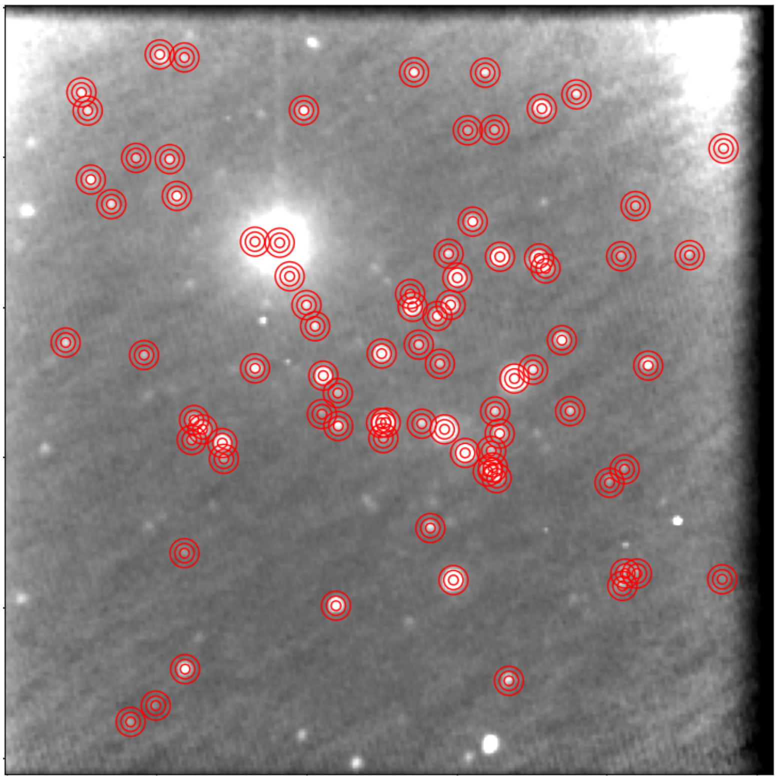

Figure 4.9: A CCD field of one of the cluster; Czernik 3, with concentric circles representing the 1×, 2×, and 3× FWHM aperture, indicating the aperture overlap of close-by stars in EMPOL observations.

required, which is calculated by aperture photometry as described above. The aperture counts of each star display variations with the angle of the half-wave plate (HWP), as depicted by the black points in Figure 4.10. This figure showcases the ADU counts of a polarized standard star HD 19820 in the R-band, folded into 12 frames corresponding to the HWP angle. As discussed in Section 4.1, the state of the polarization gets changed after interacting with the active optical elements in the instrument. So, the calculated counts represent the transformed intensity recorded on the detector, which is related to the Stokes parameters of the incoming light from equation 4.10. This equation is fitted on photometric counts of a star at each HWP position to find the best-fit Stokes parameters I, Q, and U. This fitting process is accomplished using the *curve_fit* module from the *scipy* package (Virtanen et al., 2020) in Python. The blue curve shown in Figure 4.10 represents the best-fitted model, corresponding to the observation of HD19820. The computed Stokes parameters are further used to determine the degree of polarization

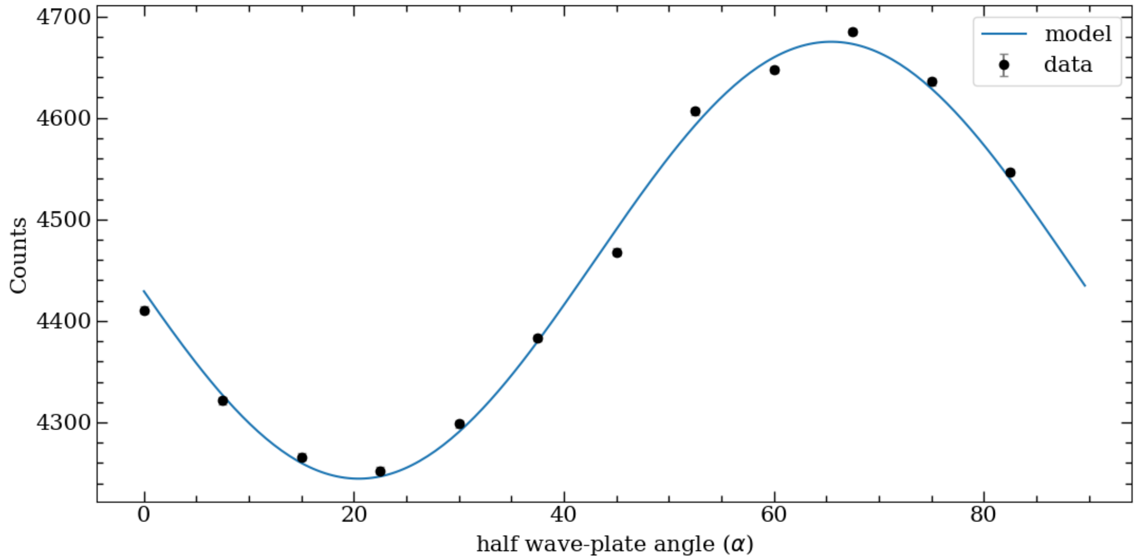

Figure 4.10: Modulation of star counts as a function of HWP angle (α). Black points represent the photometric counts of a standard star HD19820, and the blue curve corresponds to the best-fitted model given by equation 4.10.

(P) and polarization angle (θ) from the following equations 4.15 and 4.16.

$$P = \frac{\sqrt{Q^2+U^2}}{I} \tag{4.15}$$

$$\theta = \frac{1}{2}\tan^{-1}\left(\frac{U}{Q}\right) \tag{4.16}$$

The errors in the degree of polarization (σ_P, equation 4.17) and polarization angle (σ_θ, equation 4.18) were derived using fundamental error propagation methods:

$$\sigma_P = \frac{1}{I}\sqrt{\frac{Q^2\sigma_Q^2+U^2\sigma_U^2}{Q^2+U^2}+\frac{Q^2+U^2}{I^2}\sigma_I^2} \tag{4.17}$$

$$\sigma_\theta = \frac{1}{2(Q^2+U^2)}\sqrt{Q^2\sigma_U^2+U^2\sigma_Q^2} \tag{4.18}$$

4.5.2.2 AIMPOL

The AIMPOL observation involves the acquisition at four angles of HWP corresponding to 0°, 22.5°, 45°, and 67.5°) unlike 48 positions in EMPOL. As a result, the user can employ any desired exposure during the observations. We developed an automated procedure to reduce and analyze the AIMPOL data. The initial tasks involved in the reduction, such as bias subtraction, shifting, and stacking of multiple sets, are similar for the data of both instruments. The sky coordinates of stars in the field are obtained using a web-based 'astrometry.net' service. In the CCD plane of AIMPOL, two orthogonal

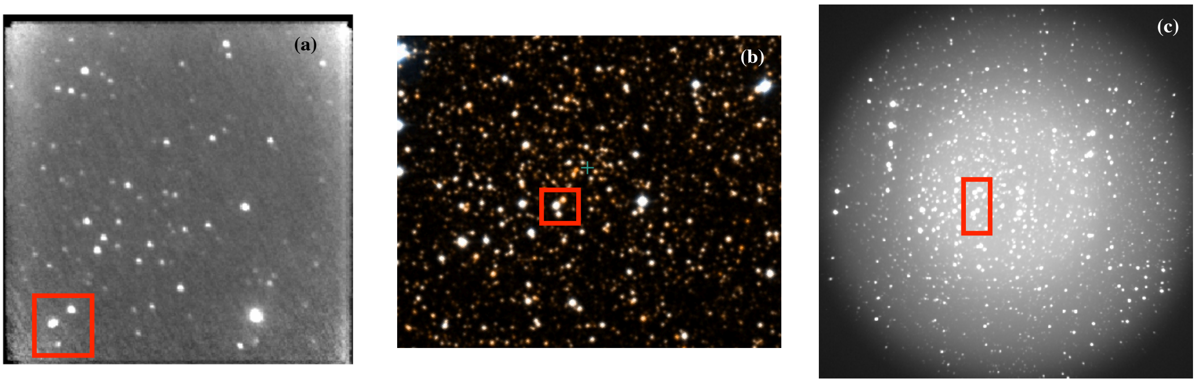

Figure 4.11: Comparison of the images taken from EMPOL (panel a) and AIMPOL (panel c) with the DSS image (panel b) of the Berkeley 69 cluster. The red box shows the difference in the image of stars obtained from both instruments.

images of a star, representing the e-ray and o-ray, are formed with constant separation (detail discussion in Section 4.3.2). A visual comparison of the Berkeley 69 cluster is presented in Figure 4.11, where the middle panel (b) showcases a cut-out from the Digitized Sky Survey (DSS) field. The left panel (a) shows the observation of the cluster using EMPOL, while the right panel (c) displays the observation from AIMPOL, where each star is represented by pairs of o-ray and e-ray images.

Separating e-ray and o-ray sources

To simplify the reduction process, the foremost task is to separate the e-ray and o-ray images of each star. The astrometric calibration gives the coordinates information corresponding to one set of stars (e-ray or o-ray). The RA, DEC information of the stars selected from the Gaia DR3 catalog with a suitable G-magnitude cut are converted into the image coordinate utilizing the 'WCS' module of *astropy* in Python. Since the separation between the o-ray and e-ray sources is fixed and can be determined by identifying a single o-ray and e-ray pair in the field, we can easily obtain the coordinates of the other set of stars (o-ray or e-ray). Thus, the image coordinated of all the e-ray and o-ray sources pairs are determined, and they are shown in red and blue points on the left and right panel of figure 4.12, respectively.

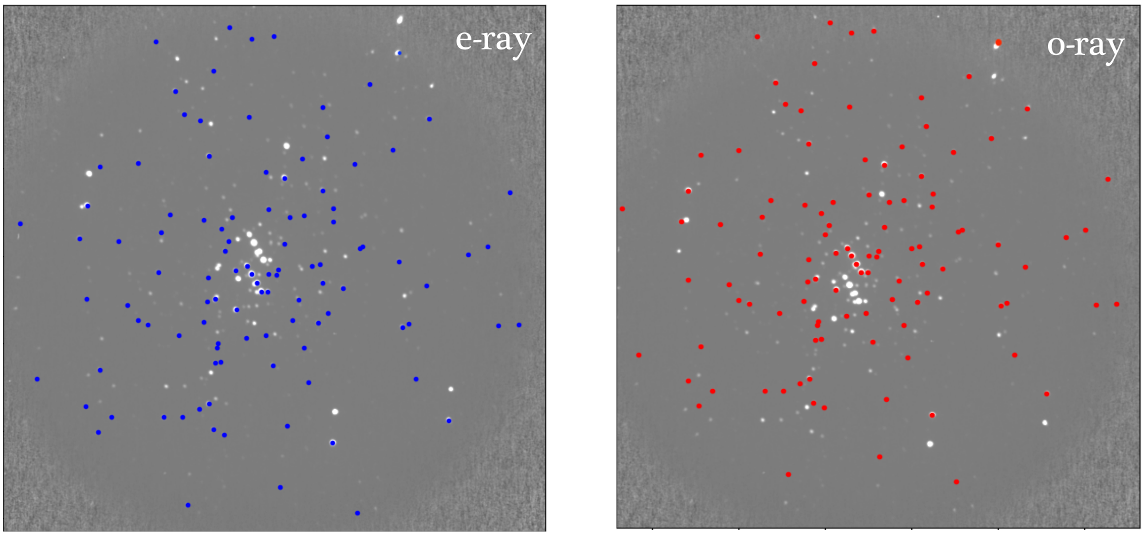

Figure 4.12: Field towards Trumpler 1 cluster in R band observed from AIMPOL. The stars corresponding to the e-ray are overlaid as blue points on the left panel and the o-ray as red points on the right panel.

Photometry

Similar to EMPOL, aperture photometry is performed on the AIMPOL images. The issue of the aperture overlap of nearby stars becomes more complex in AIMPOL due to the existence of both e-ray and o-ray images. Consequently, in addition to the close-by stars, the e-ray of one star may overlap the aperture of the o-ray of the other, and vice-versa, adding to the complexity of the analysis (see Figure 4.13). To overcome this issue, multiple apertures were defined between 1× FWHM to 3× FWHM and thereby calculating the photometric counts in each aperture.

Polarization Calculations

The polarization calculation depends on the ratio of the o-ray and e-ray counts. A modified modulation factor, $R(\alpha)$, is calculated using the e-ray and o-ray photometric

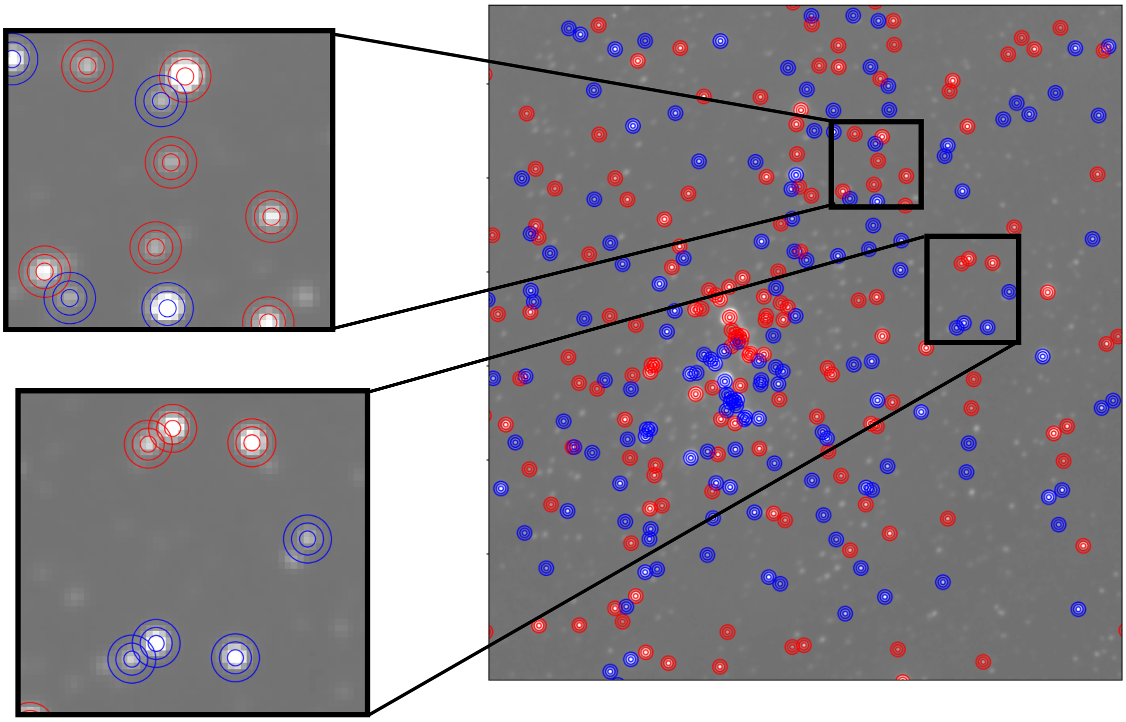

Figure 4.13: A cluster field showing the aperture-overlapping issue in AIMPOL data. The concentric circles represent the aperture corresponding to 1, 2, and 3 × FWHM, in red for o-ray and blue for e-ray.

count, as given in equation 4.19 and 4.20.

$$R(\alpha) = \frac{\frac{I_e}{I_o} \times f - 1}{\frac{I_e}{I_o} \times f + 1} \tag{4.19}$$

Here, f is a factor based on the fraction of o-ray and e-ray intensities, i.e., $\frac{I_o}{I_e}$, which may be related to the difference in the response of the system to e-ray and o-ray and/or the different response of CCD as a function of position on the surface (Ramaprakash et al., 1998). This factor is estimated as follows:

$$f = \left[\frac{I_o(0^\circ)}{I_e(45^\circ)} \times \frac{I_o(45^\circ)}{I_e(0^\circ)} \times \frac{I_o(22.5^\circ)}{I_e(67.5^\circ)} \times \frac{I_o(67.5^\circ)}{I_e(22.5^\circ)}\right]^{\frac{1}{4}} \tag{4.20}$$

The modified $R(\alpha)$ (equation 4.19), corresponding to all the apertures, is fitted with the right side of the equation 4.13. The aperture corresponding to the minimum chi-square fit is finally utilized to estimate the polarization fraction (P) and angle of polarization

(θ). The modulation and the best-fit model for a polarized standard star, BD+59 389, data are shown as blue points and red curves, respectively, in Figure 4.14.

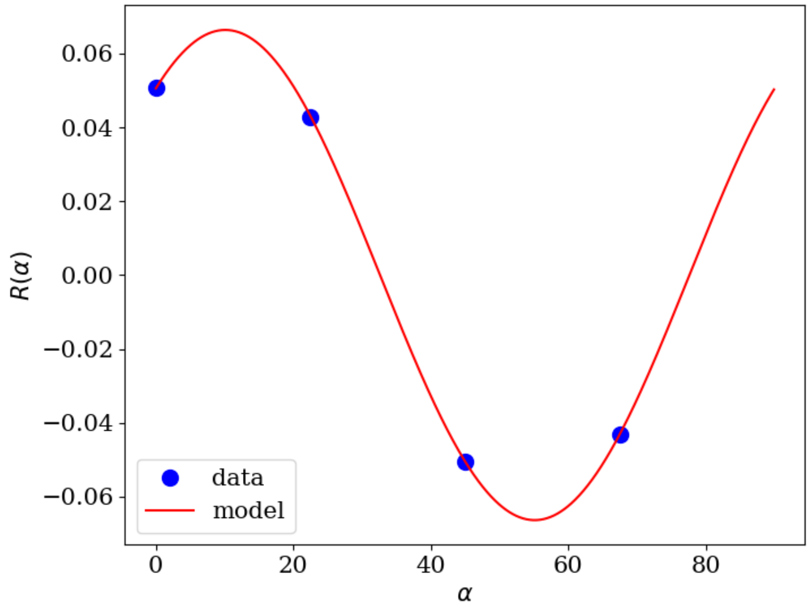

Figure 4.14: Modulation, $R(\alpha)$ as a function of α (position of HWP) for BD+59 389; a polarized standard star observed in R-band in blue points. The best-fitted curve (equation 4.13) is shown in red.

All the tasks described in the previous sections for both the EMPOL as well as AIMPOL instruments are made fully automatic. The user only needs to supply a rough right ascension (RA) and declination (DEC) of the field.

4.6 Summary

This chapter emphasizes the significance of studying dust distribution in unraveling the structure of the Galaxy. It establishes the foundation for our aim to investigate the role of interstellar medium (ISM) polarization studies in constraining dust distribution. A careful source selection for the observations that could demonstrate the potential of polarization as a tool to target dust distribution studies to understand Disk morphology is discussed in detail. The required observations of Galactic open clusters were carried out utilizing the imaging polarimeters EMPOL and AIMPOL from two state-of-the-art national observational facilities.

Furthermore, the chapter outlines the essential tasks involved in data reduction for the observed targets. Manual data reduction for polarization measurement can be time-consuming, particularly due to a large number of files (3000 for a 30 s effective exposure) in EMPOL and challenges related to field crowding in AIMPOL. To mitigate potential errors from manual or natural sources that could lead to inaccurate scientific interpretations, we have developed well-defined observational techniques and automatic pipelines for accurately estimating the degree of polarization and polarization angle, which has been systematically laid out in this chapter. We are in the process of making a user-friendly and interactive Graphical User Interface (GUI) based on these pipelines to efficiently reduce the data taken from both EMPOL and AIMPOL instruments.

This page was intentionally left blank.

Chapter 5

Polarization towards a distant cluster in the 2nd Galactic quadrant

"It is far better to grasp the universe as it really is than to persist in delusion, however satisfying and reassuring."

- Carl Sagan, *1934-1996*

We build upon the idea of using ISM linear polarization in optical wavelength to map the dust distribution in the Galaxy in Chapter 4. Our approach involves obtaining polarization measurements from distant clusters in various directions and analyzing how polarization varies with distance. To illustrate this, we selected a line of sight in the second Galactic quadrant, which offers the greatest visibility during the observational season from the locations where the observational facilities used in this thesis are situated. Previous polarimetric observations of clusters in this quadrant have predominantly focused on distances within 3 kpc. Our target selection in this quadrant is towards the direction with the highest number of existing polarimetric observed clusters but at a higher distance. Based on the selection criteria discussed in Section 4.4.1, we selected the

Czernik 3 cluster [$\alpha_{J2000}: 01^h03^m06^s$ and $\delta_{J2000}: +62°47'00''$ (Dias et al., 2002)], present towards $\ell = 124°$ at a distance of $4.4 kpc$ (Cantat-Gaudin et al., 2018). This is the best line of sight for demonstration purposes, as combining the data from the cluster in the vicinity of Czernik 3 will act as a test to verify the reduction procedure and investigate the large-scale dust distribution.

The cluster is located in the 2^{nd} Galactic quadrant ($\ell = 124°.256, b = -0°.058$). Previous studies have provided a range of ages (e.g., 100 Myr: Dias et al. (2002); 630 Myr: Kharchenko et al. (2016); 115 Myr: Bisht et al. (2017)), photometric distances (1.4-1.75 kpc), reddening E(B-V) (0.99-1.4 mag), and average extinction $A_V = 2.9$ mag (Dias et al., 2002; Bisht et al., 2017; Kharchenko et al., 2016). Recently, Cantat-Gaudin et al. (2018) have derived basic parameters and membership of 1229 Galactic open clusters using parallax and proper motion information from Gaia DR2. They showed that this cluster has 48 members with membership probability > 0.5, and about half of the member stars of this cluster lie within a radial distance of 0.82′. They also estimated the most probable distance to the cluster to be 4.47 kpc. Czernik 3 cluster has an extended morphology (Sharma et al., 2020) with a radius of the core and the whole cluster $\sim 0.5-0.6'$ and $1.2-5'$, respectively (Dias et al., 2002; Kharchenko et al., 2016; Joshi et al., 2016; Bisht et al., 2017; Sharma et al., 2020). Sharma et al. (2020) have placed the cluster at an average distance of 3.5 ± 0.9 kpc. They have claimed that it is a disintegrating old cluster with an average age of $0.9^{+0.3}_{-0.1}$ Gyr. Thus, there is a large variation in the possible ages and distances to this cluster. Astrometric data from Gaia EDR3 is expected to help better constrain the distance and membership. With this cluster, we aim to understand the dust distribution along the line of sight towards Czernik 3 at various spatial scales spanning a galactic longitude range of 110° to 140°. A detailed description of the observation of Czernik 3 and the results are provided in the following subsections.

5.1 Observations

Polarization observations of Czernik 3 were carried out on the dark nights of 2021, January 13 and February 7, using the EMPOL instrument (Ganesh et al., 2020), mounted

Table 5.1: Observed and reference polarization values (Schmidt et al., 1992) of polarized standard star: HD25443 (Vmag = 6.78 mag).

Observation epoch	P_{obs} (%)	θ_{obs} (°)	SNR[1]	P_{ref} (%)	θ_{ref} (°)	θ_{off} (°)
Jan 13, 2021	4.16 ± 0.06	18.03 ± 0.42	160	4.33	134.21 ± 0.28	116.18
Feb 7, 2021	4.43 ± 0.19	22.07 ± 1.22	130			112.14

in a 1.2 m Mount Abu telescope. The observations were taken in *Sloan i* (0.767 μm) filter with 0.5-sec exposures at each step of the HWP plate, covering the entire core region (0.5′-0.6′; Kharchenko et al., 2013; Sharma et al., 2020) in one pointing. A series of exposures were taken to get 40-sec effective exposure corresponding to each HWP step angle. Polarized standard HD25443 (see Table 5.1 for observed values) and unpolarized standard HD12021 were also observed on each night along with the cluster field, in the same filter to calibrate the polarization angle and to check the instrumental polarization, respectively. The instrumental polarization was found to be negligible (below 0.1%) as seen by the measured degree of polarization, 0.16% ± 0.12% of the unpolarized standard star (HD12021). The calibration/performance of the instrument for 100% polarized light was tested using a glan prism in the light path prior to the rotating half-wave plate with a resulting polarization value of ∼ 99%.

The observed data were reduced and analyzed using self-scripted Python routines as discussed in Section 4.5.2. The degree of polarization and polarization angle is calculated from equations 4.15 and 4.16 after doing aperture photometry on the detected stars in the observed field. The observed position angles (θ) were corrected to the reference position angle using observations of the polarized standard star HD25443. The reference degree of polarization (P_{ref}) of HD25443 star in *Sloan-i* band was not available in the literature. So, we calculated the value (provided in Table 5.1) from the Serkowski law of interstellar polarization by using P_{max}, λ_{max}, and K values for HD 25443 listed in Schmidt et al. (1992). The astrometric calibration of the polarization images was carried out using the *imwcs*[2] program of *World Coordinate System Tools* (WCSTools, Mink, 2011) software with the *UCAC4* (Zacharias et al., 2013) reference catalog. The estimated astrometric error was less than 0.5″.

[2]http://tdc-www.harvard.edu/wcstools/imwcs/

We derived the polarization measurements for 43 stars in the field from our observations. One of these, star #13, is a very bright foreground star whose glare has affected the measurement of several fainter stars in its immediate vicinity (within 18″ radial distance). Therefore, our analysis does not consider this star and its near neighbors. We also do not consider the three stars (#1, #7, and #42) having SNR < 3 for polarization. Further, we debiased the polarization measurements in order to compensate for the biasing produced due to the low signal-to-noise ratio (SNR) in some of the objects and the details are discussed in Section 5.1.1.

5.1.1 Ricean Bias Correction

The degree of polarization is determined as a quadrature sum of Stokes parameters (q and u) obtained from equations 4.15 and 4.16. The quadrature sum follows the Ricean distribution. The presence of errors in q and u, originating from various sources, contribute positively to the overall error, leading to a systematic increase in the derived degree of polarization (Patat & Romaniello, 2006; Sohn, 2011). Consequently, this introduces a bias in the polarization measurements, particularly when the error in polarization becomes comparable to the intensity of polarization.

In our case, we are considering sources with a polarization signal-to-noise ratio (P/σ_P) greater than 3. As a result, the Ricean bias is expected to be negligible. Nonetheless, we have accounted for the presence of Ricean bias in the linear polarization measurements by applying Equation 5.1.

$$P \sim \sqrt{p_{obs}^2 - \sigma_P^2} \tag{5.1}$$

Where P, p_{obs}, and σ_p are the bias-corrected degree of polarization, observed degree of polarization, and the associated error, respectively. The method used to produce debiased polarization values is based on the work by Wardle & Kronberg (1974). The debiased value of the degree of polarization thus obtained is used in our further analysis instead of polarization.

5.1.2 Additional data sets used in the analyses

We have used the astrometric and photometric data from Gaia EDR3 (Gaia Collaboration et al., 2021b; Fabricius et al., 2021) in our analysis. Instead of relying on the inverse of parallax, which is subject to large uncertainties as around 50% of our observed stars have fractional parallax error > 0.2, we considered the distance (‘r_{pgeo}’) derived from Gaia EDR3 by Bailer-Jones et al. (2021) using a Bayesian analysis method. To complement our polarimetric observations of the Czernik 3 cluster, we incorporated imaging and photometric data from Panoramic Survey Telescope and Rapid Response System (Pan-STARRS) (Chambers et al., 2016), Two Micron All-Sky Survey (2MASS) (Cutri et al., 2003), and Wide-field Infrared Survey Explorer (WISE) (NASA/IPAC Infrared Science Archive, 2020). The photometric and astrometric data were cross-matched with the stars observed in our study using the CDS crossmatch service (Boch et al., 2012) with a search radius of 1″. Furthermore, we also utilized spectral information related to neutral hydrogen (HI) and ^{12}CO obtained from the HI4PI survey (HI4PI Collaboration et al., 2016) and ^{12}CO survey (Dame et al., 2001) respectively.

In order to study the large-scale dust distribution, we have made use of polarimetric observations obtained from the literature. Heiles (2000) provide a list of polarization observations of approximately 9000 bright stars distributed in the plane of the Galaxy. From this compilation, we focused on the stars located within a 15° region surrounding

Table 5.2: Details of the nearby open clusters around Czernik 3. The average angular radius (ang. rad.) is obtained from Kharchenko et al. (2013) and average distance (dist.) from Cantat-Gaudin et al. (2018)

Cluster	ℓ (°)	b (°)	ang. dist. from Cz3 (°)	Reference	ang. rad. (′)	dist. (kpc)
NGC 457	126.631	-4.390	4.90	Topasna et al. (2017)	13.2	2.88
Berkeley 59	118.230	5.020	7.86	Eswaraiah et al. (2012)	13.2	1.06
NGC654	129.008	-0.359	4.80	Medhi et al. (2008)	9.6	2.92
IC1805	134.733	0.945	10.00	Medhi et al. (2007)	16.2	2.09
Alessi1	123.255	-13.330	13.00	Singh et al. (2020)	25.5	0.70

Czernik 3. Additionally, we identified five clusters within a 15° vicinity of Czernik 3 that have polarization measurements available. These clusters include IC 1805, NGC 654, Berkeley 59, NGC 457, and Alessi 1. Further details and relevant references can be found in Table 5.2.

5.2 Results of the polarization observations of Czernik 3

The polarimetric results of the 43 stars observed towards the Czernik 3 cluster in *Sloan i*-band are listed in Table 5.3. Serial number (ID) and astrometric positions (α_{J2000} & δ_{J2000}) obtained from *WCSTools* are given in columns 1, 2, and 3 respectively. Columns 4-12 represent the degree of polarization (P_{obs}), debiased degree of polarization (P), polarization angle (θ) (measured from north increasing towards east), normalized Stokes q, u parameters, and their respective errors ($\epsilon_P, \epsilon_\theta, \epsilon_q, \epsilon_u$). The maximum degree of polarization obtained in *Sloan i*-band is $5.89\% \pm 0.15\%$ with the polarization angle of $75^\circ.7 \pm 0^\circ.7$. The weighted average polarization (P) and polarization angle (θ) for the 39 stars considered for the analysis are 2.42% and 80° with a large dispersion 1.18% in P and $\sim 16^\circ$ in θ.

Table 5.3: Polarization observations towards Czernik 3. Details are in the text. ID with asterisk (*) marks the stars having polarization SNR < 3. These stars along with #13 (marked by **) are excluded from the analysis.

ID	$\alpha_{J2000}(^\circ)$	$\delta_{J2000}(^\circ)$	$P_{obs}(\%)$	$\epsilon_P(\%)$	P (%)	$\theta(^\circ)$	$\epsilon_\theta(^\circ)$	$q(\%)$	$\epsilon_q(\%)$	$u(\%)$	$\epsilon_u(\%)$
1*	15.73366	62.78726	0.87	0.28	0.82	76.0	9.4	-0.77	0.28	0.41	0.28
2	15.73596	62.80278	1.23	0.34	1.18	128.2	7.8	-0.29	0.34	-1.20	0.34
3	15.73702	62.80149	0.91	0.27	0.87	133.5	8.5	-0.05	0.27	-0.91	0.27
4	15.73735	62.79727	1.22	0.24	1.20	84.3	5.6	-1.20	0.24	0.24	0.24
5	15.74000	62.79577	1.05	0.26	1.02	73.0	7.0	-0.87	0.26	0.59	0.26
6	15.74345	62.79857	0.91	0.27	0.87	97.2	8.5	-0.88	0.27	-0.23	0.27
7*	15.74398	62.78652	0.40	0.25	0.31	75.8	17.6	-0.35	0.25	0.19	0.24
8	15.74801	62.79844	1.31	0.26	1.28	90.8	5.6	-1.31	0.26	-0.03	0.26
9	15.74874	62.79615	1.16	0.24	1.13	83.5	6.0	-1.13	0.24	0.26	0.24
10	15.75125	62.78201	2.42	0.20	2.41	67.1	2.4	-1.69	0.20	1.74	0.20
11	15.75418	62.78105	2.11	0.19	2.10	79.6	2.6	-1.97	0.19	0.75	0.19

Table 5.3 continued

12	15.75874	62.78557	2.01	0.21	2.00	74.0	2.9	-1.70	0.21	1.07	0.21
13**	15.76230	62.79320	1.83	0.18	1.82	87.0	2.8	-1.82	0.18	0.19	0.18
14	15.76590	62.80123	1.04	0.19	1.02	94.5	5.3	-1.03	0.19	-0.16	0.19
15	15.76660	62.78815	1.81	0.25	1.79	75.7	3.9	-1.59	0.25	0.87	0.25
16	15.76776	62.78504	3.29	0.15	3.29	76.4	1.3	-2.93	0.15	1.5	0.15
17	15.76883	62.77100	1.13	0.22	1.11	81.2	5.5	-1.08	0.22	0.34	0.22
18	15.76958	62.78195	1.72	0.25	1.70	78.0	4.1	-1.58	0.25	0.70	0.25
19	15.77562	62.78632	3.45	0.16	3.45	74.5	1.3	-2.95	0.16	1.78	0.16
20	15.77565	62.78210	4.25	0.15	4.25	75.9	1.0	-3.74	0.15	2.01	0.15
21	15.77981	62.78914	4.01	0.17	4.01	75.0	1.2	-3.47	0.17	2.00	0.16
22	15.78057	62.78682	1.83	0.27	1.81	75.6	4.2	-1.6	0.27	0.88	0.27
23	15.78078	62.80348	1.30	0.23	1.28	129.0	4.9	-0.27	0.22	-1.27	0.23
24	15.78158	62.77566	1.02	0.27	0.98	79.7	7.6	-0.96	0.27	0.36	0.27
25	15.78315	62.78855	2.41	0.22	2.40	76.8	2.6	-2.16	0.22	1.07	0.22
26	15.78333	62.78564	1.93	0.2	1.92	73.8	2.9	-1.63	0.20	1.03	0.20
27	15.78377	62.78163	5.89	0.15	5.89	75.7	0.7	-5.17	0.15	2.82	0.15
28	15.78449	62.77241	0.96	0.23	0.93	54.8	6.8	-0.32	0.23	0.91	0.23
29	15.78481	62.79230	1.16	0.27	1.13	86.4	6.8	-1.15	0.27	0.15	0.27
30	15.78491	62.78920	3.26	0.20	3.25	71.8	1.7	-2.62	0.20	1.93	0.20
31	15.78585	62.79087	3.01	0.17	3.00	80.3	1.6	-2.84	0.17	1.00	0.17
32	15.78646	62.78017	4.84	0.19	4.84	73.5	1.1	-4.06	0.19	2.64	0.18
33	15.78806	62.79425	1.92	0.18	1.91	81.1	2.7	-1.83	0.18	0.59	0.18
34	15.79002	62.77905	2.70	0.22	2.69	73.9	2.4	-2.28	0.22	1.44	0.22
35	15.79058	62.78262	1.66	0.25	1.64	75.4	4.4	-1.45	0.25	0.81	0.26
36	15.79107	62.78132	2.18	0.23	2.17	77.7	3.0	-1.98	0.23	0.90	0.23
37	15.79161	62.79209	3.49	0.15	3.49	78.5	1.2	-3.22	0.15	1.36	0.15
38	15.79319	62.78464	3.06	0.16	3.06	84.7	1.5	-3.0	0.16	0.56	0.16
39	15.79691	62.79186	3.22	0.21	3.21	82.8	1.8	-3.12	0.21	0.80	0.21
40	15.79764	62.80114	2.56	0.22	2.55	91.2	2.5	-2.56	0.22	-0.11	0.22
41	15.79963	62.78694	2.11	0.21	2.01	80.4	2.8	-1.99	0.21	0.70	0.21
42*	15.80062	62.78256	0.42	0.29	0.30	106.1	19.5	-0.36	0.29	-0.22	0.29
43	15.80225	62.80193	2.23	0.27	2.21	123.4	3.5	-0.88	0.27	-2.05	0.27

5.2.1 Sky projection and distribution of polarization

The sky projection of the 39 stars is overlaid on the PanSTARRS g-band image of the cluster using the standard convention: North at the top and East to the left in Figure 5.1. The length of each red-colored line segment is proportional to the degree of polarization, and the orientation corresponds to the polarization angle measured from the North celestial pole increasing in the direction of the Right Ascension (RA). A reference line segment of 5% polarization and 90° polarization angle is drawn on the bottom-right side of the figure. The dotted grid lines in the figure correspond to the equatorial coordinate system. The orientation of the Galactic plane at the location of the cluster, $b = -0^\circ.058$, has a position angle of $\theta_{GP} \sim 91^\circ$ (angle between the constant latitude lines with north celestial pole increasing eastwards) and is shown by a green dashed line from left to right. The dashed green line from top to bottom of the figure corresponds to the galactic longitude $\ell = 124^\circ.256$. These dashed lines intersect at the center of the cluster ($\alpha_{J2000} = 01^h03^m06^s.9; \delta_{J2000} = 62^\circ47'00''$) as determined by Sharma et al. (2020) .

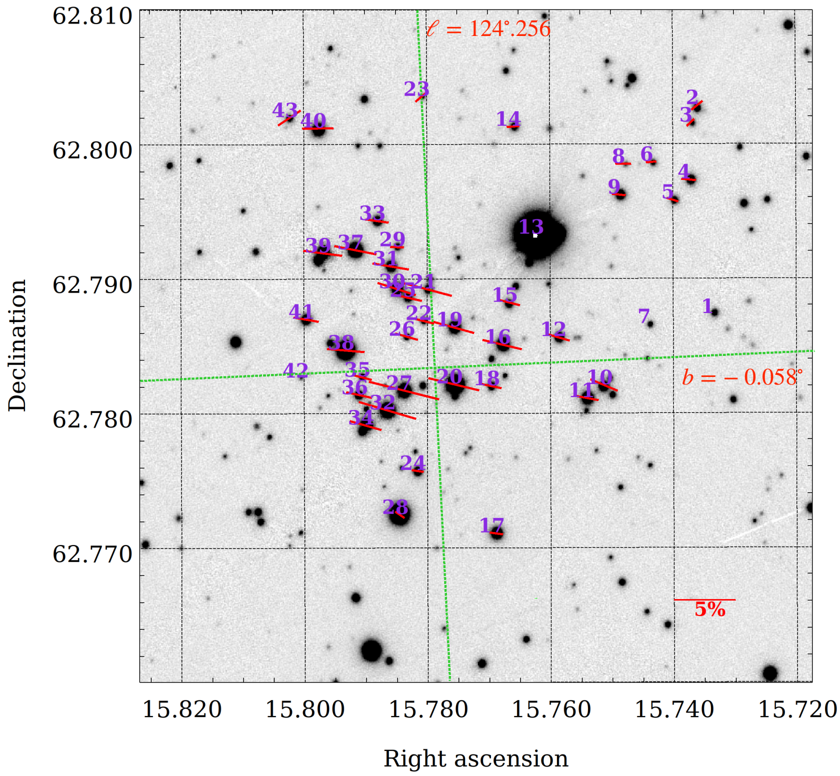

Figure 5.1: Polarization measurement of 39 stars towards the Czernik 3 open cluster superimposed on $3' \times 3'$ g-band image of PanSTARRS. Details are described in the text of Section 5.2.1.

Most of the stars in the field have polarization angles oriented at a small angle to the Galactic plane, while a few stars are showing a larger deviation. The stars with larger deviation have a slightly smaller degree of polarization (< 2.2 %) and maybe foreground objects. This is more clearly seen in the distribution of the polarization angle with the degree of polarization as shown in Figure 5.2. Based on visual inspection, we have divided the stars into three groups separated by dotted lines:

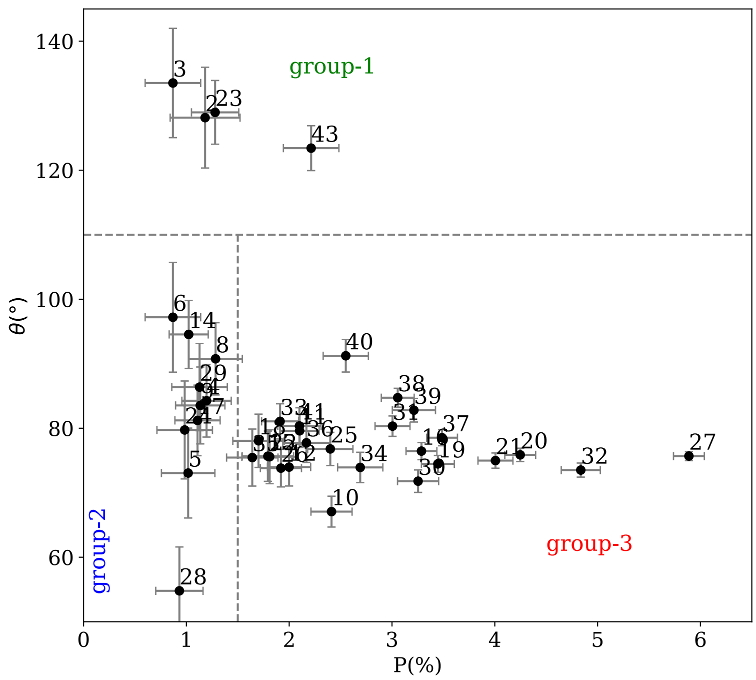

Figure 5.2: Polarization angle versus degree of polarization in *Sloan i*-band of 39 stars towards Czernik 3 cluster. The dashed lines are drawn to separate three groups in the observed sample - group-1 (green), group-2 (blue), and group-3(red).

1. The first group contains four stars #2, #3, #23, and #43 having degree of polarization ranging between $0.87\% < P < 2.21\%$ and polarization angle $123° < \theta < 133°$. The weighted mean polarization of this group is 1.39% with dispersion of 0.50%. The average polarization angle is $127° \pm 4°$ showing a large deviation from the Galactic plane. This indicates that the stars in this group may be non-members and or foreground stars.

2. The second group consists of all the stars on the left side of the vertical dotted line marking $P < 1.5\%$ (Figure 5.2). The stars present in this region have relatively smaller degrees of polarization ($0.87\% < P < 1.28\%$) with a weighted average value of 1.07% and dispersion of 0.12% but large spread in polarization angle ($55° < \theta < 97°$). The weighted average orientation of this group ($83° \pm 11°$) is nearly parallel to the Galactic plane (having a position angle of 91°). These stars are distributed randomly in the outer regions of the core of the cluster (on the plane of the sky) and maybe foreground stars.

3. The stars in the region with $P > 1.5\%$ (Figure 5.2) forms the third group. The

degree of polarization and polarization angle of stars in this group are ranging from $1.64\% < P < 5.89\%$ and $67° < \theta < 91°$ respectively. The average polarization is 2.97% with a dispersion of 1.04%. A large range in degree of polarization has been observed in many other clusters like Trumpler 27 (Feinstein et al., 2000), Hogg 22 and NGC 6204 (Martínez et al., 2004), NGC 5749 (Vergne et al., 2007), Berkeley 59 (Eswaraiah et al., 2012). The large spread in the degree of polarization could be due to several reasons, which are discussed in Section 4.1. The weighted average polarization angle of the stars in this group ($77° \pm 5°$) has a small offset from the orientation of the Galactic plane (91°). These stars are situated in relatively closer proximity to the cluster center, and their polarization angles exhibit a narrower range. This suggests a potential association with the cluster, making it likely be the cluster members.

5.2.2 Distribution of polarization in the Stokes plane

Polarization can be used as an efficient tool in determining the cluster membership even if the colors of the member stars and the field stars are the same. The light from an intrinsically unpolarized star becomes partially polarized after passing through the asymmetrical but aligned dust grains present in the dust clouds of the ISM. The degree of polarization depends on the column density of aligned dust grains along the line of sight. Stars located foreground of the dust cloud will be less polarized as compared to the stars behind the dust layers. Also, the polarization angle of the two may differ from each other depending upon the direction of the local magnetic field. It is expected that all the member stars are behind a common set of intervening clouds. Therefore, their polarization properties are expected to be similar, while the field stars may have slightly different properties. The distribution of the stars in the Stokes qu-plane (with $q = P\cos 2\theta$ and $u = P\sin 2\theta$) is useful to distinguish the cluster members from the non-members. The members of the cluster are expected to group together in this plane, while the field stars would show scattered distribution. However, intrinsic polarization, rotation of polarization angle, and patchy extinction can also give rise to the scattered distribution in the qu-plane.

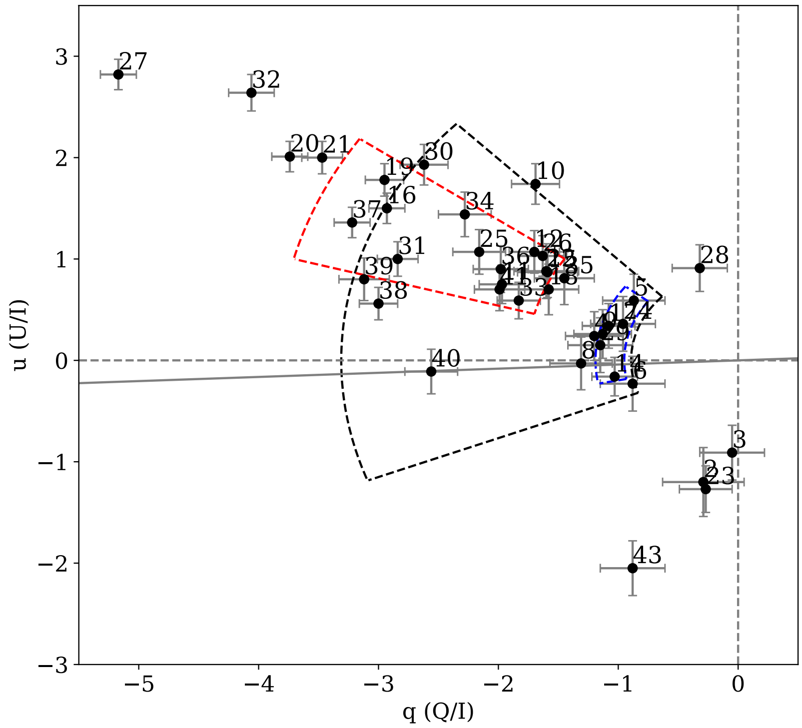

Figure 5.3: Distribution of the 39 observed stars in the qu plane. The dotted line crossing at $q = u = 0$ denotes the dustless solar neighborhood, and the solid gray line represents the Galactic parallel. The Black dashed box is the 1 sigma boundary of all the stars observed with mean polarization $2.22\% \pm 1.16\%$ and angle $84° \pm 16°$. 1σ box corresponding to mean degree of polarization ($0.93\% \pm 0.29\%$, $2.80\% \pm 1.04\%$) and polarization angles ($82° \pm 11°$, $77° \pm 5°$) of group-2 (region 2) and group-3 (region 3) of Figure 5.2 are shown as boxes of blue and red dotted lines respectively.

The normalized q ($q = Q/I$) and u ($u = U/I$) Stokes parameters are derived for all the observed stars and are plotted in Figure 5.3. The cross-section of dashed straight lines at $q = u = 0$ represents the dustless solar neighborhood, and the solid gray line corresponds to the Galactic plane ($\sim 91°$). The stars, on average, show a scattered distribution in the $q - u$ plane, which is expected for distant clusters because of the contamination by a large number of foreground and/or background field stars. This has also been seen in Stock 6, NGC 1893 (Eswaraiah et al., 2011), and Berkeley 59 (Eswaraiah et al., 2012) clusters. It is difficult to identify the grouping of member stars in such cases. We draw 1σ box (black dashed box in Figure 5.3) with boundaries of mean $P \pm \sigma_P$ and $\theta \pm \sigma_\theta$ to elucidate the probable cluster members. All the stars within this box are considered as probable members, and stars scattered away from the mean 1σ box may have less membership probability. The q, u for groups 2 and 3 (as described in Section 5.2.1) range from $-1.31 \leq q \leq -0.32$; $-0.23 \leq u \leq 0.91$ and $-5.17 \leq q \leq -1.45$; $-0.11 \leq u \leq 2.82$ respectively. To check the distribution of stars in these regions, we plotted the mean 1σ box corresponding to these two groups in blue (region 2) and red dotted lines (region 3), respectively, in Figure 5.3. The blue-dotted region is closer to the Sun and is expected to consist of the foreground stars. In contrast, the member stars may be present in Region 3. The stars outside the 1σ boxes are either field stars or have an intrinsic component of polarization.

The $q-u$ plot is also helpful in studying the evolution of the interstellar environment from the Sun to the cluster. The two regions are separated by a gap suggesting two dust layers present between the Sun and the cluster. The first layer affects only the stars of Region 2. The stars of Region 3 exhibit a cumulative effect of both dust layers in their polarization. More details of the membership are provided in Section 5.3.1.

5.3 Discussion

In the first subsection (5.3.1), we redefine the cluster membership based on the Gaia EDR3 astrometry compared to the polarization and photometry. Subsection 5.3.2 discusses the possible explanations for the large range in the polarization of the 39 stars observed towards the core of the Czernik 3 cluster in combination with different archival data. Dust distribution towards the Czernik 3 cluster is described in subsection 5.3.3. The general trend of polarization and its implications regarding the dust distribution over a large spatial range is in subsection 5.3.4.

5.3.1 Cluster membership

Identifying member stars is important to determine reliable cluster parameters like cluster radius, age, and distance. In the past, photometry and polarization have been used to identify cluster members (Eswaraiah et al., 2011, 2012, etc.). A detailed discussion

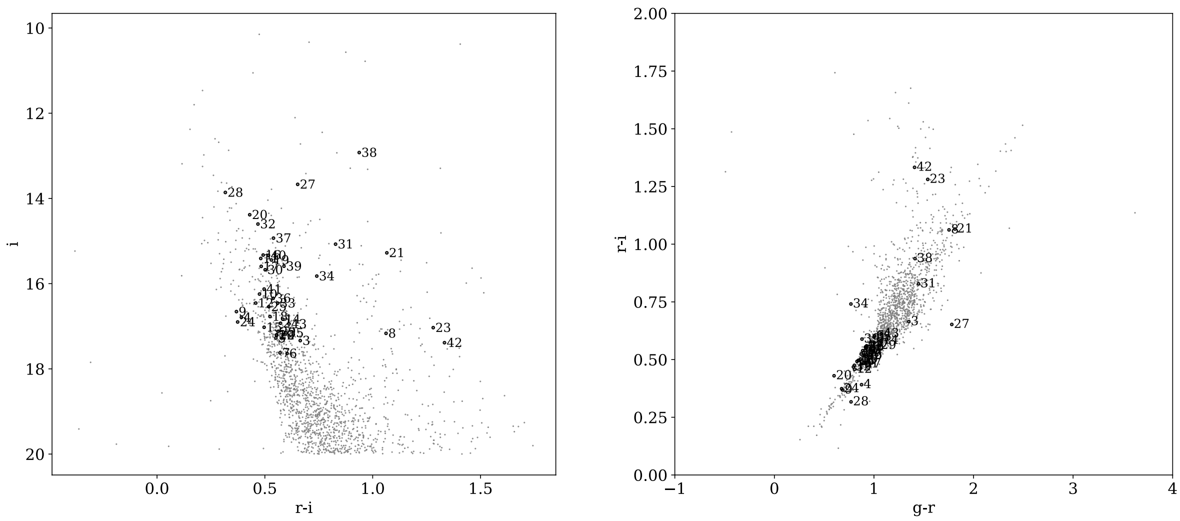

(a) CMD (r-i versus i) (b) CC diagram (g-r versus r-i in (b))

Figure 5.4: CMD (panel a) and CC diagram (panel b) using PanSTARRS data. The small dots (gray color) represents the $10' \times 10'$ field towards the Czernik 3 cluster. Black points with labels are the stars having polarization observations.

of cluster membership for Czernik 3, on the basis of polarization and photometry, is described in Section 5.3.1.1. With the availability of Gaia data, the astrometric approach is being widely used nowadays for determining cluster membership. The cluster membership based on Gaia DR3 data is presented in Section 5.3.1.2.

5.3.1.1 Photometric and polarimetric approach

All the member stars are expected to be located behind the common dust clouds. Thus, the color excess of the member stars should be comparable to the mean color excess of the cluster. In comparison, the field stars suffer varying extinction based on whether they are present foreground or background of the cluster. Medhi & Tamura (2013) have shown that the color-color (CC) diagram, together with the polarization, can be used to distinguish the cluster members from the field stars.

We now consider the stars in the $q-u$ plane of Figure 5.3 in the context of their PanSTARRS magnitudes and colors. The PanSTARRS apparent CMD and CC diagram for a $10' \times 10'$ region around the cluster is shown in Figure 5.4a and 5.4b. The ID of the stars listed in Table 5.3 are labeled in these two figures. The group-1 stars(#2, #3, #23, and #43) of Figure 5.2 have polarization angle larger than that of the Galactic plane and lie outside the mean 1σ box on qu plane (Figure 5.3) with range of $-0.8 < q < -0.4$ and $-2.0 < u < -0.9$. Stars #3 and #23 show more reddening (see Figure 5.4a and 5.4b) than the bulk of the stars. Hence, these two stars are not member stars according to both approaches (photometric and polarimetric). Though the color of stars #2 and #43 are similar to the member stars, their location in the qu plot and their position angle values indicate deviation from the polarization angle of member stars. Hence, these stars are also considered as non-members. Star #28 has q > -0.5 (outside mean 1σ box in Figure 5.3) just like #2, #3, and #23 and have large errors associated with their polarization values. It has a low value of polarization - 0.93% $\pm$ 0.23% and polarization angle 54.8 $\pm$ 6.8 which is quite different from the rest of the stars. This indicates that #28 could be a foreground star, which is consistent with a relatively bluer color r-i = 0.31 and a Gaia EDR3 distance of 409 pc. In addition, stars #27 and #38 are reddened in color (see Figure 5.4a and 5.4b). Star #27 shows the highest polarization (5.89% $\pm$ 0.15%) in our data set while the polarization angle ($75^\circ.7 \pm 0^\circ.7$) is similar to the member stars (group 3 stars). It may be a member star having some intrinsic component of polarization. On the other hand, Star #38 is outside the mean 1σ boundary of group 3 in $q-u$ plane (see Figure 5.3) and shows a deviation in polarization angle ($84^\circ.7 \pm 1^\circ.5$) from mean polarization angle of group 3 stars. It is highly probable that this star may also have intrinsic polarization. Discussion about its cluster membership is deferred to Section 5.3.1.2. The rest of the distribution in the $q-u$ plane is scattered; however, region 3 of Figure 5.3 contains the most probable cluster members.

Considering only the photo-polarimetric approach, the contribution to the cluster membership by the field stars can be overestimated if a common dust layer is situated foreground of the field stars and the cluster members. Hence, polarization alone cannot be used to estimate the membership probability of distant open clusters.

5.3.1.2 Astrometric approach

The proper motion can also be used to evaluate cluster membership. We have used parallax and proper motion information from Gaia EDR3 catalog[3]. Figure 5.5 shows the

[3]http://vizier.u-strasbg.fr/viz-bin/VizieR-3?-source=I/350/gaiaedr3

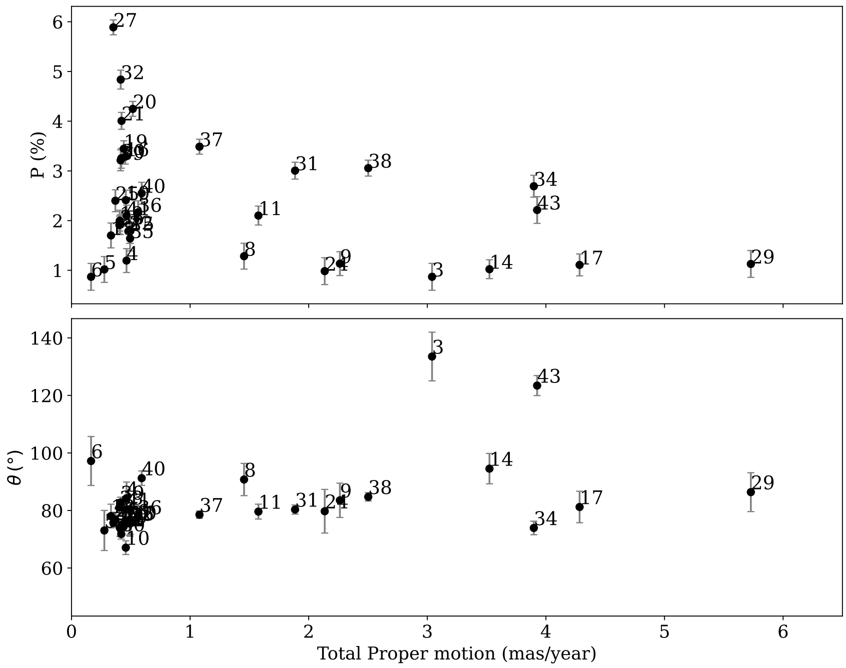

Figure 5.5: Observed polarization as a function of the total proper motion of stars observed towards the Czernik 3 cluster. Two stars (#23 and #28) are excluded from this plot having PM > 10 mas/yr.

proper motion (PM) versus the degree of polarization (upper panel) and polarization angle (lower panel) of 39 stars listed in Table 5.3. There is a prominent clump around the proper motion of ~ 0.5 mas/year. Two stars #23 and #28 are not shown in the figure because they have proper motion > 10 mas/year and are non-members from polarization and photometric methods also (see Section 5.3.1.1). According to the proper motion distribution, 23 stars - #4, #5, #6 #10, #12, #15, #16, #18, #19, #20, #21, #22, #25, #26, #27, #30, #32, #33, #35, #36, #39, #40, and #41 have higher membership probability than the other stars in the field showing scattered distribution in proper motion.

All the probable member stars (from Figure 5.5) except star #6 and #20 are also identified as members with probability ≥ 80% (see column 4 of Table 5.4) using proper motion and parallax information of Gaia DR2 in UPMASK membership assignment code by Cantat-Gaudin et al. (2018). On the other hand, Sharma et al. (2020) have selected the stars with high probability (≥ 90%) of membership based on the frequency distribution of member stars and field stars using Gaia DR2 proper motion information and have only 17 stars common with probable members from Figure 5.5 (see column 5 of Table 5.4). This has resulted in discrepancies in membership for individual stars between the two studies.

We have used the latest Gaia proper motion (PM) data (from Gaia EDR3) to redefine the membership probability. PMs, $\mu_\alpha \cos\delta$ and μ_δ are plotted as vector point diagrams (VPDs) in the top row of Figure 5.6 to see the distribution of cluster members and field stars towards the region of Czernik 3. The bottom row of this figure shows the corresponding G versus $(G_{BP} - G_{RP})$ CMDs. The left panel in the CMD shows all the stars present within a five arcmin radius around Czernik 3, while the middle and right panels show the possible cluster members and field stars, respectively. By visual inspection, we define the cluster center and radius in the VPD iteratively to reduce the contamination by the field stars while keeping a possible number of faint stars in the cluster sequence (middle panel of the CMD). A circle of 0.5 mas yr^{-1} around the center of the member stars distribution in the VPDs indicates our membership zone. We can see in the middle-bottom panel that the cluster's main sequence is separated.

To identify the cluster members quantitatively, we have estimated the membership probabilities of the stars following the method given by Balaguer-Núnez et al. (1998). Many authors have previously used this method (Bellini et al., 2009; Sharma et al., 2020; Bisht et al., 2021; Sariya et al., 2021). Two distribution functions (ϕ_c^ν) and (ϕ_f^ν) for cluster and field stars are constructed for a particular ith star, which is given as follows:

$$\phi_c^\nu = \frac{exp\left\{-\frac{1}{2}\left[\frac{(\mu_{xi}-\mu_{xc})^2}{\sigma_c^2+\epsilon_{xi}^2}+\frac{(\mu_{yi}-\mu_{yc})^2}{\sigma_c^2+\epsilon_{yi}^2}\right]\right\}}{2\pi\sqrt{(\sigma_c^2+\epsilon_{xi}^2)(\sigma_c^2+\epsilon_{yi}^2)}} \tag{5.2}$$

$$\begin{aligned}\phi_f^\nu = {} & \frac{1}{2\pi\sqrt{(1-\gamma^2)}\sqrt{(\sigma_{xf}^2+\epsilon_{xi}^2)(\sigma_{yf}^2+\epsilon_{yi}^2)}}\times \\ & exp\left[-\frac{1}{2(1-\gamma^2)}\left(\frac{(\mu_{xi}-\mu_{xf})^2}{\sigma_{xf}^2+\epsilon_{xi}^2}-\right.\right. \\ & \left.\left.\frac{2\gamma(\mu_{xi}-\mu_{xf})(\mu_{yi}-\mu_{yf})}{\sqrt{(\sigma_{xf}^2+\epsilon_{xi}^2)(\sigma_{yf}^2+\epsilon_{yi}^2)}}+\frac{(\mu_{yi}-\mu_{yf})^2}{\sigma_{yf}^2+\epsilon_{yi}^2}\right)\right]\end{aligned} \tag{5.3}$$

where, (μ_{xi}, μ_{yi}) are the PMs of i^{th} star. The PM errors are represented by $(\epsilon_{xi}, \epsilon_{yi})$. The

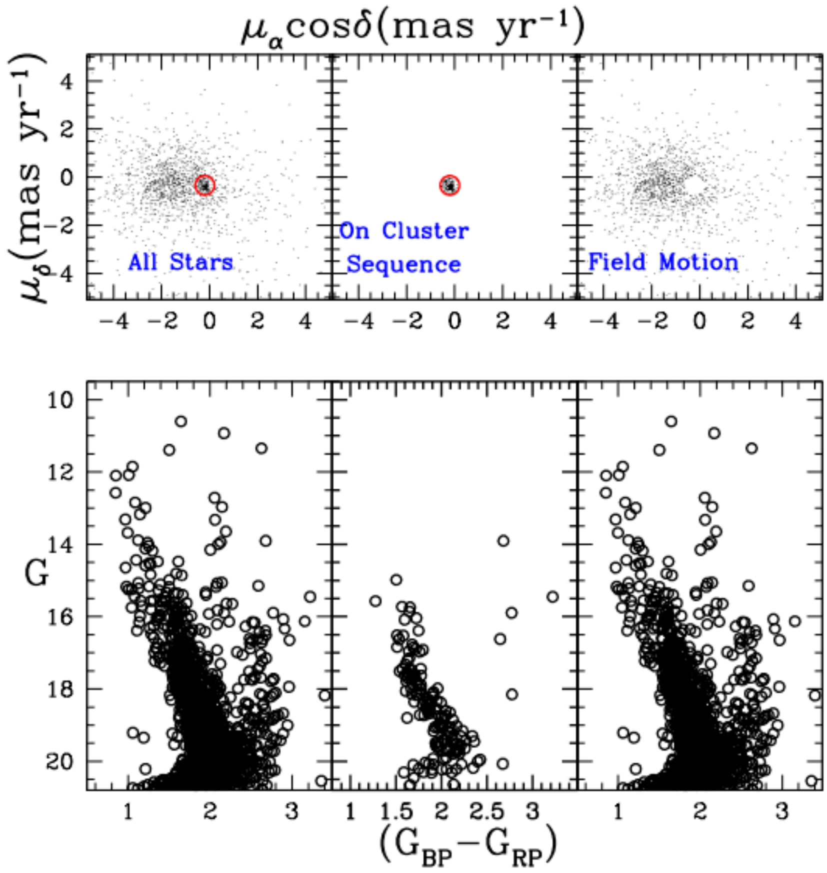

Figure 5.6: (Top row) vector point diagrams for cluster Czernik 3. (Bottom row) G versus $(G_{BP} - G_{RP})$ color-magnitude diagrams. (Bottom left panel), The entire sample. (Bottom middle panel) Stars within the circle of 0.5 $mas\ yr^{-1}$ radius. (Bottom right panel) Probable background/foreground field stars in the direction of the cluster Czernik 3.

cluster's PM center, given by (μ_{xc}, μ_{yc}) and (μ_{xf}, μ_{yf}) represents the center of field PM values. The intrinsic PM dispersion for the cluster stars is denoted by σ_c, whereas σ_{xf} and σ_{yf} provide the intrinsic PM dispersions for the field populations. The correlation coefficient γ is calculated as:

$$\gamma = \frac{(\mu_{xi} - \mu_{xf})(\mu_{yi} - \mu_{yf})}{\sigma_{xf}\sigma_{yf}} \tag{5.4}$$

In order to estimate the probability of Czernik 3 star, we used only stars having PM errors better than ∼1 mas yr^{-1}. We found a clear bunch of stars at $\mu_{xc} = -0.22$ mas yr^{-1}, $\mu_{yc} = -0.32$ mas yr^{-1} and in the circular region with a radius of 0.5 mas yr^{-1} (Figure 5.6).

We estimated dispersion (σ_c) in PMs as 0.06 mas yr^{-1} by using cluster distance of 3.5 kpc (Sharma et al., 2020) and the radial velocity dispersion of 1 km s^{-1} for open star clusters (Girard et al., 1989). For field region stars, we have estimated (μ_{xf}, μ_{yf}) = (−0.95, −0.55) mas yr^{-1} and (σ_{xf}, σ_{yf}) = (6.5, 4.4) mas yr^{-1}.

In consideration of the normalized numbers of cluster and field stars as n_c and n_f respectively (i.e., $n_c + n_f = 1$), the total distribution function can be estimated as

$$\phi = (n_c \times \phi_c^{\nu}) + (n_f \times \phi_f^{\nu}), \tag{5.5}$$

Finally, the membership probability for the i^{th} star is given by

$$P_{\mu}(i) = \frac{\phi_c(i)}{\phi(i)}. \tag{5.6}$$

We obtain 72 cluster members in Czernik 3 cluster with membership probability higher than 90% and $G \leq 18.5$ mag.

The stellar density of the cluster region is affected by the presence of field region stars. So, we have calculated the effectiveness of membership determination for Czernik 3 using the formula given in eq. (5.7) (Shao & Zhao, 1996):

$$E = 1 - \frac{N \times \Sigma[P_i(1-P_i)]}{\Sigma P_i \Sigma(1-P_i)} \tag{5.7}$$

where, N is the total number of cluster members and P_i, indicates the probability of i^{th} star of the cluster. The effectiveness (E) value is obtained as ~ 0.70 for Czernik 3. Shao & Zhao (1996) shows that the effectiveness of membership determination of 43 open clusters ranges from 0.20 to 0.90 with the peak value of 0.55. Our estimated value is on the higher side but lies within the above limits. The mean distance of the Czernik 3 cluster is calculated using the distance information (Bailer-Jones et al., 2021) of the member stars present in the core (0.5′, Sharma et al., 2020) of the cluster. The average distance of the core members comes out to be 3.6 ± 0.8 kpc, which matches well with the distance determined by Sharma et al. (2020) using Gaia DR2 data. The membership probability of the observed stars is given in column 6 of Table 5.4.

Table 5.4: Czernik 3 cluster members with membership probabilities (MP) from literature (columns 4 and 5) and our study (column 6) with IDs (column 1) and polarization measurements (columns 2 and 3). Asterisk (*) and double asterisk (**) IDs represents the member YSO candidates selected from Marton et al. (2019) and Q-parameter method discussed in the Section 5.3.2.3

ID	$P \pm \epsilon_P$ (%)	$\theta \pm \epsilon_\theta$ (°)	MP (%) (Cantat-Gaudin et al., 2018)	MP (%) (Sharma et al., 2020)	MP (%) (our study)
4	1.20 ± 0.24	84 ± 6	100	-	99.61
5**	1.02 ± 0.26	73 ± 7	90	-	99.93
6	0.87 ± 0.27	97 ± 8	-	90	99.72
10*	2.41 ± 0.20	67 ± 2	100	100	99.9
12**	2.00 ± 0.21	74 ± 3	80	99	99.43
15	1.79 ± 0.25	75 ± 4	100	99	99.93
16	3.29 ± 0.15	76 ± 1	100	100	99.97
18	1.70 ± 0.25	78 ± 4	100	100	99.94
19*	3.45 ± 0.16	74 ± 1	100	100	99.98
20	4.25 ± 0.15	76 ± 1	-	100	99.66
21	4.01 ± 0.17	75 ± 1	80	-	99.76
22	1.81 ± 0.27	76 ± 4	100	100	99.88
25**	2.40 ± 0.22	77 ± 3	100	100	99.95
26	1.92 ± 0.20	74 ± 3	80	-	99.96
27	5.89 ± 0.15	76 ± 1	100	99	99.83
30**	3.25 ± 0.20	72 ± 2	100	100	99.97
32	4.84 ± 0.19	73 ± 1	100	100	99.97
33	1.91 ± 0.18	81 ± 3	100	-	99.64
35	1.64 ± 0.25	75 ± 4	90	99	99.89
36	2.17 ± 0.23	78 ± 3	100	100	99.80
39	3.21 ± 0.21	83 ± 2	100	100	99.98
40*	2.55 ± 0.22	91 ± 2	100	-	98.52
41	2.01 ± 0.21	80 ± 3	100	99	99.96

A similar procedure is adopted to redefine the membership of the clusters IC 1805, NGC 654, Berkeley 59, NGC 457, and Alessi 1 using Gaia EDR3 data. From the revised cluster membership, the mean distance of each cluster is constrained to be 2.55 ± 0.89, 2.89 ± 0.72, 1.21 ± 0.73, 2.87 ± 0.72, and 0.72 ± 0.17 kpc respectively. These values closely match with the average distance of the respective clusters in Cantat-Gaudin et al. (2018) (see Table 5.2).

To compare both methods for cluster membership determination, we calculated the success rate of membership determination from polarization in comparison to the astrometric method. The analysis yielded a success rate of only 58.3% for the polarization with respect to the astrometric approach. The photo-polarimetric approach would work best if all the member stars are present behind the same dust clouds. The 53% success rate for the photo-polarization approach indicates that the light from the cluster members may pass through different clouds that may not be uniformly distributed across the face of the cluster.

5.3.2 On the variation of polarization over the Czernik 3 cluster

In this section, we discuss the possible reasons for the large range in polarization observed over the stars of the Czernik 3 cluster, as shown in Figure 5.2.

5.3.2.1 Patchy dust distribution from WISE W4 image

Large dispersion in polarization values (Figure 5.2) could be due to the patchy distribution of dust along the line of sight towards the Czernik 3 cluster or because of the presence of dust within the cluster. This is further examined by analyzing 22μm, WISE W4-band image[4]. Figure 5.7 shows the spatial distribution of dust (integrated emission along the line of sight) traced by the WISE W4 band in 3′ field around Czernik 3. The red color contours represent the equal flux density points. Patchiness is well observed from the contour levels varying from 113.02 DN to 113.508 DN with an interval of 0.054 DN. The uncertainty levels are ~ 0.04 DN. This implies that the dust is not distributed

[4]https://irsa.ipac.caltech.edu/applications/wise/

uniformly. It may be constant in small spatial areas but is highly variable across the face of the cluster. For example, the central region of the cluster has a higher flux density. Higher polarization in the same region is also observed, as seen by the length of the white-colored polarization measurements centered at the star location. This is further discussed in Section 5.3.2.4. Cyan and blue-colored open circles in the figure denote the member and non-member stars, respectively. The patchy distribution has also been observed earlier in NGC 6823 open cluster embedded in the highly extincted region towards the inner Galaxy (Medhi et al., 2010).

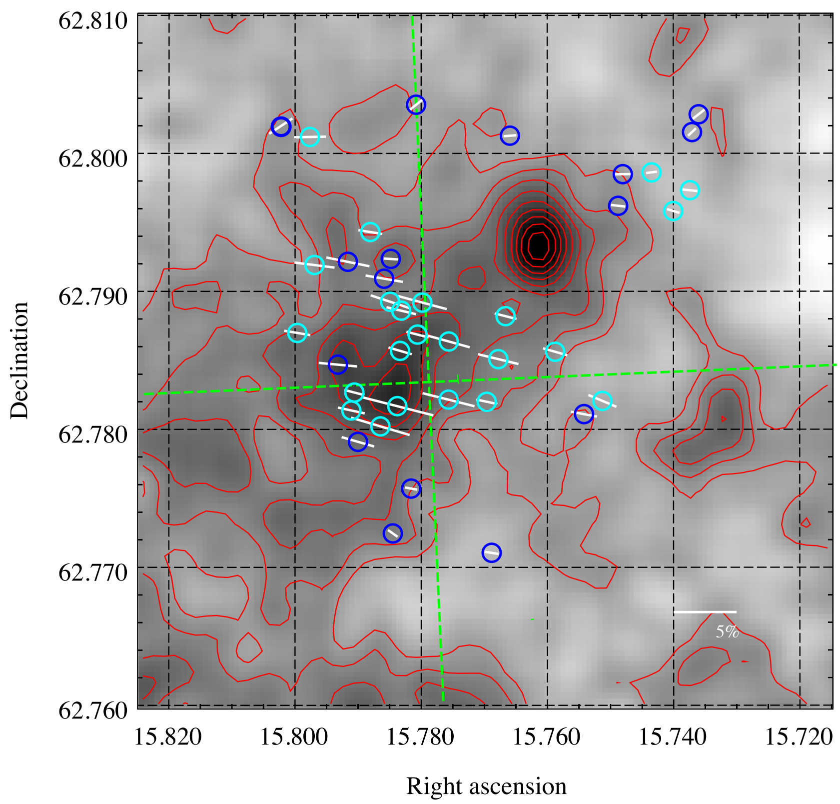

Figure 5.7: WISE W4 integrated intensity map of 3′ region around Czernik 3 with ten contour levels between 113.02-113.508 DN at the interval of 0.054 DN. Polarization measurements are denoted by white colored lines. The cyan and blue circles centered at the star location represent the members and non-member stars, respectively. The green dashed lines correspond to the Galactic coordinate grid passing through the center of the cluster.

Stars #4, #5, and #6 have low polarization $1.20\% \pm 0.24\%$, $1.02\% \pm 0.26\%$, and $0.87\% \pm 0.27\%$ with large uncertainty in the polarization angle ($84^\circ.3 \pm 5^\circ.6$, $73^\circ.0 \pm 7^\circ.0$, and 97° ± 8°). Even though these stars are present in the 1σ box of group-2 (Figure 5.3), their proper motion data categorizes them as member stars with high membership probability (> 99.5%). The low value of the polarization can be explained by the lesser dust column density traversed by the light coming from these stars, as seen by the contour level being ≤ 113.02 DN. On the contrary, the core region stars #21, #27, and #32 show large degrees of polarization (4.01 ± 0.17%, 5.89 ± 0.15 and 4.84 ± 0.19%) because of higher dust density at the central region as compared to the peripheral region. The proper motion and polarization angle (75°.0 ± 1°.2, 75.7° ± 0°.7 and 73.5 ± 1°.1) of these stars are similar to the member stars but lying outside region 3 in qu-plot (Figure 5.3), which may be due to non-uniform dust distribution.

5.3.2.2 Polarization efficiency

The degree of polarization produced for a given amount of extinction is referred to as the polarization efficiency of the intervening dust grains. It is known that the polarization efficiency of the ISM is non-uniform. This can be seen from the large scatter in Figure 5.8, which shows the relation between color excess and i-band polarization for the stars observed by us along the line of sight of the Czernik 3 cluster. The efficiency depends on the degree of alignment of the dust grains with the magnetic field, the inclination of the magnetic field with the line of sight, and the amount of depolarization due to radiation traversing more than one cloud with different magnetic field directions. The updated empirical upper limit (Panopoulou et al., 2019) for maximum polarization efficiency of diffuse ISM at visual wavelengths assuming $R_V = 3.1$ (Seaton, 1979) is given by

$$\frac{P_V}{E_{B-V}} < 13.0\,\%\, mag^{-1} \tag{5.8}$$

The polarization efficiency in *Sloan* *i*-band ($\lambda_{eff} = 0.767\mu m$) is determined using Serkowski's law for interstellar polarization by assuming maximum polarization at average wavelength $\lambda_{max} \sim 0.55\mu m$ with K= 1.15 (Whittet, 2003) and is given by eq. (5.9) (dashed line in Figure 5.8).

$$\frac{P_i}{E(B-V)} < 11.5\,\%\, mag^{-1} \tag{5.9}$$

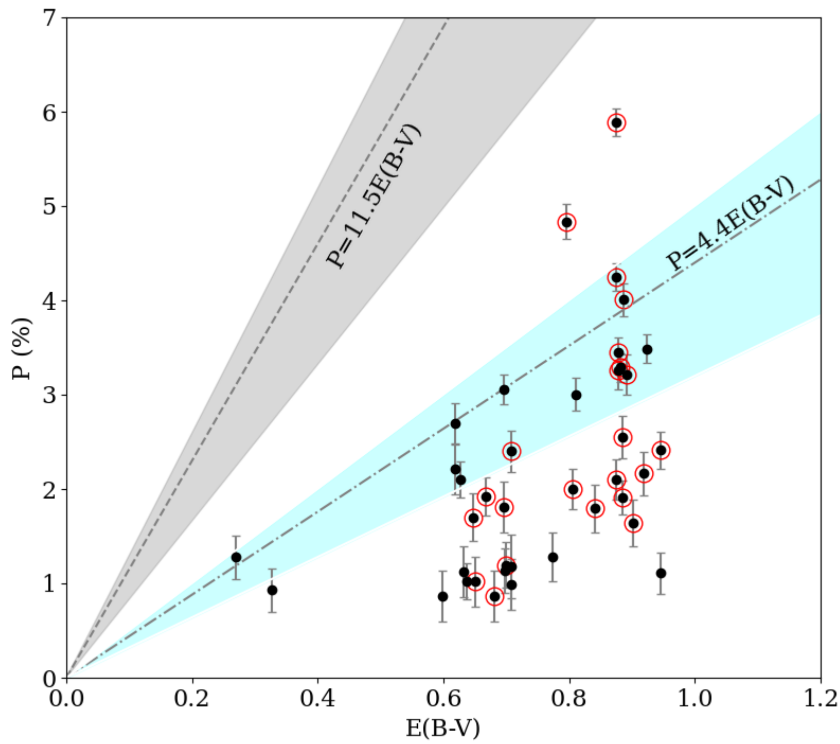

Figure 5.8: Polarization efficiency towards Czernik 3 cluster. Two gray lines: dashed and dashed-dotted represent the empirical upper limit and the average value for the diffuse ISM respectively in *Sloan i*-band using λ_{max} = 0.55 μm and K = 1.15. See the text for further details on the shaded regions.

However, the λ_{max} varies from star to star and has a typical range of $0.3\mu m - 0.8\mu m$ (Whittet, 2003). Many studies (e.g, Wilking et al., 1980, 1982; Clayton et al., 1995; Martin et al., 1999) have shown that the λ_{max} and K are linearly correlated by the Wilking law:

$$K = C_1 \, \lambda_{max} + C_2 \tag{5.10}$$

Where the constants C_1 and C_2 are given by 1.66 ± 0.01 μm^{-1} and 0.01 ± 0.05 in visible to near-infrared (VIR) wavelength regime ($0.35\mu m \leq \lambda \leq 2.2\mu m$) (Whittet, 1992). In order to explore the effect of polarization efficiency in the *Sloan i*-band, we have considered $0.3\mu m \leq \lambda_{max} \leq 0.8\mu m$ and eq. (5.10) for the K values, in the Serkowski law of interstellar polarization. The resulting broad range of empirical relations covers an area demarcated by a light grey colored region in Figure 5.8. The polarization efficiency of the diffuse ISM, in general, follows the mean relation $P_{max} = 5\ E(B-V)$ (Serkowski et al., 1975). The corresponding *Sloan i*-filter polarization as a function of E(B-V) is calculated to be

$P_i = 4.4\ E(B-V)$ and it is shown by dash-dotted line (with λ_{max} = 0.55 μm, K=1.15) and cyan shaded region (corresponding to the range in λ_{max}) in the same figure. The observed polarization efficiency towards the cluster is less than the empirical upper limit defined by the light grey-shaded region described earlier. A few stars (member as well as non-member) are showing efficiency more than the general diffuse ISM considering varying λ_{max} as seen from their appearance above the lower limit of the cyan-shaded region. Out of these, two stars (#27 and #32) are lying above the maximum of the cyan-shaded region, indicating different polarization behavior as compared to the diffuse ISM. These two stars are near the center of the cluster, where there is an excess of dust (see the discussion in Section 5.3.2.1). It is also possible that they are both intrinsically polarized (see the discussion in Section 5.3.2.3) for example, #27 is an evolved (probable AGB) star where one may expect intrinsic polarization due to an asymmetric dust shell.

5.3.2.3 Intrinsic polarization

Stars having circumstellar dust can show intrinsic polarization, which may be different from interstellar polarization. Young stellar objects and evolved stars are the possible candidates to show intrinsic polarization. Recently, Marton et al. (2019) classified stars into four categories, i.e., extincted main sequence stars, evolved stars, extra-galactic sources, and young stellar objects using machine learning techniques by considering Gaia DR2 and ALLWISE data. We have found entries for 10 of our observed stars in this catalog[5]. The probabilities of each category with their errors are listed in Table 5.5. We have opted to use their probability columns which do not consider the W3 and W4 band fluxes since the 'R' parameter (first column in the Table 5.5), which represents the probability for W3 and W4 detections to be real, is less than 75% for all 10 stars. From Table 5.5, seven stars (#3, #10, #17, #19, #23, #28, and #40) are highly probable YSO candidates, out of which #10 #19 and #40 (with underlined ID) are cluster members and stars #27 and #38 have a high probability of being evolved stars.

YSO candidates can also be identified using reddening parameter Q. The stars are considered as a candidate young stellar object if the reddening-free parameter Q

[5] https://vizier.u-strasbg.fr/viz-bin/VizieR?-source=II/360

Table 5.5: Probability of source being Evolved (SE), Extra-galactic (SEG), Main sequence (SMS), or YSOs (SY) with their errors from the catalog by Marton et al. (2019). R - the probability that the W3 and W4 detections are real. The probabilities are written in bold for the most probable category, and the IDs of the member stars are underlined.

ID	R	SE	ϵ_{SE}	SEG	ϵ_{SEG}	SMS	ϵ_{SMS}	SY	ϵ_{SY}
3	0.378	0.0784	0.04382	0.1492	0.06497	2.0E-4	6.3E-4	**0.7722**	0.09265
<u>10</u>	0.448	0.0768	0.03213	0.2426	0.11013	0.0236	0.06561	**0.657**	0.10294
17	0.438	0.0572	0.0351	0.0664	0.04666	0.0094	0.01276	**0.867**	0.07939
<u>19</u>	0.278	0.0704	0.0182	0.0848	0.02443	0.0048	0.00492	**0.84**	0.03307
23	0.43	0.1234	0.06507	0.0482	0.01853	0.0012	0.0038	**0.8272**	0.07272
<u>27</u>	0.646	**0.6674**	0.08052	0.0076	0.0044	0.0112	0.01237	0.3138	0.07726
28	0.348	0.2232	0.03774	0.0172	0.01084	0.0336	0.01622	**0.726**	0.04233
38	0.65	**0.9118**	0.04445	0.0224	0.02948	0.0084	0.00858	0.0574	0.01718
<u>40</u>	0.45	0.101	0.03923	0.0576	0.02965	0.0058	0.00577	**0.8356**	0.04639

becomes less than −0.05 (Buckner & Froebrich, 2013). The Q value can be estimated for a star using the VVV photometric magnitude relationship given by

$$Q = (J - H) - 1.55 \times (H - K) \tag{5.11}$$

We used the 2MASS photometric values for our stars transformed to VVV using transformation equations of 1.5 version of CASU photometry (González-Fernández et al., 2018) to obtain the Q parameter. We find 5 candidate YSOs (#5, #12, #24, #25, #30) using the above relation of which #5, #12, #25, and #30 are cluster members.

Thus, in total 7 member YSOs candidates have been detected in Czernik 3. The intrinsic polarization due to the circumstellar disk can be a cause of scattered position in the qu-plane for some of these stars. These stars are marked with an asterisk and double asterisk in the ID column of Table 5.4.

5.3.2.4 Spatial variation of polarization

The first two panels of Figure 5.9 show the variation of the degree of polarization and polarization angle with angular distance from the center of the cluster. The angular distance of a star having equatorial coordinates (α, δ) from the center of the cluster (α_c, δ_c) is given by the eq. (5.12).

$$d = 2sin^{-1}\left\{\sqrt{sin^2\frac{|\delta - \delta_c|}{2} + cos\delta\; cos\delta_c\; sin^2\frac{|\alpha - \alpha_c|}{2}}\right\} \tag{5.12}$$

The third panel represents the WISE W4 flux (in Jy) as a function of angular distance. This flux is obtained by using aperture photometry on the position of the stars using a fixed aperture. A decrease is seen in the WISE flux as well as the degree of polarization radially outwards. The polarization angle exhibits a very small dispersion in the core region (core radius = 0.5′, Sharma et al., 2020, marked by a dashed line) while the dispersion increases in the outer directions. This suggests that the dust is more concentrated towards the center and the density decreases with the radial distance from the cluster center. The small dispersion in polarization angle with an increased degree of polarization also indicates that the dust in the cluster is oriented in the same direction as the dust in the interstellar medium. This implies that the dust in the cluster seems to be relaxed with reference to the interstellar magnetic field i.e., the dust grains in the cluster are magnetically aligned with the large-scale magnetic field at the location of the cluster.

5.3.3 Dust distribution towards Czernik 3

The polarization value changes when light from the stars encounters dust layers at different distances in the line of sight. The degree of polarization increases after passing through each dust layer if the orientation of the magnetic field is uniform in all dust clouds and becomes depolarized if the orientation of the magnetic field is different. The number of such changes in the degree of polarization as well as in extinction corresponds to the number of dust layers. Thus, the distribution of dust along the line of sight can be

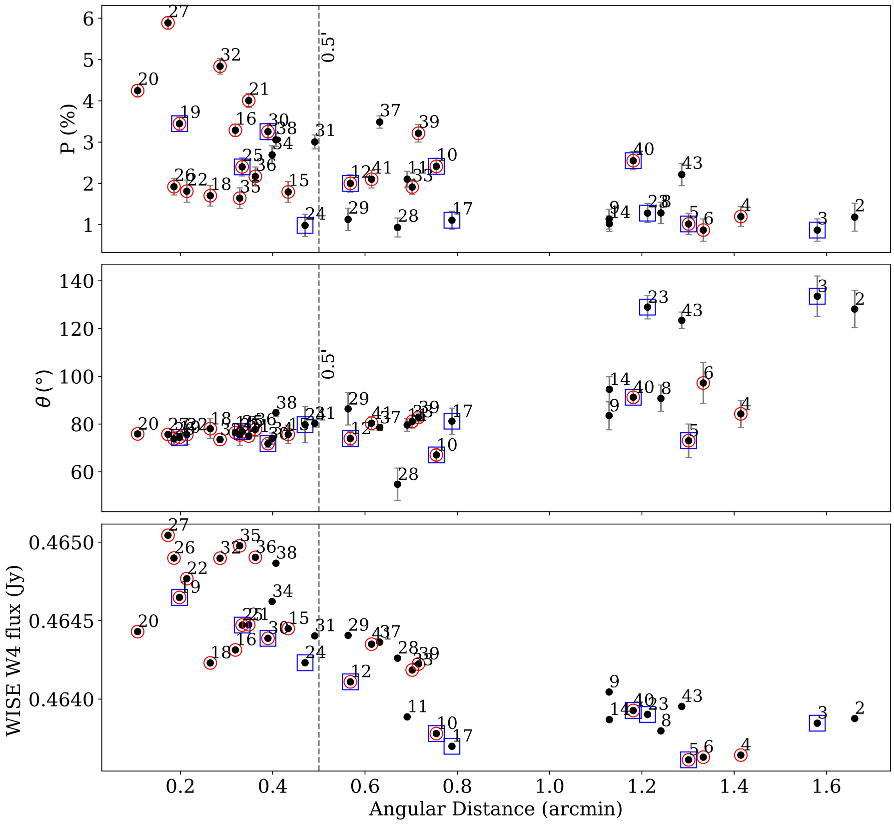

Figure 5.9: Variation of degree of polarization, polarization angle, and WISE flux counts of stars towards Czernik 3, with angular distance from the center of the cluster. Member stars and YSO candidates are denoted in red circles and blue squares respectively.

studied by analyzing polarization with distance. To quantify the distances of the dust clouds, we have used distance information (r_{pgeo}) of individual stars from Bailer-Jones et al. (2021). One star, #20, does not have the r_{pgeo} value. Consequently, we have used the r_{geo} (distance estimated from EDR3 parallax using geometric prior only) value for that source. Figure 5.10 shows the variation of polarization, position angle, and E(B-V) with distance (r_{pgeo}). The E(B-V) values are taken from Green et al. (2019) (calculated using a python-based script presented by Green, 2018). The cluster members are marked as red open circles. The middle panel of Figure 5.10 reveals a significant change in the polarization angle between star #43 and #34. This indicates the presence of a dust layer at a distance < 1800 pc (upper limit). We also note an increase (top panel) in the degree of polarization just beyond ~ 1000 pc. Due to the lack of polarization data for stars below 2000 pc, it is difficult to constrain the distance of the foreground dust cloud. However, the E(B-V) values show a jump at a distance < 1200 pc (see bottom panel of

Figure 5.10). This could be because of the presence of LDN1306, a Lynd's dark cloud (Lynds, 1962). The cloud has an angular extent of ~ 200′ (Dutra & Bica, 2002), and it is present south-east to the cluster with an angular separation of ~ 31′. The reported 50^{th} percentile distance to the cloud is 941 pc (Zucker et al., 2020), which is consistent with the location of the observed change in the degree of polarization as well as in E(B-V) close to ~ 1200 pc.

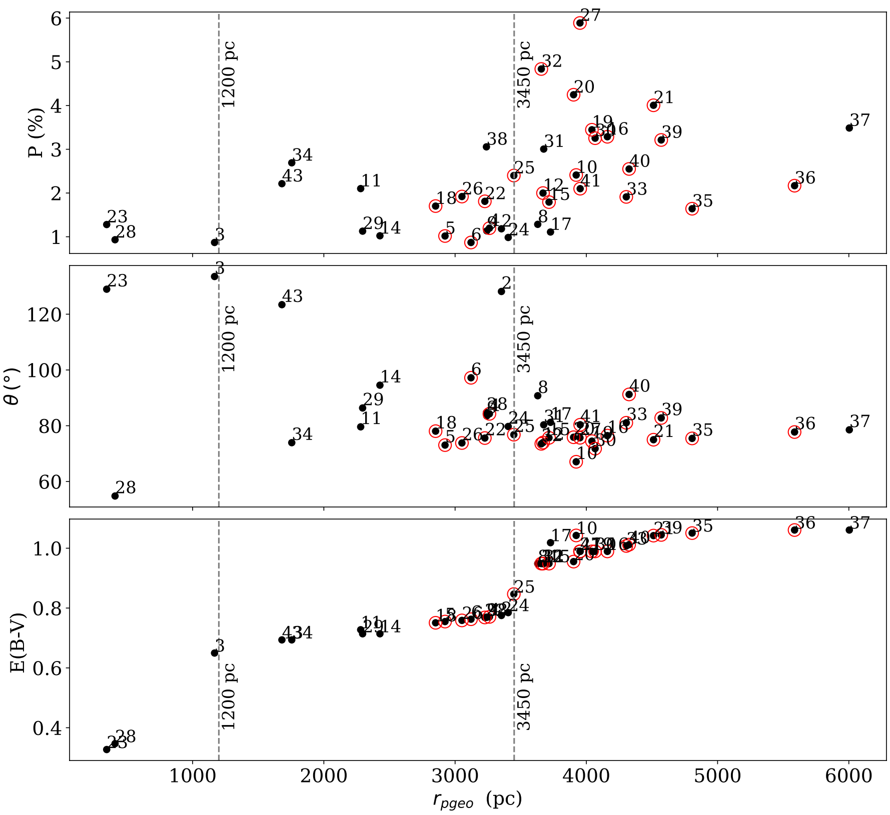

Figure 5.10: Variation of degree of polarization, polarization angle, and 50^{th} percentile reddening; E(B-V) of stars observed in the line of sight of Czernik 3 as a function of distance.

Stars beyond 2000 pc have large uncertainties (see Figures 5.11a and 5.11b, along with Figure 5.10) associated with the distance (r_{pgeo}). However, E(B-V) value shows a systematic change with distance, indicating another dust layer around 3450 pc. The spread in the distance of the member stars (shown as red open circles in Figure 5.10) is the result of large fractional parallax errors of these distant sources. The presence of a dust layer around 3450 pc nearly coinciding with the average distance to the cluster (3600 ± 800 pc) indicates the following possibilities:

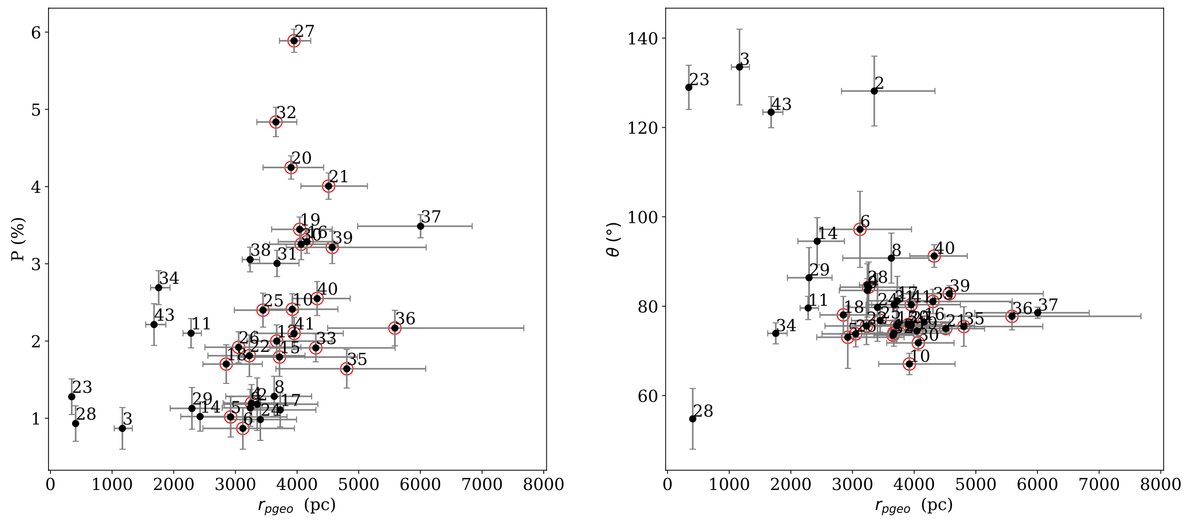

(a) Degree of polarization versus distance (b) Polarization angle versus distance

Figure 5.11: Variation of degree of polarization (a) and polarization angle (in b) with the distance of observed stars in Czernik 3 direction. The errors in the Gaia EDR3 distances (r_{pgeo}) and degree of polarization/polarization angle are also shown. The member stars are marked as red open circles.

1. the cluster may be embedded in the dust layer
2. the cluster is passing through a dense region of the galactic plane and coincidentally has a similar distance as that of a cloud near that location
3. The dust layer is present just before the cluster.

To confirm the presence of the second dust layer, we consider the fact that dust and HI are correlated in the diffuse ISM (e.g., Bohlin et al., 1978). Therefore, we use kinematic information of HI line emission spectra from HI4PI survey (HI4PI Collaboration et al., 2016) to infer the distribution of atomic gas along the line of sight in the selected region. The spectrum (blue line in Figure 5.12) reveals the existence of four well-separated velocity peaks (-114.7, -100.4, -43.8, -13.0 K ms^{-1}) and implies the neutral ISM mass is distributed in at least four spatially distinct components along the line of sight. The kinematic distance of the HI and ^{12}CO clouds are calculated from the web interface[6] corresponding to the source code provided by Reid et al. (2009). The resulting distances of corresponding dust layers are tabulated in Table 5.6.

[6]http://bessel.vlbi-astrometry.org/revised_kd_2014?

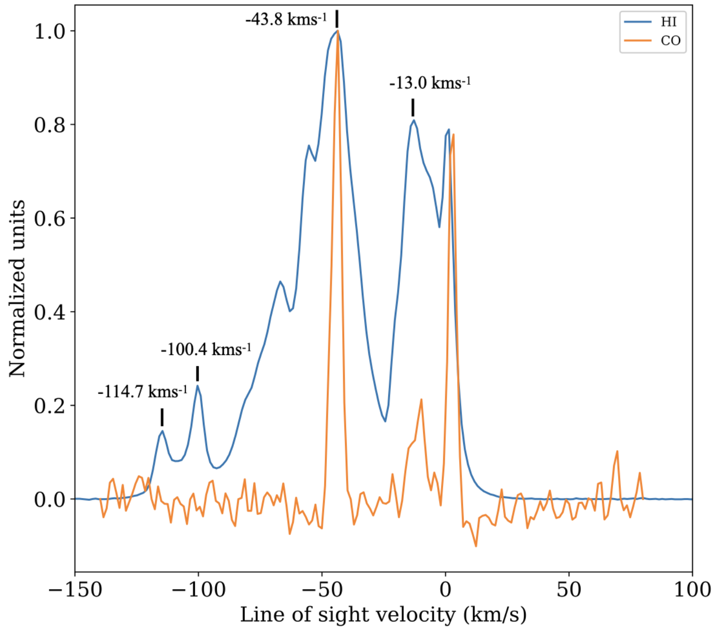

Figure 5.12: Spectrum of neutral hydrogen clouds *HI*- 21 cm line (in blue color) within 16′ of the center of Czernik 3 cluster and ^{12}CO (orange) within 30′ of the center of the cluster. Y-axis represents the normalized brightness temperature for HI and normalized antenna temperature for ^{12}CO.

Clouds with peak velocity -114.7 km s^{-1} and -100 km s^{-1} are in the background of the cluster (distance > 6 kpc). Thus, they will not contribute to the observed polarization. The main contribution comes from the clouds having the distance of $3.17^{+0.63}_{-0.59}$ kpc and $0.74^{+0.52}_{-0.52}$ which is consistent with the color excess and polarization jumps observed in the Figure 5.10. The same two clouds with a radial velocity of −43.8 km s^{-1}, −13.0 km s^{-1} are also seen in the molecular data (orange line in Figure 5.12), i.e., spectral information of ^{12}CO from Dame et al. (2001). This confirms the presence of at least two

Table 5.6: Peak velocity in HI spectrum in 5′ field centered on cluster center and corresponding kinematic distance in kpc.

Line of sight velocity (Km s^{-1})	Kinematic distance (kpc)
-114.7	$12.86^{+1.74}_{-1.50}$
-100.4	$10.0^{+1.30}_{-1.15}$
-43.7	$3.17^{+0.63}_{-0.59}$
-13.0	$0.74^{+0.52}_{-0.52}$

clouds along our line of sight.

5.3.4 General trend of dust distribution: a signature of Inter-arm region

In this section, we study the global properties of dust distribution that can be derived by combining the polarization data of Czernik 3, one of the most distant clusters with polarization data, and other clusters present within 15° region around it (see Table 5.2) along with the Heiles (2000) stars (Figure 5.13).

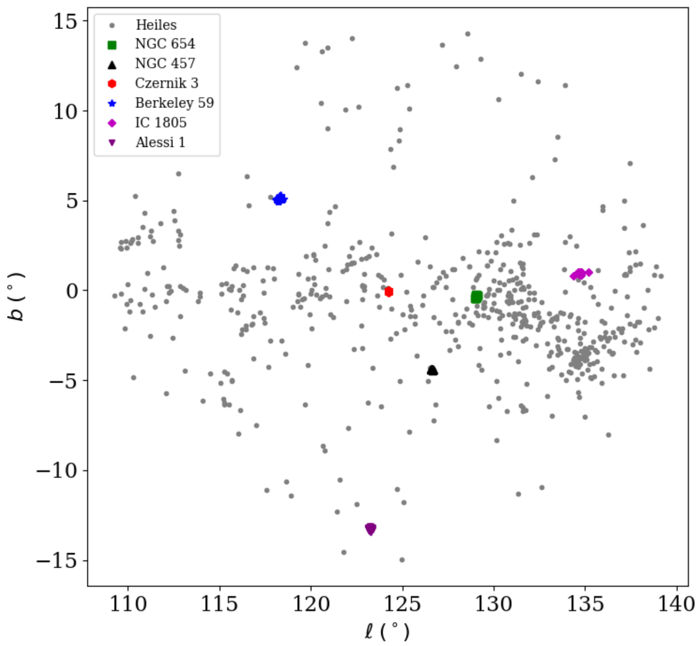

Figure 5.13: Distribution of clusters (color & symbols represents different cluster) and Heiles (2000) stars (gray dots) in Galactic coordinates (ℓ-b) centered on Czernik 3.

The polarization measurements of these clusters were converted to equivalent values in the *Sloan* - *i* band by utilizing the respective λ_{max} and P_{max} values in the Serkowski law for the wavelength dependence of polarization. The degree of polarization of all the available clusters in *sloan* *i*-band, along this direction, is plotted as a function of distance (r_{pgeo}, pc) in Figure 5.14. The polarization measurements of stars within a 15° radius of Czernik 3, obtained from Heiles (2000), have been included in gray color. The

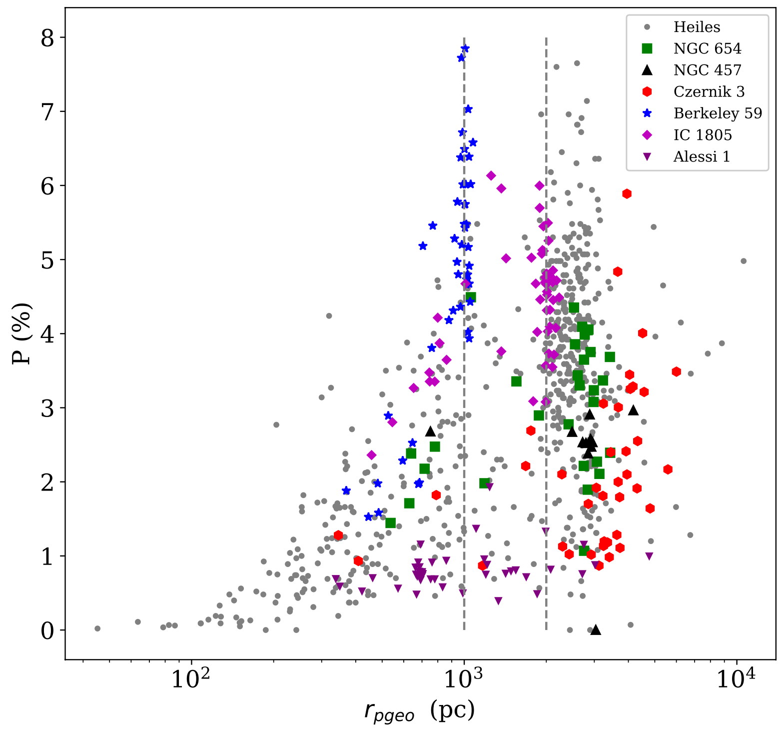

Figure 5.14: Variation of degree of polarization of stars towards different clusters as a function of distance in logarithmic scale. (Heiles, 2000) polarization within 15° is also added in gray colored dots.

analysis reveals a gradual increase in the degree of polarization with distance in the solar neighborhood, as expected from the uniform dust distribution in the vicinity of the solar neighborhood. However, at ~ 700 pc, a sudden rise in polarization is observed, likely attributed to the presence of a dust patch located approximately 700 pc away (Eswaraiah et al., 2012). Notably, there is a decrease in the number of stars observed between 1-2 kpc across all cluster fields and the field stars listed in the Heiles catalog. Moreover, no systematic change in polarization is observed before and after the gap. The polarization angle also remains consistent in the two regions (< 1kpc & > 2kpc). This peculiar decrease in the number of stars and no observed systematic change in polarization indicates that this region may contain minimal dust to affect the polarization of the background stars. This decrease in the number of stars with polarization measurement is not due to sample incompleteness. Rather, we note that the overall stellar number density (detection in the 2MASS bands with the quality flag of 'AAA') also shows a significant drop between 1 and 2 Kpc. The decline in stellar density, as well as dust density (from polarization data), suggests that the 1-2 Kpc region could be the inter-arm

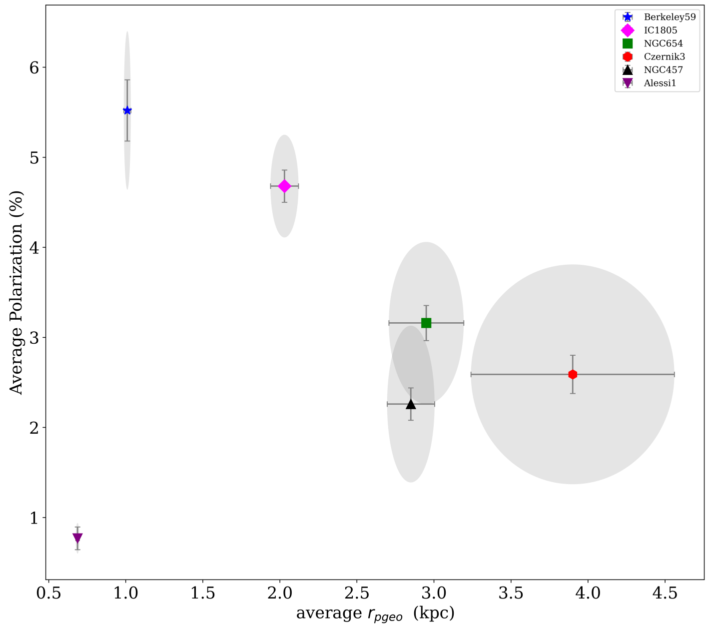

Figure 5.15: Variation of average polarization towards each cluster as a function of the mean distance to the corresponding cluster.

region between the local arm (below 1 kpc) and the Perseus arm (> 2kpc, Xu et al., 2006).

The variation of the average degree of polarization of each cluster with the mean distance of the member stars (membership probability > 90%) with polarization measurement is depicted in Figure 5.15. This figure shows a decrease in the mean polarization of the cluster with distance.

We note that Alessi 1 is a high latitude cluster (see Figure 5.13), suffering lesser dust extinction as compared to other clusters, hence showing an exceptionally low degree of polarization in comparison to the others. On the other hand, Berkeley 59 is a young cluster having intra-cluster dust, due to which many cluster members have intrinsic (non-interstellar) polarization up to 2% (Eswaraiah et al., 2012). The other clusters considered here are relatively older. With these caveats in mind, we still see an overall decrease in the degree of polarization with distance (Figure 5.15), which could be due to a decrease in polarization efficiency with increasing path length.

5.4 Summary

In this work, we presented the linear polarization study towards a distant open cluster, Czernik 3, and 15° region around it, with the aim to estimate the dust distribution on different spatial scales. We also redefined the membership of Czernik 3 as well as the other nearby clusters, having polarization information considered in this work. The polarimetric observations of Czernik 3 were carried out using the EMPOL instrument at the 1.2 m telescope at Mount Abu. A total of 42 stars are observed towards the core region of the cluster in *Sloan i*-band. We have arrived at the following conclusions from our study:

1. From the observed changes in the degree of polarization and extinction, we infer the presence of two dust clouds along the line of sight towards the Czernik 3 cluster at distances of ~ 1 kpc and ~ 3.4 kpc. The first cloud corresponds to the Lynds dark nebula LDN 1306.

2. The large range in the observed polarization ($0.87\% \leq P \leq 5.89\%$) of Czernik 3 stars may result from a non-uniform polarization efficiency. It could also arise from the non-uniform/patchy distribution of dust towards the cluster. We observed more dust density in the core of the cluster as compared to the peripheral regions.

3. The cluster membership of Czernik 3, as well as other nearby clusters, is redefined using the astrometric and photometric data from the latest Gaia EDR3. The distance to the Czernik 3 cluster is well constrained using member stars present in the core, and it comes out to be 3.6 ± 0.8 kpc.

4. The polarization efficiency for most of the observed stars towards Czernik 3 is less than the upper limit of the empirical relation for ISM polarization. Two stars with exceptionally high polarization are closer to the center of the cluster, indicating different polarization behavior as compared to the general diffuse ISM. They may also be intrinsically polarized.

5. For the clusters studied here, we find that the average polarization of the cluster decreases with distance to the cluster, indicating a decrease in polarization efficiency

with increasing path length.

6. There is a decrease in the dust as well as stellar density in the distance range of 1 to 2 kpc in a 15° wide region around Czernik 3. This is speculated to be the inter-arm region between the local arm and the Perseus arm.

This page was intentionally left blank.

Chapter 6

Optical linear polarization towards the anti-center direction

"Science progresses best when observations force us to alter our preconceptions."

- Vera Rubin, *1928-2016*

In Chapter 5, we examined the polarization observations of a distant cluster, Czernik 3, towards $\ell \approx 124°$, to demonstrate the role of polarization in deciphering the dust distribution. Building upon the same foundation, this chapter presents the study of the polarization of open clusters in the anticenter direction. The anticenter direction has lesser dust extinction (Gaia Collaboration et al., 2021a), providing us with a unique opportunity to perform polarization observations of open clusters at distant locations of the disk. In contrast to other directions, the kinematic distance of clouds towards the anticenter direction is known to produce highly erroneous results (Wenger et al., 2018). Therefore, the polarization of background starlight, combined with distance information, becomes the primary tool for determining distances to the foreground dust layers in this direction. These aspects motivated us to carry out polarization observations of distant

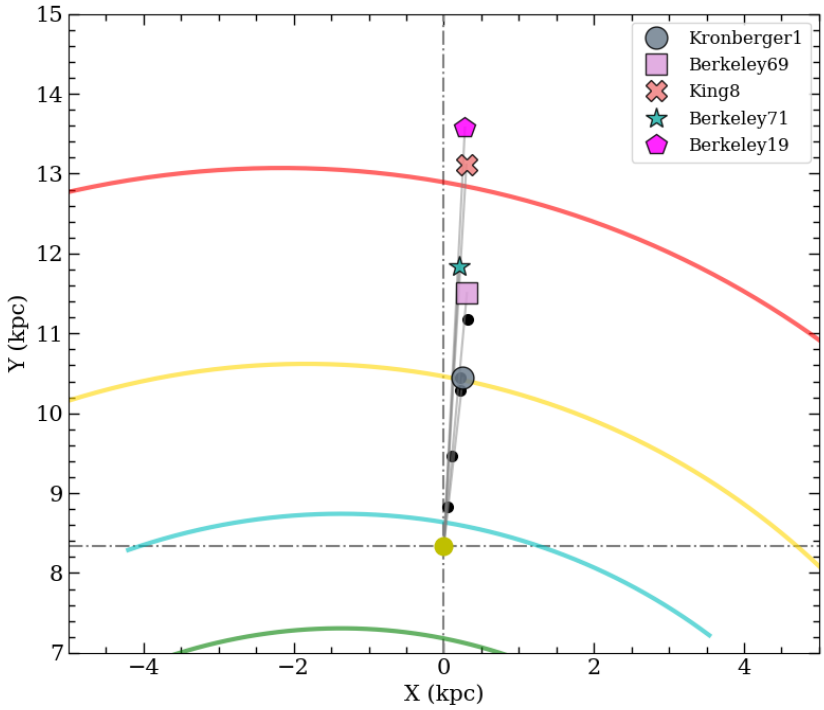

Figure 6.1: The XY-plane depiction of open clusters studied in this thesis towards the anticenter direction. The observed clusters are indicated by different color symbols, while black points denote the clusters with polarimetric measurements from the literature. The color-coding of spiral arms is similar to Figure 4.4.

clusters toward the anticentre direction.

In the literature, five clusters have been studied toward the anticenter direction in terms of their polarization measurements. These include NGC 2281 (Eswaraiah et al., 2011), NGC 1960 (Eswaraiah et al., 2011), Stock 8 (Eswaraiah et al., 2011), NGC 1931 (Pandey et al., 2013), and NGC 1893 (Eswaraiah et al., 2011; Bijas et al., 2022). However, it is noteworthy that most of these clusters are located at distances less than 2.5 kpc. In order to investigate the dust distribution in the distant regions, we targeted Galactic open clusters towards a similar line of sight and distributed according to distance. In accordance with the target selection criteria elucidated in Section 4.4.1, we selected five clusters, including Kronberger 1, Berkeley 69, Berkeley 71, King 8, and Berkeley 19. These clusters span a distance range of $\sim 2-6$ kpc.

This chapter provides an overview of the polarization observations conducted on five Galactic open clusters. We discuss the results obtained and their implications for the line of sight dust distribution in the local regions towards individual clusters. Additionally, we analyze the overall distribution of dust by comparing the polarization of the observed clusters and incorporating the polarization measurements from nearby clusters reported in the existing literature. Furthermore, a brief discussion is provided on the different methods that can be used to quantify the distances of the foreground dust layers from polarization measurements.

6.1 Observations

The observations of all the clusters in the anticenter direction were carried out using AIMPOL instrument mounted at the Cassegrain focus of the 1.04 m f/13 Sampurnanand telescope (see Section 4.3.2 for details). Three clusters, Berkeley 69, Berkeley 71, and Berkeley 19, were observed on March 1-3, 2022, in R and V bands. Due to poor SNR and telescope focus issues, these clusters were re-observed along with two additional clusters, Kronberger 1 and King 8, during the dark nights of October 19-23, 2022. The observations of all five clusters were performed in the R-band ($\lambda_{eff} = 0.63\mu m$), with a readout speed of 100 kHz (noise 4 e^{-}), and medium gain. To enhance the SNR, more than five frames were acquired at each position of the HWP. Different exposure times, based on the cluster brightness, were used to cover the bright as well as the faint stars (up to 17 mag) in the field. The details of the exposure time for each cluster are presented in the 4^{th} column of Table 6.1. We have covered the $\sim 12'$ diameter of each cluster completely covering the core regions of the cluster, $2'.4$, $3'$, $2'.4$, $2'.4$, and $1'.8$ for Kronberger1, Berkeley 69, Berkleye 71, Berkeley 19 and King 8, respectively (Kharchenko et al., 2013). In addition to the clusters, three to five polarized standards (see Table 6.2) and two un-polarized standards were observed each night in the same filter to calibrate the polarization angle and check the instrumental polarization, respectively. The instrumental polarization was found to be around ($\sim 0.1\%$).

The observed frames at each HWP position were processed using the self-scripted pipeline (described in Section 4.5.2.2). To resolve the overlapping issue in AIMPOL photometry, as shown in Figure 4.13, we utilized multiple apertures ranging from 1× to

Table 6.1: Observation log for open clusters observed towards anticenter from AIMPOL.

Cluster	RAJ2000	DECJ2000	Obs. date	exposure time* (s)
Berkeley 71	85.233	32.272	October 19, 2022	60, 30
Berkeley 19	81.014	29.575	October 21, 2022	75, 60
Berkeley 69	81.090	32.607	October 22, 2022	60, 20, 01
Kronberger 1	82.089	34.777	October 23, 2022	60, 30, 10
King 8	87.324	33.633	October 23, 2022	75, 60, 30

*The exposure time set at each position of HWP.

3× FWHM. The stars overlapping within 1× FWHM were excluded and not considered in the results and analysis. The degree of polarization, polarization angle and the Stokes parameters (q and u) were calculated using equation 4.13, 4.15, 4.16, on the photometric count ratio of e-ray and o-ray (equation 4.19 and 4.20) as discussed in section 4.5.2.2. The measured values were corrected for instrumental polarization by subtracting the Stokes q and u parameters of unpolarized stars from that of the target objects. Furthermore, the measured position angle of stars in each field was corrected to the reference position angle using observations of the polarized standard stars. The degree of polarization, polarization angle, and offset in angle for different standard stars observed each night, compared to their literature values (Schmidt et al., 1992), are listed in Table 6.2. The polarization angle (θ) is in the equatorial coordinate system measured from the North Celestial pole towards the increasing Right Ascension (RA) direction. The offset estimated from observing various standard stars within a night is in close agreement with each other, giving an average offset of $\sim 79°$.

6.2 Polarization results and analysis towards individual cluster

This section highlights the polarization results obtained from the observations of five clusters and the subsequent analysis conducted to infer the dust distribution towards each cluster direction. Our analysis included only stars with a brightness greater than

Table 6.2: Details of the observed polarized standard stars.

Star	$P \pm \epsilon_P$ (our work)	$\theta_{obs} \pm \epsilon_\theta$ (our work)	$P \pm \epsilon_P$ (Schmidt et al., 1992)	$\theta \pm \epsilon_\theta$ (Schmidt et al., 1992)	offset
Oct 19, 2022					
Hiltner 960	5.53 ± 0.14	-25.16 ± 0.90	5.210 ± 0.029	54.54 ± 0.16	79.70
HD236954	6.13 ± 0.15	30.78 ± 0.84	5.790 ± 0.099	111.20 ± 0.49	80.42
BD +64106	5.35 ± 0.07	18.18 ± 0.37	5.150 ± 0.098	96.74 ± 0.54	78.56
HD19820	4.32 ± 0.14	36.38 ± 0.76	4.562 ± 0.025	114.46 ± 0.16	78.08
Oct 21, 2022					
BD +64106	5.43 ± 0.16	17.67 ± 0.62	5.150 ± 0.098	96.74 ± 0.54	79.07
HD19820	4.46 ± 0.08	35.25 ± 0.46	4.562 ± 0.025	114.46 ± 0.16	79.21
HD25443	4.74 ± 0.03	56.45 ± 0.33	4.734 ± 0.045	133.65 ± 0.28	77.20
HD7927	3.22 ± 0.04	11.34 ± 0.66	3.026 ± 0.037	90.84 ± 0.35	79.50
HD236633	5.58 ± 0.12	12.77 ± 0.62	5.576 ± 0.028	94.04 ± 0.15	80.27
Oct 22, 2022					
HD19820	4.58 ± 0.15	36.60 ± 1.00	4.562 ± 0.025	114.46 ± 0.16	80.86
BD+59 389	6.52 ± 0.15	19.35 ± 0.19	6.430 ± 0.022	98.14 ± 0.10	78.79
Oct 23, 2022					
BD +64106	5.55 ± 0.38	19.17 ± 0.37	5.150 ± 0.098	96.74 ± 0.54	77.57
HD19820	4.56 ± 0.11	36.28 ± 0.99	4.562 ± 0.025	114.46 ± 0.16	78.18
HD25443	4.84 ± 0.2	57.20 ± 1.04	4.734 ± 0.045	133.65 ± 0.28	76.45
BD+59 389	6.58 ± 0.09	18.45 ± 0.50	6.430 ± 0.022	98.14 ± 0.10	79.69

Gmag > 17 mag, as fainter stars tend to have low SNR and may produce unreliable results. Additionally, we considered stars with a degree of polarization more than the $3\sigma_p$ threshold in our analysis. While these criteria led to the exclusion of many nearby foreground stars with low polarization and large uncertainties, we prioritized the selection of the most reliable measurements in our study. After applying these two criteria, we are left with 159, 152, 80, 88, and 161 stars towards Kronberger 1, Berkeley 69, Berkeley 71, Berkeley 19, and King 8, respectively. The determination of the degree of polarization using q and u Stokes parameters may produce a systematic bias due to low SNR as discussed in Section 5.1.1. We are considering the sources having polarization SNR (P/σ_P) more than 3; hence, the Ricean bias in our case will be negligible. Nevertheless, we corrected the polarization fraction for Ricean bias using equation 5.1. The polarization results of each cluster are added in the electronic media as extended tables[1]. The extended table of chapter 6 lists the degree of polarization (P), debiased polarization (P_{debias}), polarization angle (θ), Stokes parameters (q and u), and their errors (ϵ_P, ϵ_θ, ϵ_q, and ϵ_u) for each individual cluster labeled by the cluster name. The corresponding Gaia source Id of the observed stars is also appended to the tables. The detailed description and analysis towards each cluster are presented in the following subsections, sorted by cluster distance.

6.2.1 Kronberger 1

Kronberger 1 is deeply embedded in the Galactic plane, having Galactic latitude of $b = 0.049°$ towards the anticenter direction, i.e., Galactic longitude, $\ell = 173°.106$. It is the nearest cluster in our observation campaign, having a distance of ~ 2.34 kpc (Cantat-Gaudin et al., 2020) and a core radius of 1.2′ (Kharchenko et al., 2013). According to Cantat-Gaudin et al. (2020), half of the cluster members would lie within a radius of only 0.84′ radius. The core radius of the cluster was fully observed on October 23, 2022, with the AIMPOL instrument. We obtained polarization measurements of 159 stars with polarization SNR greater than 3. The weighted 1σ average of the degree of polarization and polarization angles for all the stars towards this direction are found to be $2.99 \pm 1.29\%$ and $\theta = 154° \pm 30°$. To identify probable cluster members, we considered stars with an astrometric membership probability of more than 0.5. Out of the 32 members (Cantat-Gaudin et al., 2020), we observed 19 probable cluster members having Gmag < 17 mag. These members exhibit an average degree of polarization of $2.52 \pm 0.60\%$ and a polarization angle of $154° \pm 6°$. The uncertainty in the quoted values denotes the spread or dispersion around the mean value. The remaining stars (159-19 = 140) are field stars, either located in the foreground or background relative to the cluster.

[1]https://drive.google.com/file/d/1MoqpSfXwIG9SwEw12FnuVrpTOmpcQlQH/view?usp=sharing

Polarization vector map

The sky projection of the polarization vector for all the observed stars towards Kronberger 1 is overlaid on a DSS R-band image (in equatorial coordinates) and shown in Figure 6.2. The length of each vector represents the degree of polarization while the orientation of the vector is in accord with the polarization angle measured from the North celestial pole, increasing towards the East. In the lower right corner of each figure, a reference line segment is drawn, in blue color, indicating a polarization of 5% and polarization angle of 90°. Additionally, the cluster center is marked by a blue cross. The figure also includes a solid gray line, illustrating the Galactic parallel (constant latitude line), having a position angle of 140°.9. Polarisation vectors for most stars exhibit similar orientations, with slight deviations observed in certain foreground or background stars. The polarization vectors predominantly align parallel to the Galactic plane. In the figure, the most probable member stars, highlighted with red vectors, show consistent polarization angles.

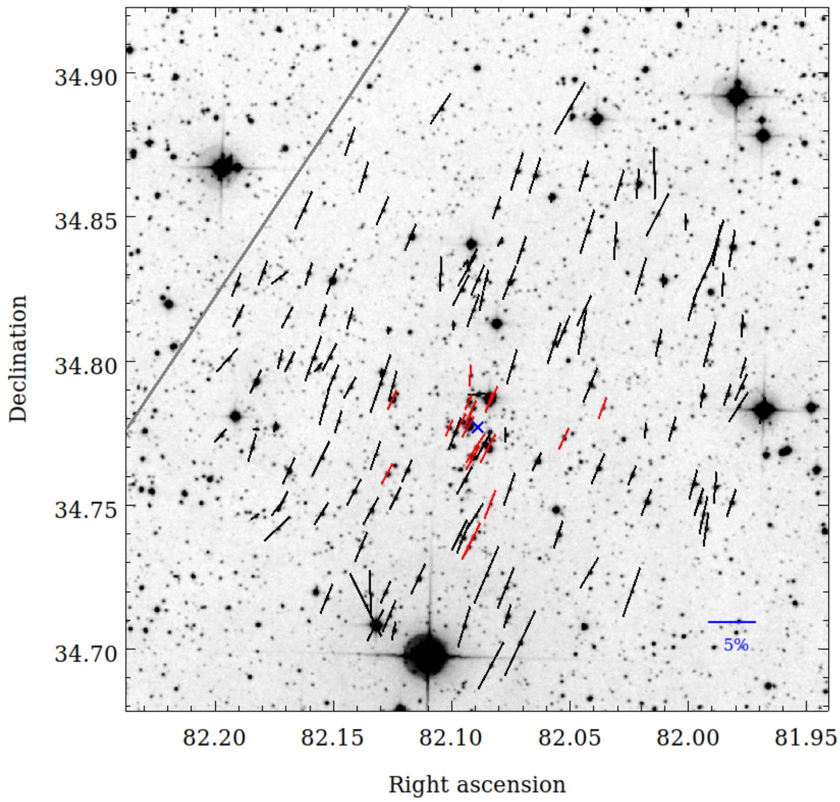

Figure 6.2: Polarization vectors overlaid on DSS, R-band 25′ × 25′ field towards Kronberger 1 cluster. The polarization vectors of member stars are shown in red. A detailed description of the figure is presented in the text.

Distribution in $p-\theta$ plane

A clear picture of the comparison of polarization angle and degree of polarization can be studied with the distribution of stars in the $p-\theta$ plane, shown in Figure 6.3. For visualization purposes, we displayed the polarization angle in $-90° \leq \theta \leq 90°$. The gray dashed line in the figure represents the orientation of the Galactic plane (= 140°.9 − 180°). It is evident from the plot that, on average, most of the stars exhibit similar orientations but show a small deviation from the Galactic plane. This suggests that the magnetic field in this direction is approximately aligned with the Galactic plane. The member stars are indicated by hollow red circles, while the field stars are represented by black points. It is worthwhile to note that the polarization angle demonstrates a significant dispersion for low-polarized stars, with the spread decreasing as the degree of polarization increases. Most of the member stars exhibit uniform polarization angles with small dispersion of $\sim 6°$. Only one member star, with a membership probability of 90%, exhibits a larger polarization angle (= 174° − 180° = −6°) in contrast to the remaining detected member stars.

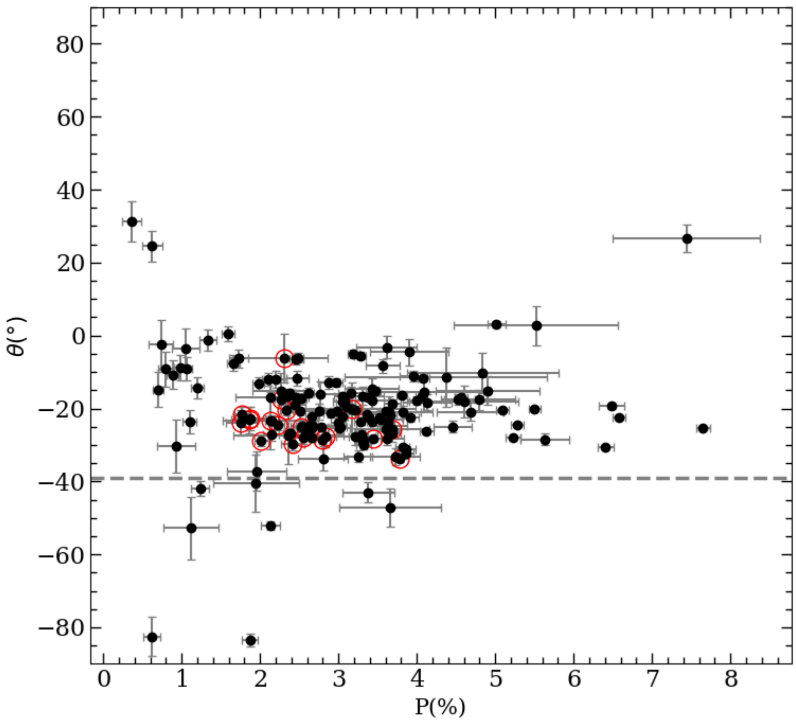

Figure 6.3: Distribution of observed stars towards Kronberger 1 in P-θ plane. Member stars are highlighted as red hollow circles, and the gray dotted line shows the position angle of the Galactic plane towards the cluster direction.

Dust distribution

The number of dust layers foreground to the cluster direction can be inferred from polarization and/or extinction measurements. The degree of polarization or extinction is expected to show a jump when the starlight encounters any dust layer. Hence, the degree of polarization as a function of distance is a measure of dust distribution along the line of sight.

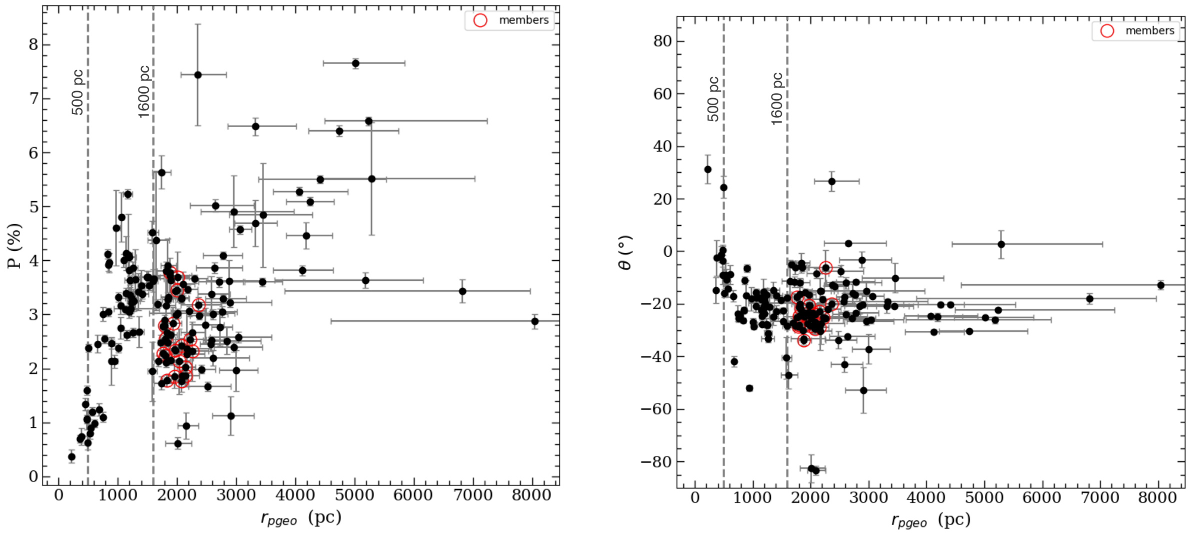

(a) Distance versus degree of polarization

(b) Distance versus polarization angle

Figure 6.4: Variation of degree of polarization (panel a) and polarization angle (panel b) of stars observed towards Kronberger 1 as a function of distance, r_{pgeo}. The vertical dashed gray lines show the predicted dust layers in the foreground of the cluster.

In order to determine the dust distribution towards Kronberger 1 cluster, we cross-matched the observed stars with the Gaia EDR3 distance catalog (Bailer-Jones et al., 2021). The degree of polarization and polarization angle is plotted as a function of 'r_{pgeo}' distance in Figure 6.4a and 6.4b, respectively, with errorbars in both x and y-axis in gray color. In addition, for the comparison of polarization with extinction, we plotted the variation of the degree of polarization (in the upper panel), polarization angle (middle panel), and extinction, E(B-V) from Bayestar 3D extinction map (Green et al., 2019, bottom panel) with r_{pgeo} in Figure 6.5. We binned the data in the distance axis to reveal the smooth variation in polarization and extinction. The average degree of polarization, polarization angle, and extinction in 500 pc bins of distance are plotted in

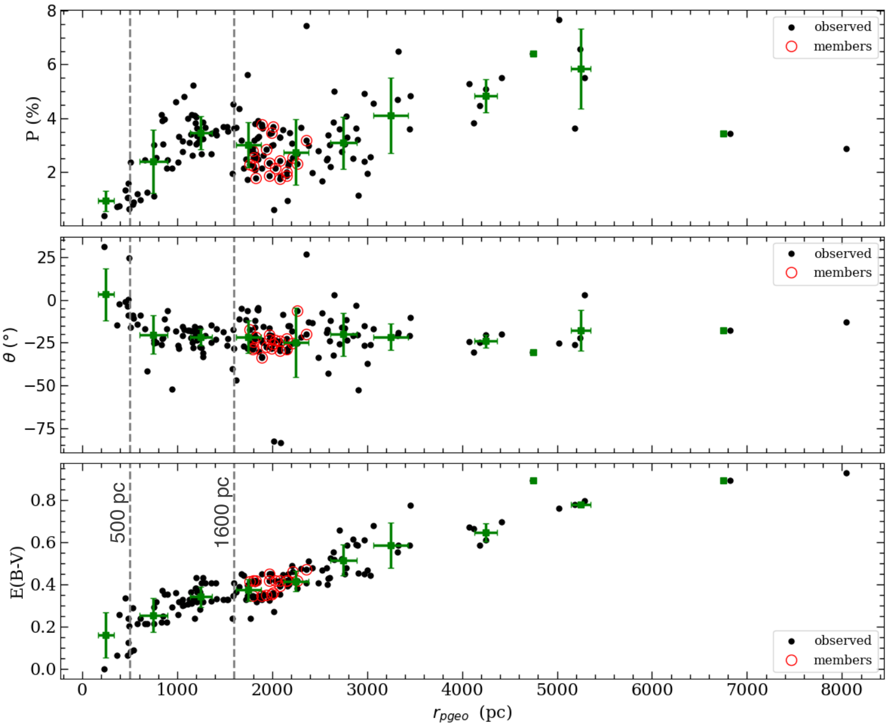

Figure 6.5: Variation of degree of polarization (P), polarization angle (θ) and reddening, E(B-V) as a function of distance. The mean P, θ, and E(B-V) in 500 pc bins are represented by the green squares in corresponding panels, with the error bar representing the dispersion in the respective parameter. The vertical dashed gray lines are the same as that of Figure 6.4.

green square points with error bars representing the dispersion in the x- and y-axes within the corresponding bin. Stars with membership probability greater than 50% are shown in red open circles in both figures.

A careful inspection of Figure 6.4, upper and middle panels of Figure 6.5 reveals a change in the degree of polarization at $\sim$ 500 pc and the same can also be seen in the polarization angle. The number of stars is less in this region to fully constrain the distance of the cloud, but roughly a cloud layer must exist $\sim$ 500 pc. The jump at $\sim$ 500 pc is also consistent with the extinction values (as seen in the bottom panel of Figure 6.5). Thereafter, the polarization uniformly increases with distance till $\sim$ 1600 pc. At this distance, the starlight seems to get depolarized. This region coincides with the cluster position, as denoted by the location of members in the figures. The cluster is close to the star-forming region, S234 (Dewangan et al., 2018), having a distance of $\sim$ 2.8 kpc. The dust in the star-forming region could be the reason for the decrease in the degree of polarization. However, the polarization angle does not show any significant change. This is possible as the foreground cloud is the dominant source of extinction as indicated by the extinction jump at $\sim$ 500pc. In such cases, according to Malus' law, the polarization angle of stars behind both clouds will still be dominated by the foreground cloud but the degree of polarization will decrease if the B-field of the distant cloud is not aligned with the foreground one. Beyond 3000 pc there is again an increase in the polarization, which could also be a possible dust layer at that distance, but this is beyond our cluster distance. Hence we are not considering this in our interpretation. Overall, this cluster shows a clear presence of two dust layers at $\sim$ 500 pc and $\sim$ 1600 pc.

6.2.2 Berkeley 69

Berkeley 69 cluster is located at $\ell = 174^\circ.442$ and $b = -1^\circ.851$. It is present at a farther distance than Kronberger 1, i.e., at r = 3.2 kpc. The core radius of the cluster, as determined by photometric analysis, is $\sim 1.5'$ (Kharchenko et al., 2013). However, a recent study by Hunt & Reffert (2023) found the core radius to be larger, approximately $3.7'$, surpassing the values obtained solely based on photometry. About 50% of the stars in the cluster are situated within a radius of $3.942'$, which is fully covered by our observations. This cluster was observed on October 22, 2023, with the AIMPOL instrument. 151 stars are observed with more than 3σ polarization measurements towards this direction and have Gaia counterparts. The degree of polarization toward this direction ranges from 0.5 to 8.6% with the weighted mean value of 2.66% and dispersion of 1.28%. The weighted average polarization angle of the observed stars corresponds to 143° with a relatively large spread of around 29°.

By cross-matching the observed stars with the membership catalog of Hunt & Reffert (2023), we identified 48 member stars out of 216 potential members with a membership probability of more than 50%. The limited number of member stars detected in our study can be attributed to the combined effect of

- a brightness cutoff at 17 mag on Gmag.
- the overlapping of closely spaced stars within 1$\times$ FWHM that cannot be resolved

and hence excluded.

- the threshold on the polarization SNR. As described in Section 6.2, the stars with a degree of polarization more than 3σ are considered in our results and analysis.

The observed probable cluster members demonstrate a consistent degree of polarization, with a weighted mean of $3.25 \pm 0.89\%$. However, there is some variation in the polarization angle, with a spread of 21° around the mean value of 142°.5.

Polarization vector map

In Figure 6.6, the polarization measurements towards the Berkeley 69 cluster are plotted as pseudo-vectors on the DSS image of the $25' \times 25'$ field around the cluster. The

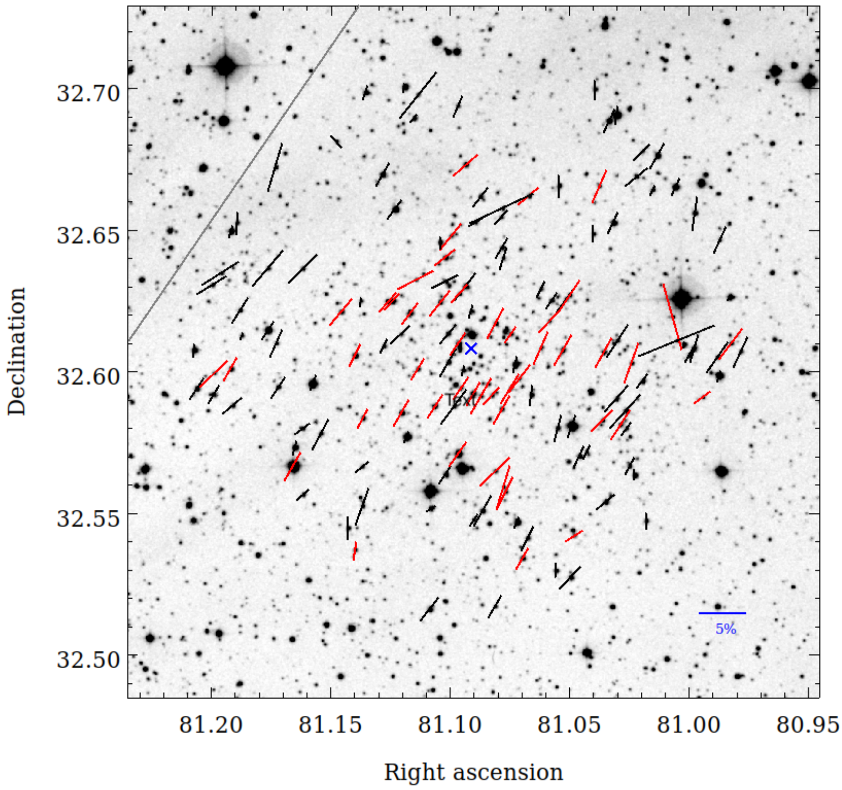

Figure 6.6: Polarization vectors overlaid on DSS, R-band $25' \times 25'$ field towards Berkeley 69 cluster. The color description is similar to Figure 6.2.

North-East direction is similar to that of the Kronberger 1, Figure 6.2. The Figure shows that most of the polarization vectors for the stars towards the cluster are aligned with the Galactic plane (represented by a gray line), having an orientation of 141°.04. This implies the magnetic field towards this direction is oriented with the Galactic plane.

The cluster members are highlighted in red vectors, while the field stars are shown in black. A closer inspection of the figure reveals that the cluster members located closer to the center of the cluster exhibit a similar degree of polarization, and the polarization angle closely matches with the orientation of the Galactic plane, while the member stars located away from the center show some deviation. It could be related to the inhomogeneous distribution of the dust layer towards the face of the cluster or the difference in the polarization efficiency in the two regions.

Distribution in $p-\theta$ plane

Figure 6.7a illustrates the distribution of stars in the $p-\theta$ plane. The member stars are marked by a red circle on the black points, and the gray dashed line represents the orientation of the Galactic plane. The distribution of stars roughly denotes three different groupings;

- The first group consists of four stars with a low degree of polarization and polarization angles around 50°.
- The second group exhibits a slightly higher degree of polarization (approximately 1.5%) and a polarization angle of $\theta \approx 165°$.
- The third group primarily consists of all the member stars, showing a higher average polarization (around 3%) compared to the other groups. These stars also have a lower polarization angle (approximately 145°) compared to the stars in the second group.

The differences in polarization among these three groups provide evidence for the presence of multiple dust layers along the line of sight, leading to distinct polarization properties.

In addition, the majority of the member stars are present in the third group except two stars. One star exhibits the polarization measurements of $1.99 \pm 0.35\%$ and $169° \pm 5°$, indicating a similar polarization as that of group 2. The other star shows the degree of polarization $7.22 \pm 0.69\%$ and polarization angle $15° \pm 3°$. These stars also display significant deviations in their q and u values, raising doubts about their membership status. The sky position of these two stars reveals that they are located towards the edges

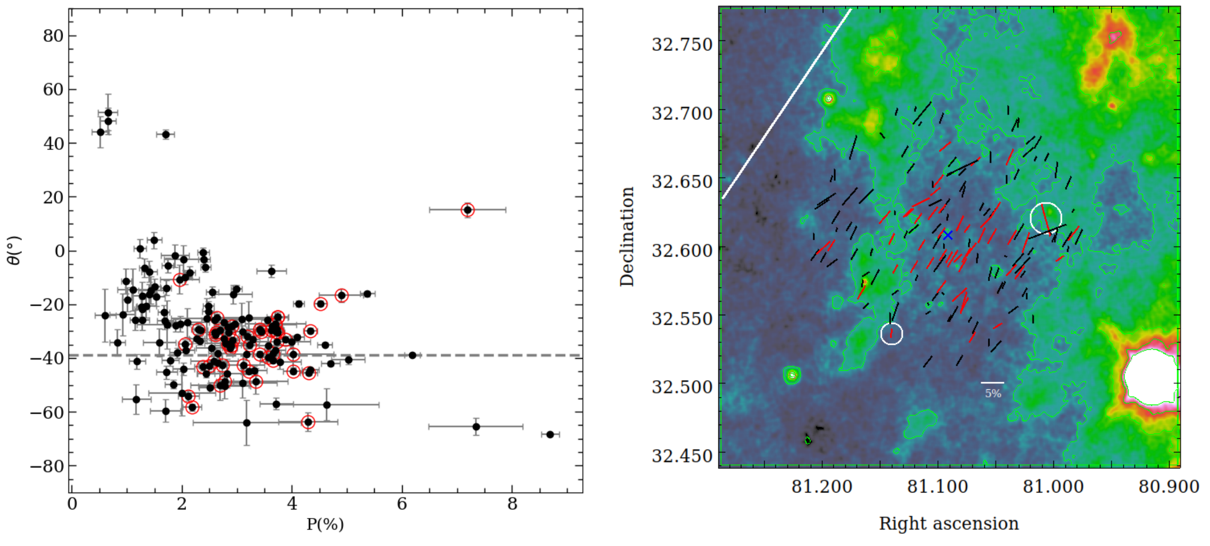

(a) $P-\theta$ distribution.

(b) P vectors overlaid on WISE W4 image.

Figure 6.7: Polarization measurements of stars towards Berkeley 69 cluster. The left panel represents their distribution in the $P-\theta$ plane, and the right panel illustrates the polarization vector overlaid on the WISE W4 image. The vector length and alignment are similar to Figure 6.6.

of the observed region, indicating the possibility of inhomogeneous dust distribution towards the edges. To investigate this further, we plotted the polarization vectors on the WISE W4 image in Figure 6.7b. The solid white line on the left edge represents the orientation of the Galactic plane. The plot clearly illustrates a non-uniform distribution of dust along the face of the cluster. Interestingly, the central region exhibits less dust compared to the periphery of the cluster. Here, one particular star stands out with a higher polarization value of 7.22%, denoted by a larger white circle. This higher polarization could be attributed to either intrinsic polarization or the presence of warm dust as suggested by the increased WISE W4 intensity in Figure 6.7b. Conversely, the stars marked by smaller white circles exhibit lower polarization and do not appear to have an excess of surrounding dust. Therefore, it could possibly be a non-member. Excluding these two stars, the weighted average of the degree of polarization and polarization angle of the cluster is estimated to be $3.25 \pm 0.67\%$ and $144° \pm 10°$.

Dust distribution

To analyze the dust distribution along the field of Berkeley 69, we generated Figure 6.8, which displays the degree of polarization (Figure 6.8a) and polarization angle (Figure

6.8b) as a function of r_{pgeo}, similar to Figure 6.4. Additionally, Figure 6.9 illustrates the variations in the degree of polarization, polarization angle, and reddening E(B-V). Below 600 pc, the stars are showing low polarization, both the degree of polarization

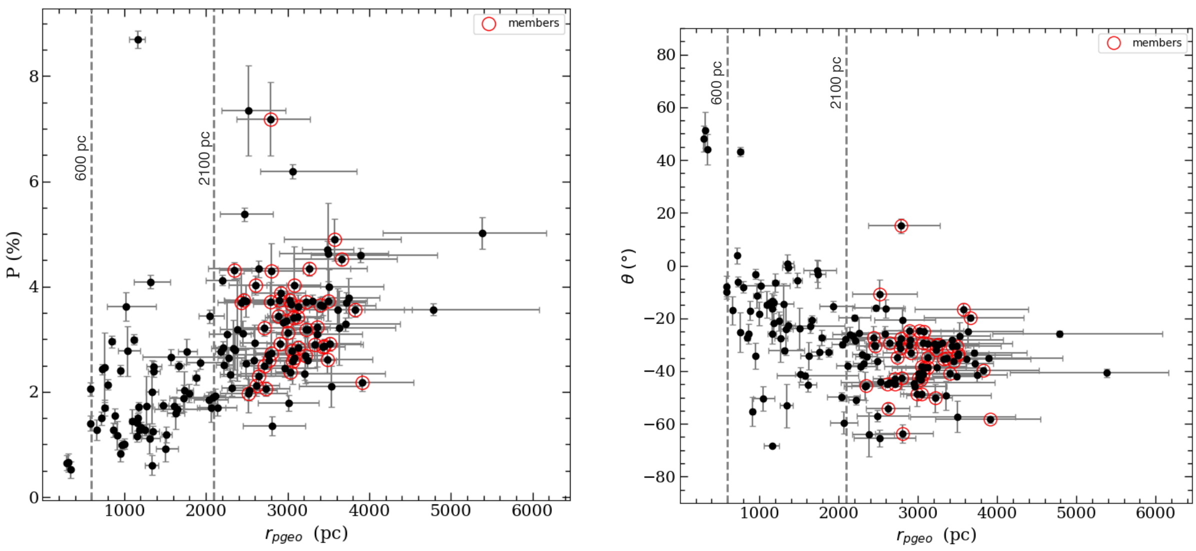

(a) Distance versus degree of polarization.

(b) Distance versus polarization angle.

Figure 6.8: Variation of degree of polarization and polarization angle of stars observed towards Berkeley 69 as a function of distance, r_{pgeo} in panel (a) and (b), respectively.

and polarization angle ($\sim 50°$). The degree of polarization increases, accompanied by an abrupt change in the polarization angle after 600 pc. This suggests the presence of a dust layer that is polarizing the stars located behind it. However, due to the limited number of stars at this distance, we cannot accurately determine the distance of the foreground layer. Therefore, we can only provide upper limits for the predicted dust layers in this region. Furthermore, the stars laying between 500-2000 pc shows large variation in the degree of polarization and polarization angle. Nevertheless, at ~ 2100 pc, the average polarization angle drops from $\sim 160°$ ($\sim -20°$) to $\sim 144°$ ($\sim -36°$), and the average degree of polarization increases to approximately 3%. These observations indicate the existence of another dust layer around 2100 pc. The degree of polarization, polarization angle in 500 pc bins of distance, shown in Figure 6.9 also gives the signature of two dust layers foreground to the cluster direction at the predicted distances ($\sim 600, 2100$). Not only the polarization measurements but the extinction also exhibit variations at these distances. Therefore, we conclude that there exists at least two dust layers at ~ 600 pc and ~ 2100 pc, foreground to the Berkeley 69 cluster.

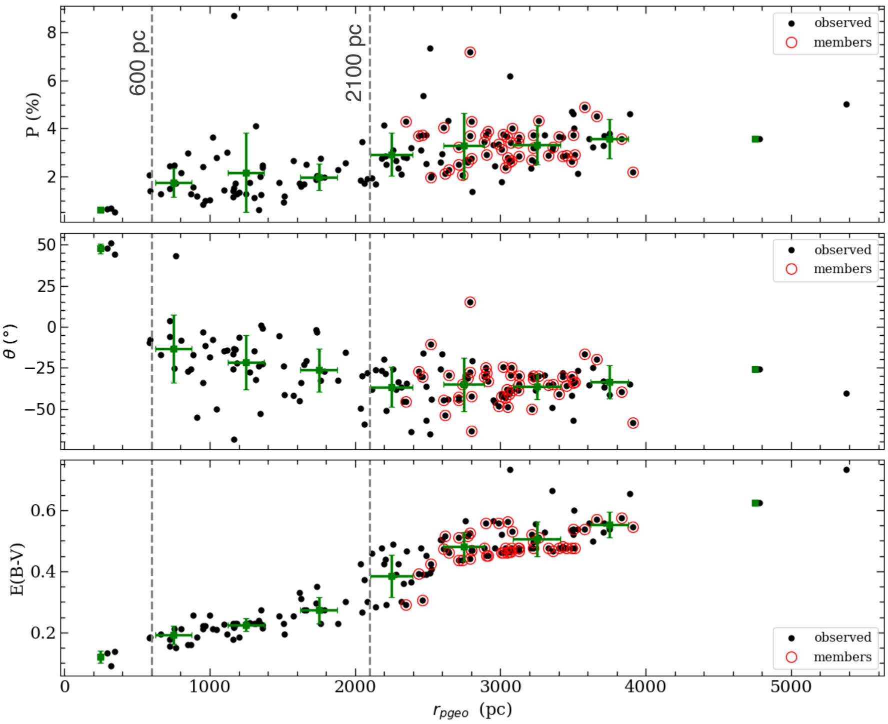

Figure 6.9: Variation of degree of polarization, polarization angle, and reddening, E(B-V) as a function of r_{pgeo}. The vertical lines at r_{pgeo} = 600 and 2100 pc represent the distance of predicted dust clouds towards Berkeley 69.

6.2.3 Berkeley 71

Berkeley 71 is a cluster present in a relatively higher extinction region (A_v = 3.02, Hunt & Reffert, 2023) towards the anticenter direction, ℓ = 176°.635 and b = 0°.900. The observations were conducted in the R-band on October 21, 2022, using the AIMPOL instrument. The cluster is reported to have a core angular radius of 1.2′ (Kharchenko et al., 2013) or 2.21′ according to Hunt & Reffert (2021). Our observations covered the central part of the cluster, with an angular radius of 4′.8. We observed a total of 80 stars towards this cluster, out of which 28 stars have a membership probability exceeding 50%. The literature reports the cluster to be at a distance of approximately 3.5 kpc. The average degree of polarization decreases towards Berkeley 71 with an average value of 1.61% and polarization angle of 114°. The measurements exhibit large dispersion both in the degree of polarization (1.42%) and polarization angle (42°). Within the cluster member stars, the average degree of polarization is 1.58%, with a standard deviation of 0.86%, while the mean polarization angle is 135°, with a dispersion of 24°. These results suggest that the decrease in the degree of polarization and the variation in the polarization angle, in comparison to the previously discussed clusters in this chapter, may arise from the influence of specific dust patches confined to this region and absent in other clusters. Further interpretation of these observations is discussed in the following subsections.

Polarization vector map

The most reliable polarization measurements of stars observed toward Berkeley 71 are plotted as vectors on DSS 25′ × 25′ in Figure 6.10 similar to Figure 6.2. The orientation

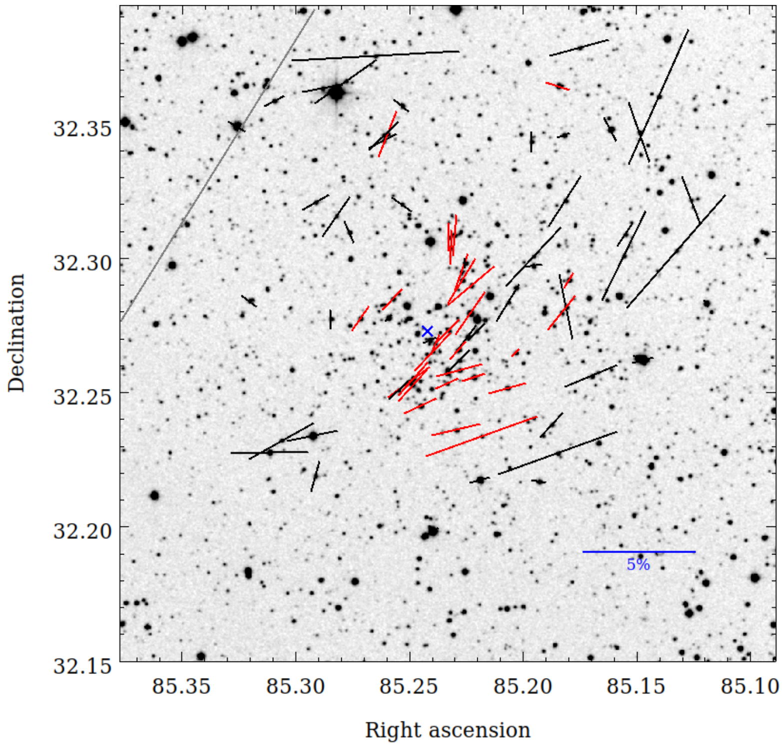

Figure 6.10: Polarization vectors overlaid on DSS, R-band 25′ × 25′ field towards Berkeley 71. The color description is similar to Figure 6.2.

of the Galactic plane at the location of the cluster has a position angle of 143°.52 and is denoted by a gray solid line. It is noted that the degree of polarization and polarization angle of member stars and field stars show a large deviation. This may represent the origin of polarization by the dust layers having different properties or could be a patchy distribution of dust towards the face of the cluster. Furthermore, the polarization angles of only a few member stars in Berkeley 71 exhibit alignment with the Galactic plane,

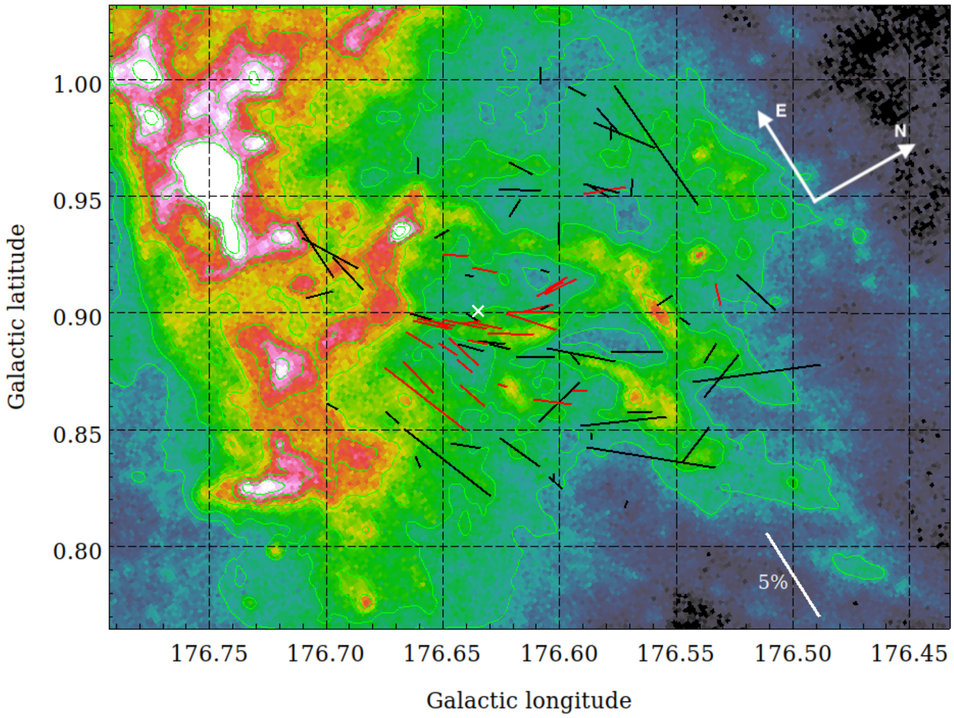

Figure 6.11: Herschel 250 μm dust map of Berkeley 71 field in Galactic coordinates. The polarization measurements are over-plotted on the dust map. The equatorial North and East are denoted in white arrows. The 5% polarization line perpendicular to the celestial North is also added at the bottom-right side.

while most of the field stars and cluster members display a scattered orientation. This suggests that the magnetic field in this direction exhibits inhomogeneity in small-scale regions. To investigate the distribution of integrated dust on larger spatial scales, we utilized Herschel 250-micron maps, which provide information about the cold dust distribution. Figure 6.11 illustrates the line-of-sight integrated cold dust distribution, revealing filamentary structures (follow the contours). Notably, the polarization vectors appear to align with the 250-micron dust features, particularly in the vicinity of the cluster center. This correlation between the inhomogeneous cold dust emission and the polarization explains the significant scatter observed in the polarization angles.

Distribution in $p - \theta$ plane

As discussed in the last section, the degree of polarization and polarization angle exhibit large variation, which can be clearly seen in Figure 6.12. The member stars show large scatter around the Galactic plane. Another group of stars exhibits a low degree of polarization and large deviation from the Galactic plane ($\theta > 30°$), mostly comprised of foreground stars.

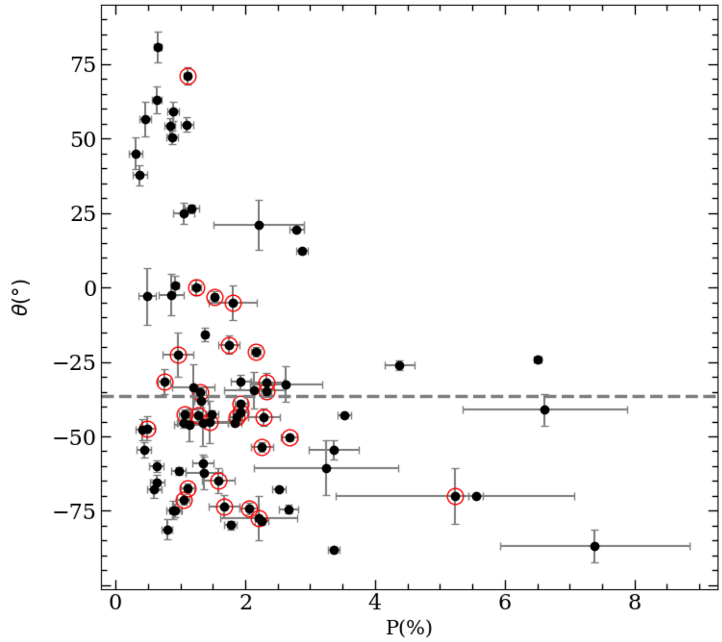

Figure 6.12: Distribution of stars observed towards Berkeley 71 in $p-\theta$ plane.

Dust distribution

The variation of the degree of polarization and polarization angle with distance, as shown in Figure 6.13a and 6.13b, suggest a jump in the polarization angle at ∼ 700 pc. The Figure depicts the lower degree of polarization for stars located at a distance less than ∼ 2000 pc. The polarization angle also shows a large scatter up to the 2000 pc distance. The dispersion decreases in the polarization angle beyond 2 kpc, and simultaneously, there is an increase in the degree of polarization as well. Hence, there should be a dust layer at ∼ 2 kpc, responsible for the background stars' polarization. This is also confirmed in the variation of extinction with distance (bottom panel of Figure 6.14), where the extinction shows a sudden change in the slope at ∼ 2 kpc. This confirms the existence of two dust layers at ∼ 700 pc and ∼ 2 kpc towards Berkeley 71.

6.2.4 King 8

The King 8 cluster is situated at a relatively higher latitude, with $b = 3^{\circ}.104$, towards the direction of $\ell = 176.384$. It is located at a distance of 4.8 kpc from the Sun. The central

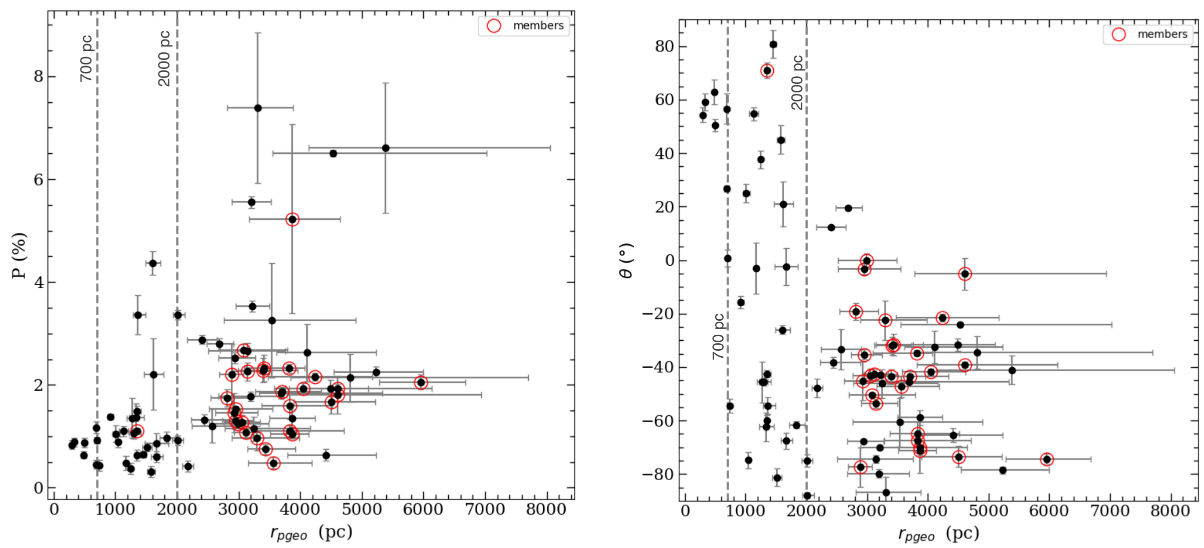

(a) Distance versus degree of polarization.

(b) Distance versus polarization angle.

Figure 6.13: Variation of degree of polarization and polarization angle as distance, r_{pgeo} towards Berkeley 71 in panels (a) and (b), respectively.

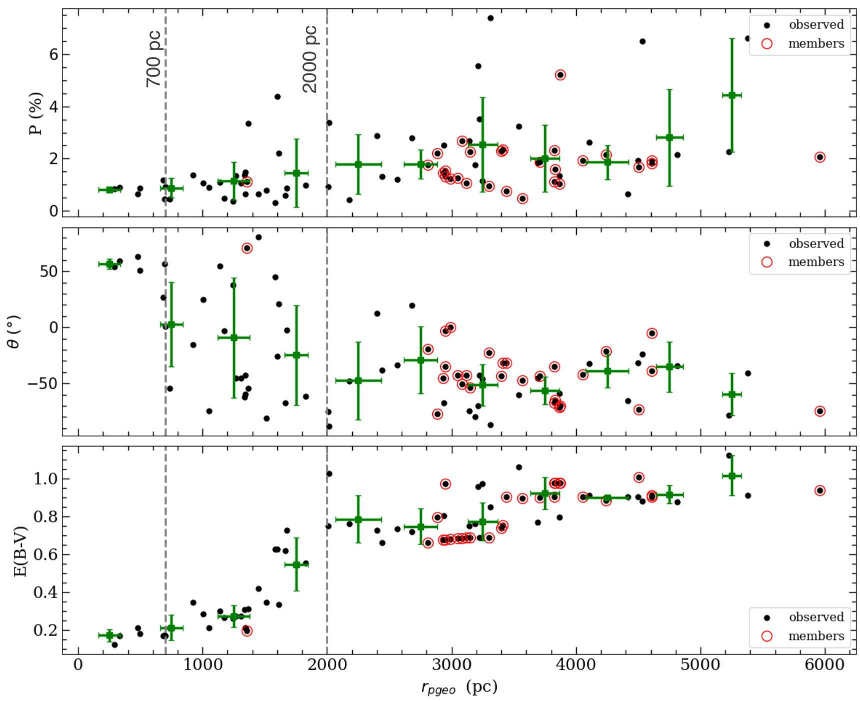

Figure 6.14: Variation of degree of polarization, polarization angle, and reddening, as a function of r_{pgeo} towards Berkeley 71. Detail description is provided in the text.

region of the cluster extends over an angular size of 3.6′, encompassing a core of size 0.63′. Approximately 50% of the member stars are found within a radius of 1.73′. The observations of the central region of the King 8 cluster were conducted on October 23, 2022, employing the AIMPOL instrument. These observations yielded polarization measurements for a total of 161 stars. The weighted mean degree of polarization for all the stars observed in this direction is calculated to be 1.95%, with a large spread of 1.08%. The polarization angle is close to 145°, exhibiting a dispersion of 49°. According to Hunt & Reffert (2023), based on Gaia DR3 data, the cluster has 128 members, having a membership probability of more than 50%. While we observed 161 stars towards King 8 cluster, only 38 have a membership probability of more than 50%. The detected member stars show similar polarization with a weighted average degree of polarization within 1σ, $3.19\% \pm 0.78\%$ and polarization angle of $156° \pm 8°$.

Polarization vector map

Figure 6.15 displays the polarization vectors superimposed on a DSS R-band image of $25' \times 25'$ field around King 8. The orientation of the Galactic plane in this direction is approximately 144°.33, denoted by a solid gray line. The figure reveals

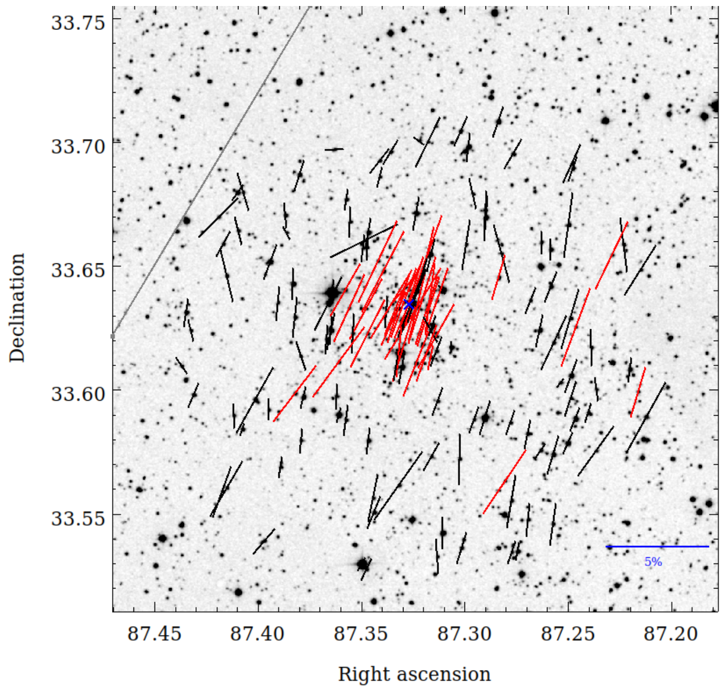

Figure 6.15: Polarization vectors overlaid on DSS, R-band $25' \times 25'$ field towards King 8. The color description is similar to Figure 6.2.

an interesting segregation of the member stars and the field stars. The member stars, indicated by red vectors, are predominantly situated closer to the center of the cluster and exhibit a consistent orientation parallel to the Galactic plane (gray line). In contrast, non-members are primarily located in the outer regions of the cluster, away from the cluster center. Some field stars also display a similar orientation, while a few exhibit significant deviations. In addition, the length of the vectors suggests that most of the member stars possess a similar degree of polarization. On the other hand, the field stars exhibit a considerable scatter in their degree of polarization.

Distribution in $p-\theta$ plane

The distribution of stars in the $p-\theta$ plane reveals two distinct groupings as well as a scattered distribution of some stars. The stars with a low degree of polarization exhibit a wide dispersion in the angle. A bunch of stars characterized by a degree of polarization of approximately 1.5% displays a larger polarization angle of around 165°. In contrast, the other group shows a higher degree of polarization of $\sim 3.3\%$ and has a similar orientation ($\sim 160°$) with lesser dispersion. The latter group contains the

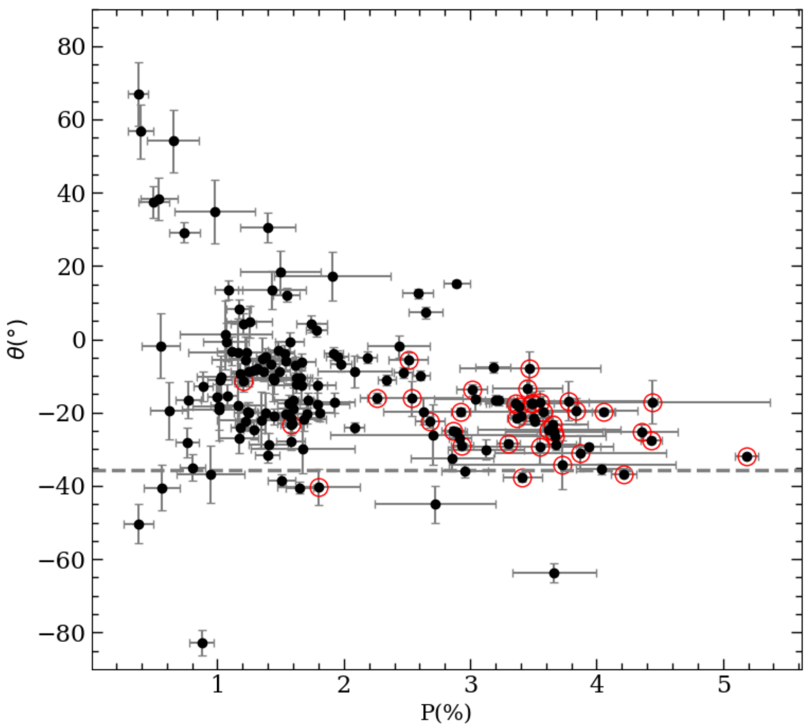

Figure 6.16: Distribution of stars observed towards King 8 in $p-\theta$ plane.

majority of the member stars. However, three-member stars deviate from the trend and display relatively lower degrees of polarization compared to the rest of the member stars (as seen in the former group in Figure 6.16). These stars are located in closer proximity to the central bunch in the spatial distribution.

Dust distribution

To examine the dust distribution at the distant locations, we analyze the variation of the degree of polarization, polarization angle, and extinction with distance as shown in Figure 6.17a and 6.17b. The foreground three stars have a low degree of polarization, a small polarization angle, and lesser dust extinction (see Figure 6.18). The degree of polarization and angle show a jump to higher values but exhibit large dispersion beyond ~ 630 pc. This suggests the presence of a dust layer at ~ 630 pc. The increased degree of polarization at ~ 2200 pc indicates the possibility of a dust layer, but it is not clearly evident due to the substantial dispersion in the degree of polarization and polarization angle. Therefore, we are not considering any layer at ~ 2200 pc. However, a discernible jump in the degree of polarization is observed at ~ 3500 pc. The corresponding polarization angle beyond this layer decreases to ~ 160 with reduced spread. This implies the two foreground layers at ~ 630 and ~ 3500 pc may have similar orientations of the dust grains, causing an increase in the polarization. The variation of extinction also shows similar jumps at these distances.

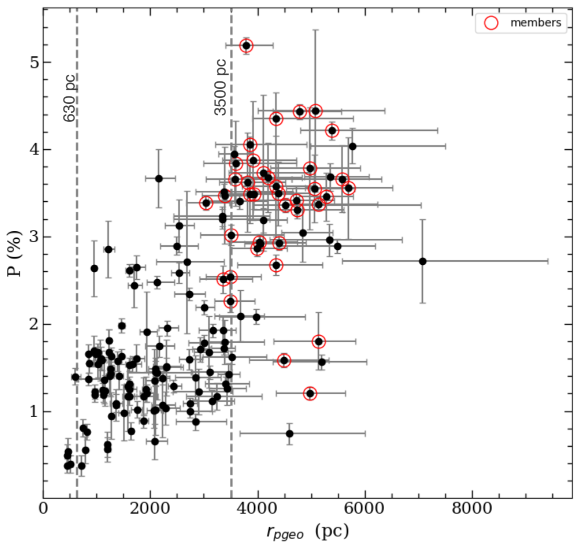

(a) Distance versus degree of polarization

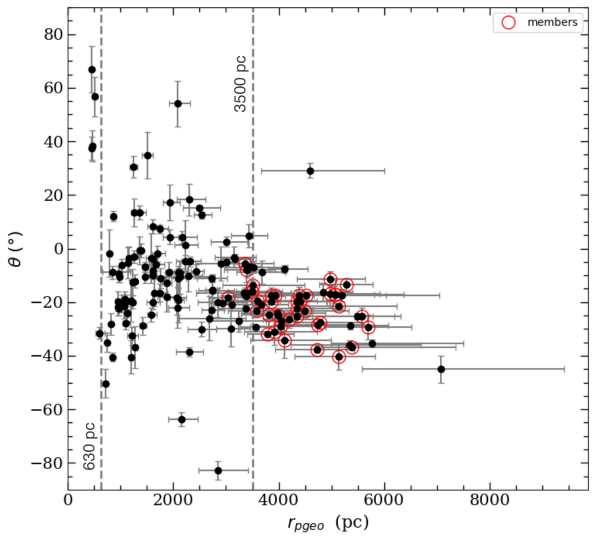

(b) Distance versus polarization angle

Figure 6.17: Variation of degree of polarization and polarization angle as distance, r_{pgeo} towards King 8 in panels (a) and (b), respectively.

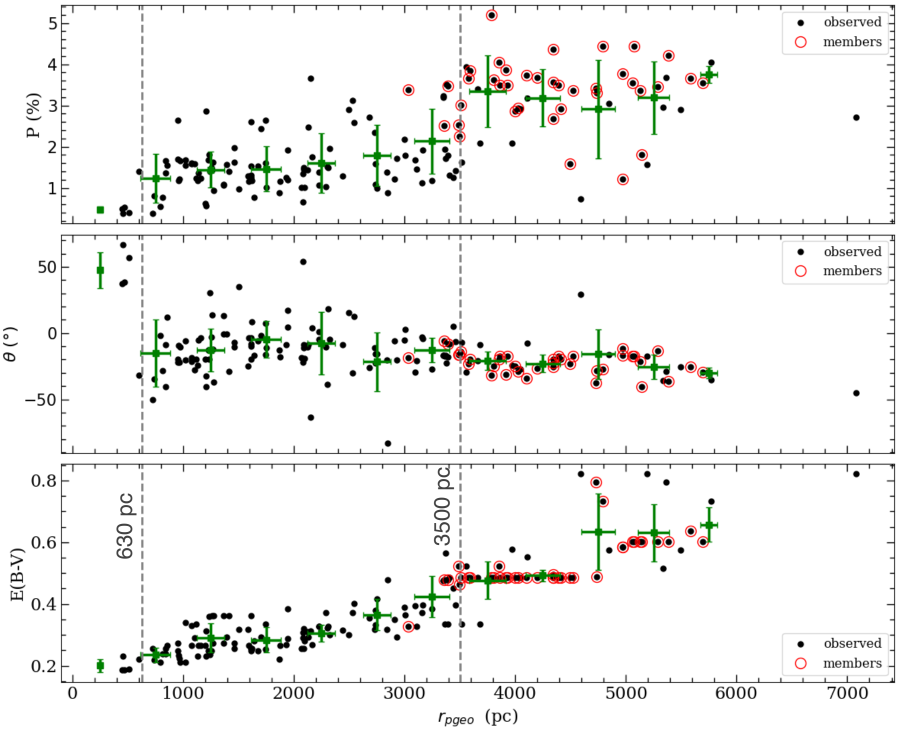

Figure 6.18: Variation of degree of polarization, polarization angle, and reddening, E(B-V) as a function of r_{pgeo}. The vertical lines at r_{pgeo} = 630 and 3500 pc represent the distance of predicted dust clouds towards King 8.

6.2.5 Berkeley 19

This cluster is the most distant cluster in our observation campaign, having a distance of 5.2 kpc towards $\ell = 176^\circ.919$. Like King 8, this cluster is also located at higher latitudes but in the opposite direction, i.e., $b = -3^\circ.62$. Being a very distant cluster, the angular extent of the cluster (= 5.4′, Kharchenko et al., 2013) is lesser than the nearby clusters. The observations of this cluster were performed on October 21, 2022. We observed 88 stars with high-quality polarization measurements; the results are listed in the extended tables. The cluster has 114 members with more than 50% membership probability (Hunt & Reffert, 2023). Out of 114 probable members, only thirty-three stars have Gmag < 17 mag. Thus, observing distant clusters with good SNR with meter-class telescopes becomes difficult. Only four of the eighty-eight stars observed in this direction correspond to the member stars. The weighted polarization of all the eighty-eight stars towards the cluster is 1.32%, 87° and shows large dispersion 1.16% and 50°, respectively, in the degree of polarization and polarization angle.

Polarization vector map

The polarization vectors of 4 members (in red) and 84 field stars (in black) are plotted above the DSS R-band image of Berkeley 19 in Figure 6.19a. The Figure depicts a large scatter in the degree of polarization and the orientation of vectors towards the field, which is expected from the field stars located at different distances.

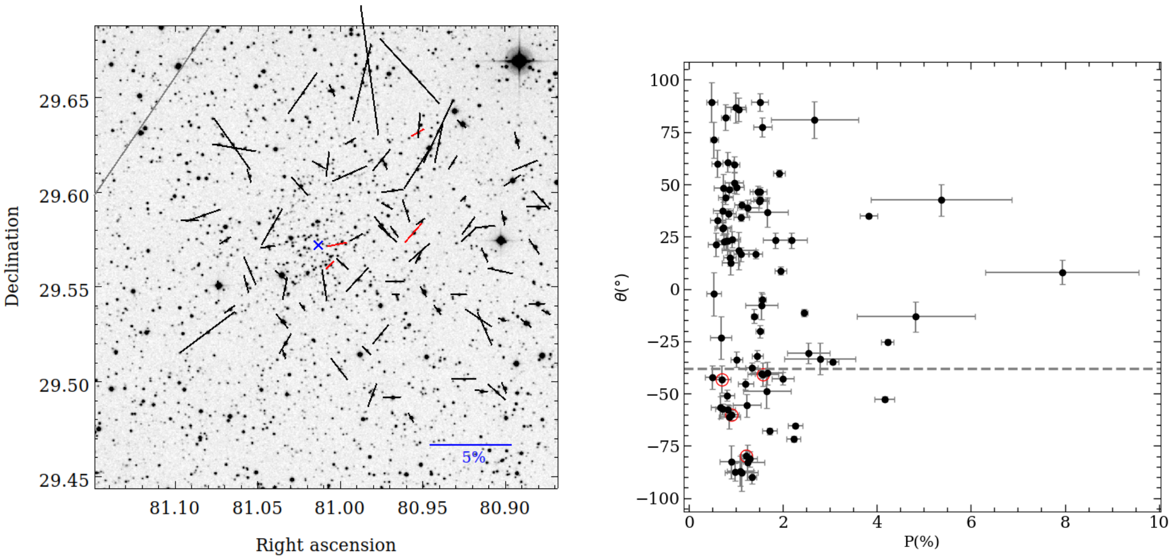

(a) Polarization vector map (b) $P-\theta$ plane distribution

Figure 6.19: Polarization measurements of stars towards Berkeley 19 overlaid on DSS image in the left panel and $P-\theta$ plane in the right panel

Distribution in $p-\theta$ plane

The distribution of stars in the $p-\theta$ plane, shown in Figure 6.19b, does not represent any specified clustering but rather exhibits a low degree of polarization and large scatter in polarization angle. Due to the limited number of member stars (only 4) detected towards this direction, it is difficult to make conclusive statements about the degree of polarization and polarization angle for the cluster.

Dust distribution

The polarization angle shows a change at ~ 970 pc in Figure 6.20b. The stars located at a distance r_{pgeo} < 970 pc exhibit a narrow range in polarization angle with an average of around ~ 40°. However, beyond this distance, the background stars display a

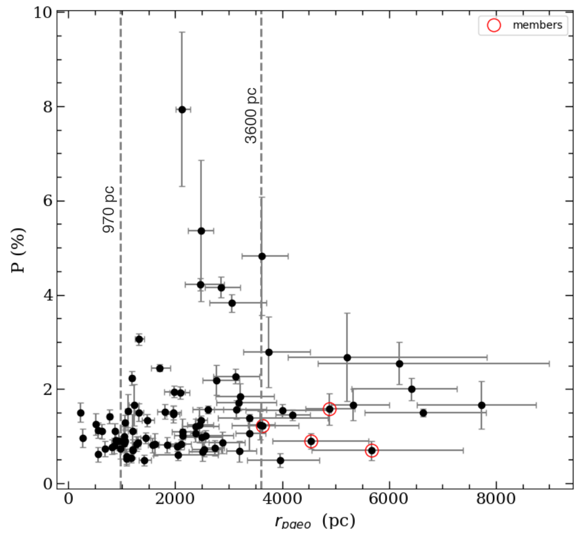

(a) Distance versus degree of polarization

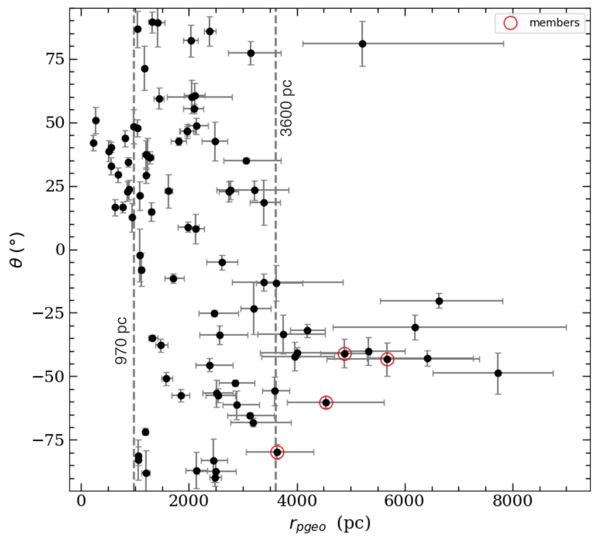

(b) Distance versus polarization angle

Figure 6.20: Variation of degree of polarization (panel a) and polarization angle (panel b) with r_{pgeo} for Berkeley 19.

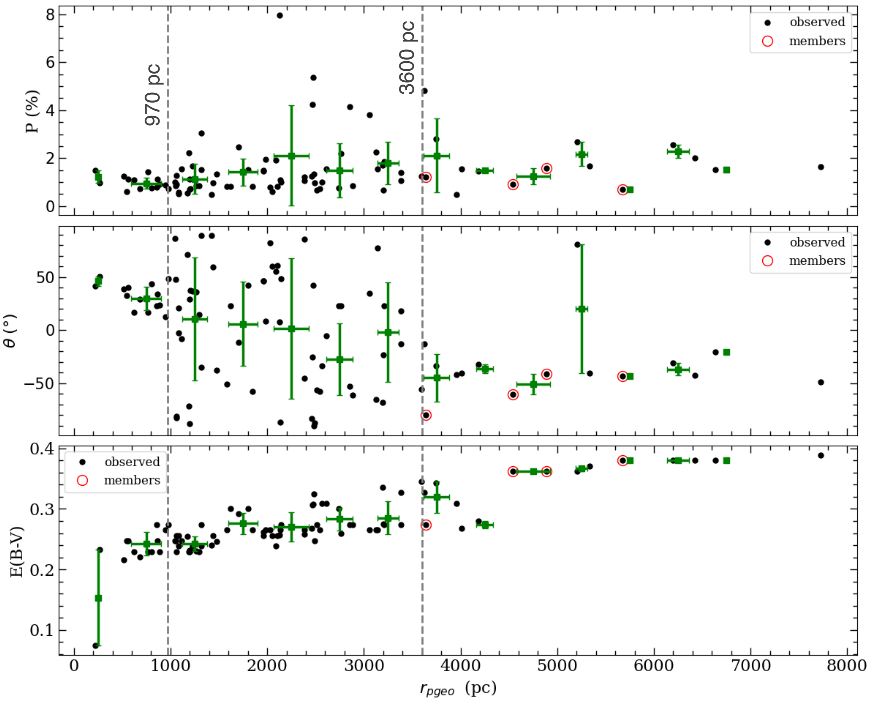

Figure 6.21: Variation of degree of polarization, polarization angle, and reddening, E(B-V) as a function of r_{pgeo} towards Berkeley 19.

significant dispersion in the angle ranging from 0° to 180° (or −90° to +90° as shown in the figure). This suggests the presence of a potential dust layer at around ∼ 970 pc. The dispersion in the angle decreases at approximately 3600 pc. The bottom panel of Figure

6.21 displays the reddening, which also exhibits a jump at ~ 4000 pc. This indicates the presence of a dust layer within the range of $3600-4000$ pc. Furthermore, the E(B-V) in Figure 6.21 shows an abrupt change at around 200 pc, but the corresponding change in the polarization is relatively small. However, it is important to note that this discussion is based on only two stars at that distance. Therefore, due to the limited number of stars available at this location, we do not consider this layer in our interpretation.

6.3 Reconciliation/Validation of distance to the dust layers

The analysis of dust distribution within individual clusters, as discussed in Section 6.2, has revealed the presence of multiple dust layers along the line of sight. However, determining the precise distances to these predicted dust clouds remains challenging, as visual inspection alone provides only rough estimates. To address this issue, we attempted to employ kinematic distance measurements based on spectral information obtained from the HI4PI survey (HI4PI Collaboration et al., 2016) for the diffuse neutral medium, as well as molecular emission data from the ^{12}CO survey by (Dame et al., 2001). However, the obtained kinematic distance corresponding to the HI and CO data towards the anti-center direction using the A5 model following Reid et al. (2014) method (as described in Section 5.3.3) give unreliable values with large uncertainties, as discussed briefly at the beginning of this Chapter. Therefore, a robust criterion is required to quantify the distance of the dust layer toward each line of sight. The two methods used to quantify the distance of the foreground layer are discussed in the following subsections.

6.3.1 Clustering Algorithm

It is supposed that the stars located behind the common dust cloud should exhibit similar polarization and suffer the same extinction unless they have a circumstellar disk or show intrinsic polarization. With this idea, we employed unsupervised machine learning clustering algorithms where the data points are grouped into different sets

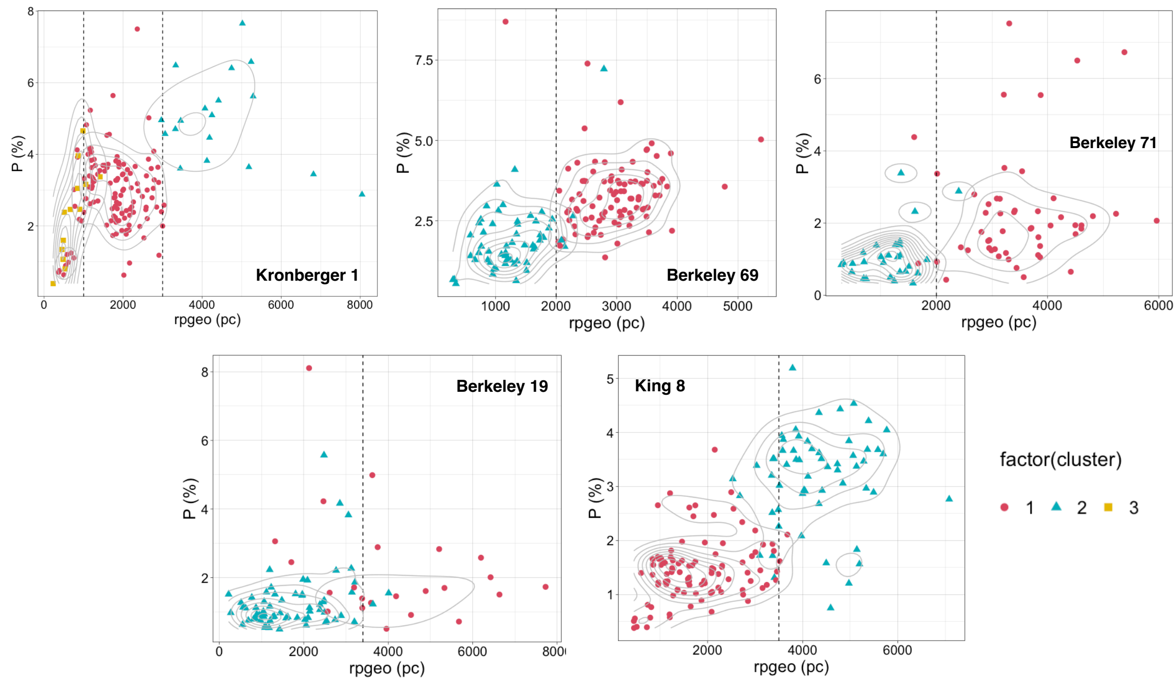

Figure 6.22: Result of K-means clustering algorithm as indicated in the distance versus degree of polarization. The yellow, red, and cyan points represent different K-means clusters, and the dashed vertical lines represent a rough boundary between them. The contours correspond to the number density of stars.

(termed clusters) based on the degree of similarity. In our analysis, we used the K-means clustering method to confirm the presence of predicted dust layers. The K-means algorithm iteratively computes centroids until the optimal centroid is found, i.e., minimizing the sum of squares from the points to their assigned cluster centers.

We utilized various parameters such as the sky position (RAJ2000, DECJ2000), stokes parameter (q and u), reddening, E(B-V), proper motions (pmra and pmdec), and (BP-RP) Gaia colors along with the distance information of each star. These parameters were used as input data for the *kmeans* clustering function in the *stats* library of the R programming language. The function requires the number of clusters to be fitted. The optimal number of clusters (groups) is obtained from the *Nbclust* package of the Nbclust library. It provides 30 indices for determining the best number of clusters for a given data-set. The resulting segregated groups from the clustering algorithm for stars towards each open cluster are visualized using different colors in the plot of r_{pgeo} versus the degree of polarization (see Figure 6.22). The dashed black line in all the panels of the aforementioned figures represents the demarcation of the K-means cluster in the distance. Hence, the line beyond which the ISM properties are changed may represent the location of the dust layer. The clustering algorithm we employed is a statistical method that relies heavily on the sample size. Therefore, the limited number of stars in nearby distances resulted in missing foreground layers in most clusters.

6.3.2 Use of BISP-I algorithm

A Bayesian Inference of starlight polarization algorithm in 1D (BISP-1) has recently been introduced (Pelgrims et al., 2023). This algorithm is specifically designed to estimate the number of foreground dust layers and their distances based on linear polarization measurements of stars along with their distance information. It was developed in the framework of the upcoming PASIPHAE polarization survey. BISP-1 is the first Bayesian inference method developed for the tomographic decomposition of the plane of the sky magnetic field. The algorithm incorporates the polarization signal from the magnetized and dusty interstellar medium (ISM), which is characterized by thin layers at different distances. It uses directly observed quantities such as Stokes q and u parameters, parallax, and their associated errors as input parameters rather than relying on derived polarization and distance information.

We have employed the BISP-1 algorithm on our observation results to confirm and better constrain the distance of the dust layers present along the line of sight. Here, we utilized all the stars without any constraints on the polarization SNR. However, we applied some quality flags to ensure the reliability of a few parameters. Specifically, we considered stars with positive parallax values and a renormalized unit weight error (RUWE) greater than 1.4. A RUWE value above 1.4 indicates the presence of blended sources, which may lead to unreliable parallax information. The results of the BISP-1 algorithm for each cluster direction are presented in Figure 6.23. The figure illustrates the variation of q (in blue) and u (in green) as a function of distance modulus ($\mu = 5\log d - 5$). The solid vertical lines in the figure denote the distance moduli corresponding to the resulting dust layers. The 16^{th} and 84^{th} percentile is marked by the dark-shaded region, while the 2.5 and 97.5 percentile is denoted by the lightly shaded area. The figure clearly demonstrates the presence of multiple dust layers in each cluster direction. The

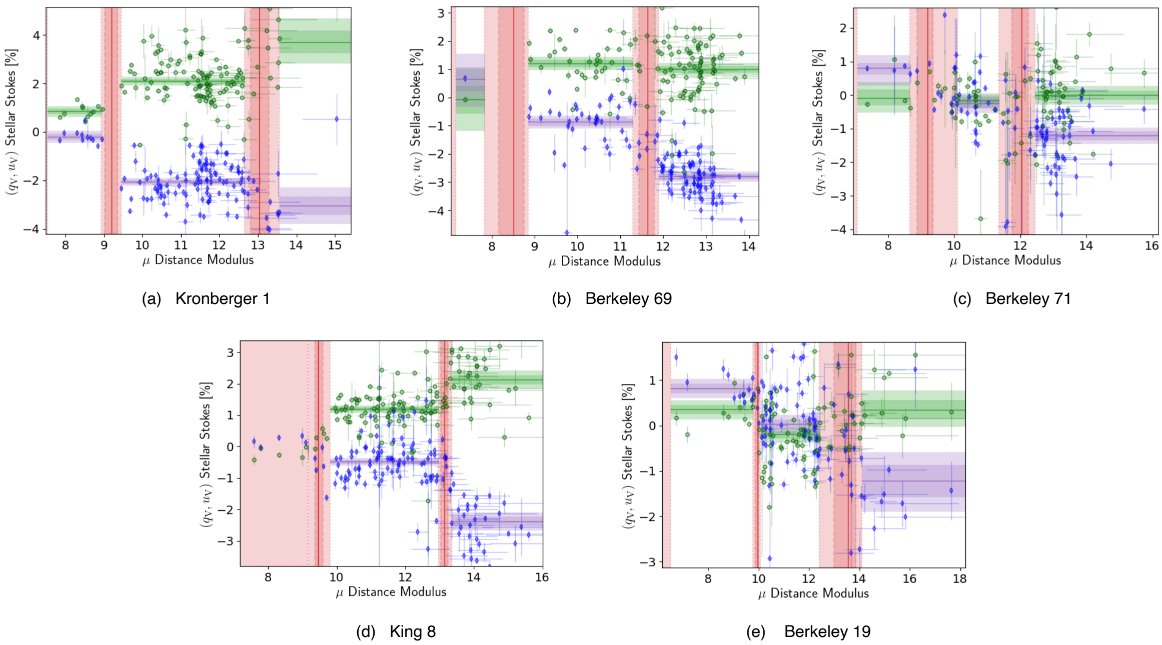

(a) Kronberger 1 (b) Berkeley 69 (c) Berkeley 71

(d) King 8 (e) Berkeley 19

Figure 6.23: Result of BISP-I algorithm indicated in the distance versus q and u plots.

respective distances of these layers are listed in the corresponding column of Table 6.3.

6.4 Signature of Spiral arms

The section 6.3 shows that multiple dust layers exist towards each cluster direction independent of the method employed. The distance of the predicted dust layers from different methods is cataloged in Table 6.3. As described in Section 6.3.1, the clustering algorithm predicted only one layer towards each cluster direction except Kronberger 1. The overlapped region represents uncertainty in the distance of the dust layers along the lines of sight. The distance of the dust layer, within the uncertainties, matches with the prediction from visual inspection. Hence, we are not using the results from the clustering algorithm separately in further analysis.

For better visualization, we plotted the estimated distance of all the dust layers resulting from visual inspection (in the light-red squares) and BISP-1 algorithm (in black points) with error-bars representing 2.5, 16, 84, and 97.5 percentile values in Figure 6.24. The solid vertical lines represent the approximate distance of the spiral arms towards the anticenter direction (Local arm: cyan, Perseus arm: yellow, and Outer

Table 6.3: Details of foreground dust clouds

Cluster	Distance of predicted dust layers		
	Visual inspection	Clustering algorithm	BISP-1 algorithm
Kronberger 1	500, 1600	1000, 3000	89, 688, 4031
Berkeley 69	600, 2100	2000	86, 508, 2128
Berkeley 71	700, 2000	2000	85, 687, 2548
King 8	630, 3500	3400	95, 777, 4242
Berkeley 19	970, 3600	3500	78, 980, 5147

arm: red) determined from Reid et al. (2019) and Castro-Ginard et al. (2021). The cluster names are placed based on their relative latitudes. It is worth noting that the BISP-I estimates the parallax and normalized Stokes parameters of dust layers along the line of sight. Consequently, 1/parallax is used as the distance estimation of those clouds. However, we utilized r_{pgeo} as the distance estimator in the visual inspection and clustering algorithm. For the distant stars (e.g., stars towards the King 8 and Berkeley 19 clusters), the uncertainty in the parallax measurement can increase, and the r_{pgeo} distance will largely depend on the prior assumptions. Hence, the distant clouds may show large deviations in their distance estimated from two methods merely due to the use of 1/parallax in one case and r_{pgeo} in the other. Additionally, BISP-I predicts a dust layer in close proximity to the Sun, i.e., at the distances $d < 100$ pc. Given the limited number of stars within this distance, we cannot infer the presence of this layer from visual inspection. However, since the Stokes parameters of the nearest star (first star according to the distance) do not coincide with $(q, u) = (0, 0)$, it suggests the presence of a dust layer foreground to the nearest star. The distance of this layer deduced by BISP-I is highly reliant on the chosen prior, resulting in the dust layer close to the boundary of the Local bubble.

A careful inspection of Figure 6.1 and 6.24 reveals that Berkeley 69 and Berkeley 71, located between the Perseus arm and the Outer arm, show a presence of a dust cloud at ~ 2000 pc. Notably, this location aligns with the anticipated position of the Perseus arm (depicted by the yellow line) in the anticenter direction. Additionally, NGC 1893 ($\ell = 173°.582$, $b = -1°.659$, and r = 2.8 kpc), another cluster in a similar direction,

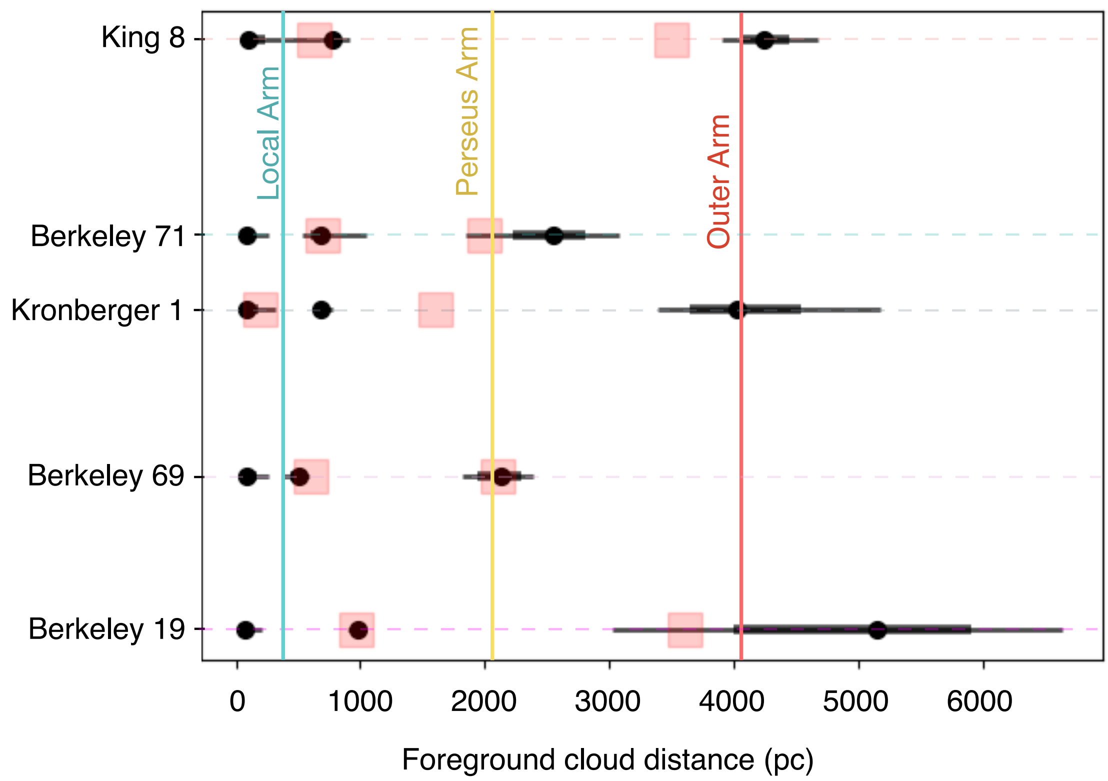

Figure 6.24: The distance of the dust layers towards observed cluster directions predicted from visual inspection (in the light-red squares) and BISP-I algorithm (as black points). The vertical lines represent the distance of the Spiral arms; the Local arm in cyan, the Perseus arm in yellow, and the Outer arm in red.

has been reported to have a dust cloud at a distance of ~ 2 kpc (Bijas et al., 2022). This implies the dust present in the Perseus arm is responsible for the polarization of background stars towards this direction. The Kronberger 1 cluster itself is present in the dusty environment of this arm; hence, difficult to predict the signature of the arm towards this cluster. Furthermore, the distant clusters, Berkeley 19 and King 8, located beyond the Outer arm (see Figure 6.1), despite having opposite latitudes ($-3^\circ.6$ and $3^\circ.1$, respectively), both show a dust layer at approximately $3500 - 4500$ pc. The Outer arm of the Galaxy may also be located at ~ 4000 pc (solid red line, as predicted from the Reid et al. (2019) model on HMSFR data). This suggests that the major changes in the polarization are occurring near the spiral arms of the Galaxy. Thus making polarization an effective tool for understanding the large-scale dust distribution and mapping the underlying structure.

In addition, to our surprise, we noted that the polarization measurements of stars towards the Berkeley 19 and King 8 do not show any strong signatures of the Perseus arm, contrary to our initial expectations. The lack of a dust component around the Perseus arm raises the possibility of variations in the thickness of the spiral arms, with the vertical thickness of the Perseus arm possibly being smaller than that of the Outer arm. As a consequence, the effect of the Perseus arm may be less pronounced at higher latitudes. This speculation is further supported by the fact that the Galactic disk exhibits a flare, i.e., the scale height of the Galactic disk increases with the Galactocentric distance. Therefore, the Outer arm is anticipated to have a greater thickness than the Perseus arm. Another plausible explanation could be the existence of a low extinction window within the Perseus arm, specifically towards King 8 and Berkeley 19. The Mid-IR images obtained from the James Webb Space Telescope (JWST) provide evidence of variations in the dust distribution within the arm. It is possible that the line of sight we are targeting may have less dust to polarize the background stars. To further investigate the possibility, we require polarization observations of distant clusters beyond the Outer arm with large spatial coverage. In any case, our polarization results provide insight into the signature of the large-scale or small-scale structures of the Galactic disk.

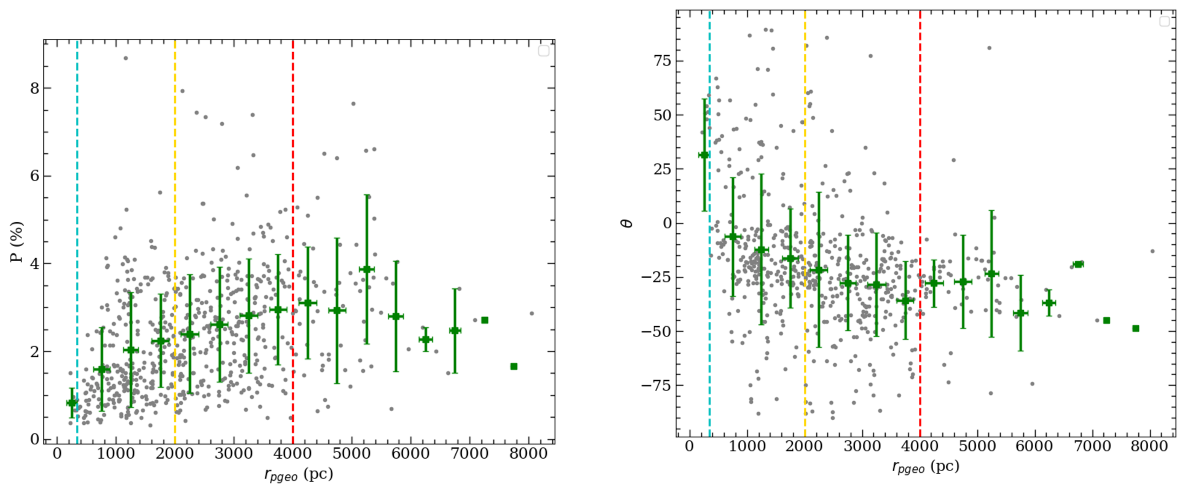

(a) Distance versus degree of polarization

(b) Distance versus polarization angle

Figure 6.25: Variation of degree of polarization (panel a) and polarization angle (panel b) with r_{pgeo} for all the stars observed towards the anticenter direction.

The variation of the degree of polarization and polarization angle of all the stars observed towards the anticenter direction (combined 5 clusters), shown in Figure 6.25, clearly demonstrates the presence of spiral arms. The mean degree of polarization and polarization angle, represented by green squares with error bars indicating the standard deviation of P or θ within each 500 pc bin of r_{pgeo}, exhibit slight changes in proximity to the spiral arms. The positions of the spiral arms are indicated by dashed vertical lines, with color-coding consistent with Figure 6.24.

6.5 Comparative study of all the clusters in the anticenter direction

In this section, we examine the dust distribution on a larger scale by combining our observed cluster data with the data from clusters in the same line of sight available in the literature. We utilize the data of five clusters (represented by black points in Figure 6.1): NGC 2281, Stock 8, NGC 1960, NGC 1931, and NGC 1893, obtained from Eswaraiah et al. (2011); Pandey et al. (2013); Bijas et al. (2022). Among these selected clusters, NGC 1931 and Stock 8 are located in close proximity to the star-forming region in the Perseus arm. NGC 2281 is a foreground cluster situated at a high latitude ($b = 16^{\circ}.9$) and a distance of approximately 500 pc. NGC 1960 is also a foreground cluster with a distance of 1.12 kpc. Only one cluster, NGC 1893, is situated between the Perseus and Outer arms. We cross-matched these clusters with the Hunt & Reffert (2023) catalog to find the member stars having a membership probability of more than 50%. The Galactic position of the clusters (Glon, Glat), their distance (dis), log age, and extinction (A_V) values obtained from Hunt & Reffert (2023) are tabulated in Table 6.4. The number of member stars detected (col: members) after cross-matching, their average degree of polarization (Pol), and polarization angle (PA) are also listed in the table, along with their dispersion (spol and sPA) and measurement uncertainties (epol and ePA). Thus we get the polarization information of 10 clusters (five from the literature and five from our observation) in the anticenter direction, distributed in the distance.

To investigate the variation of polarization of clusters with the distance, we plotted the distribution of the clusters in the Galactocentric XY coordinates in Figure 6.26. Each cluster is represented by a different symbol, and the color of the symbol corresponds to

Table 6.4: The parameters of ten Galactic clusters towards anticenter direction, having polarization measurements from our observations and the literature.

cluster	Glon (deg)	Glat (deg)	dis (kpc)	Pol (%)	spol (%)	epol (%)	PA (deg)	sPA (deg)	ePA (deg)	members	log age	Av
NGC2281	174.892	16.9	0.508	0.9	0.23	0.19	016	06	05	09	8.44	0.22
NGC1960	174.544	1.076	1.125	1.28	0.13	0.22	159	05	05	08	7.43	0.79
Stock8	173.375	-0.190	1.959	2.88	0.7	0.31	153	10	03	05	6.98	1.76
NGC1931	173.914	0.269	2.114	2.62	1.59	0.33	151	11	04	18	7.07	1.92
Kron1	173.106	0.049	2.118	2.53	0.61	0.2	156	06	03	19	6.90	1.19
NGC1893	173.582	-1.659	2.854	2.68	0.34	0.32	160	04	03	23	7.32	1.52
Berkeley69	174.442	-1.851	3.179	3.34	0.89	0.25	142	21	02	48	8.62	2.01
Berkeley71	176.635	0.901	3.502	1.79	0.9	0.23	135	24	03	28	8.57	3.02
King8	176.384	3.104	4.788	3.38	0.79	0.3	158	08	03	38	8.70	2.10
Berkeley19	176.919	-3.612	5.252	1.12	0.33	0.2	124	16	04	04	8.77	1.32

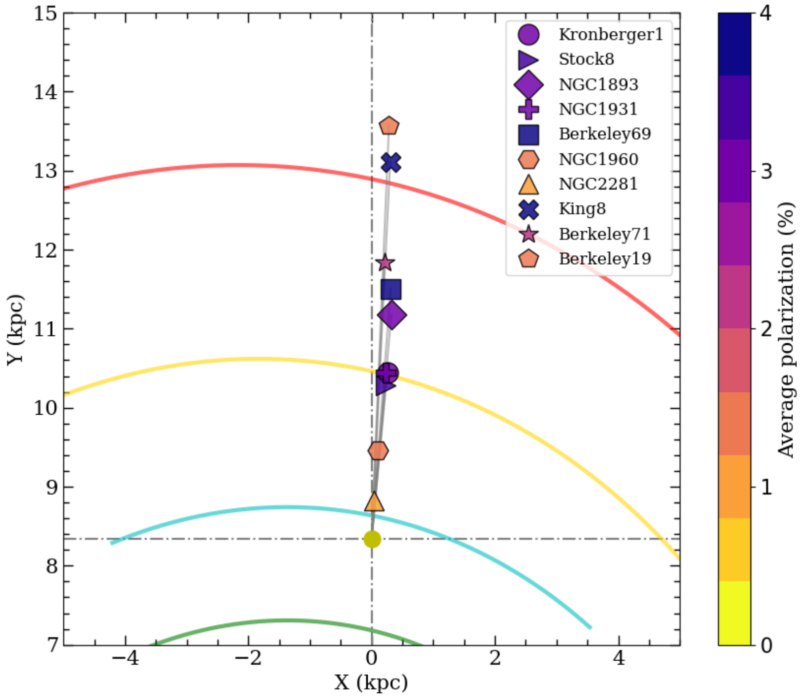

Figure 6.26: Distribution of open clusters (in different symbols) having polarization measurements (from literature and observed as part of the thesis) in anticenter direction with the color-gradient showing the degree of polarization.

the degree of polarization. The color gradient suggests that the polarization increases with distance, except for Berkeley 71 and Berkeley 19. It should be noted that the average degree of polarization for Berkeley 19 is based only on four member stars, which would not be statistically significant. Therefore, we exclude this cluster from our further discussion. A clearer picture of the change in polarization with distance is presented in Figure 6.27a and 6.27b. In these figures, the ellipse surrounding the central symbol represents the dispersion in polarization (P and θ, along the y-axis) of the member stars and the distance of the cluster (determined from the upper bound given in Hunt & Reffert, 2023, in x-axis). The error bar denotes the propagated measurement errors. Figure 6.27 shows that the degree of polarization increases with distance while the polarization angle remains relatively constant. This suggests that the magnetic field in the ISM towards this direction remains almost constant. In this analysis, Berkeley 71 stands out as a special case where there is a localized variation in dust distribution in front of the cluster, resulting in a lower degree of polarization and a wider spread in the polarization distribution. Overall, the anticenter direction represents a low extinction direction with a uniform magnetic field orientation.

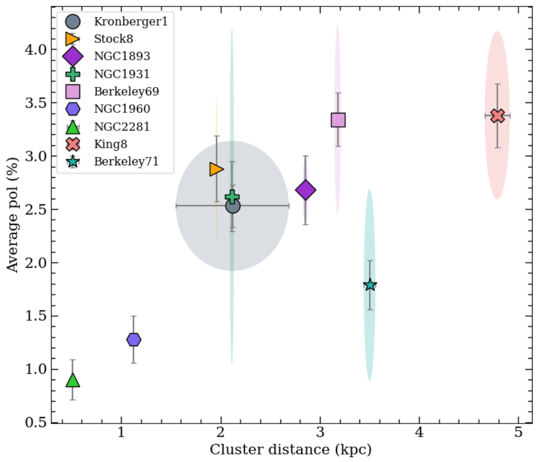

(a) Distance versus average degree of polarization

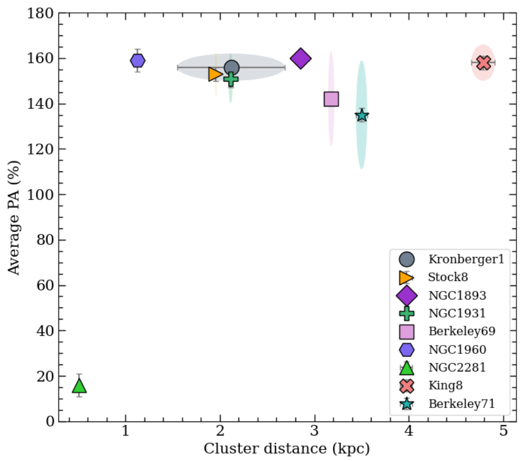

(b) Distance versus average polarization angle

Figure 6.27: Weighted average degree of polarization (panel a) and polarization angle (panel b) versus the distance of each cluster. Further details are described in the text.

6.6 Summary

This chapter provides a detailed study of the polarization observations of five Galactic open clusters distributed with distance in the anticenter direction. Being a low extinction direction, this line of sight offers a great opportunity to probe the polarization of clusters in the distant regions of the Galaxy. The chapter highlights the existence of multiple dust layers along each cluster direction in the local region. By estimating the distances of these dust layers, a coherent global perspective of the dust distribution is established. Our findings indicate that the dust, which contributes to the observed polarization and extinction variations beyond the solar neighborhood (approximately 1 kiloparsec), is primarily concentrated within the Perseus arm and Outer arm of the Galaxy. However, the absence of a discernible Perseus arm signature in the higher latitude regions ($|b| > 3°$) could either be related to the local structures within the spiral arm or the difference in the thickness of the two arms. An interpretation that the Perseus arm is thinner than the outer arm is consistent with the increase in thickness due to disk flaring. Systematic, deep polarization observations are required towards the distant regions of the Galactic plane to investigate both aspects and infer the small-scale and large-scale structures of the spiral arms. Based on the analysis described in this chapter, we conclude that the anticenter direction is characterized by low extinction and minimal local or small-scale variations. Any observed changes in polarization or extinction along this direction can be attributed to global features, such as the presence of spiral arms. Overall this chapter provides a comprehensive study highlighting the applications of linear polarization observation in deciphering the structure of the Galaxy at different scales.

Chapter 7

Polarization study in a direction tangential to the spiral arms

"The reward of the young scientist is the emotional thrill of being the first person in the history of the world to see something or understand something. Nothing can compare with that experience."

- Cecilia Payne-Gaposchkin, *1977*

The anticenter direction, discussed in Chapter 6, offered a unique opportunity to study the dust distribution at distant regions due to lesser extinction. In contrast, the inner regions of our Galaxy, particularly those towards the first Galactic quadrants, are characterized by a high concentration of stars and dust. Despite the presence of numerous stars, only four Galactic open clusters, NGC 6871 (Grigorian, 1968), NGC 6611 (Bastien et al., 2004), NGC 6823 (Medhi et al., 2010), and NGC 6709 (Topasna et al., 2022) have been previously observed using polarimetry towards this direction. The location of these four clusters in the Galactocentric XY-plane is shown as black points in Figure 7.1. The different color solid lines represent the position of spiral arms

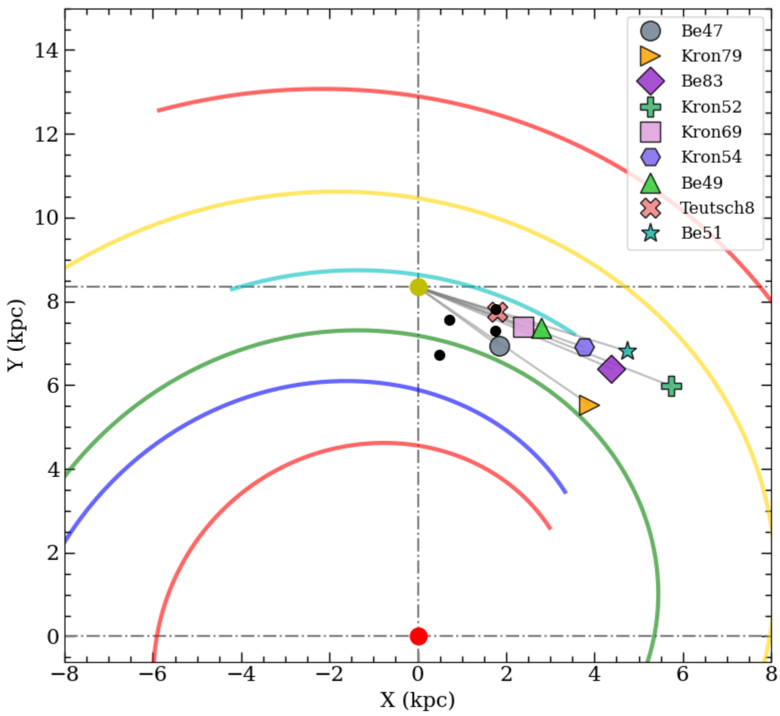

Figure 7.1: The distribution of Galactic open clusters (colored symbols) studied in this thesis towards the first Galactic quadrant. The black points represent the clusters with polarimetric measurements available in the literature.

with similar color-coding as shown in Figure 4.4. Moreover, these clusters are located at a distance of less than 2 kpc. The limited observations in this direction could be attributed to the larger dust extinction and high crowding. We, attempted to observe multiple clusters located at different distances towards the first Galactic quadrant with the aim of investigating the dust distribution and exploring both the large-scale as well as small-scale structures of the Galactic disk. Unlike the other two directions discussed in Chapter 5 and Chapter 6, where the line of sight intersected the spiral arms, the line of sight in this particular direction allowed us to focus our observations along the direction tangential to the spiral arms. We selected nine clusters, Teutsch 8, Berkeley 47, Kronberger 69, Berkeley 49, Kronberger 54, Kronberger 79, Berkeley 83, Berkeley 51, and Kronberger 52, in this direction, as shown by different color symbols in Figure 7.1. The clusters are selected carefully based on the target selection criteria discussed in Section 4.4.1. The selected targets are distributed at different distances, covering a range of $2-6$ kpc and are aligned along two closely spaced lines of sight. All the selected clusters reside in the Galactic plane ($|b| < 3°$).

In this chapter, We analyze the polarization results of each individual cluster to gain insights into the dust distribution in local regions. Additionally, we combine the observation results from all clusters to investigate the large-scale morphology and magnetic field in the diffuse ISM of the Galaxy.

7.1 Observation and data reduction

The polarization observations of Galactic open clusters in the first Galactic quadrant were conducted on multiple nights from January 2021 to October 2022. The optimal visibility of objects in this Galactic quadrant, from the observational facilities used in this thesis (discussed in Chapter 4), occurs mainly during the Indian monsoon season, typically from June to August. Therefore, observing open clusters in this direction becomes challenging due to the reduced number of clear nights during the monsoon season. Nonetheless, we targeted twelve clusters for observations in the months of April, October, and November, when the clusters were visible during the rising or setting phase. The observations were primarily carried out using the EMPOL instrument at Mount Abu, PRL. Due to poor sky conditions on many nights, we could not use the multiple pointings to capture the entire cluster. Nevertheless, we successfully observed the core region of nine clusters, covering a longitude range of $\ell = [52^\circ, 72^\circ]$ within the Galactic plane. Among these nine clusters, the distant clusters have smaller apparent sizes but higher crowding. Since the overlapping issue becomes multifold in the case of AIMPOL, the distant clusters were preferably observed from the EMPOL. On the other hand, the nearby clusters with sparse distribution were targeted by AIMPOL. The EMPOL observations include, Berkeley 83, Kronberger 52, Kronberger 79, Berkeley 51, Kronberger 54, and Teutsch 8. All the observations were carried out in an R-band filter. Detailed information regarding the observations from EMPOL is listed in Table 7.1. It is important to note that the table only includes dates where observations were successful.

As discussed in Section 4.3.1, the HWP rotates in 48 steps in EMPOL, with a time of 0.5 sec between each step. Therefore, 0.5 sec is the individual exposure time per frame. The number of frames obtained for a given effective exposure is calculated by equation

Table 7.1: Observational details of the clusters targeted in the first Galactic quadrant from EMPOL.

Cluster	RAJ2000 (°)	DECJ2000 (°)	Observation date	exposure per per HWP*
Berkeley 83	300.356	28.643	November 2, 2021	10×6,
			November 3, 2021	10×7
Kronberger 52	299.539	30.879	December 3, 2021	$10\times2+20\times1$
Kronberger 79	293.476	18.518	April 01, 2022	30×3
Berkeley 51	302.972	34.404	April 27, 2022	30×4
			April 28, 2022	$30\times3+20\times1$
Kronberger 54	300.780	31.964	October 23, 2022	10×7
			October 24, 2022	30×3
Teutsch 8	300.602	35.307	November 27, 2022	30×2

*The effective exposure time × number of sets observed at each position of HWP position.

4.5. We utilized ~30 s effective exposure for most of the cluster observations. Hence, a total of 2928 frames were captured, with each frame having an effective exposure time of 0.5 s. Acquiring this number of frames takes approximately 48.8 minutes of observation time. Multiple sets of such exposures were captured to enhance the SNR. The fifth column in Table 7.1 indicates the effective exposure acquired per HWP position, multiplied by the number of sets for the same exposure. The variation in exposure time among different clusters listed in the table primarily depends on the availability of the cluster on a given night.

Unlike EMPOL, the observations carried out with AIMPOL do not face any limitations regarding exposure per frame. This is because the HWP in AIMPOL rotates in four steps and requires user input to move from one position to another. With the allotted observation time on the Sampurnanand telescope, we observed three nearby clusters belonging to the first Galactic quadrant; Berkeley 47, Kronberger 69, and Berkeley 49. The observation details of these clusters are presented in Table 7.2. Apart from the cluster observations, many calibration frames were acquired in both instruments to test the instrument efficiency, especially in the case of EMPOL. Polarized

Table 7.2: Observational details of the clusters targeted in the first Galactic quadrant from AIMPOL.

Cluster	RAJ2000 (°)	DECJ2000 (°)	Obs date	Exposure time**
Berkeley 47	292.126	17.361	October 19, 2022	30, 10, 3
Kronberger 69	300.509	31.420	October 21, 2022,	75, 60, 30
Berkeley 49	299.869	34.643	October 23, 2022	75, 60

**The exposure time set at each position of HWP position.

and unpolarized stars were observed on each night to correct the measurements for instrumental polarization and position angle corrections.

The observed data were processed using fully-automated self-scripted Python routines discussed in Section 4.5.2 both for EMPOL and AIMPOL. The measured degree of polarization and angle is corrected from the instrumental polarization. The obtained polarization angle of the stars were also corrected to the reference angle (measured from the North to the East) from the polarized standard star observations. Since the AIMPOL observations of the first quadrant clusters were carried out on the same night as that of the anticenter clusters, we used common standard stars, and the details of those are already described in Table 6.2. A similar table depicting the measured polarization of the standard star from the EMPOL and the reference values from Schmidt et al. (1992) is presented in Table 7.3.

7.2 Polarization results

This section discusses the results obtained from the observation of nine clusters in the first Galactic quadrant. In the case of the three clusters observed from AIMPOL, we included the stars having polarization SNR of more than 3 in our analysis. In the case of EMPOL observations, since we targeted distant clusters, which are expected to be fainter than the nearby clusters selected for AIMPOL observations, we utilized a cut of polarization SNR of more than 1. Nevertheless, we have implemented the Ricean bias correction (as explained in Section 5.1.1) in all the observed polarization to account

Table 7.3: Details of the observed polarized standard stars from EMPOL.

Date	Star	$P \pm \epsilon_P$ (our work)	$\theta_{obs} \pm \epsilon_\theta$ (our work)	$P \pm \epsilon_P$ (Schmidt et al., 1992)	$\theta \pm \epsilon_\theta$ (Schmidt et al., 1992)	offset
Nov 02, 2021	HD25443	4.77 ± 0.19	-79 ± 6	4.734 ± 0.045	133.65 ± 0.28	213
	HD245310	4.01 ± 0.07	-65 ± 7	4.690	146	211
Nov 03, 2021	HD25443	4.95 ± 0.06	-55 ± 6	4.734 ± 0.045	133.65 ± 0.28	189
	HD245310	3.95 ± 0.23	-54 ± 6	4.690	146	200
Dec 03, 2021	HD25443	4.45 ± 0.16	-39 ± 1	4.734 ± 0.045	133.65 ± 0.28	173
	HD245310	3.67 ± 0.29	-06 ± 2	4.690	146	152
Apr 01, 2022	HD154445	3.41 ± 0.14	-66 ± 1	3.683 ± 0.072	88.91 ± 0.56	155
	HD155197	3.97 ± 0.15	-63 ± 1	4.274 ± 0.027	102.88 ± 0.18	165
	HD161056	4.04 ± 0.20	77 ± 1	4.012 ± 0.032	67.33 ± 0.23	170
Apr 27, 2022	HD154445	3.78 ± 0.16	-54 ± 2	3.683 ± 0.072	88.91 ± 0.56	143
	HD155197	4.15 ± 0.21	-54 ± 3	4.274 ± 0.027	102.88 ± 0.18	157
Apr 28, 2022	HD154445	3.83 ± 0.06	-62 ± 1	3.683 ± 0.072	88.91 ± 0.56	151
Oct 23, 2022	BD+59 389	6.35 ± 0.12	-65 ± 2	6.430 ± 0.022	98.14 ± 0.10	163
Oct 24, 2022	HD25443	4.76 ± 0.12	-28 ± 4	4.734± 0.045	133.65 ± 0.28	162
	BD+59 389	5.53 ± 0.86	-67 ± 4	6.430 ± 0.022	98.14 ± 0.10	165
Nov 27, 2022	HD245310	4.17 ± 0.43	-15 ± 5 4.690	4.690	146	161
	BD+59 389	6.37 ± 0.01	-66 ± 1	6.430 ± 0.022	98.14 ± 0.10	164
	BD +64106	5.11 ± 0.32	-63 ± 3	5.150 ± 0.098	96.74 ± 0.54	160
	HD19820	4.66 ± 0.28	-50 ± 3	4.562 ± 0.025	114.46 ± 0.16	164

for any bias occurring due to the low SNR. The polarization measurements, i.e., the debiased degree of polarization, polarization angle, and Stokes q and u parameters, along with their errors for stars observed towards each cluster, are presented in the extended tables[1] of Chapter 7 in the electronic format. Furthermore, the stars with membership probability greater than 50% are considered as member stars (Hunt & Reffert, 2023). A brief discussion of the obtained results is presented in the following subsections.

[1]https://drive.google.com/file/d/1MoqpSfXwIG9SwEw12FnuVrpTOmpcQlQH/view?usp=sharing

7.2.1 Polarization vector maps

The polarization results, i.e., the debiased degree of polarization and polarization angle, are visually represented as vectors overlaid on PanSTARRS g-band images (for EMPOL) or DSS R-band images (for AIMPOL) to illustrate the sky projection (Figure 7.2). Various panels from 7.2a to 7.2i correspond to the clusters placed in increasing order of longitude. The red lines in the figures represent the polarization vectors of probable member stars, while the black lines correspond to the non-member stars. A solid gray line in all the panels depicts the Galactic parallel corresponding to the orientation of the Galactic plane. At the bottom-right side of each panel, a blue reference line is displayed, which indicates 5% polarization oriented at 90° to the North celestial pole. Panel 7.2a, 7.2e, and 7.2g depict a larger field as the corresponding clusters were observed from AIMPOL, while the rest of the panels represent various clusters observed from EMPOL, with a field size of 3′ around each cluster.

In Panel 7.2a, it is evident that all the member stars in the Berkeley 47 cluster exhibit a consistent orientation, while non-member stars show some deviation. Notably, none of the stars, whether members or field stars, are aligned parallel to the Galactic plane. Furthermore, this direction is nearly tangential to the Sagittarius arm. In contrast, Panel 7.2b, which represents a line of sight located approximately 2° away in longitude but at a larger distance ($\sim$ 4.7 kpc), exhibits an even larger deviation in the polarization angle from the Galactic plane. Additionally, the size of the vector lines, representing the degree of polarization, decreases compared to the foreground cluster, Berkeley 47 (at a distance of $\sim$ 2.3 kpc).

The remaining clusters in the line of sight ranging from $66° \leq \ell \leq 72°$ are presented in panels 7.2c to 7.2i. Teutsch 8 (panel 7.2h) is the closest cluster in this direction, situated at a distance of approximately 1.9 kpc. We observed this cluster with a single EMPOL pointing, considering it to be a small cluster with a core radius of 0.9′ (Kharchenko et al., 2013). However, a recent study by Hunt & Reffert (2023) utilizing the latest Gaia data release, Gaia DR3, estimated the core radius of the cluster to be approximately 37′.35. Nevertheless, the observed field stars and the member stars exhibit a low degree of polarization and an approximately similar orientation as that of the Galactic plane.

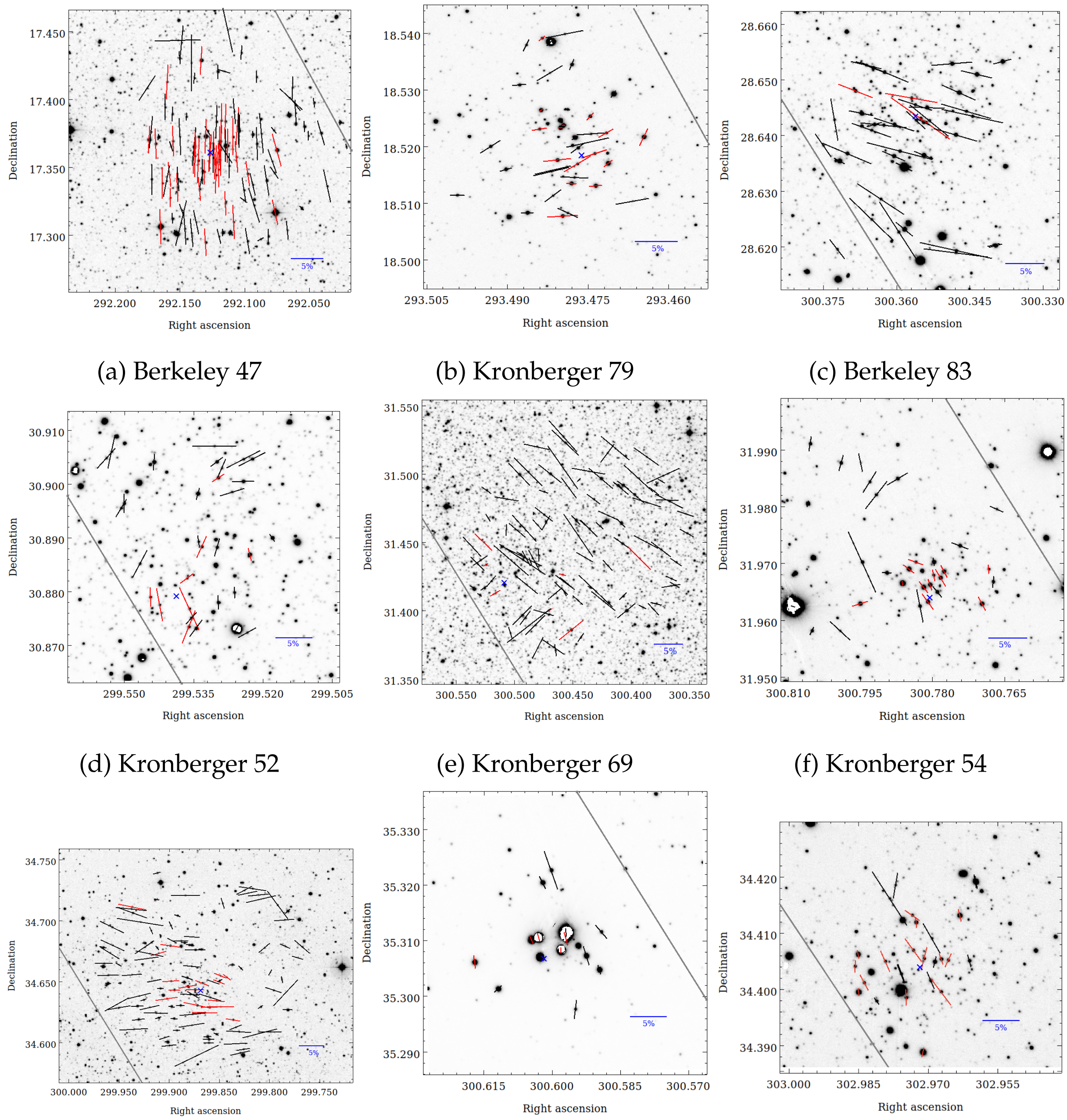

(a) Berkeley 47 (b) Kronberger 79 (c) Berkeley 83

(d) Kronberger 52 (e) Kronberger 69 (f) Kronberger 54

(g) Berkeley 49 (h) Teutsch 8 (i) Berkeley 51

Figure 7.2: Sky projection of polarization vector towards respective clusters.

The average degree of polarization of the member stars is found to be ~ 1.14%. Similar results were obtained for the cluster NGC 6871 (Serkowski, 1965) ($\ell = 72^\circ.658$, and $b = 2^\circ.012$), located at a similar distance (1.8 kpc) in the line of sight. Moving towards longer distances, Kronberger 69 (panel 7.2e), located at approximately 2.6 kpc, shows predominantly off-centered measurements, with most of the stars being field stars. These stars align more closely with the Galactic plane and demonstrate a relatively higher degree of polarization. Additionally, the polarization angle appears to get changed closer to the center of the cluster. This suggests a possible change in the plane of the sky magnetic field in local regions, although further confirmation would require polarization measurements centered on the cluster region. Panel 7.2g displays the polarization vector plot of stars observed towards Berkeley 49, which is situated at a slightly higher Galactic latitude ($b = 2^\circ.58$) but at a similar distance (~ 2.9 kpc) as that of Kronberger 69. The polarization vectors of the members, as well as field stars, exhibit a large deviation from the Galactic plane with an average degree of polarization of $\sim 3.5\%$. It is interesting to note that the degree polarization of the cluster members decreases with increasing distance to the cluster. For instance, the polarization vector plot of Kronberger 54, located at a distance of ~ 4 kpc (shown in panel 7.2f), exhibits a decrease in the degree of polarization, and the polarization angle seems to become more aligned with the Galactic plane. The more distant clusters Berkeley 83 (panel 7.2c, distance = 4.8 kpc), Berkeley 51 (panel 7.2i, distance = 5 kpc), and Kronberger 52 (panel 7.2d, distance = 6.2 kpc) also exhibit similar orientation with the Galactic plane.

7.2.2 Dust distribution towards individual clusters

To investigate the dust distribution along the line of sight, we cross-matched the polarization data of stars observed towards each cluster with the Gaia EDR3 distance catalog and plotted the degree of polarization and polarization angle as a function of distance. As discussed in Section 6.2, the number of jumps observed in the polarization of stars depicts the number of foreground layers, and the location of the jump is considered as the probable location of the dust layer along the line of sight. The variation of the degree of polarization and polarization angle towards each cluster are displayed in multiple panels of Figure 7.3 and 7.4.

In the case of Berkeley 47, situated deep within the Galactic plane with $\ell = 52^\circ.544$ and $b = -0^\circ.048$, we observed that the minimum degree of polarization among nearby stars (distance < 400 pc) is approximately 1%. However, the first nearest star in Figure 7.3a shows a degree of polarization of $\sim 2\%$. It is worth noting that this particular star has a RUWE parameter of 2.024 (> 1.4), indicating a potential blended source. Consequently,

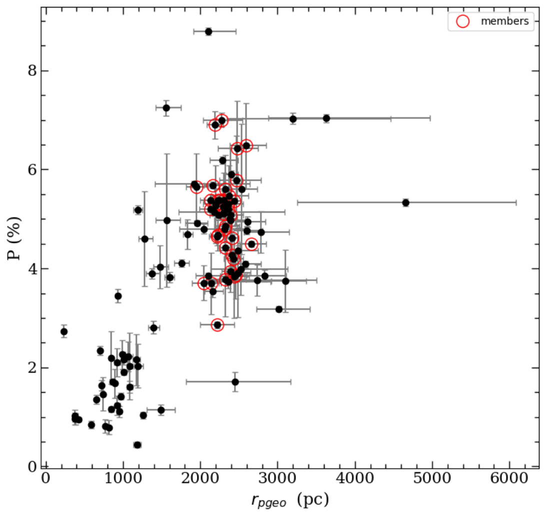

(a) Distance versus degree of polarization

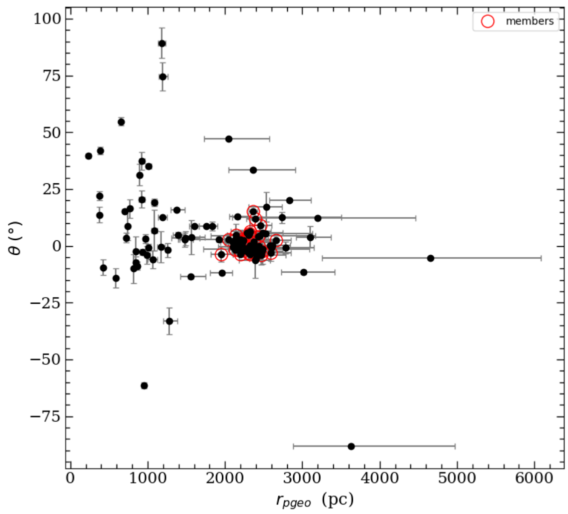

(b) Distance versus polarization angle

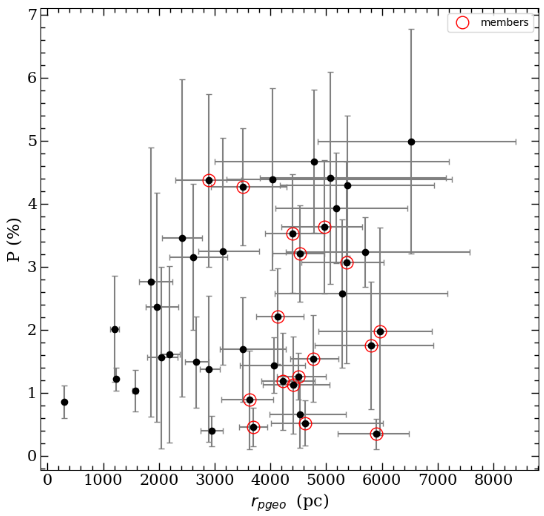

(c) Distance versus degree of polarization

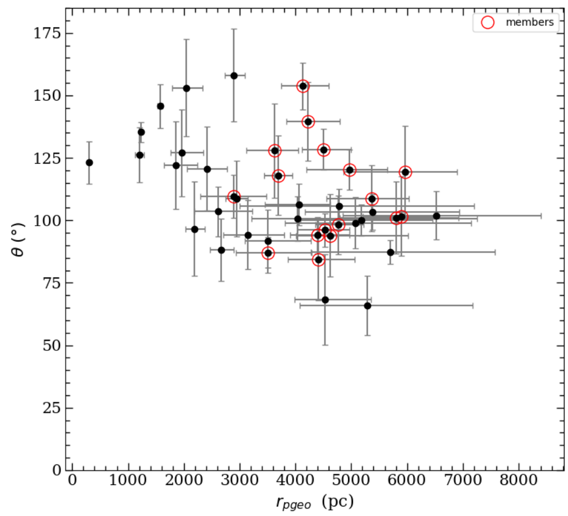

(d) Distance versus polarization angle

Figure 7.3: Variation of degree of polarization and polarization angle as a function of distance (r_{pgeo}) for Berkeley 47 (in the panel a and b) and Kronberger 79 (in panels c and d).

the astrometry and derived distance for this star may be erroneous. Nevertheless, the presence of other nearby sources with a degree of polarization of approximately 1% suggests the existence of a foreground layer below 400 pc that polarizes stars located beyond it. As we increase the distance, the degree of polarization gradually increases, indicating a uniform distribution of dust but displaying a significant spread in the polarization angle. Furthermore, a distinct increase in the degree of polarization from 2.5% to approximately 4% is noted at a distance of ~ 1200 pc. Interestingly the dispersion in the polarization angle also decreases beyond this distance, implying the presence of a dust cloud at approximately 1200 pc. This observed jump in polarization measurements aligns with the predicted change in extinction from the extinction maps by Green et al. (2019).

The distant cluster Kronberger 79 is located approximately 4.8 kpc from the Sun, at Galactic coordinates $\ell = 54°$ and $b = -0°.611$, roughly ~ 2 degrees away from Berkeley 47. The variation in the degree of polarization and polarization angle with distance towards Kronberger 79 are shown in Figure 7.3c and 7.3d. Similar to Berkeley 47, the closest star shows the degree of polarization of $\sim 1\%$ and then increases. However, as the distance increases, the degree of polarization demonstrates a significant scatter, ranging from approximately 0.1% to 5%. The corresponding polarization angle also displays substantial dispersion. This may suggest the presence of a foreground layer similar to what was observed for Berkeley 47. However, due to the limited number of stars in the foreground region, it is challenging to accurately determine the distance of this layer. In contrast to Berkeley 47, the polarization measurements of stars towards Kronberger 79 do not exhibit a similar pattern of a sudden increase in the degree of polarization from 2% to 4%. This absence suggests the lack of a dust layer at approximately 1200 pc in the direction of Kronberger 79. Therefore, it can be inferred that the dust layer observed around 1200 pc towards Berkeley 47 could possibly be confined to localized regions specific to that particular cluster.

In the second line of sight, with Galactic longitude ranging from $l = [66°, 72°]$, Teutsch 8 is the nearest cluster. Despite observing only 15 stars in this direction, the variation of the degree of polarization with distance, as displayed in the top panels of Figure 7.4, shows a systematic decrease in the degree of polarization with increasing distance. However, the stars towards Kronberger 69, shown in the second row from the top in Figure 7.4, exhibit an increase in polarization with a large spread in the degree of polarization. There is an indication of a foreground cloud at ~ 500 pc, beyond which the degree of polarization exhibits a wide range. This suggests that the dust distribution along this line of sight may be relatively uniform, but the orientation of the dust grains changes with distance. In other words, the magnetic field does not seem to exhibit a preferred orientation when observing towards this line of sight.

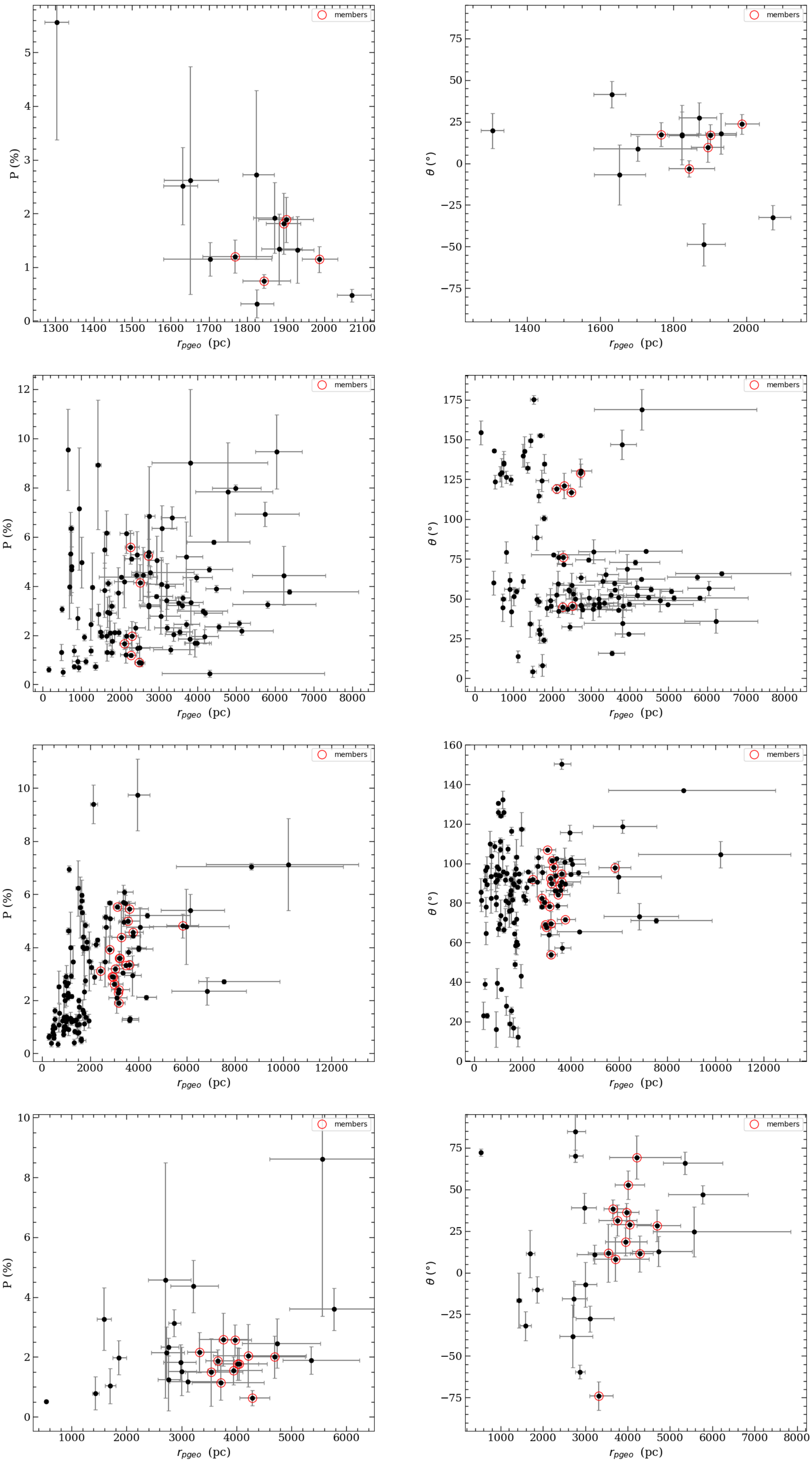

Figure 7.4: Similar to Figure 7.3 but for Teutsch 8, Kronberger 69, Berkeley 49, and Kronberger 54 in the first, second, third and fourth row, from the top, respectively.

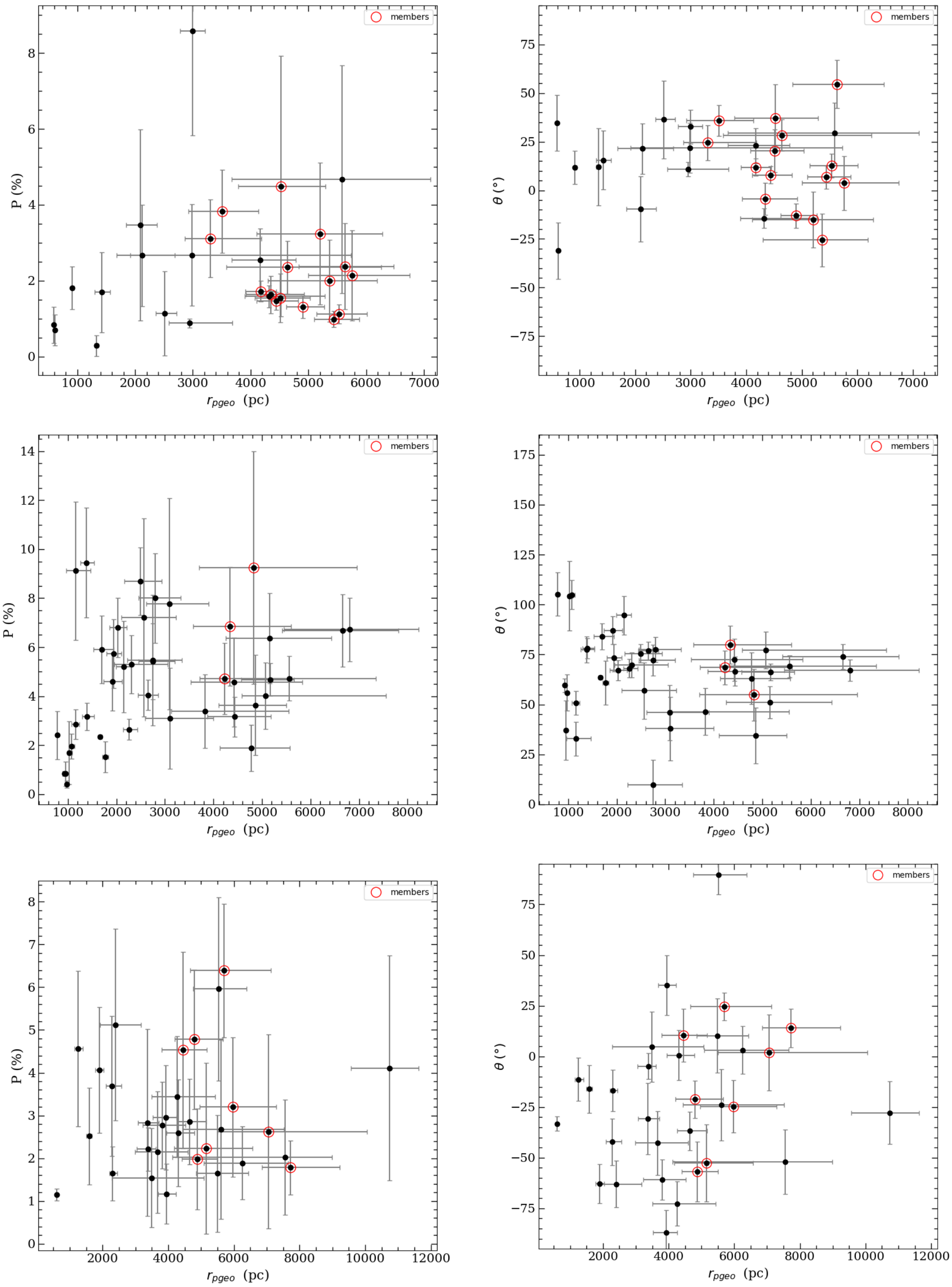

Figure 7.5: Variation of degree of polarization and polarization angle as a function of distance (r_{pgeo}) for Berkeley 51 (top panels), Berkeley 83 (middle panels), and Kronberger 52 (bottom panels).

Stars towards Berkeley 49 (top third row panels of Figure 7.4) display the presence of multiple dust layers below 2000 pc, i.e., at 200, 500, and 800 pc. However, the polarization angles exhibit significant spread. The foreground dust layers observed in Berkeley 49 (from AIMPOL, covering a larger field) cannot be predicted in the case of the EMPOL data, as the observations only encompass a smaller area of $3' \times 3'$. This region primarily consists of the cluster core, which is expected to be dominated by cluster members and distant stars. Consequently, due to the limited statistics for the foreground stars at that specific location, it becomes challenging to determine the distances of those layers. Moving to the more distant cluster Kronberger 54 (bottom panels of Figure 7.4), having a distance of 4.0 kpc, we observe greater deviations in both polarization and polarization angle for the foreground stars, while these deviations seem to decrease for the cluster members. The wide range of polarization angles and degrees of polarization indicates significant variations in the plane of the sky magnetic field. The remaining distant clusters, Berkeley 51, Berkeley 83, and Kronberger 52 (Figure 7.5), also exhibit a similar pattern, suggesting the presence of a foreground layer probably around 500 pc, but beyond that, the distribution of polarization measurements with distance shows considerable variation.

7.3 Galactic structure and Galactic magnetic field

Section 7.2.2 provides a detailed analysis of the variations in the degree of polarization and polarization angle of stars towards each cluster as a function of distance. The results reveal that, in the majority of cases, a foreground dust layer is present, typically situated at distances within $\lesssim 500$ pc. However, as we observe the more distant regions in the direction of each cluster, a significant scatter in both the degree of polarization and polarization angle becomes evident. This pattern could be attributed to the clumpy distribution of the dust towards the observed regions. The speculation is supported by the non-existence of the dust layer at ~ 1200 pc for the stars observed towards Kronberger 79, in comparison to Berkeley 47, which is located in the line of sight merely $\sim 2^{\circ}$ away, indicating the presence of patchy dust distribution in a small region. The non-uniform or clumpy dust distribution explains the large range of polarization observed at similar distances.

Moreover, the large scatter in the degree of polarization and polarization with distance could be due to the varying alignment of the magnetic field itself. This variation in alignment can lead to the random plane of sky orientation of dust grains, thus introducing a large scatter in the observed polarization. Studies of external galaxies such as M51 and others have revealed that the magnetic field tends to align parallel to the spiral arms (Fletcher et al., 2011; Beck, 2015). Considering the similar alignment of the magnetic field in our Milky Way Galaxy (as shown in Figure 7.6) implies that the direction examined in this chapter, i.e., tangential to the spiral arms in the first Galactic quadrant, is nearly parallel to the magnetic field direction. Consequently, the magnetic field component projected onto the plane of the sky, which is parallel to the polarization angle, experiences varying orientations along the line of sight at different distances. Therefore, when light from a distant star reaches us, it encounters varying magnetic field orientations. Thus, the line of sight effect exhibits the changing dust grain alignment and, subsequently, results in a large dispersion in the polarization angle and degree of polarization.

The parallel alignment of the magnetic field with the spiral arms is also supported by the results obtained in the anticenter direction presented in Chapter 6 and towards Czernik 3 cluster in Chapter 5. Along the anticenter direction, our line of sight intersects the spiral arms perpendicularly, resulting in the magnetic field orientation being nearly perpendicular to the line of sight, even at varying distances. As a consequence, the orientation of the dust grains along this line of sight remains uniform, which results in an increase in the degree of polarization with distance, as seen in our measurements (Figure 6.26). On the other hand, towards the Czernik 3 direction, the line of sight intersects the spiral arms at an oblique angle. This leads to a slight change in the plane of the sky component of the magnetic field with increasing distance. This change is reflected in the decrease in polarization efficiency with an increasing path length, as discussed in Section 5.3.4. Hence, all the polarization observations presented in this thesis strongly suggest that the orientation of the magnetic field in our galaxy is parallel to the spiral arms.

In addition, our analysis in section 7.2.2 has revealed interesting details concerning

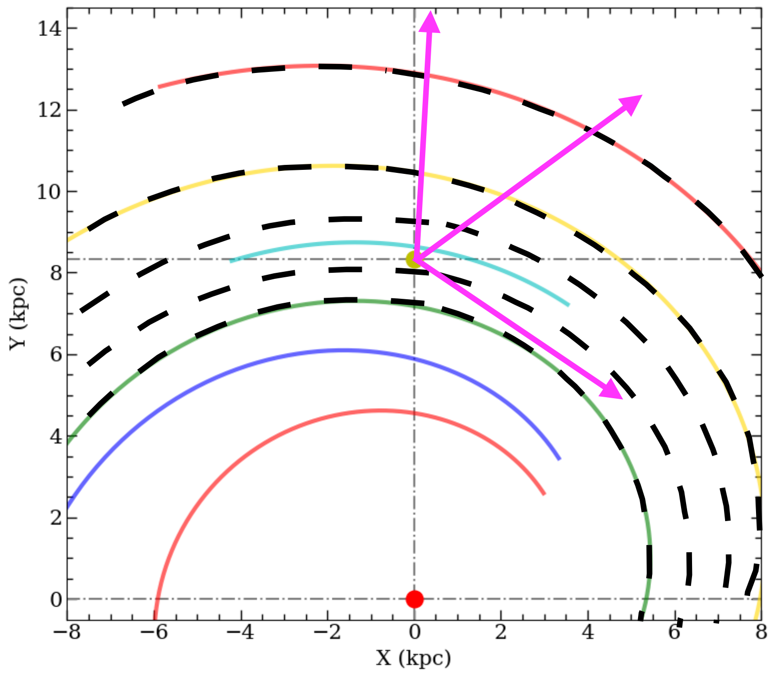

Figure 7.6: Schematic diagram representing the orientation of magnetic fields (black lines) aligned parallel to the spiral arms. The colored lines represent the spiral arms with color coding as to Figure 4.4. The magenta arrows correspond to the lines of sight studied in the thesis.

certain directions, such as Berkeley 47 and Berkeley 49. In these directions, we have identified indications of foreground dust layers with aligned grains, resulting in an increase in the degree of polarization and a more confined polarization angle. However, it is important to note that these features are localized within specific regions, as a slight change in the line of sight results in the absence of the same feature. Hence, they should not be associated with global structures like spiral arms. Moreover, the distances of these layers correspond to the inter-arm regions. This suggests that the inter-arm region is not devoid of dust; it may contain low-density structures, also observed in numerous external spiral galaxies.

To explore and uncover these small-scale structures within our Galaxy, conducting polarization observations encompassing large volumes of the Galactic plane becomes crucial. Such a systematic study of polarization observations will enable us to obtain a more comprehensive understanding of the distribution and characteristics of dust structures on a small scale as well as a larger scale.

7.4 General trend of polarization

When the degree of polarization of stars observed towards each cluster is plotted together as a function of distance, a uniform increase in polarization is observed, albeit with a significant spread (see Figure 7.7a). Besides this, the polarization angle, shown in Figure 7.7b also exhibits a wide range, spanning from 0° to 180°. This suggests that the dust could be distributed uniformly, owing to the increasing trend in the degree of polarization. At the same time, line of sight effect leads to encountering changing magnetic field direction, giving a large scatter in the polarization angle as well as the degree of polarization. This can be explained if the Galactic magnetic field aligns parallel to the spiral arms as discussed in Section 7.3.

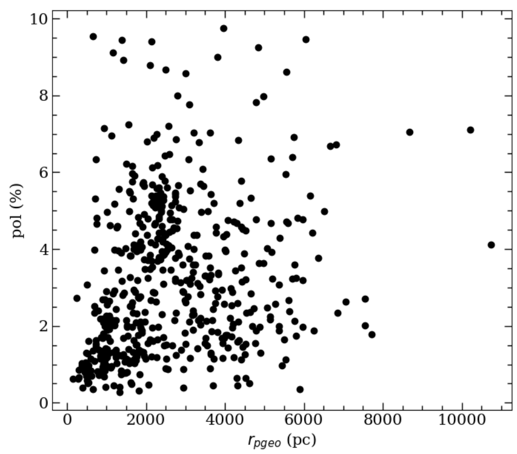

(a) Distance versus degree of polarization

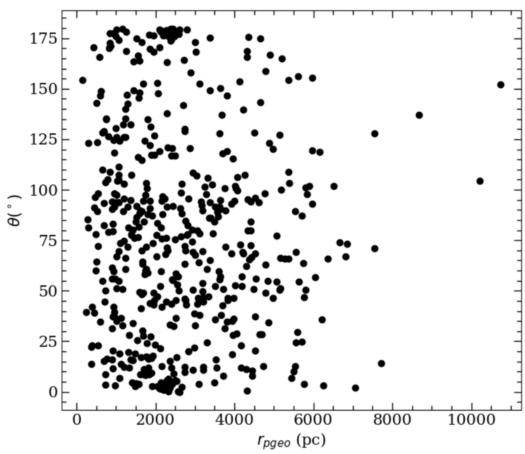

(b) Distance versus polarization angle

Figure 7.7: Variation of degree of polarization and polarization angle as a function of distance (r_{pgeo}) for all the stars observed in the first Galactic quadrant.

In addition to the total stars observed in this chapter, we also analyzed the average polarization of the cluster based on the available cluster members and their respective distances. The average degree of polarization, polarization angle, the respective dispersion in the measurements of members stars, and the propagated measurement error are listed in Table 7.4. Figure 7.8a and 7.8b illustrate the weighted average degree of polarization (left) and polarization angle (right) versus the cluster distances in the

Table 7.4: The parameters of nine Galactic open clusters towards the first Galactic quadrant discussed in this chapter.

clusters	ℓ	b	r_{50}	r_c	observed	members	P_{av}	σ_P	ϵ_P	θ_{av}	σ_θ	ϵ_θ	d	log age	Av
Berkeley 47	52.544	-0.042	2.6	1.6	110	38	4.96	0.90	0.07	82.19	86.64	.43	2.3	7.03	4.62
Kronberger 79	54.176	-0.611	.7	.5	38	15	1.32	1.09	0.23	112.37	18.74	3.53	4.8	7.04	5.49
Berkeley 83	66.094	-0.931	1.5	1.4	43	3	6.12	1.85	1.84	68.96	10.21	6.07	4.8	8.48	5.49
Kronberger 52	67.623	0.848	2.0	2.1	31	8	3.12	1.53	0.61	72.91	65.43	4.83	6.2	8.01	3.88
Kronberger 69	68.520	0.426	3.4	4.4	107	7	1.69	1.83	0.30	91.77	34.28	2.05	2.6	7.75	2.91
Kronberger 54	69.104	0.519	1.5	1.1	30	12	1.66	0.53	0.20	38.27	26.91	2.98	4.0	7.03	3.96
Berkeley 49	70.977	2.580	2.1	1.2	128	18	3.62	1.12	0.08	84.43	13.05	.63	3.0	8.04	4.12
Teutsch 8	71.859	2.420	18.2	32.7	21	5	1.14	0.43	0.16	59.23	64.17	2.97	1.9	6.63	2.54
Berkeley 51	72.147	0.295	2.4	2.3	31	15	1.66	0.99	0.32	52.68	64.79	2.66	5.0	7.69	5.64

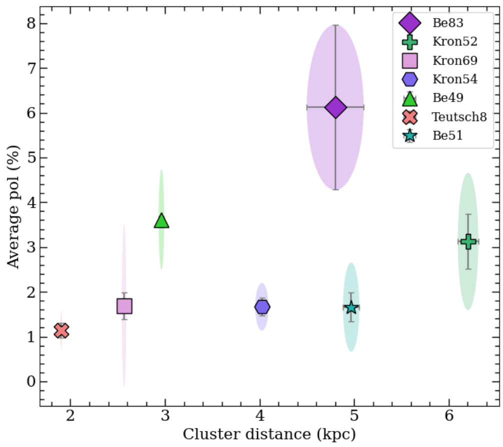

(a) Distance versus degree of polarization

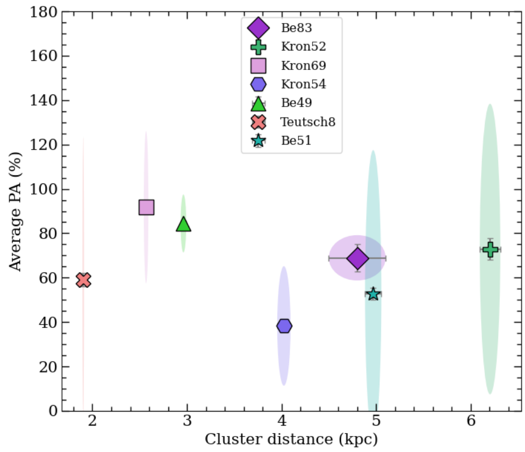

(b) Distance versus polarization angle

Figure 7.8: The weighted average degree of polarization (a) and polarization angle (b) as a function of cluster distance from Hunt & Reffert (2023).

longitude range of 66° to 72°. In the Figure, the polarization measurements shown for Berkeley 83 are based on only three stars, and these stars have low SNR. Hence, we excluded this cluster from our subsequent discussion. On the whole, the average degree of polarization and polarization angle for the remaining clusters exhibit consistency with each other, as their variations fall within the range of dispersion. This suggests that the line of sight under consideration may not encounter a dense dust layer causing an abrupt change in the polarization. While there may be local variations due to the presence of low-density dust clouds, no prominent high-density global features, such as spiral arms, are present in this region.

7.5 Summary

This chapter highlights the importance of polarization observations in regions tangential to the spiral arms of the Galaxy to understand the distribution of dust. We present observations and a detailed analysis of nine Galactic open clusters, primarily located along the tangential direction to the spiral arms in the first Galactic quadrant. These clusters were observed using both instruments, i.e., EMPOL and AIMPOL. The resulting degree of polarization and polarization angle exhibits a wide range of values. By comparing our observations with patterns observed in external galaxies from the literature, we find evidence for the alignment of the Galactic magnetic field along the spiral arms of the Galaxy. Furthermore, the local variations in polarization within the inter-arm regions support the notion of a complex structure in the Galactic disk, where the inter-arm space contains small-scale dust features rather than being completely devoid of dust. These findings provide observational evidence of the large-scale and small-scale structures of the Galactic disk based on dust distribution using linear polarization measurements.

Chapter 8

Summary and Future work

"All truths are easy to understand once they are discovered; the point is to discover them."

- Galileo Galilei, *1564-1642*

8.1 Summary of the work

Understanding the structure, formation, and evolution of our Milky Way galaxy are the key goals in the field of galactic astronomy. This Ph.D. thesis is dedicated to the objective of mapping the disk structure of our home galaxy. For nearly a hundred years, the story of building a picture of the Milky Way has been the story of finding good tracers of disk structures and credible methods of measuring their distances. The advancement of technology and availability of large-scale sky surveys has opened up a new era of Galactic astronomy. In order to investigate the age dependency on the disk structure of the Galaxy, we chose red clump stars to trace the structure. Having nearly constant luminosity and temperature during their evolutionary phase makes them a good distance indicator and hence can serve as a tracer for mapping the disk morphology. However, the extraction of RC stars amongst all other stars available in a line of sight is a difficult task. The selection of RC stars in the selected fields has been performed in the past in certain studies. But extracting the RC stars from the whole Galactic plane required an automatic procedure that could accurately segregate the RC stars from the other populations in the line of sight. We developed an automatic procedure to select the red clump stars from publicly available data. For this task, we utilized NIR data from 2MASS and Gaia counterparts to clean the sample. Gaia data plays a crucial role in selecting the pure RC sample by eliminating the foreground dwarf contamination. We present the largest sample of red clump stars containing 8.8 million sources, covering 5800 sq. degree field in the Galactic plane ranging from $40^\circ \leq \ell \leq 320^\circ$ and $-10^\circ \leq b \leq 10^\circ$. Making the method automatic was quite challenging and required many iterations of the code to trace the locus in different lines of sight suffering from varying extinctions. The distance estimated from our method is reliable even above 5 kpc, beyond which the uncertainties in the Gaia distance increase. This makes this catalog a potential sample to explore the distant regions of the Galactic disk, which was limited by other methods.

The distribution of RC stars as such does not provide any spiral structure information. However, the overdensity maps of the selected sample of RC stars trace the spiral morphology of the Disk. There is only one study in the literature reporting the detection of the spiral arm of the Galaxy using RC stars but by utilizing distance information from the Gaia Catalog. They only detected the overdensity in the Local arm of the Galaxy. The major highlight of our work is that we, for the first time, detected the so far poorly constrained Outer arm of the Galaxy with the distribution of RC stars. This newly detected feature not only traces the Outer arm but also extends significantly beyond (approximately 6 kpc) the previously understood boundaries based on other tracers, such as radio wavelengths. The detected part of the arm is highlighted as a thick purple band in Figure 8.1, overlaid on an artistic impression of what the Milky Way may look like. The thin curves in the figure illustrate the extent and location of the spiral arms patches constrained from other tracers as per recent literature results. This updated picture of the spiral arm presented in this study has improved our prevailing understanding about the extent of the spiral arms, i.e., in order to map the complete

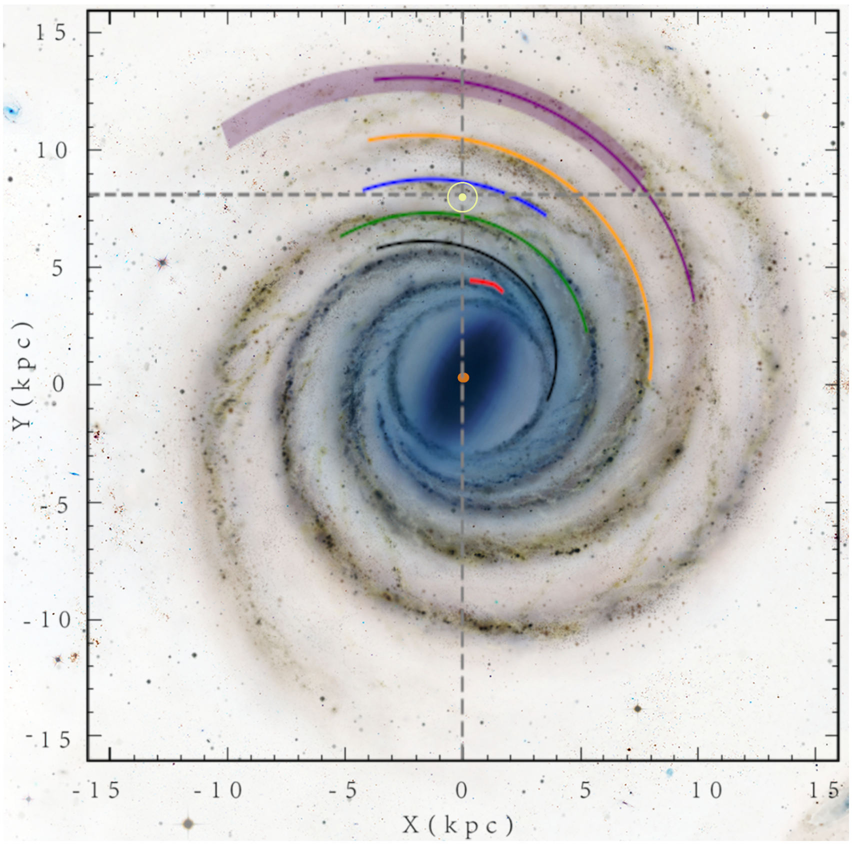

Figure 8.1: Updated face-on view of Our Milky Way Galaxy. The detection of the Outer arm from our study is highlighted in the purple band. While the spiral patches from the literature are marked by thin colored lines. This figure is an updated version of the figure created by Xing-Wu Zheng and Mark Reid, BeSSeL/NJU/CFA

structure of the spiral arms, we require homogeneous data covering the entire Galactic plane and distance indicators with good distance accuracy. Additionally, the detection of the Outer arm using RC stars, which serve as indicators of the intermediate-to-old age population, challenges the longstanding belief that only two arms, Scutum and Perseus arms, are traced by the older population, in contrast to the younger population accounts for four arms. Our results emphasize that the Outer arm could also be traced by the older population. Hence, Perseus arm and Scutum are not the only major arms being traced in the older population.

In addition to this, we analyzed the north-south asymmetry of the Galaxy using RC stars and found signatures of Disk warping. It is expected that the spiral arms of our Galaxy should also show asymmetry with respect to above and below the Galactic plane, but such an observation has never been reported earlier. Our analysis provides the first observational signature of the warping of the spiral arm.

Furthermore, in order to build a 3D map of our Galaxy, we modeled the disk with a simplistic assumption of decreasing space density away from the Galactic center both radially and vertically. The resulting density distribution provides the signature of the flaring in the Disk traced by RC stars. Additionally, the disk shows the warp structure, which was also modeled to constrain the geometry of the warp. The resulting flare and warp obtained from the RC distribution were compared with various other tracers from literature to constrain the formation and evolution mechanism of these features. From the comparison, we found age dependency on these structures implying both to be long-lived features. The age dependency on the strength of the flare favors the secular evolution of the disk while constraining the formation mechanism of the warp, further requiring the dynamics of the population to be considered.

Overall, our study of RC stars covering a large part of the Galactic disk highlights the importance of the requirement to study different age populations over a wide area of the Galactic disc. This approach is essential for effectively constraining the flare and warp formation mechanism. In the future, we hope to combine kinematic information with the stellar distribution of various age populations to investigate these intriguing questions in greater detail.

The RC stars or other stellar populations can be used as tracers to map the structure of the Disk. However, the stars may move out of their birthplace during their course of evolution, i.e., come out of the spiral arms into the inter-arm region. But the dust remains confined to the Disk and, more specifically, to the spiral arms of the Galaxy. Studying the dust distribution in the Galaxy directly in longer wavelengths is quite challenging. However, the properties of dust, i.e., extinction and polarization, can be used as indirect methods to study dust distribution. Extinction has been studied extensively to infer the Disk structure, but the use of polarization has been limited for mapping the 3D structure of the Galactic disk. We explored the polarization along with the distance information from Gaia as a tool to investigate dust distribution. With this aim, we selected Galactic open clusters present in a similar line of sight but distributed in the distance for polarization observations. We broadly selected three lines of sight in the Galactic disk available in the northern sky. The selected sight lines correspond to the high, intermediate, and low extinction regions. The observations of selected clusters were performed using two different imaging polarimeters (EMPOL and AIMPOL) at two Indian observational facilities; 1.2 m Mount Abu telescope of PRL and 1.04 m Sampurnanand telescope. Automatic pipelines were developed in Python to reduce the data acquired from both instruments. The summary of the results in each line of sight is indicated as follows.

1. To investigate the role of polarization in studying dust distribution, we first selected a distant cluster in the second Galactic quadrant. The polarization results towards the Czernik 3 cluster reveal that the dust is not uniformly distributed across the face of the cluster and along the line of sight, we found the indication of at least two dust layers. Combining the polarization data of clusters in the 15° vicinity of Czernik 3 from literature reveals the presence of a low-density region with lesser dust and stellar contents between the Local arm and Perseus arm. In other words, the variation of polarization with distance reveals the inter-arm region in the line of sight.

2. The second line of sight represents a low extinction region, where we could target distant clusters, even within or beyond the Outer arm. Towards this region, we found that major changes in polarization occur when the background starlight encounters dust in the spiral arms of the Galaxy. In addition, our results infer the local variation in the spiral arms, like holes observed in Phantom Galaxy (M74), or could signify the disk flaring. To confirm a preferred phenomenon, we require a large number of polarization observations of distant clusters or field stars with well-constrained distances, spatially covering both spiral arms along the lines of sight.

3. The third line of sight is nearly a tangential direction to the spiral arms in the first Galactic quadrant. The polarization results towards this line of sight show a relatively high degree of polarization but large scattering in both the degree of polarization as well as polarization angle with distance. The results highlight that the inner direction of the Galaxy contains high dust density and patchy distribution of dust, even in small areas, as observed in the case of Czernik 3. The large scattering in the angles with distance also indicates that the direction

of the magnetic fields is parallel to the spiral arms and is almost parallel to our direction of observation. Hence, in our line of sight, the projected component of the magnetic field on the plane of the sky seems to follow different orientations and hence we observe large dispersion in the polarization measurements.

Overall, the polarization study in three different lines of sight provides strong evidence that polarization can be utilized to trace the global structure of the Galaxy. It not only helps to uncover the dust distribution but also helps to construct the magnetic tomography of the Galaxy. The polarization studies have opened up new horizons to study both small-scale and large-scale dust distribution in unprecedented detail.

8.2 Major highlights of the thesis

1. Detection of the Outer arm of the Galaxy from the distribution of red clump stars, an intermediate-to-old age stellar population.
2. Tracing a 6 kpc long extension of the Outer arm - farther into the third quadrant than previously known limits.
3. The systematic warping of the disk and the first observational signature of the warping of the spiral arms.
4. Uncovering the warp and flare structures in the outer regions of the disk.
5. Demonstrate the use of polarization as a strong tool to study dust structures at different scales in the disk.
6. Indication of the presence of thin and patchy dust structures in the inter-arm region in the first quadrant
7. Signatures of the alignment of the magnetic field parallel to the spiral arms of the Galaxy
8. Combining the polarization measurements over a large scale can help to trace the spiral arms of the Galaxy

8.3 Future work

1. A few recent studies discuss the age dependency of spiral arms. In order to investigate this aspect, a comparative study of the spiral arms traced by younger and older populations should be performed. In our analysis related to the spiral structure traced by RC stars, we detected the Outer arm of the Galaxy. The selection region used in our study limits our ability to select the RC stars in the inner arms. We have developed a method to select the RC stars from the Galactic disk bounded by $40° \leq \ell \leq 320°$. The same method may not work in the remaining region (longitude range $\ell < 40°$ & $> 320°$) to select the RC stars of the Disk due to the contamination by the Bulge RGB and RC populations. A systematic method should be devised to disentangle the populations from two different regions to investigate the inner spiral arms of the RC stars. Thus enabling us to effectively trace the inner arm to study age dependency on spiral arms in more detail.

2. In our study, we detected the flare and warp in the Galactic disk traced by the RC stars. While we presented compelling evidence of an age dependency in these structures, further confirmation is needed to understand their formation and evolution mechanisms. Incorporating the dynamical information of the selected RC stars could help in investigating and validating the possible hypotheses.

3. Our interpretation of the alignment of the Galactic magnetic field from optical polarization data requires further investigation while repeating the observations in different lines of sight to gain strong evidence.

4. Our results provide strong evidence that ISM polarization plays an important role in deciphering the dust distribution in the Galaxy on small-scale as well as large scales. However, complete coverage of the Galactic plane is necessary to trace large-scale spiral arms. Hence, a dedicated polarization survey of the Galactic plane is needed, covering the entire Galactic plane with an accuracy better than 0.1%. An all-sky optical polarization survey, PASIPHAE (Polar-Areas Stellar-Imaging in Polarization High-Accuracy Experiment), is planned to study the magnetic field tomography of the Milky Way Galaxy by combining the polarization measurement

from the Survey with the Gaia distances. However, as the name depicts, this survey will only cover high-latitude fields. A similar survey is required in the Galactic plane to study the dust distribution and investigate the role of the magnetic field in spiral arm formation from the magnetic field tomography of the disk.

5. Finally, many upcoming sky surveys in different wavelength regimes with enhanced technology would be expected to probe deeper into the Galaxy. These surveys are expected to provide a better picture of the Milky Way disk. For example, the upcoming Gaia releases are expected to improve the parallax uncertainties, which will lead to an improvement in the distance uncertainties. In addition, the next generations' telescopes, like the Square Kilometer Array (SKA), Large Synoptic Survey Telescope (LSST), and Gaia NIR will provide an unprecedented view of the Galaxy that will help to solve many long-standing debates.

References

Abdurro'uf, Accetta, K., Aerts, C., et al. 2022, The Seventeenth Data Release of the Sloan Digital Sky Surveys: Complete Release of MaNGA, MaStar, and APOGEE-2 Data, ApJS, 259, 35 [Cited on page 51.]

Alard, C. 2001, Another bar in the Bulge, A&A , 379, L44 [Cited on page 9.]

Alexander, S. 1852, On the origin of the forms and the present condition of some of the clusters of stars, and several of the nebulae, AJ, 2, 95 [Cited on page 11.]

Amôres, E., Robin, A., & Reylé, C. 2017, Evolution over time of the Milky Way's disc shape, Astronomy & Astrophysics, 602, A67 [Cited on pages 15, 16, and 81.]

Amôres, E. B., López-Corredoira, M., González-Fernández, C., et al. 2013, The long bar as seen by the VVV Survey. II. Star counts, A&A , 559, A11 [Cited on page 9.]

Anderson, L. D., Bania, T. M., Balser, D. S., & Rood, R. T. 2012, The Green Bank Telescope H II Region Discovery Survey. III. Kinematic Distances, ApJ, 754, 62 [Cited on page 86.]

Anderson, M. E. & Bregman, J. N. 2010, Do Hot Halos Around Galaxies Contain the Missing Baryons?, ApJ, 714, 320 [Cited on page 8.]

Andrae, R., Fouesneau, M., Sordo, R., et al. 2022, Gaia Data Release 3: Analysis of the Gaia BP/RP spectra using the General Stellar Parameterizer from Photometry, arXiv e-prints, arXiv:2206.06138 [Cited on pages 38, 45, and 51.]

Ann, H. B., Seo, M., & Ha, D. K. 2015, A Catalog of Visually Classified Galaxies in the Local ($z \sim 0.01$) Universe, ApJS, 217, 27 [Cited on page 11.]

Axon, D. J. & Ellis, R. S. 1976, A catalogue of linear polarization measurements for 5070 stars., MNRAS , 177, 499 [Cited on page 91.]

Baade, W. 1944, NGC 147 and NGC 185, Two New Members of the Local Group of Galaxies, ApJ, 100, 147 [Cited on page 5.]

Babusiaux, C. & Gilmore, G. 2005, The structure of the Galactic bar, MNRAS , 358, 1309 [Cited on pages 8 and 34.]

Bahcall, J. N. 1986, Star counts and galactic structure., ARA&A, 24, 577 [Cited on page 64.]

Bailer-Jones, C. A. 2015, Estimating distances from parallaxes, Publications of the Astronomical Society of the Pacific, 127, 994 [Cited on page 50.]

Bailer-Jones, C. A. L., Rybizki, J., Fouesneau, M., Demleitner, M., & Andrae, R. 2021, Estimating Distances from Parallaxes. V. Geometric and Photogeometric Distances to 1.47 Billion Stars in Gaia Early Data Release 3, AJ, 161, 147 [Cited on pages 38, 51, 121, 134, 143, and 161.]

Bailer-Jones, C. A. L., Rybizki, J., Fouesneau, M., Mantelet, G., & Andrae, R. 2018, Estimating Distance from Parallaxes. IV. Distances to 1.33 Billion Stars in Gaia Data Release 2, AJ, 156, 58 [Cited on page 43.]

Bailin, J. 2003, Evidence for Coupling between the Sagittarius Dwarf Galaxy and the Milky Way Warp, ApJ , 583, L79 [Cited on page 16.]

Bailin, J. & Steinmetz, M. 2003, Tidal torques and galactic warps, Ap&SS, 284, 701 [Cited on page 16.]

Balaguer-Núnez, L., Tian, K. P., & Zhao, J. L. 1998, Determination of proper motions and membership of the open clusters NGC 1817 and NGC 1807, A&AS , 133, 387 [Cited on page 132.]

Bastien, P., Ménard, F., Corporon, P., et al. 2004, Polarization in the young cluster NGC 6611: circumstellar, interstellar, or ... both?, Ap&SS, 292, 427 [Cited on page 191.]

Battaner, E., Florido, E., & Sanchez-Saavedra, M. L. 1990, Intergalactic magnetic field and galactic warps., A&A , 236, 1 [Cited on page 16.]

Battaner, E. & Jiménez-Vicente, J. 1998, A simple model of magnetically induced WARPS, A&A , 332, 809 [Cited on page 16.]

Beck, R. 2015, Magnetic fields in spiral galaxies, A&A Rev., 24, 4 [Cited on page 205.]

Bellini, A., Piotto, G., Bedin, L. R., et al. 2009, Ground-based CCD astrometry with wide field imagers. III. WFI@2.2m proper-motion catalog of the globular cluster ω Centauri, A&A , 493, 959 [Cited on page 132.]

Belokurov, V., Zucker, D. B., Evans, N. W., et al. 2006, The Field of Streams: Sagittarius and Its Siblings, ApJ , 642, L137 [Cited on page 7.]

Benjamin, R. A., Churchwell, E., Babler, B. L., et al. 2005, First GLIMPSE Results on the Stellar Structure of the Galaxy, ApJ , 630, L149 [Cited on pages 9, 13, and 28.]

Berdyugin, A., Piirola, V., & Teerikorpi, P. 2014, Interstellar polarization at high galactic latitudes from distant stars. VIII. Patterns related to the local dust and gas shells from observations of $\sim$3600 stars, A&A , 561, A24 [Cited on page 91.]

Bertin, E. & Arnouts, S. 1996, SExtractor: Software for source extraction., A&AS , 117, 393 [Cited on page 108.]

Bijas, N., Eswaraiah, C., Wang, J.-W., et al. 2022, Revealing the dust grain polarization properties as a function of extinction and distance towards NGC 1893, MNRAS , 515, 3352 [Cited on pages 154, 184, and 186.]

Binney, J. & Merrifield, M. 1998, Galactic Astronomy [Cited on page 10.]

Bisht, D., Yadav, R. K. S., & Durgapal, A. K. 2017, 2MASS analytical study of four open cluster candidates, New A, 52, 55 [Cited on page 118.]

Bisht, D., Zhu, Q., Yadav, R., et al. 2021, Multicolour photometry and Gaia EDR3 astrometry of two couples of binary clusters (NGC 5617 and Trumpler 22) and (NGC 3293 and NGC 3324)., MNRAS , 503, 5929B [Cited on page 132.]

Bland-Hawthorn, J. & Gerhard, O. 2016, The Galaxy in Context: Structural, Kinematic, and Integrated Properties, ARA&A, 54, 529 [Cited on pages 7 and 63.]

Boch, T., Pineau, F., & Derriere, S. 2012, in Astronomical Society of the Pacific Conference Series, Vol. 461, Astronomical Data Analysis Software and Systems XXI, ed. P. Ballester, D. Egret, & N. P. F. Lorente, 291 [Cited on page 121.]

Bohlin, R. C., Savage, B. D., & Drake, J. F. 1978, A survey of interstellar H I from Lalpha absorption measurements. II., ApJ, 224, 132 [Cited on page 145.]

Bovy, J., Nidever, D. L., Rix, H.-W., et al. 2014, The APOGEE Red-clump Catalog: Precise Distances, Velocities, and High-resolution Elemental Abundances over a Large Area of the Milky Way's Disk, ApJ, 790, 127 [Cited on pages 35, 43, and 46.]

Bovy, J., Rix, H.-W., Liu, C., et al. 2012, The Spatial Structure of Mono-abundance Sub-populations of the Milky Way Disk, ApJ, 753, 148 [Cited on pages 20 and 78.]

Bovy, J., Rix, H.-W., Schlafly, E. F., et al. 2016, The Stellar Population Structure of the Galactic Disk, ApJ, 823, 30 [Cited on pages 18 and 78.]

Buckner, A. S. M. & Froebrich, D. 2013, Properties of star clusters - I. Automatic distance and extinction estimates, MNRAS , 436, 1465 [Cited on page 141.]

Burke, B. F. 1957, Systematic distortion of the outer regions of the galaxy., AJ, 62, 90 [Cited on page 16.]

Cannon, R. D. 1970, Red giants in old open clusters., MNRAS , 150, 111 [Cited on page 33.]

Cantat-Gaudin, T., Anders, F., Castro-Ginard, A., et al. 2020, Painting a portrait of the Galactic disc with its stellar clusters, A&A , 640, A1 [Cited on pages 58 and 158.]

Cantat-Gaudin, T., Jordi, C., Vallenari, A., et al. 2018, A Gaia DR2 view of the open cluster population in the Milky Way, A&A , 618, A93 [Cited on pages 118, 121, 131, 135, and 136.]

Castellani, V., Degl'Innocenti, S., Girardi, L., et al. 2000, The puzzling theoretical predictions for the luminosity of clumping He burning stars, A&A , 354, 150 [Cited on page 33.]

Castro-Ginard, A., McMillan, P. J., Luri, X., et al. 2021, Milky Way spiral arms from open clusters in Gaia EDR3, A&A , 652, A162 [Cited on pages 57, 58, 99, and 183.]

Chakrabarti, S., Saito, R., Quillen, A., et al. 2015, Clustered Cepheid Variables 90 Kiloparsecs from the Galactic Center, ApJ , 802, L4 [Cited on page 17.]

Chambers, K. C., Magnier, E. A., Metcalfe, N., et al. 2016, The Pan-STARRS1 Surveys, arXiv e-prints, arXiv:1612.05560 [Cited on page 121.]

Chen, B. Q., Huang, Y., Yuan, H. B., et al. 2019a, Three-dimensional interstellar dust reddening maps of the Galactic plane, MNRAS , 483, 4277 [Cited on page 21.]

Chen, X., Wang, S., Deng, L., et al. 2019b, An intuitive 3D map of the Galactic warp's precession traced by classical Cepheids, Nature Astronomy, 3, 320 [Cited on pages 15, 16, and 81.]

Cheng, X., Anguiano, B., Majewski, S. R., et al. 2020, Exploring the Galactic Warp through Asymmetries in the Kinematics of the Galactic Disk, ApJ, 905, 49 [Cited on pages 15, 16, and 35.]

Cheng, X., Liu, C., Mao, S., & Cui, W. 2019, Ripple Patterns in In-plane Velocities of OB Stars from LAMOST and Gaia, ApJ , 872, L1 [Cited on pages 18 and 78.]

Chrobáková, Ž., Nagy, R., & López-Corredoira, M. 2020, Structure of the outer Galactic disc with Gaia DR2, A&A , 637, A96 [Cited on pages 15, 16, 68, 80, and 81.]

Chrobáková, Ž., Nagy, R., & López-Corredoira, M. 2022, Warp and flare of the Galactic disc revealed with supergiants by Gaia EDR3, A&A , 664, A58 [Cited on pages 15, 18, 20, 68, 70, 71, 73, 74, 77, and 80.]

Churchwell, E., Babler, B. L., Meade, M. R., et al. 2009, The Spitzer/GLIMPSE Surveys: A New View of the Milky Way, PASP, 121, 213 [Cited on pages 9, 13, and 28.]

Clarkson, W., Sahu, K., Anderson, J., et al. 2008, Stellar Proper Motions in the Galactic Bulge from Deep Hubble Space Telescope ACS WFC Photometry, ApJ, 684, 1110 [Cited on page 8.]

Clayton, G. C., Wolff, M. J., Allen, R. G., & Lupie, O. L. 1995, Ultraviolet Interstellar Linear Polarization. II. The Wavelength Dependence, ApJ, 445, 947 [Cited on page 139.]

Clemens, D. P., Cashman, L. R., Cerny, C., et al. 2020, The Galactic Plane Infrared Polarization Survey (GPIPS): Data Release 4, ApJS, 249, 23 [Cited on page 91.]

Cutri, R. M., Skrutskie, M. F., van Dyk, S., et al. 2003, 2MASS All Sky Catalog of point sources. [Cited on page 121.]

Dame, T. M., Hartmann, D., & Thaddeus, P. 2001, The Milky Way in Molecular Clouds: A New Complete CO Survey, ApJ, 547, 792 [Cited on pages 121, 146, and 179.]

Davis, L. & Greenstein, J. L. 1949, The Polarization of Starlight by Interstellar Dust Particles in a Galactic Magnetic Field, Physical Review, 75, 1605 [Cited on page 90.]

de Grijs, R. & Peletier, R. F. 1997, The shape of galaxy disks: how the scale height increases with galactocentric distance., A&A , 320, L21 [Cited on page 18.]

De Lucia, G. & Helmi, A. 2008, The Galaxy and its stellar halo: insights on their formation from a hybrid cosmological approach, MNRAS , 391, 14 [Cited on page 7.]

de Vaucouleurs, G. 1964, in The Galaxy and the Magellanic Clouds, ed. F. J. Kerr, Vol. 20, 195 [Cited on page 8.]

Debattista, V. P. & Sellwood, J. A. 1999, Warped Galaxies from Misaligned Angular Momenta, ApJ , 513, L107 [Cited on page 16.]

Dewangan, L. K., Baug, T., Ojha, D. K., Zinchenko, I., & Luna, A. 2018, Filamentary Structures and Star Formation Activity in the Sites S234, V582, and IRAS 05231+3512, ApJ, 864, 54 [Cited on page 162.]

Dias, W. S., Alessi, B. S., Moitinho, A., & Lépine, J. R. D. 2002, New catalogue of optically visible open clusters and candidates, A&A , 389, 871 [Cited on page 118.]

Dolphin, A. E., Saha, A., Skillman, E. D., et al. 2001, Deep Hubble Space Telescope Imaging of IC 1613. I. Variable Stars and Distance, ApJ, 550, 554 [Cited on page 35.]

Drimmel, R., Smart, R. L., & Lattanzi, M. G. 2000, The Galactic warp in OB stars from Hipparcos, A&A , 354, 67 [Cited on pages 13, 16, 28, 70, and 77.]

Drimmel, R. & Spergel, D. N. 2001, Three-dimensional Structure of the Milky Way Disk: The Distribution of Stars and Dust beyond 0.35 R_{solar}, ApJ, 556, 181 [Cited on pages 15, 17, 21, 68, 76, and 80.]

Dutra, C. M. & Bica, E. 2002, A catalogue of dust clouds in the Galaxy, A&A , 383, 631 [Cited on page 144.]

Eggen, O. J., Lynden-Bell, D., & Sandage, A. R. 1962, Evidence from the motions of old stars that the Galaxy collapsed., ApJ, 136, 748 [Cited on page 7.]

Eswaraiah, C., Pandey, A. K., Maheswar, G., et al. 2012, Broad-band optical polarimetric studies towards the Galactic young star cluster Berkeley 59, MNRAS , 419, 2587 [Cited on pages 22, 86, 121, 126, 127, 128, 148, and 149.]

Eswaraiah, C., Pandey, A. K., Maheswar, G., et al. 2011, A multiwavelength polarimetric study towards the open cluster NGC 1893, MNRAS , 411, 1418 [Cited on pages 127, 128, 154, and 186.]

Fabricius, C., Luri, X., Arenou, F., et al. 2021, Gaia Early Data Release 3. Catalogue validation, A&A , 649, A5 [Cited on page 121.]

Faulkner, D. J. & Cannon, R. D. 1973, Models of Population i Clump Giants, ApJ, 180, 435 [Cited on page 33.]

Feast, M. W., Menzies, J. W., Matsunaga, N., & Whitelock, P. A. 2014, Cepheid variables in the flared outer disk of our galaxy, Nature, 509, 342 [Cited on page 17.]

Feinstein, C., Baume, G., Vazquez, R., Niemela, V., & Cerruti, M. A. 2000, The Highly Polarized Open Cluster Trumpler 27, AJ, 120, 1906 [Cited on page 126.]

Ferguson, D., Gardner, S., & Yanny, B. 2017, Milky Way Tomography with K and M Dwarf Stars: The Vertical Structure of the Galactic Disk, ApJ, 843, 141 [Cited on page 61.]

Fletcher, A., Beck, R., Shukurov, A., Berkhuijsen, E. M., & Horellou, C. 2011, Magnetic fields and spiral arms in the galaxy M51, MNRAS , 412, 2396 [Cited on page 205.]

Freudenreich, H. T., Berriman, G. B., Dwek, E., et al. 1994, DIRBE Evidence for a Warp in the Interstellar Dust Layer and Stellar Disk of the Galaxy, ApJ , 429, L69 [Cited on page 15.]

Gaia Collaboration, Antoja, T., McMillan, P. J., et al. 2021a, Gaia Early Data Release 3. The Galactic anticentre, A&A , 649, A8 [Cited on page 153.]

Gaia Collaboration, Brown, A. G. A., Vallenari, A., et al. 2021b, Gaia Early Data Release 3. Summary of the contents and survey properties, A&A , 649, A1 [Cited on pages 38 and 121.]

Gaia Collaboration, Drimmel, R., Romero-Gomez, M., et al. 2022, Gaia Data Release 3: Mapping the asymmetric disc of the Milky Way, arXiv e-prints, arXiv:2206.06207 [Cited on pages 51 and 53.]

Galilei, G. 2016, Sidereus Nuncius, or the sidereal messenger (University of Chicago Press) [Cited on page 3.]

Ganesh, S., Omont, A., Joshi, U. C., et al. 2009, Stellar populations in a standard ISOGAL field in the Galactic disc, A&A , 493, 785 [Cited on pages 20 and 42.]

Ganesh, S., Rai, A., Aravind, K., et al. 2020, in Society of Photo-Optical Instrumentation Engineers (SPIE) Conference Series, Vol. 11447, Society of Photo-Optical Instrumentation Engineers (SPIE) Conference Series, 114479E [Cited on pages 92 and 118.]

Gilmore, G. & Reid, N. 1983, New light on faint stars - III. Galactic structure towards the South Pole and the Galactic thick disc., MNRAS , 202, 1025 [Cited on page 9.]

Gingerich, O. 1985, in The Milky Way Galaxy, ed. H. van Woerden, R. J. Allen, & W. B. Burton, Vol. 106, 59–70 [Cited on page 5.]

Girard, T. M., Grundy, W. M., Lopez, C. E., & van Altena, W. F. 1989, Relative Proper Motions and the Stellar Velocity Dispersion of the Open Cluster M67, AJ, 98, 227G [Cited on page 134.]

Girardi, L. 2016, Red Clump Stars, ARA&A, 54, 95 [Cited on pages 29, 31, 33, and 36.]

Girardi, L., Barbieri, M., Groenewegen, M. A. T., et al. 2012, in Astrophysics and Space Science Proceedings, Vol. 26, Red Giants as Probes of the Structure and Evolution of the Milky Way, 165 [Cited on page 37.]

Girardi, L., Groenewegen, M. A. T., Hatziminaoglou, E., & da Costa, L. 2005, Star counts in the Galaxy. Simulating from very deep to very shallow photometric surveys with the TRILEGAL code, A&A , 436, 895 [Cited on page 37.]

Gontcharov, G. A. 2017, 3D stellar reddening map from 2MASS photometry: An improved version, Astronomy Letters, 43, 472 [Cited on page 21.]

Gonzalez, O. A., Rejkuba, M., Minniti, D., et al. 2011, The inner Galactic bar traced by the VVV survey, A&A , 534, L14 [Cited on page 9.]

González-Fernández, C., Hodgkin, S. T., Irwin, M. J., et al. 2018, The VISTA ZYJHKs photometric system: calibration from 2MASS, MNRAS , 474, 5459 [Cited on page 141.]

Goodman, A. A., Bastien, P., Myers, P. C., & Menard, F. 1990, Optical Polarization Maps of Star-forming Regions in Perseus, Taurus, and Ophiuchus, ApJ, 359, 363 [Cited on page 91.]

Grabelsky, D. A., Cohen, R. S., Bronfman, L., Thaddeus, P., & May, J. 1987, Molecular Clouds in the Carina Arm: Large-Scale Properties of Molecular Gas and Comparison with H i, ApJ, 315, 122 [Cited on pages 15 and 17.]

Green, G. M. 2018, dustmaps: A Python interface for maps of interstellar dust, The Journal of Open Source Software, 3, 695 [Cited on page 143.]

Green, G. M., Schlafly, E., Zucker, C., Speagle, J. S., & Finkbeiner, D. 2019, A 3D Dust Map Based on Gaia, Pan-STARRS 1, and 2MASS, ApJ, 887, 93 [Cited on pages 21, 86, 143, 161, and 201.]

Grigorian, K. H. 1968, Polarization Observations of Stars in the Clusters NGC 6871 and NGC 6823, Communications of the Byurakan Astrophysical Observatory, 39, 19 [Cited on page 191.]

Guijarro, A., Peletier, R. F., Battaner, E., et al. 2010, Near-infrared and optical observations of galactic warps: a common, unexplained feature of most discs, A&A , 519, A53 [Cited on page 15.]

Hall, J. S. 1949, Observations of the Polarized Light from Stars, Science, 109, 166 [Cited on page 90.]

Hawkins, K., Leistedt, B., Bovy, J., & Hogg, D. W. 2017, Red clump stars and Gaia: calibration of the standard candle using a hierarchical probabilistic model, MNRAS , 471, 722 [Cited on page 35.]

He, Z.-H., Xu, Y., & Hou, L.-G. 2021, Search for age pattern across spiral arms of the Milky Way, Research in Astronomy and Astrophysics, 21, 009 [Cited on page 14.]

Heiles, C. 2000, 9286 Stars: An Agglomeration of Stellar Polarization Catalogs, AJ, 119, 923 [Cited on pages 121, 147, and 148.]

Helmi, A. 2004, Velocity Trends in the Debris of Sagittarius and the Shape of the Dark Matter Halo of Our Galaxy, ApJ , 610, L97 [Cited on page 7.]

Henderson, A. P. 1979, in The Large-Scale Characteristics of the Galaxy, ed. W. B. Burton, Vol. 84, 493 [Cited on page 15.]

Henry, A. L., Quillen, A. C., & Gutermuth, R. 2003, Star Formation and Asymmetry in the Spiral Arms of M51: Variable Star Formation Caused by More than One Spiral Density Wave, AJ, 126, 2831 [Cited on page 61.]

Herschel, W. 1785, On the Construction of the Heavens., Philosophical Transactions of the Royal Society of London Series I, 75, 213 [Cited on page 3.]

HI4PI Collaboration, Ben Bekhti, N., Flöer, L., et al. 2016, HI4PI: A full-sky H I survey based on EBHIS and GASS, A&A , 594, A116 [Cited on pages 121, 145, and 179.]

Hiltner, W. A. 1949, Polarization of Light from Distant Stars by Interstellar Medium, Science, 109, 165 [Cited on page 90.]

Hoskin, M. 1985, in The Milky Way Galaxy, ed. H. van Woerden, R. J. Allen, & W. B. Burton, Vol. 106, 11–24 [Cited on page 4.]

Hoskin, M. A. 1976, The 'Great Debate': What Really Happened, Journal for the History of Astronomy, 7, 169 [Cited on page 4.]

Hou, L. G. 2021, The spiral structure in the Solar neighbourhood, Frontiers in Astronomy and Space Sciences, 8, 103 [Cited on pages 10, 11, 12, and 54.]

Hou, L. G. & Han, J. L. 2015, Offset between stellar spiral arms and gas arms of the Milky Way, MNRAS , 454, 626 [Cited on page 14.]

House, E. L., Brook, C. B., Gibson, B. K., et al. 2011, Disc heating: comparing the Milky Way with cosmological simulations, MNRAS , 415, 2652 [Cited on pages 18 and 78.]

Hubble, E. P. 1922, A general study of diffuse galactic nebulae., ApJ, 56, 162 [Cited on page 4.]

Hubble, E. P. 1925, Cepheids in Spiral Nebulae, Popular Astronomy, 33, 252 [Cited on page 5.]

Hunt, E. L. & Reffert, S. 2021, Improving the open cluster census. I. Comparison of clustering algorithms applied to Gaia DR2 data, A&A , 646, A104 [Cited on page 168.]

Hunt, E. L. & Reffert, S. 2023, Improving the open cluster census. II. An all-sky cluster catalogue with Gaia DR3, A&A , 673, A114 [Cited on pages 99, 101, 163, 168, 173, 176, 186, 188, 196, 197, and 209.]

Indebetouw, R., Mathis, J. S., Babler, B. L., et al. 2005, The Wavelength Dependence of Interstellar Extinction from 1.25 to 8.0 μm Using GLIMPSE Data, ApJ, 619, 931 [Cited on page 42.]

Joshi, Y. C., Dambis, A. K., Pandey, A. K., & Joshi, S. 2016, Study of open clusters within 1.8 kpc and understanding the Galactic structure, A&A , 593, A116 [Cited on page 118.]

Kalberla, P. M. W., Dedes, L., Kerp, J., & Haud, U. 2007, Dark matter in the Milky Way. II. The HI gas distribution as a tracer of the gravitational potential, A&A , 469, 511 [Cited on page 18.]

Kapteyn, J. C. 1922, First Attempt at a Theory of the Arrangement and Motion of the Sidereal System, ApJ, 55, 302 [Cited on page 4.]

Kapteyn, J. C. & van Rhijn, P. J. 1920, On the Distribution of the Stars in Space Especially in the High Galactic Latitudes, ApJ, 52, 23 [Cited on page 4.]

Kazantzidis, S., Bullock, J. S., Zentner, A. R., Kravtsov, A. V., & Moustakas, L. A. 2008, Cold Dark Matter Substructure and Galactic Disks. I. Morphological Signatures of Hierarchical Satellite Accretion, ApJ, 688, 254 [Cited on pages 18, 19, and 78.]

Kerr, F. J. 1957, A Magellanic effect on the galaxy., AJ, 62, 93 [Cited on page 15.]

Kharchenko, N. V., Piskunov, A. E., Schilbach, E., Röser, S., & Scholz, R. D. 2013, Global survey of star clusters in the Milky Way. II. The catalogue of basic parameters, A&A , 558, A53 [Cited on pages 119, 121, 155, 158, 163, 168, 176, and 197.]

Kharchenko, N. V., Piskunov, A. E., Schilbach, E., Röser, S., & Scholz, R. D. 2016, Global survey of star clusters in the Milky Way. V. Integrated JHK_S magnitudes and luminosity functions, A&A , 585, A101 [Cited on page 118.]

Kim, J. H., Peirani, S., Kim, S., et al. 2014, Formation of Warped Disks by Galactic Flyby Encounters. I. Stellar Disks, ApJ, 789, 90 [Cited on page 16.]

Kim, M., Kim, E., Lee, M. G., Sarajedini, A., & Geisler, D. 2002, Determination of the Distance to M33 Based on the Tip of the Red Giant Branch and the Red Clump, AJ, 123, 244 [Cited on page 35.]

Kuminski, E. & Shamir, L. 2016, A Computer-generated Visual Morphology Catalog of ~3,000,000 SDSS Galaxies, ApJS, 223, 20 [Cited on page 11.]

Lacey, C. G. 1984, The influence of massive gas clouds on stellar velocity dispersions in galactic discs, MNRAS , 208, 687 [Cited on pages 18 and 78.]

Lallement, R., Capitanio, L., Ruiz-Dern, L., et al. 2018, Three-dimensional maps of interstellar dust in the Local Arm: using Gaia, 2MASS, and APOGEE-DR14, A&A , 616, A132 [Cited on pages 21 and 86.]

Lambert, J. H. 1761, Cosmologische Briefe über die Einrichtung des Weltbaues [Cited on page 3.]

Laporte, C. F. P., Johnston, K. V., Gómez, F. A., Garavito-Camargo, N., & Besla, G. 2018, The influence of Sagittarius and the Large Magellanic Cloud on the stellar disc of the Milky Way Galaxy, MNRAS , 481, 286 [Cited on pages 19 and 78.]

Lemasle, B., Lala, H. N., Kovtyukh, V., et al. 2022, Tracing the Milky Way warp and spiral arms with classical Cepheids, A&A , 668, A40 [Cited on pages 15, 74, 76, and 80.]

Levine, E. S., Blitz, L., & Heiles, C. 2006a, The Spiral Structure of the Outer Milky Way in Hydrogen, Science, 312, 1773 [Cited on pages 17, 76, and 80.]

Levine, E. S., Blitz, L., & Heiles, C. 2006b, The Vertical Structure of the Outer Milky Way H I Disk, ApJ, 643, 881 [Cited on page 15.]

Li, C., Zhao, G., Jia, Y., et al. 2019, Flare and Warp of Galactic Disk with OB Stars from Gaia DR2, ApJ, 871, 208 [Cited on pages 15, 17, 20, 68, 70, 71, 77, 78, and 80.]

Li, X., Wang, H.-F., Luo, Y.-P., et al. 2023, Evidence for Population-dependent Vertical Motions and the Long-lived Nonsteady Lopsided Milky Way Warp, ApJ, 943, 88 [Cited on pages 15, 16, and 81.]

Li, X. Y., Huang, Y., Chen, B. Q., et al. 2020, Mapping the Galactic Disk with the LAMOST and Gaia Red Clump Sample. IV. The Kinematic Signature of the Galactic Warp, ApJ, 901, 56 [Cited on pages 15 and 54.]

Lin, C. C. & Shu, F. H. 1964, On the Spiral Structure of Disk Galaxies., ApJ, 140, 646 [Cited on pages 11 and 21.]

Lin, Z., Xu, Y., Hou, L., et al. 2022, Local Spiral Structure Traced by Red Clump Stars, ApJ, 931, 72 [Cited on pages 27, 54, 58, and 59.]

Lindegren, L., Klioner, S. A., Hernández, J., et al. 2021, Gaia Early Data Release 3. The astrometric solution, A&A , 649, A2 [Cited on page 38.]

López-Corredoira, M. 2016, A case against an X-shaped structure in the Milky Way young bulge, A&A , 593, A66 [Cited on page 8.]

López-Corredoira, M., Abedi, H., Garzón, F., & Figueras, F. 2014, Vertical velocities from proper motions of red clump giants, A&A , 572, A101 [Cited on pages 15 and 68.]

López-Corredoira, M. & Betancort-Rijo, J. 2009, Azimuthal dependence of the density distribution in outer galactic discs accreting intergalactic flows, A&A , 493, L9 [Cited on page 18.]

López-Corredoira, M., Betancort-Rijo, J., & Beckman, J. E. 2002, Generation of galactic disc warps due to intergalactic accretion flows onto the disc, A&A , 386, 169 [Cited on page 16.]

López-Corredoira, M., Cabrera-Lavers, A., Garzón, F., & Hammersley, P. 2002, Old stellar Galactic disc in near-plane regions according to 2MASS: Scales, cut-off, flare and warp, Astronomy & Astrophysics, 394, 883 [Cited on pages xvi, 15, 17, 20, 35, 37, 54, 61, 63, 68, 69, 70, 71, 74, 75, and 76.]

López-Corredoira, M., Cabrera-Lavers, A., & Gerhard, O. E. 2005, A boxy bulge in the Milky Way. Inversion of the stellar statistics equation with 2MASS data, A&A , 439, 107 [Cited on page 8.]

López-Corredoira, M., Cabrera-Lavers, A., Mahoney, T. J., et al. 2007, The Long Bar in the Milky Way: Corroboration of an Old Hypothesis, AJ, 133, 154 [Cited on page 9.]

López-Corredoira, M., Garzón, F., Wang, H. F., et al. 2020, Gaia-DR2 extended kinematical maps. II. Dynamics in the Galactic disk explaining radial and vertical velocities, A&A , 634, A66 [Cited on page 15.]

López-Corredoira, M. & Molgó, J. 2014, Flare in the Galactic stellar outer disc detected in SDSS-SEGUE data, A&A , 567, A106 [Cited on pages 18, 70, and 77.]

Lucey, M., Ting, Y.-S., Ramachandra, N. S., & Hawkins, K. 2020, From the inner to outer Milky Way: a photometric sample of 2.6 million red clump stars, MNRAS , 495, 3087 [Cited on pages 47 and 53.]

Lynds, B. T. 1962, Catalogue of Dark Nebulae., ApJS, 7, 1 [Cited on page 144.]

Majewski, S. R., Schiavon, R. P., Frinchaboy, P. M., et al. 2017, The Apache Point Observatory Galactic Evolution Experiment (APOGEE), AJ, 154, 94 [Cited on page 46.]

Marrese, P. M., Marinoni, S., Fabrizio, M., & Altavilla, G. 2022, Gaia DR3 documentation Chapter 15: Cross-match with external catalogues, Gaia DR3 documentation, European Space Agency; Gaia Data Processing and Analysis Consortium. Online at https://gea.esac.esa.int/archive/documentation/GDR3/index.html, id. 15 [Cited on page 44.]

Marshall, D. J., Robin, A. C., Reylé, C., Schultheis, M., & Picaud, S. 2006, Modelling the Galactic interstellar extinction distribution in three dimensions, A&A , 453, 635 [Cited on pages 15, 21, 45, and 76.]

Martig, M., Minchev, I., & Flynn, C. 2014, Dissecting simulated disc galaxies - I. The structure of mono-age populations, MNRAS , 442, 2474 [Cited on page 79.]

Martin, P. G., Clayton, G. C., & Wolff, M. J. 1999, Ultraviolet Interstellar Linear Polarization. V. Analysis of the Final Data Set, ApJ, 510, 905 [Cited on page 139.]

Martínez, R., Vergne, M. M., & Feinstein, C. 2004, Optical polarization observations in Hogg 22 and NGC 6204, A&A , 419, 965 [Cited on page 126.]

Martinez-Valpuesta, I. & Gerhard, O. 2011, Unifying A Boxy Bulge and Planar Long Bar in the Milky Way, ApJ , 734, L20 [Cited on pages 8 and 9.]

Marton, G., Ábrahám, P., Szegedi-Elek, E., et al. 2019, Identification of Young Stellar Object candidates in the Gaia DR2 x AllWISE catalogue with machine learning methods, MNRAS , 487, 2522 [Cited on pages 135, 140, and 141.]

Mateu, C. & Vivas, A. K. 2018, The Galactic thick disc density profile traced with RR Lyrae stars, MNRAS , 479, 211 [Cited on page 28.]

Mathewson, D. S. & Ford, V. L. 1971, Polarization observations of 1800 stars, MNRAS , 153, 525 [Cited on page 91.]

May, J., Alvarez, H., & Bronfman, L. 1997, Physical properties of molecular clouds in the southern outer Galaxy., A&A , 327, 325 [Cited on pages 15 and 17.]

McWilliam, A. & Zoccali, M. 2010, Two Red Clumps and the X-shaped Milky Way Bulge, ApJ, 724, 1491 [Cited on pages 8 and 34.]

Medhi, B. J., Maheswar, G., Brijesh, K., et al. 2007, Broad-band optical polarimetric study of IC 1805, MNRAS , 378, 881 [Cited on page 121.]

Medhi, B. J., Maheswar, G., Pandey, J. C., Kumar, T. S., & Sagar, R. 2008, Optical polarimetric study of open clusters: distribution of interstellar matter towards NGC 654, MNRAS , 388, 105 [Cited on pages 86 and 121.]

Medhi, B. J., Maheswar G., Pandey, J. C., Tamura, M., & Sagar, R. 2010, Polarization towards the young open cluster NGC 6823, MNRAS , 403, 1577 [Cited on pages 137 and 191.]

Medhi, B. J. & Tamura, M. 2013, Cluster membership probability: polarimetric approach, MNRAS , 430, 1334 [Cited on page 129.]

Minchev, I., Famaey, B., Quillen, A. C., et al. 2012, Radial migration does little for Galactic disc thickening, A&A , 548, A127 [Cited on pages 19 and 78.]

Minchev, I., Martig, M., Streich, D., et al. 2015, On the Formation of Galactic Thick Disks, ApJ , 804, L9 [Cited on pages 19 and 78.]

Mink, J. 2011, WCSTools: Image Astrometry Toolkit [Cited on page 119.]

Miyachi, Y., Sakai, N., Kawata, D., et al. 2019, Stellar Overdensity in the Local Arm in Gaia DR2, ApJ, 882, 48 [Cited on pages 27 and 28.]

Momany, Y., Zaggia, S., Gilmore, G., et al. 2006, Outer structure of the Galactic warp and flare: explaining the Canis Major over-density, A&A , 451, 515 [Cited on pages 15 and 17.]

Monet, D. G. 1998, in American Astronomical Society Meeting Abstracts, Vol. 193, American Astronomical Society Meeting Abstracts, 120.03 [Cited on page 108.]

Monet, D. G., Levine, S. E., Canzian, B., et al. 2003, The USNO-B Catalog, AJ, 125, 984 [Cited on page 108.]

Morgan, W. W., Sharpless, S., & Osterbrock, D. 1952, Some features of galactic structure in the neighborhood of the Sun., AJ, 57, 3 [Cited on page 5.]

Morgan, W. W., Whitford, A. E., & Code, A. D. 1953, Studies in Galactic Structure. I. a Preliminary Determination of the Space Distribution of the Blue Giants., ApJ, 118, 318 [Cited on page 5.]

Nakanishi, H. & Sofue, Y. 2003, Three-Dimensional Distribution of the ISM in the Milky Way Galaxy: I. The H I Disk, PASJ, 55, 191 [Cited on pages 15 and 17.]

Narayan, C. A. & Jog, C. J. 2002, Vertical scaleheights in a gravitationally coupled, three-component Galactic disk, A&A , 394, 89 [Cited on pages 18, 19, and 78.]

NASA/IPAC Infrared Science Archive. 2020, WISE All-Sky 4-band Atlas Coadded Images [Cited on page 121.]

Nassau, J. J. & Morgan, W. W. 1951, Distribution of Early Type Stars of High Luminosity Near the Galactic Equator, Publications of Michigan Observatory, 10, 43 [Cited on page 5.]

Ness, M., Freeman, K., Athanassoula, E., et al. 2013, ARGOS - III. Stellar populations in the Galactic bulge of the Milky Way, MNRAS , 430, 836 [Cited on page 8.]

Ness, M. & Lang, D. 2016, The X-shaped Bulge of the Milky Way Revealed by WISE, AJ, 152, 14 [Cited on page 8.]

Nishiyama, S., Nagata, T., Baba, D., et al. 2005, A Distinct Structure inside the Galactic Bar, ApJ , 621, L105 [Cited on pages 9 and 34.]

Oort, J. H., Kerr, F. J., & Westerhout, G. 1958, The galactic system as a spiral nebula (Council Note), MNRAS , 118, 379 [Cited on page 15.]

Oort, J. H. & Muller, C. A. 1952, Spiral Structure and Interstellar Emission, Monthly Notes of the Astronomical Society of South Africa, 11, 65 [Cited on page 6.]

Ostriker, E. C. & Binney, J. J. 1989, Warped and tilted galactic discs, MNRAS , 237, 785 [Cited on page 16.]

Paczyński, B. & Stanek, K. Z. 1998, Galactocentric Distance with the Optical Gravitational Lensing Experiment and HIPPARCOS Red Clump Stars, ApJ , 494, L219 [Cited on pages 28 and 34.]

Pancharatnam, S. 1955, Achromatic combinations of birefringent plates, Proceedings of the Indian Academy of Sciences - Section A, 41, 137 [Cited on page 94.]

Pandey, A. K., Eswaraiah, C., Sharma, S., et al. 2013, Optical Photometric and Polarimetric Investigation of NGC 1931, ApJ, 764, 172 [Cited on pages 154 and 186.]

Pandey, J. C., Singh, S., Yadav, R. K. S., et al. 2023, Upgradation of AIMPOL Instrument on the 104-cm Sampurnanand Telescope of ARIES, Journal of Astronomical Instrumentation, 12, 2240008 [Cited on page 96.]

Panopoulou, G. V., Hensley, B. S., Skalidis, R., Blinov, D., & Tassis, K. 2019, Extreme starlight polarization in a region with highly polarized dust emission, A&A , 624, L8 [Cited on page 138.]

Patat, F. & Romaniello, M. 2006, Error Analysis for Dual-Beam Optical Linear Polarimetry, PASP, 118, 146 [Cited on page 120.]

Pelgrims, V., Panopoulou, G. V., Tassis, K., et al. 2023, Starlight-polarization-based tomography of the magnetized ISM: PASIPHAE's line-of-sight inversion method, A&A , 670, A164 [Cited on pages 22, 86, and 181.]

Pietrukowicz, P., Kozłowski, S., Skowron, J., et al. 2015, Deciphering the 3D Structure of the Old Galactic Bulge from the OGLE RR Lyrae Stars, ApJ, 811, 113 [Cited on pages 8, 9, and 34.]

Plevne, O., Önal Taş, Ö., Bilir, S., & Seabroke, G. M. 2020, Multiwavelength Absolute Magnitudes and Colors of Red Clump Stars in the Gaia Era, ApJ, 893, 108 [Cited on pages 29 and 43.]

Poggio, E., Drimmel, R., Andrae, R., et al. 2020, Evidence of a dynamically evolving Galactic warp, Nature Astronomy, 4, 590 [Cited on pages 15, 16, and 81.]

Poggio, E., Drimmel, R., Cantat-Gaudin, T., et al. 2021, Galactic spiral structure revealed by Gaia EDR3, A&A , 651, A104 [Cited on pages 56 and 58.]

Poggio, E., Drimmel, R., Lattanzi, M. G., et al. 2018, The Galactic warp revealed by Gaia DR2 kinematics, MNRAS , 481, L21 [Cited on pages 15 and 16.]

Poggio, E., Drimmel, R., Smart, R. L., Spagna, A., & Lattanzi, M. G. 2017, The kinematic signature of the Galactic warp in Gaia DR1. I. The Hipparcos subsample, A&A , 601, A115 [Cited on page 15.]

Queiroz, A., Anders, F., Chiappini, C., et al. 2020, From the bulge to the outer disc: StarHorse stellar parameters, distances, and extinctions for stars in APOGEE DR16 and other spectroscopic surveys, Astronomy & Astrophysics, 638, A76 [Cited on pages 16 and 49.]

Quinn, T. & Binney, J. 1992, Galactic accretion and angular momentum re-orientation, MNRAS , 255, 729 [Cited on page 16.]

Ramaprakash, A. N., Gupta, R., Sen, A. K., & Tandon, S. N. 1998, An imaging polarimeter (IMPOL) for multi-wavelength observations, A&AS , 128, 369 [Cited on page 113.]

Rautela, B. S., Joshi, G. C., & Pandey, J. C. 2004, ARIES imaging polarimeter., Bulletin of the Astronomical Society of India, 32, 159 [Cited on page 96.]

Reid, M. J., Menten, K. M., Brunthaler, A., et al. 2019, Trigonometric Parallaxes of High-mass Star-forming Regions: Our View of the Milky Way, ApJ, 885, 131 [Cited on pages 13, 57, 58, 99, 183, and 184.]

Reid, M. J., Menten, K. M., Brunthaler, A., et al. 2014, Trigonometric Parallaxes of High Mass Star Forming Regions: The Structure and Kinematics of the Milky Way, ApJ, 783, 130 [Cited on pages 55, 58, and 179.]

Reid, M. J., Menten, K. M., Zheng, X. W., et al. 2009, Trigonometric Parallaxes of Massive Star-Forming Regions. VI. Galactic Structure, Fundamental Parameters, and Noncircular Motions, ApJ, 700, 137 [Cited on page 145.]

Reshetnikov, V. & Combes, F. 1998, Statistics of optical WARPS in spiral disks, A&A , 337, 9 [Cited on page 14.]

Reylé, C., Marshall, D. J., Robin, A. C., & Schultheis, M. 2009, The Milky Way's external disc constrained by 2MASS star counts, A&A , 495, 819 [Cited on pages 15, 17, 20, and 76.]

Rezaei Kh., S., Bailer-Jones, C. A. L., Hogg, D. W., & Schultheis, M. 2018, Detection of the Milky Way spiral arms in dust from 3D mapping, A&A , 618, A168 [Cited on pages 21 and 86.]

Rizzi, L., Held, E. V., Saviane, I., Tully, R. B., & Gullieuszik, M. 2007, The distance to the Fornax dwarf spheroidal galaxy, MNRAS , 380, 1255 [Cited on page 35.]

Robin, A. C., Reylé, C., Derrière, S., & Picaud, S. 2004, Erratum: A synthetic view on structure and evolution of the Milky Way, A&A , 416, 157 [Cited on page 44.]

Romero-Gómez, M., Mateu, C., Aguilar, L., Figueras, F., & Castro-Ginard, A. 2019, Gaia kinematics reveal a complex lopsided and twisted Galactic disc warp, A&A , 627, A150 [Cited on pages 15, 16, 54, 74, 76, and 81.]

Ruiz-Dern, L., Babusiaux, C., Arenou, F., Turon, C., & Lallement, R. 2018, Empirical photometric calibration of the Gaia red clump: Colours, effective temperature, and absolute magnitude, A&A , 609, A116 [Cited on pages 29, 43, and 64.]

Saha, K., Levine, E. S., Jog, C. J., & Blitz, L. 2009, The Milky Way's Dark Matter Halo Appears to be Lopsided, ApJ, 697, 2015 [Cited on page 18.]

Salaris, M., Percival, S., Brocato, E., Raimondo, G., & Walker, A. R. 2003, The Distance to the Large Magellanic Cloud Cluster NGC 1866 and the Surrounding Field, ApJ, 588, 801 [Cited on page 35.]

Sale, S. E., Drew, J. E., Barentsen, G., et al. 2014, A 3D extinction map of the northern Galactic plane based on IPHAS photometry, MNRAS , 443, 2907 [Cited on page 21.]

Sánchez-Saavedra, M. L., Battaner, E., & Florido, E. 1990, Frequency of warped spiral galaxies at visible wavelengths., MNRAS , 246, 458 [Cited on page 14.]

Sánchez-Saavedra, M. L., Battaner, E., Guijarro, A., López-Corredoira, M., & Castro-Rodríguez, N. 2003, A catalog of warps in spiral and lenticular galaxies in the Southern hemisphere, A&A , 399, 457 [Cited on page 14.]

Sánchez-Salcedo, F. J., Saha, K., & Narayan, C. A. 2008, The thickness of HI in galactic discs under MOdified Newtonian Dynamics: theory and application to the Galaxy, MNRAS , 385, 1585 [Cited on page 18.]

Sanna, A., Reid, M. J., Dame, T. M., Menten, K. M., & Brunthaler, A. 2017, Mapping spiral structure on the far side of the Milky Way, Science, 358, 227 [Cited on page 11.]

Sanna, A., Reid, M. J., Moscadelli, L., et al. 2009, Trigonometric Parallaxes of Massive Star-Forming Regions. VII. G9.62+0.20 and the Expanding 3 kpc ARM, ApJ, 706, 464 [Cited on page 21.]

Santiago, B. X., Brauer, D. E., Anders, F., et al. 2016, Spectro-photometric distances to stars: A general purpose Bayesian approach, A&A , 585, A42 [Cited on page 49.]

Sariya, D., Jiang, I.-G., Bisht, D., Yadav, R., & Rangwal, G. 2021, Astrometric and Photometric Investigation of Three Old Age Open Clusters in the Gaia Era: Berkeley 32, Berkeley 98, and King 23, AJ, 161, 102S [Cited on page 132.]

Schmidt, G. D., Elston, R., & Lupie, O. L. 1992, The Hubble Space Telescope Northern-Hemisphere Grid of Stellar Polarimetric Standards, AJ, 104, 1563 [Cited on pages xxi, 119, 156, 157, 195, and 196.]

Schultheis, M., Chen, B. Q., Jiang, B. W., et al. 2014, Mapping the Milky Way bulge at high resolution: the 3D dust extinction, CO, and X factor maps, A&A , 566, A120 [Cited on page 21.]

Searle, L. & Zinn, R. 1978, Composition of halo clusters and the formation of the galactic halo., ApJ, 225, 357 [Cited on page 7.]

Seaton, M. J. 1979, Interstellar extinction in the UV., MNRAS , 187, 73 [Cited on page 138.]

Sellwood, J. A. 2013, in Planets, Stars and Stellar Systems. Volume 5: Galactic Structure and Stellar Populations, ed. T. D. Oswalt & G. Gilmore, Vol. 5, 923 [Cited on pages 15, 18, and 78.]

Serkowski, K. 1965, Polarization of Galactic Clusters M25, NGC 869, 884, 1893, 2422, 6823, 6871, and Association VI Cygni., ApJ, 141, 1340 [Cited on page 198.]

Serkowski, K., Mathewson, D. S., & Ford, V. L. 1975, Wavelength dependence of interstellar polarization and ratio of total to selective extinction., ApJ, 196, 261 [Cited on pages 101 and 139.]

Shao, Z. & Zhao, J. 1996, Effectivity of membership probability calculations for clustering celestial bodies, Acta Astron. Sinica, 37, 377S [Cited on page 134.]

Shapley, H. 1918a, Globular clusters and the structure of the galactic system, Publications of the Astronomical Society of the Pacific, 30, 42 [Cited on page 4.]

Shapley, H. 1918b, Studies based on the colors and magnitudes in stellar clusters. VII. The distances, distribution in space, and dimensions of 69 globular clusters., ApJ, 48, 154 [Cited on page 4.]

Shapley, H. 1919a, Studies based on the colors and magnitudes in stellar clusters. XI. A comparison of the distances of various celestial objects., ApJ, 49, 249 [Cited on page 4.]

Shapley, H. 1919b, Studies based on the colors and magnitudes in stellar clusters. XII. Remarks on the arrangement of the sidereal universe., ApJ, 49, 311 [Cited on page 4.]

Shapley, H. & Shapley, M. B. 1919, Studies based on the colors and magnitudes in stellar clusters. XIV. Further remarks on the structure of the galactic system., ApJ, 50, 107 [Cited on page 4.]

Sharma, S., Ghosh, A., Ojha, D. K., et al. 2020, The disintegrating old open cluster Czernik 3, MNRAS , 498, 2309 [Cited on pages 118, 119, 124, 131, 132, 134, 135, and 142.]

Shen, J. & Sellwood, J. A. 2006, Galactic warps induced by cosmic infall, MNRAS , 370, 2 [Cited on page 16.]

Siebert, A., Bienaymé, O., & Soubiran, C. 2003, Vertical distribution of Galactic disk stars. II. The surface mass density in the Galactic plane, A&A , 399, 531 [Cited on page 35.]

Singh, S., Pandey, J. C., Yadav, R. K. S., & Medhi, B. J. 2020, Optical Linear Polarization toward the Open Star Cluster Casado Alessi 1, AJ, 159, 99 [Cited on pages 86 and 121.]

Sirko, E., Goodman, J., Knapp, G. R., et al. 2004, Blue Horizontal-Branch Stars in the Sloan Digital Sky Survey. II. Kinematics of the Galactic Halo, AJ, 127, 914 [Cited on page 7.]

Skowron, D. M., Skowron, J., Mróz, P., et al. 2019a, A three-dimensional map of the Milky Way using classical Cepheid variable stars, Science, 365, 478 [Cited on pages 14 and 15.]

Skowron, D. M., Skowron, J., Mróz, P., et al. 2019b, Mapping the Northern Galactic Disk Warp with Classical Cepheids, Acta Astron., 69, 305 [Cited on pages 15 and 76.]

Skrutskie, M. F., Cutri, R. M., Stiening, R., et al. 2006, The Two Micron All Sky Survey (2MASS), AJ, 131, 1163 [Cited on page 108.]

Sohn, B. W. 2011, Ricean Bias Correction in Linear Polarization Observation, Journal of Astronomy and Space Sciences, 28, 267 [Cited on page 120.]

Soubiran, C., Bienaymé, O., & Siebert, A. 2003, Vertical distribution of Galactic disk stars. I. Kinematics and metallicity, A&A , 398, 141 [Cited on pages 33 and 35.]

Sparke, L. S. & Gallagher, John S., I. 2000, Galaxies in the universe : an introduction [Cited on page 9.]

Stanek, K. Z. & Garnavich, P. M. 1998, Distance to M31 with the Hubble Space Telescope and HIPPARCOS Red Clump Stars, ApJ , 503, L131 [Cited on page 35.]

Stanek, K. Z., Mateo, M., Udalski, A., et al. 1994, Color-Magnitude Diagram Distribution of the Bulge Red Clump Stars: Evidence for the Galactic Bar, ApJ , 429, L73 [Cited on page 34.]

Streich, D., de Jong, R. S., Bailin, J., et al. 2016, Extragalactic archeology with the GHOSTS Survey. I. Age-resolved disk structure of nearby low-mass galaxies, A&A , 585, A97 [Cited on page 78.]

Taylor, M. B. 2006, in Astronomical Society of the Pacific Conference Series, Vol. 351, Astronomical Data Analysis Software and Systems XV, ed. C. Gabriel, C. Arviset, D. Ponz, & S. Enrique, 666 [Cited on page 39.]

Ting, Y.-S., Hawkins, K., & Rix, H.-W. 2018, A Large and Pristine Sample of Standard Candles across the Milky Way: ~100,000 Red Clump Stars with 3% Contamination, ApJ , 858, L7 [Cited on page 35.]

Topasna, G. A., Daman, E. A., & Kaltcheva, N. T. 2017, Interstellar Polarization and Extinction towards the Open Cluster NGC 457, PASP, 129, 104201 [Cited on page 121.]

Topasna, G. A., Gibson, S. D., & Kaltcheva, N. T. 2022, Interstellar Extinction and Polarization of Stars in the Open Cluster NGC 6709, PASP, 134, 084301 [Cited on page 191.]

Trumpler, R. J. 1930a, Absorption of Light in the Galactic System, PASP, 42, 214 [Cited on page 5.]

Trumpler, R. J. 1930b, Preliminary results on the distances, dimensions and space distribution of open star clusters, Lick Observatory Bulletin, 420, 154 [Cited on page 5.]

Udalski, A. 1998, The Optical Gravitational Lensing Experiment. The Distance Scale: Galactic Bulge – LMC – SMC., Acta Astron., 48, 113 [Cited on page 35.]

Uppal, N., Ganesh, S., & Bisht, D. 2022, Optical Linear Polarization Study toward Czernik 3 Open Cluster at Different Spatial Scales, AJ, 164, 31 [Cited on pages 22 and 24.]

Uppal, N., Ganesh, S., & Schultheis, M. 2023, The Outer spiral arm of the Milky Way using red clump stars. Tracing the asymmetry across the disc, A&A , 673, A99 [Cited on pages 23 and 24.]

Uppal, N., Ganesh, S., & Schultheis, M. 2024, Warp and flare of the old Galactic disc as traced by the red clump stars, MNRAS , 527, 4863 [Cited on page 24.]

Vallée, J. P. 2022, The observed age gradient in the Milky Way—as a test for theories of spiral arm structure, Ap&SS, 367, 26 [Cited on page 14.]

Van de Hulst, H. C., Muller, C. A., & Oort, J. H. 1954, The spiral structure of the outer part of the galactic system derived from the hydrogen emission at 21 cm wavelength, Bulletin of the Astronomical Institutes of the Netherlands, 12, 117 [Cited on page 6.]

Vergne, M. M., Feinstein, C., & Martínez, R. 2007, Optical multicolor polarization observations in the region of the open cluster NGC 5749, A&A , 462, 621 [Cited on page 126.]

Villalobos, Á. & Helmi, A. 2008, Simulations of minor mergers - I. General properties of thick discs, MNRAS , 391, 1806 [Cited on pages 19 and 78.]

Virtanen, P., Gommers, R., Oliphant, T. E., et al. 2020, SciPy 1.0: Fundamental Algorithms for Scientific Computing in Python, Nature Methods, 17, 261 [Cited on pages 107 and 109.]

Wan, J.-C., Liu, C., & Deng, L.-C. 2017, Red Clump Stars from LAMOST II: the outer disc of the Milky Way, Research in Astronomy and Astrophysics, 17, 079 [Cited on page 20.]

Wang, H.-F., Liu, C., Xu, Y., Wan, J.-C., & Deng, L. 2018, Mapping the Milky Way with LAMOST- III. Complicated spatial structure in the outer disc, MNRAS , 478, 3367 [Cited on pages 15, 17, 19, 20, 35, 68, and 78.]

Wang, H. F., López-Corredoira, M., Huang, Y., et al. 2020, Mapping the Galactic Disk with the LAMOST and Gaia Red Clump Sample. VI. Evidence for the Long-lived Nonsteady Warp of Nongravitational Scenarios, ApJ, 897, 119 [Cited on pages 16 and 81.]

Wardle, J. F. C. & Kronberg, P. P. 1974, The linear polarization of quasi-stellar radio sources at 3.71 and 11.1 centimeters., ApJ, 194, 249 [Cited on page 120.]

Weaver, H. & Williams, D. R. W. 1974, The Berkeley Low-Latitude Survey of Neutral Hydrogen Part III. an Extension to Latitude +30°, Profiles and Contour Maps, A&AS , 17, 251 [Cited on page 15.]

Wegg, C. & Gerhard, O. 2013, Mapping the three-dimensional density of the Galactic bulge with VVV red clump stars, MNRAS , 435, 1874 [Cited on pages 8 and 9.]

Weinberg, M. D. & Blitz, L. 2006, A Magellanic Origin for the Warp of the Galaxy, ApJ , 641, L33 [Cited on page 16.]

Wenger, T. V., Balser, D. S., Anderson, L. D., & Bania, T. M. 2018, Kinematic Distances: A Monte Carlo Method, ApJ, 856, 52 [Cited on page 153.]

Westerhout, G. 1957, The distribution of atomic hydrogen in the outer parts of the Galactic System, Bull. Astron. Inst. Netherlands, 13, 201 [Cited on page 15.]

Whittet, D. 2003, Dust in the galactic environment, Dust in the galactic environment [Cited on pages 89, 138, and 139.]

Whittet, D. C. B. 1992, Dust in the galactic environment [Cited on page 139.]

Wilking, B. A., Lebofsky, M. J., Martin, P. G., Rieke, G. H., & Kemp, J. C. 1980, The wavelength dependence of interstellar linear polarization., ApJ, 235, 905 [Cited on page 139.]

Wilking, B. A., Lebofsky, M. J., & Rieke, G. H. 1982, The wavelength dependence of interstellar linear polarization: stars with extreme values of lambda max., AJ, 87, 695 [Cited on page 139.]

Willett, K. W., Lintott, C. J., Bamford, S. P., et al. 2013, Galaxy Zoo 2: detailed morphological classifications for 304 122 galaxies from the Sloan Digital Sky Survey, MNRAS , 435, 2835 [Cited on page 11.]

Wouterloot, J. G. A., Brand, J., Burton, W. B., & Kwee, K. K. 1990, IRAS sources beyond the solar circle. II. Distribution in the galactic warp., A&A , 230, 21 [Cited on page 15.]

Wright, T. 1750, An Original Theory or New Hypothesis of the Universe. . . (London, England: H. Chapelle, 1750) [Cited on page 3.]

Xu, Y., Hou, L. G., Bian, S. B., et al. 2021, Local spiral structure based on the Gaia EDR3 parallaxes, A&A , 645, L8 [Cited on page 54.]

Xu, Y., Hou, L.-G., & Wu, Y.-W. 2018, The spiral structure of the Milky Way, Research in Astronomy and Astrophysics, 18, 146 [Cited on page 11.]

Xu, Y., Liu, C., Tian, H., et al. 2020, Exploring the Perturbed Milky Way Disk and the Substructures of the Outer Disk, ApJ, 905, 6 [Cited on pages 20 and 78.]

Xu, Y., Reid, M. J., Zheng, X. W., & Menten, K. M. 2006, The Distance to the Perseus Spiral Arm in the Milky Way, Science, 311, 54 [Cited on page 149.]

Yu, Y., Wang, H.-F., Cui, W.-Y., et al. 2021a, The Flare and Warp of the Young Stellar Disk Traced with LAMOST DR5 OB-type Stars, ApJ, 922, 80 [Cited on pages 15, 17, 18, 19, 20, 35, 54, 70, 73, 77, and 78.]

Yu, Z., Li, J., Chen, B., et al. 2021b, Mapping the Galactic Disk with the LAMOST and Gaia Red Clump Sample. VII. The Stellar Disk Structure Revealed by the Mono-abundance Populations, ApJ, 912, 106 [Cited on pages 17 and 35.]

Yusifov, I. 2004, in The Magnetized Interstellar Medium, ed. B. Uyaniker, W. Reich, & R. Wielebinski, 165–169 [Cited on pages 18, 70, 71, 76, 77, and 80.]

Zacharias, N., Finch, C. T., Girard, T. M., et al. 2013, The Fourth US Naval Observatory CCD Astrograph Catalog (UCAC4), AJ, 145, 44 [Cited on page 119.]

Zhao, G., Qiu, H. M., & Mao, S. 2001, High-Resolution Spectroscopic Observations of Hipparcos Red Clump Giants: Metallicity and Mass Determinations, ApJ , 551, L85 [Cited on page 33.]

Zoccali, M., Hill, V., Lecureur, A., et al. 2008, The metal content of bulge field stars from FLAMES-GIRAFFE spectra. I. Stellar parameters and iron abundances, A&A , 486, 177 [Cited on page 8.]

Zoccali, M. & Valenti, E. 2016, The 3D Structure of the Galactic Bulge, PASA, 33, e025 [Cited on pages 8 and 34.]

Zucker, C., Speagle, J. S., Schlafly, E. F., et al. 2020, A compendium of distances to molecular clouds in the Star Formation Handbook, A&A , 633, A51 [Cited on page 144.]